Structural and charge transporting properties of pure liquid crystalline organic semiconductors and composites for applications in organic electronics

Kirill Kondratenko

UNIVERSITE DU LITTORAL COTE D'OPALE

Doctoral School **Sciences de la Matière, du Rayonnement et de l'Environnement (SMRE 104)**

Unité de Dynamique et Structure des Matériaux Moléculaires

Thesis by **Kirill Kondratenko**

In order to become **Doctor of Philosophy in Physics**

Specialty **Condensed matter, Materials and Components**

Structural and charge transporting properties of pure liquid crystalline organic semiconductors and composites for applications in organic electronics

---

Thesis supervised by

	Christian LEGRAND	Supervisor
	Abdelylah DAOUDI	Co-Supervisor
	Yahia BOUSSOUALEM	Co-Monitor

Committee members

Referees	Jeroen BEECKMAN	Professor at Ghent University	
	Bernard RATIER	Professor at Université de Limoges	
Examiners	Kamal LMIMOUNI	Professor at Université de Lille	*Committee president*
	Marc TERNISIEN	Associate Professor at Université de Toulouse	
	Laurence VIGNAU	Professor at Université de Bordeaux	
Supervisors	Christian LEGRAND	Professor at ULCO	
	Abdelylah DAOUDI	Professor at ULCO	
	Yahia BOUSSOUALEM	Associate Professor at ULCO	

UNIVERSITE DU LITTORAL COTE D'OPALE

Ecole doctorale **Sciences de la Matière, du Rayonnement et de l'Environnement (SMRE 104)**

Unité de recherche **Unité de Dynamique et Structure des Matériaux Moléculaires**

Thèse par **Kirill Kondratenko**

En vue de l'obtention du grade de **Docteur en Physique**

Spécialité **Milieux denses, Matériaux et Composants**

Propriétés structurales et de transport de charge de semi-conducteurs organiques cristaux liquides purs et de composites pour applications en électronique organique

---

Thèse dirigée par

	Christian LEGRAND	Directeur
	Abdelylah DAOUDI	Co-Directeur
	Yahia BOUSSOUALEM	Co-Encadrant

Composition du jury

Rapporteurs	Jeroen BEECKMAN	Professeur à l'Université de Gand	
	Bernard RATIER	Professeur à l'Université de Limoges	
Examinateurs	Kamal LMIMOUNI	Professeur à l'Université de Lille	*Président du jury*
	Marc TERNISIEN	MCF à l'Université de Toulouse	
	Laurence VIGNAU	Professeur à l'Université de Bordeaux	
Directeurs de thèse	Christian LEGRAND	Professeur à l'ULCO	
	Abdelylah DAOUDI	Professeur à l'ULCO	
	Yahia BOUSSOUALEM	MCF à l'ULCO	

Dans la vie, rien n'est à craindre, tout est à comprendre.

Marie Curie

Acknowledgment

This PhD thesis is a result of three-year-long journey, which I would not be able to complete alone. This section is dedicated to people who helped me on my way to becoming a Doctor of Philosophy in Physics.

First of all, I would like to thank Pr. Abdelhak Hadj Sahraoui, the director of Unité de Dynamique et Structure des Matériaux Moléculaires (UDSMM), where I have conducted my research. His help and support have allowed me to succeed in this endeavor.

Next, I would like to thank my thesis supervisor, Pr. Christian Legrand, for accepting my candidature for this PhD project, as well as his guidance and thorough help with experimental part, fruitful discussions and his wisdom which altogether benefited the present work.

I am sincerely thankful to my thesis co-supervisor, Pr. Abdelylah Daoudi. I learned a great deal from him. He is somebody who always listens and has an open mind for new ideas and discussions. In our work, he always supported and encouraged me to pursuit my project despite numerous difficulties. His professionalism and experience has helped me to bring out the best of my experimental results and compile this manuscript.

I am grateful to Dr. Yahia Boussoualem, with whom we worked side by side every day for over last three years. He is the person who first introduced me to the topic of liquid crystals, when I arrived at UDSMM for my Master 2 internship. He was my mentor during that time, and with his contribution I have completed my Master studies, which has allowed me to join this PhD project. He was further directly involved with my research, and his availability, help and support were indeed invaluable.

My gratitude is also extended to all committee members: rapporteurs Pr. Bernard Ratier (XLIM, Université de Limoges) and Pr. Jeroen Beeckman (Ghent University) and examiners Pr. Laurence Vignau (IMS Bordeaux, Université de Bordeaux), Dr. Marc Ternisien (LAPLACE, Université de Toulouse) and Pr. Kamal Lmimouni (IEMN, Université de Lille). I am sincerely thankful to them for their time and expertise put into the evaluation of this work, as well as their participation in my defense.

I would like to express my gratitude to our research engineer, Benoît Duponchel, for his hard work and availability. His great experience and deep knowledge of various experimental techniques have enabled me to learn by his side and obtain the results without which the present work would not be possible.

I am thankful to Pr. Stephan Longuemart, who taught me many things about development of experimental setups, instrument programming and signal conditioning. His pedagogical gift has also allowed me to extend my knowledge in condensed matter physics.

I am also thankful to Dr. Dharmendra Pratap Singh, whose great energy, curiosity and cheerful attitude helped to keep my morale up during these years. His ideas always inspired me and his perseverance showed me a great personal example.

I was delighted by the chance to work with my colleagues from UDSMM. I have shared many moments of my work and spare time with them: Michael Depriester, Sylvain Delenclos, Mathieau Bardoux, Fabrice Goutier, Philippe Hus, Abdelaziz Elass, Frederic Dubois, Freddy Krasinsky and others.

I am particularly thankful to Veronique and Virginie, whose organizational and administrative talents are greatly appreciated. Also, their homemade cakes and cookies are a true delight.

It would be impossible to accomplish the multidisciplinary goals of my PhD project without the help from other people outside of UDSMM. In the beginning of this PhD, my co-supervisor, Pr. Daoudi, has introduced me to his collaborator, Pr. Nicolae Hurduc from Technical University «Gheorghe Asachi» in Iasi, Romania. His expertise as well as his open mind has helped us to establish the preliminary chemical structure of perspective materials based on 2-amino-anthracene. He has also granted us his support in establishing a collaboration with the Laboratory of Natural and Synthetic Polymers at his university. Professor Dan Scutaru, who was the head of that laboratory at the time, has generously accepted my candidature to visit his laboratory in the end of the second year of my PhD. During the one month stay (which was funded by Collège doctoral Lille Nord de France) I have had chance to work with his team and was thoroughly helped in the synthetic procedures which have resulted in the new material presented in the Chapter 4 of the present manuscript. I am especially thankful to Dr. Irina Carlescu and Dr. Simeon Aurel for their collaborative work and great help.

I express my sincere gratitude to Dr. Pierre-Edouard Danjou from UCEIV, ULCO for his great help with purification of my substances, as well as characterization of their chemical structure.

I am thankful to Pr. Arnaud Cuisset and Dr. Daniel Fontanari from LPCA, ULCO for their support and great advices on the *ab initio* simulations.

I would like to thank as well Dr. Jean-François Blach from Université d'Artois, who was my supervisor during the second year of my Master studies, where I was first introduced to Raman spectroscopy. He also helped me to carry out the experiments at his facilities in Lens during my second year of PhD.

I greatly appreciate the help received from Pierre Kulinski in preparation of facilities for the practical classes of physics and Amaury Kasprowiak for his help with optical spectroscopy.

I am also thankful to the PhD students and postdocs from ULCO for the good moments which will stay in my memory: Karim, Allen, Eliane, Elie, Nassima, Said, Yoan, Yaochen, Alla, Sarah, Asmita, Clémence, Tarek, Corentin, Somenath and others.

Finally, I would like to express my sincere gratitude to my family, friends and everybody else who supported we along the way. I consider myself lucky to be surrounded by these people during my lifetime. I hope that I did not forget to mention anybody in this section. If I did, please forgive me.

Kirill
17th of December 2019

Structural and charge transporting properties of pure liquid crystalline organic semiconductors and composites for applications in organic electronics

Abstract

This thesis is dedicated to various aspects of liquid crystalline (LC) organic semiconductors (OSCs) in regard to their applications in the field of organic electronics.

The first part of this work deals with a well-known LC OSC based on phenylnaphthalene. Two major ways of performance improvement are proposed and investigated: stabilization of LC structure by *in situ* photo-polymerization and introduction of electron acceptor doping impurity. In the first case, the influence of polymer network on mesophase order and charge transport is investigated by conventional experimental techniques and Time-of-Flight (TOF) mobility measurements. For the doped materials, *ab initio* calculations are employed to predict their spectroscopic properties which is exhaustively compared with the experimental data obtained by optical and vibrational spectroscopy. The charge transport is studied by TOF method in the mesophase, while crystalline phase is investigated via conductive atomic force microscopy. A prototype of organic field effect transistor (OFET) is prepared to obtain an estimate of performance for a relevant real-world application.

The second part of this work includes design and synthesis of a novel LC semiconductor based on anthracene, additional attention is made to obtain an easy-to-make and low production cost material. Novel molecule is fully characterized: molecular structure is confirmed by relevant techniques; frontier molecular energy levels are studied by optical spectroscopy and cyclic voltammetry and confronted to values obtained via *ab initio* calculations; mesophase properties are investigated by optical microscopy and scanning calorimetry. Charge transporting properties are characterized by means of an OFET device: it is found that new anthracene-molecule exhibits significant improvement of field-effect hole mobility over previously studied phenyl naphthalene derivative. Finally, photoconductive properties of the novel material are addressed in order to investigate its potential applications to organic phototransistors.

Keywords: organic semiconductors, liquid crystals, photopolymers, doping, time of flight, organic field effect transistors

Propriétés structurales et de transport de charge de semi-conducteurs organiques cristaux liquides purs et de composites pour applications en électronique organique

Résumé

Cette thèse est dédiée à divers aspects des semi-conducteurs organiques (SCO) cristaux liquides (CL) qui concernent leurs applications dans le domaine de l'électronique organique.

La découverte au début du XIX siècle du phénomène de photo-conductivité dans les cristaux d'anthracène a marqué l'apparition d'une nouvelle classe de matériaux organiques aux propriétés semi-conductrices. Il a été clairement démontré dans les années 1960, par la découverte du phénomène d'électroluminescence dans les matériaux organiques π-conjugué que les SCOs possèdent un réel intérêt pratique. La découverte des propriétés de transport de charge électrique dans le poly-acétylène (Figure 1) en 1977 [1] a apporté le prix Nobel de chimie à Heeger, MacDiarmid et Shirakawa en 2000 pour leur contribution au développement de l'électronique organique.

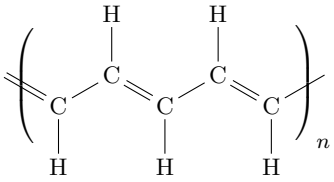

Figure 1 – Système π-conjugué de base, poly-acétylène.

Depuis les années 1980, plusieurs exemples d'applications pratiques (diodes luminescentes, dispositifs photovoltaïques, transistors à effet de champ) ont vu leur performances augmenter de façon remarquable. Aujourd'hui, l'une des applications les plus développés concerne les diodes luminescentes (OLEDs) qui sont en train de remplacer les dispositifs classiques à base des cristaux liquides dans le domaine de l'affichage.

Bases théoriques

Premièrement, les concepts basiques concernant les matériaux SCO nécessitent une introduction détaillée. Il s'agit de matériaux organiques possédant des structures π-conjugué très fortement développées à travers leur structure moléculaire, ce qui permet d'avoir un certain degré de *délocalisation* de densité des électrons.

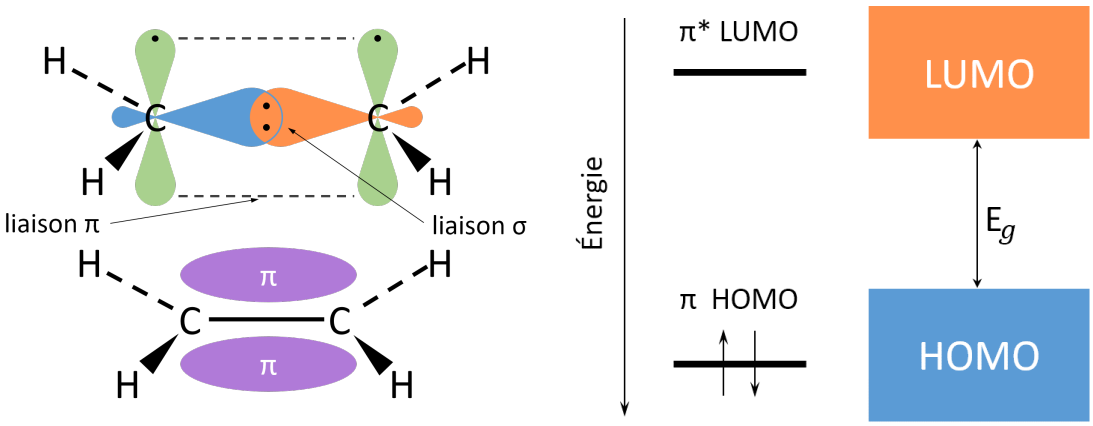

(a) (b)

Figure 2 – (a) Structure des liaisons σ et π dans la molécule d'éthylène. (b) Diagramme des niveaux d'énergies des orbitaux moléculaires pour une simple molécule (à gauche) et dans le SCO massif (à droite).

Les structures conjuguées sont majoritairement constituées d'atomes de carbone en hybridation de type sp^2 (comme dans la molécule d'éthylène, Figure 2, (a)). Cette délocalisation est une condition nécessaire afin de permettre aux porteurs de charge (les électrons et les trous) de se déplacer à travers la structure moléculaire ou une chaine polymérique, ou même sauter d'une molécule à l'autre (souvent appelée "hopping") [2]. Il faut bien souligner que le transport est effectué par les électrons situés dans le domaine énergétique des liaisons π, et les électrons impliqués dans les liaisons σ ne sont pas concernés par ce procédé.

Les notions des semi-conducteurs classiques, dit inorganiques (SCIs) sont bien applicables aux SCOs. Le concept d'une bande interdite (le "band gap", E_g) dans le cas des SCOs est basé sur les niveaux d'énergie des orbitales moléculaires frontières (Figure 2, (b)) : orbitale haute occupée - HO, souvent appelée HOMO (de *highest occupied molecular orbital*) et basse vacante - BV ou LUMO (de *lowest unoccupied molecular orbital*).

Cette considération est directement liée à la nature moléculaire des matériaux SCOs, qui sont des systèmes à couche d'électrons fermée, contrairement aux SCIs, où le matériau massif est à l'état solide, donc constitué d'atomes liés par des liaisons covalentes. En effet, la grande majorité des particularités des SCOs par rapport aux matériaux inorganiques est liée à leur nature moléculaire. Il s'agit de matériaux constitués de molécules ou de

chaines polymériques qui sont liées par des interactions de Van der Waals [3].

Les exemples typiques des SCOs incluent les molécules aromatiques polycycliques comme les oligoacènes (anthracène, tetracène, pentacène (Figure 3, a)) ou hétérocycles (comme plusieurs dérivés du thiophène). Un autre type des matériaux se compose de polymères conjugués (poly-para-phenylène, poly-fluorene, poly-thiophène (Figure 3, b)).

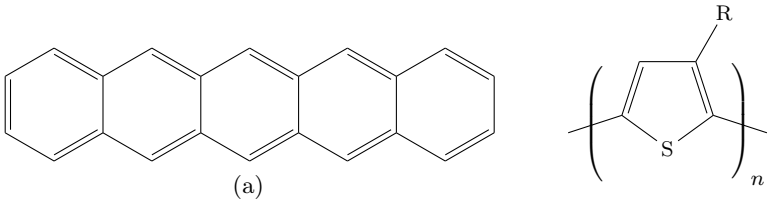

(a) (b)

Figure 3 – Exemples des SCOs les plus connus: (a) pentacène et (b) poly-thiophène .

La nature des interactions intermoléculaires intervient directement au niveau des mécanismes de transport de charge dans les matériaux SCOs. La densité de courant électrique j dans le cas d'un matériau massif peut être exprimée à l'aide de l'équation suivante :

$$j = en\mu E, \tag{1}$$

où e représente la charge élémentaire, n la densité des porteurs de charge, μ leur mobilité et E le champ électrique appliqué au matériau. On peut remarquer que j dépend de deux paramètres intrinsèques au matériau : la densité des porteurs de charge n et leur mobilité μ. Ces deux paramètres font l'objet d'une grande partie de la recherche consacrée aux SCOs. La mobilité d'un porteur de charge est généralement très influencée par l'ordre du système, donc pour les matériaux fortement désordonnés (le cas des SCOs) ce paramètre peut atteindre quelques dizaines de $\mathrm{cm}^2/(\mathrm{V\,s})$ dans le meilleur des cas. La densité des porteurs de charge est directement liée à la densité des états des électrons (ou des trous) disponibles dans un matériau, à la concentration des états "pièges" ainsi qu'à l'énergie de la bande interdite et la température.

Tenant compte de ces considérations, deux voies d'amélioration des propriétés de transport électrique pour les matériaux SCOs ont été proposées: amélioration de la mobilité par augmentation ou stabilisation d'ordre du système, ou accroissement du nombre de porteurs de charge par dopage.

Pour contrôler l'ordre d'un matériau massif d'une manière simple et efficace, on peut faire appel aux cristaux liquides. Ce type de substances possède des propriétés thermodynamiques et structurales très particulières. Généralement ils montrent un comportement dit *mésogenique*, c'est-à-dire intermédiaire entre l'état solide et liquide : une *mésophase* [4]. Il existe plusieurs types de mésophases selon la forme de la molécule du cristal liquide : calamitiques ou discotiques. Nous nous sommes intéressé aux phases calamitiques (Figure 4). Les mésophases calamitiques sont formées par des molécules en

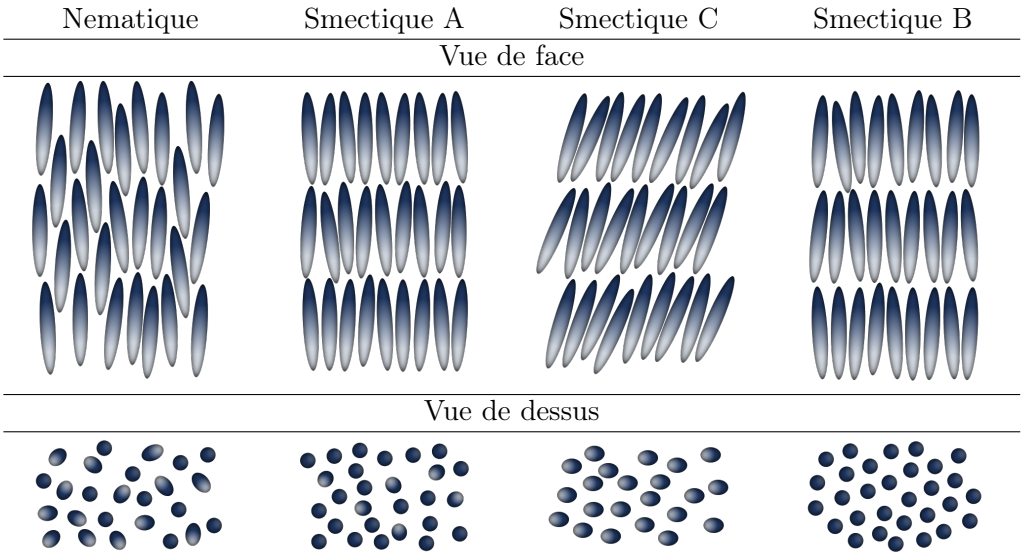

Figure 4 – Représentation schématique des mésophases calamitiques: nématique (N), smectique A (Sm_A), smectique C (Sm_C) et smectique B (Sm_B).

forme de bâtonnets et sont divisées en deux groupes : nématiques et smectiques. Les phases nématiques ne possèdent qu'un seul degré d'ordre intermoléculaire : les axes longs des molécules (dit *directeurs*) sont plus ou moins orientés dans une direction préférentielle, en revanche leurs centres de masse sont distribués de manière aléatoire (il n'y a pas d'ordre à courte distance). Les phases smectiques ont une structure plus élaborée : les molécules sont rangées sous forme de couches et leurs axes (*directeurs*) sont orientés généralement dans une même direction (sauf pour les phases torsadées). Il existe plusieurs types de

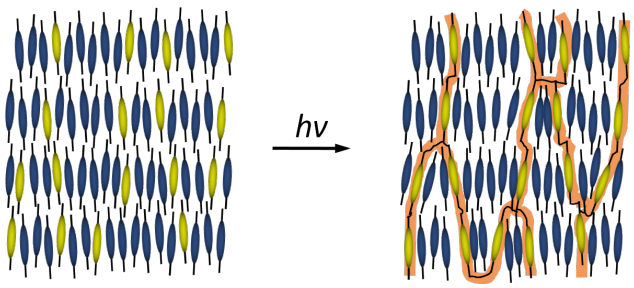

Figure 5 – Polymérisation *in situ* d'un mésogène réactif dans le massif d'un SCO.

mésophases smectiques selon l'ordre dans la couche.

Les phases les plus simples sont (Figure 4) : smectique A (les axes *directeurs* sont normaux au plan de la couche, il n'y a pas d'ordre dans la couche), smectique C (les molécules ont un certain angle de tilt dans les couches) et smectique B (idem que smectique A, mais avec un ordre local pseudo-hexagonal).

Certains SCOs présentent des propriétés mésogeniques si la forme de la molécule favorise l'organisation en structures mésomorphes. Certains travaux ont également démontré un lien fort de la mobilité des porteurs de charge avec l'ordre de la mésophase.

L'avantage de combiner les propriétés semi-conductrices avec des propriétés mésomorphes est lié à la diversité de moyens qui permettent de contrôler l'ordre et l'alignement d'un matériau par des facteurs externes : champ magnétique ou électrique, photo-alignement ou mécaniquement par l'incorporation de différents types des couches d'alignement. Dans ce travail nous exploiterons l'utilisation de matériaux composites en stabilisant la structure de la mésophase par photo polymérisation *in situ*.

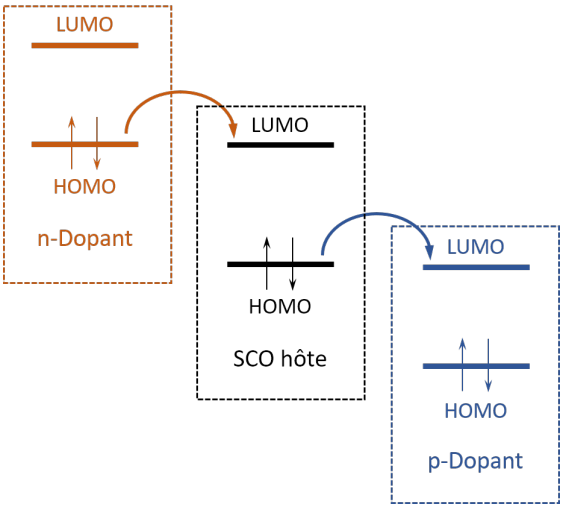

Figure 6 – Relation entre les niveaux d'énergie des orbitales moléculaires d'une molécule de SCO et d'une molécule de dopant.

L'introduction d'un réseau de polymère peut nous permettre d'améliorer les propriétés mécaniques du matériau et de stabiliser son alignement permettant aussi d'améliorer les propriétés de transport de charge.

La modification de la densité des porteurs de charge n par dopage constitue une deuxième voie d'amélioration de propriétés de transport de charge. Il est nécessaire de préciser quelques différences importantes entre le dopage d'un SCO et celui d'un matériau inorganique. Dans le cas des matériaux SCI, les porteurs de charge sont créés par l'introduction d'atomes d'éléments chimiques avec un excès (dans le cas de dopage de type n) ou un manque (dopage p) d'un électron, ce qui change la distribution des porteurs de charge libres dans un matériau massif. Cette approche n'est pas applicable aux matériaux SCOs à cause de leur nature moléculaire. Les premiers travaux qui ont abordé ce sujet démontrent l'instabilité et la non-reproductibilité des caractéristiques des

matériaux organiques dopés à cause de la diffusion et de la migration de sites de dopage.

La solution à ce problème inclut l'utilisation d'une autre molécule avec les niveaux HOMO et LUMO adaptés qui lui permettent d'accepter (dans le cas de dopage p) ou de donner (dopage n) un électron à la molécule SCO et en même temps de rester associé avec elle [5]. L'étude de dopage d'un SCO CL et ses effets sur la structure de mésophase ainsi que le transport des trous constitue une partie des travaux développés dans cette thèse.

Techniques de caractérisation

Les matériaux élaborés à base de cristaux liquides semi-conducteurs ont été caractérisés au moyen d'un ensemble de techniques expérimentales. On peut classer ces techniques selon les groupes suivants : caractérisation structurale et thermodynamique, techniques spectroscopiques, techniques de caractérisation de transport de charge électrique et techniques complémentaires. Le premièr groupe se compose de la microscopie optique sous lumière polarisée qui permet d'observer les textures de mésophases, de la microscopie électronique à balayage (MEB) et de la microscopie à force atomique (AFM) (équipé d'un module C-AFM pour mesurer la conductivité de l'échantillon) pour observer la structure des matériaux à l'échelle nanométrique, de la calorimétrie différentielle à balayage (DSC) pour étudier les transitions de phase et de la diffusion des rayons X (WAXS) afin de caractériser la structure des mésophases.

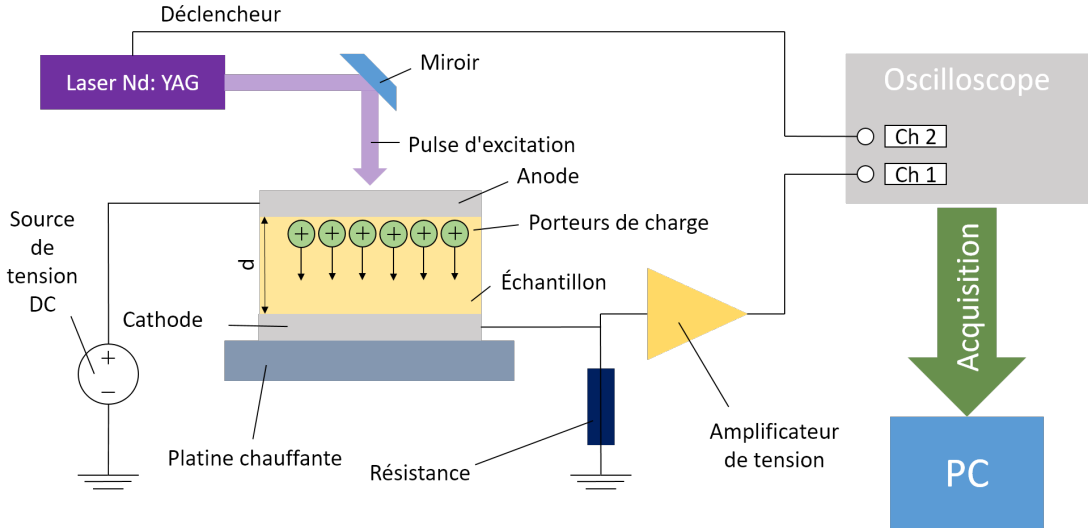

Figure 7 – Montage expérimental de **TOF** dans le cas des études de transport des trous.

Les techniques de mesure de transport de charge inclut la méthode de Temps de Vol (TOF de *time of flight*) et la mesure des caractéristiques d'un transistor à effet de champ. La technique TOF est basée sur la mesure du temps de transit d'un porteur de charge (électron ou trou) photo-généré à travers l'épaisseur de l'échantillon soumis à l'action d'un champ électrique continu [6]. Dans un échantillon d'épaisseur connue d, la mobilité μ peut être calculée en utilisant l'équation suivante:

$$\mu = \frac{d^2}{\tau_{tr} V}, \tag{2}$$

où V est la tension appliquée entre deux faces d'un échantillon et τ_{tr} le temps de transit d'un porteur de charge.

Dans cette technique, les porteurs de charge sont générés par un pulse de lumière laser de l'ordre de quelques ns (donc négligeable par rapport à τ_{tr}) à l'interface entre l'échantillon et l'électrode, ce qui nécessite l'utilisation d'électrodes transparentes en ITO.

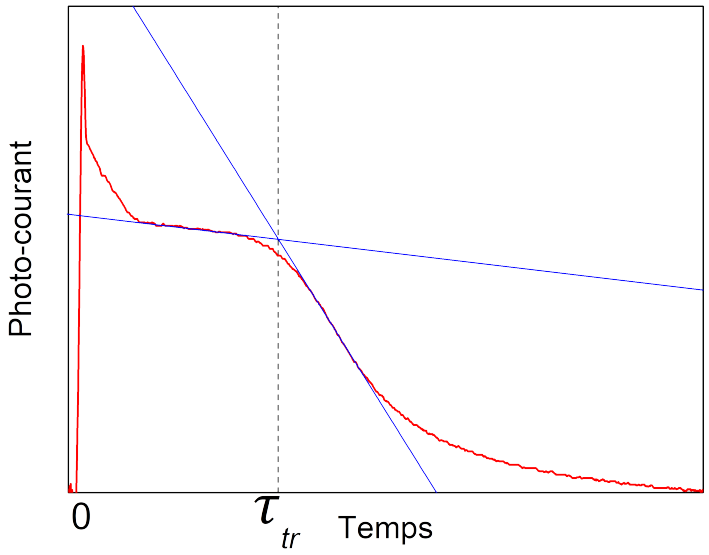

Figure 8 – Exemple d'un profil de photo-courant en fonction de temps permettant l'extraction d'un temps de transit τ_{tr}.

Le montage expérimental (Figure 7) est constitué d'un laser pulsé à une longueur d'onde λ=355 nm et de durée de pulse de 5 ns, une source de tension continu, un four avec un contrôleur de type PID, une résistance de 1 kΩ et un amplificateur de tension.

Le signal de photo-courant est visualisé sur un oscilloscope qui nous permet d'extraire le temps de transit τ_{tr} en traçant deux ajustements numériques des parties linéaires de la courbe de photo-courant (Figure 8)

La caractérisation des transistors à effet de champ organiques (OFETs) nous permet également de remonter à la mobilité d'un porteur de charge. Cette technique est très avantageuse car elle nous donne l'estimation de la performance d'un matériau dans les conditions réelles. Elle nous permet également de connaître l'influence du procédé de fabrication d'un dispositif OFET sur le transport de charge.

Un OFET est un dispositif actif qui permet de contrôler l'intensité de courant électrique en utilisant l'effet de champ. Ce phénomène décrit le comportement de la densité des porteurs de charge dans un semi-conducteur en fonction d'un champ électrique externe.

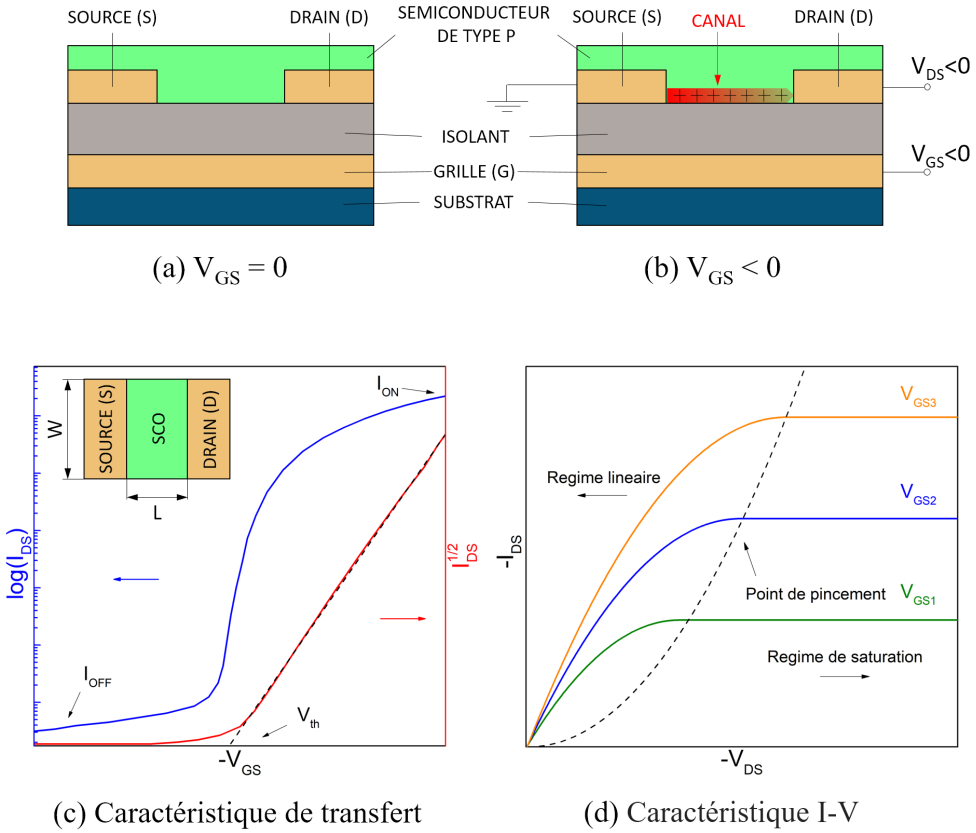

Figure 9 – Structure schématique d'un **OFET** de type p : (a) le dispositif se trouve en état OFF; (b) le canal conducteur est formé grâce a la tension de grille négative V_{GS}. Les caractéristiques d'un **OFET** de type p : (c) de transfert en échelle logarithmique (en bleu) et de tension de seuil V_{th} (en rouge), l'encart représente la géométrie du canal d'un **OFET** (vue de dessus) ; (d) caractéristique courant-tension pour les valeurs de V_{GS} divers ($|V_{G3}| > |V_{G2}| > |V_{G1}|$).

Concernant les OFETs, on peut appliquer un champ électrique entre les électrodes de grille (G) et de source (S) (Figure 9 (a) et (b)) afin de contrôler le nombre de porteurs de charge disponibles situés près de l'interface SCO/couche d'isolant.

L'une des caractérisations typiques d'un OFET est la caractéristique de transfert (Figure 9 (c), en bleu) où la tension de grille V_{GS} est balayée en fixant la tension entre les électrodes de source et drain V_{SD}. En traçant la racine carrée du courant de canal I_{SD} en fonction de V_{GS}, on récupère la tension de seuil V_{th} à laquelle la voie de conduction se forme (Figure 9 (c), en rouge). La courbe I_{SD} en fonction de V_{SD} nous donne la caractéristique de sortie courant-tension pour les différentes valeurs de V_{GS} (Figure 9 (d)). Ce graphique contient deux régimes de courant I_{SD} : *linéaire* et *saturation*. Dans le premier régime, I_{SD} est proportionnel à V_{SD} jusqu'au "point de pincement" où la densité

de porteurs de charge dans le canal ne dépend plus de la tension V_{SD}. Dans ce régime, I_{SD} est décrit par l'équation suivante [7] :

$$I_{DS} = \left(\frac{W}{2L}\right) \mu_F C_i \left(V_{GS} - V_{th}\right)^2 , \tag{3}$$

où W est la largeur du canal, L la longueur du canal (encart de Figure 9 (c)), C_i la capacité par unité de surface de la couche d'isolant de grille et μ_F la mobilité sous effet de champ.

Matériaux à base de 2-dodecyloxy-6-(4-octylphényle)-naphthalène

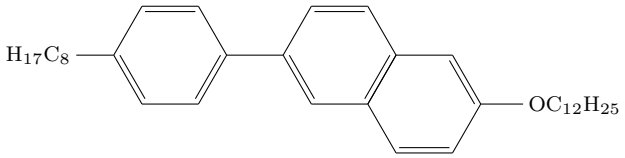

Figure 10 – Structure moléculaire du 2-dodecyloxy-6-(4-octylphényle)- naphthalène (**8-PNP-O12**).

La première partie de ce travail concerne un SCO CL bien connu à base de phényle naphtalène, le 2-dodecyloxy-6-(4-octylphényle)-naphthalène ou **8-PNP-O12** (SYNTHON Chemicals GmbH & Co. KG (Chemie Park Bitterfeld Wolfen, Allemagne), pureté de 99%.).

Ce matériau possède les propriétés mésogeniques de caractère smectique: Smectique B (Sm_B, de 66 °C à 101 °C) et Smectique A (Sm_A, de 101 °C à 121 °C).

Le transport des porteurs de charge de ce matériau a été précédemment étudié par de nombreuses équipes de recherche [8, 9, 10, 11, 12, 13]. La mobilité des trous atteint des valeurs de l'ordre de $10^{-3}\,\mathrm{cm}^2/(\mathrm{V\,s})$ en Sm_B et presque dix fois moins ($10^{-4}\,\mathrm{cm}^2/(\mathrm{V\,s})$) en Sm_A. Deux moyens principaux d'amélioration des performances de **8-PNP-O12** sont proposés et étudiés : la stabilisation *in situ* de la structure du CL par photo polymérisation et l'insertion d'une molécule dopante (accepteur d'électrons).

Dispersion d'un photo-polymère

Dans le premier cas, l'influence du réseau polymère sur l'ordre et le transport de charge est étudiée à l'aide de techniques expérimentales classiques et par la mesure de la mobilité par la technique du Temps de Vol.

Le polymère utilisé dans cette étude est une molécule disponible commercialement chez Merck (**RM82**) : le 2-methyl-1,4-phénylène bis(4-((6-(acryloyloxy)hexyl)oxy)benzoate) [14], ayant une mésophase nématique de 86 °C à 116 °C. Ce monomère a été utilisé avec un photo-amorceur (**Irgacure 369**) et un stabilisant thermique 2,6-di-tert-butyl-4-methylphenol (**BHT**).

Nous avons preparé 4 dispersions contenant 1 (**g1**), 3 (**g2**), 5 (**g3**) et 10 (**g4**) % wt. de **RM82**. Les échantillons ont été polymérisés en phase Sm_B (90 °C), qui ont donnés

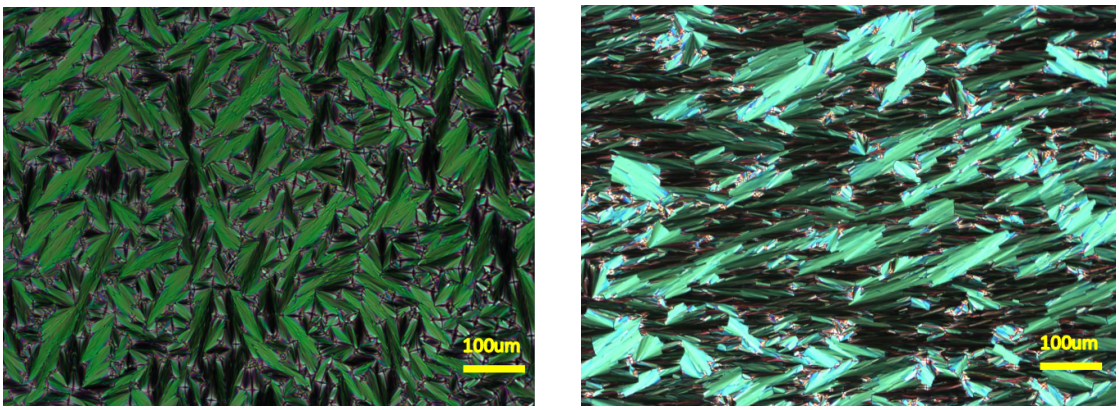

(a) (b)

Figure 11 – Texture des échantillons : (a) **8-PNP-O12** et (b) **g2** par la microscopie optique en lumière polarisée.

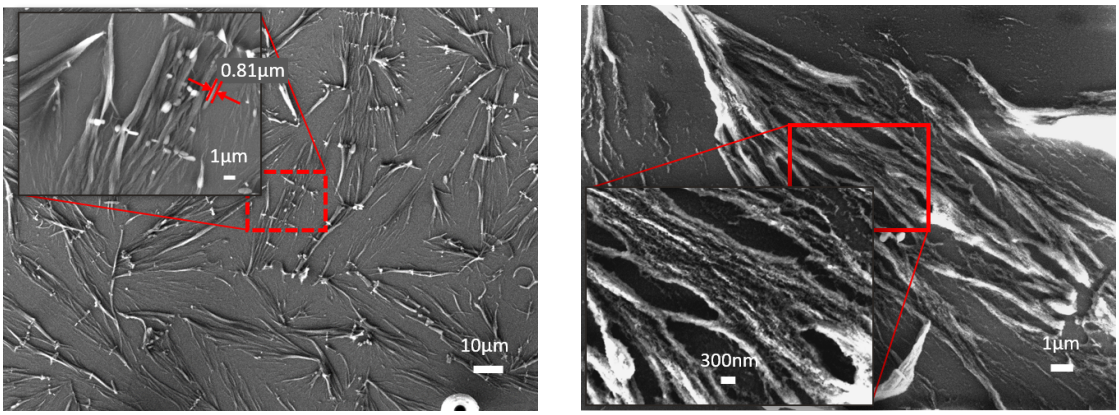

(a) (b)

Figure 12 – Structure du réseau de polymère de **g2** étudié par MEB.

lieu à la formation d'un réseau polymérisé portant une empreinte de cette mésophase. Ce réseau a été caractérisé à l'aide de la microscopie optique en lumière polarisée pour observer la texture de ce matériau composite (Figure 11, (a) et (b)). On a pu observer les structures polymèriques à l'échelle sub-micrométrique par la microscopie électronique à balayage (Figure 12, (a) et (b)).

Afin de caractériser le transport de charge dans les composites préparés, nous avons effectué les mesures de mobilité par la méthode de temps de vol. La mobilité des trous dans les matériaux composites est peu affectée par l'introduction d'un réseau de polymère: on a remarqué qu'elle diminue légèrement avec l'augmentation du taux de **RM82** (Figure 13, (a) et (b)). On peut relier ce comportement à une baisse de l'ordre local dans les deux

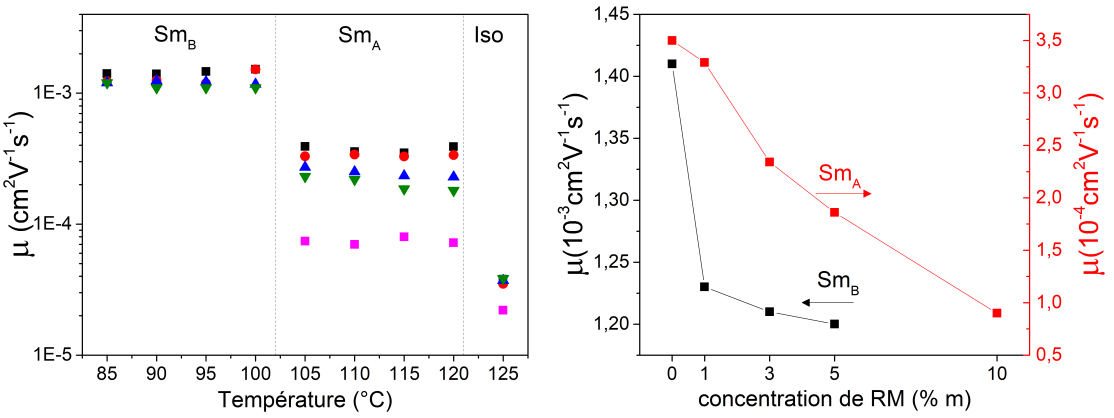

(a) (b)

Figure 13 – (a) Mobilité des trous en fonction de la température pour **8-PNP-O12** pur (symbols noires), **g1** (rouges), **g2** (bleus), **g3** (verts) et **g4** (roses). (b) Mobilité des trous en fonction de la concentration de **RM82** en phases Sm_B (85 °C, noir) et Sm_A (115 °C, rouge).

mésophases (Sm_B et Sm_A). On remarque aussi une stabilité thermique de la mobilité des trous, ce qui nous permet de supposer un taux de piégeage assez faible par les défauts à cause de la présence du réseau polymère. Ceci nous permet d'avancer l'hypothèse d'une bonne compatibilité des matériaux **RM82** et **8-PNP-O12**.

Dopage par un accepteur d'électrons

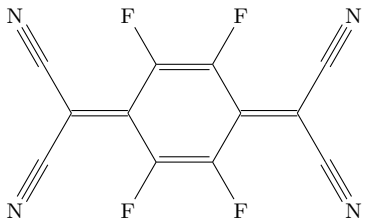

Figure 14 – Structure moléculaire de 2,3,5,6-tetrafluoro-7,7,8,8-tetracyanoquinodimèthane.

L'étude des propriétés des matériaux dopés par un accepteur d'électrons constitue l'étape suivante de cette thèse. Dans cette partie nous avons utilisé un accepteur d'électrons bien connu, le 2,3,5,6-tetrafluoro-7,7,8,8-tetracyanoquinodimèthane (**F_4TCNQ**, Figure 14) [15, 16, 17]. Cette molécule possède un niveau LUMO assez profond (de l'ordre de −5.3 eV) qui nous permet de prévoir un transfert de charge entre cette molécule et le SCO hôte (HOMO de **8-PNP-O12** est de −5.6 eV).

Les calculs *ab initio* (*Gaussian 16*, Rev. A03 [18], Figure 15) ont été utilisés pour prédire les propriétés spectroscopiques des matériaux dopés, qui ont été comparées de

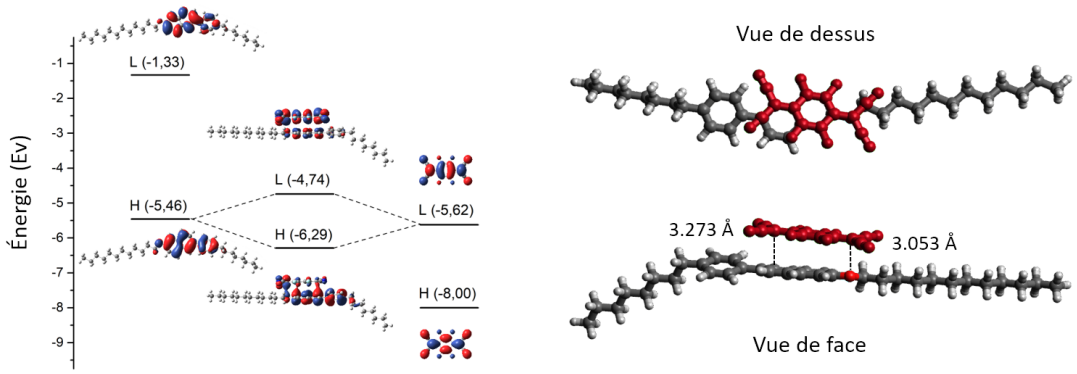

(a) (b)

Figure 15 – (a) Diagramme des niveaux d'énergie des orbitales moléculaires des composés initiaux (**8-PNP-O12** et **F_4TCNQ**) et du complexe avec transfert de charge (**CTC**) entre ces deux composés. (b) La géométrie de **CTC**. Ces données sont obtenues au niveau théorique B3LYP/6-31++G(d,p).

manière exhaustive aux données expérimentales obtenues par spectroscopie optique et vibratoire.

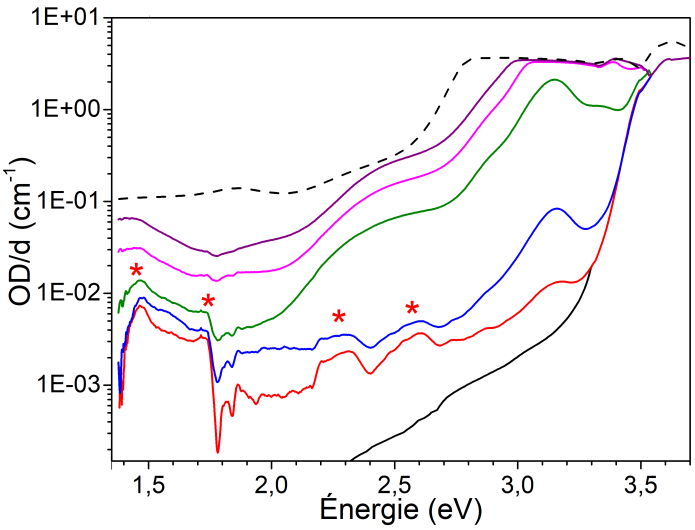

Figure 16 – Spectres d'absorption optique pour les matériaux étudiés : **8-PNP-O12** pur (noir), **F_4TCNQ** (noir pointillé) **c1** (rouge), **c2** (bleu), **c3** (vert), **c4** (rose) et **c5** (violet).

Cinq mélanges ont été préparés selon la concentration massique du dopant : 0.1 (**c1**), 0.5 (**c2**), 1 (**c3**), 3 (**c4**), 5 (**c5**) % wt. La spectroscopie optique nous montre que

les matériaux composites ont des caractéristiques spectrales très particulières : on voit l'apparition de nouveaux pics d'absorption optique dans le domaine proche infrarouge (à partir de 1.16 eV, Figure 16).

L'intensité de cette réponse spectrale est directement proportionnelle au contenu de **F_4TCNQ**. Nous avons également effectué des calculs TD-DFT (*time dependent density functional theory*) et les avons confrontés aux résultats expérimentaux pour confirmer la formation d'un complex avec transfert de charge (**CTC**) (Figure 16, marquées avec les étoiles rouges).

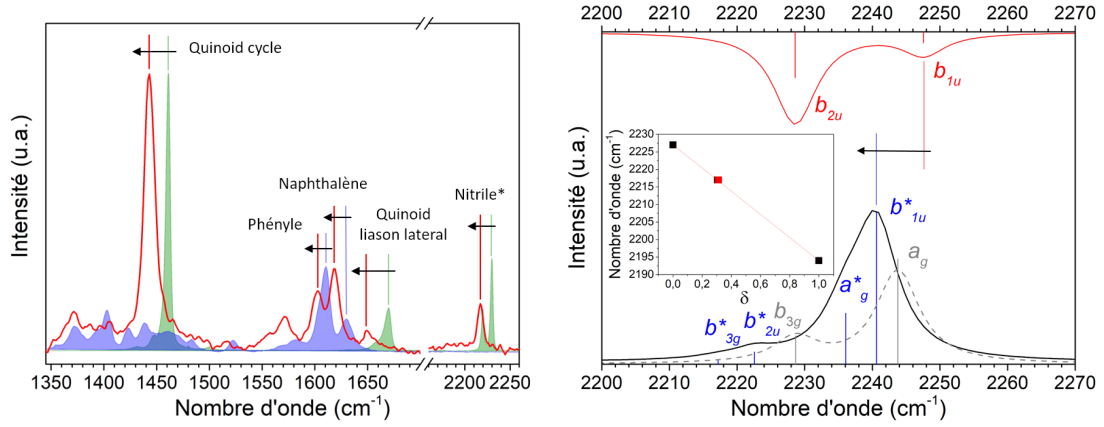

(a) (b)

Figure 17 – (a) Spectres Raman de **8-PNP-O12** pur (bleu), **F_4TCNQ** (vert) et composite **c5** (rouge). (b) Spectres vibrationels calculés pour **CTC** (noire, Raman) et **F_4TCNQ** (Raman en gris et FTIR en rouge). Encart : Fréquence de mode b_{1u} de **F_4TCNQ** en fonction du degré de transfert de charge.

La spectroscopie Raman nous a permis de confirmer les résultats observés par la spectroscopie d'absorption ainsi que de quantifier ce transfert de charge entre les deux composantes du **CTC**. Les vibrations moléculaires liées aux systèmes aromatiques de **8-PNP-O12** et quinoïdes de **F_4TCNQ** sont clairement affectées par leur interaction lors de la formation du **CTC** (Figure 17, (a)). Le décalage des fréquences vibrationelles est lié au changement de la longueur des liaisons chimiques dans ces molécules, induit par le phénomène de transfert de charge.

Nous avons choisi le mode de vibration b_{1u} de la molécule **F_4TCNQ** afin d'estimer le degré de transfert de charge δ. Ce mode est accessible uniquement par la spectroscopie FTIR dans la molécule neutre **F_4TCNQ** et l'anion moléculaire **F_4TCNQ$^-$** à cause des effets de symétrie. Dans notre cas, les contraintes géométriques dans le **CTC** perturbent la symétrie, ce qui nous permet de sonder ce mode de vibration par la spectroscopie Raman (Figure 17, (b)). Le degré de transfert de charge a été estimé à **0.31**, ce qui est en bon accord avec les données issues des calculs *ab initio*.

Les propriétés de transport de charge ont aussi été étudiées. Nous avons effectuées les

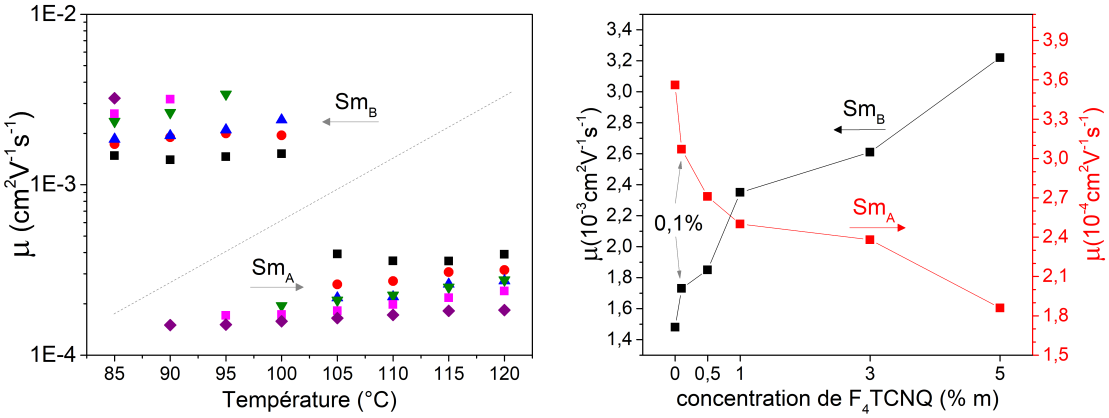

(a) (b)

Figure 18 – (a) Mobilité des trous en fonction de la température pour **8-PNP-O12** pur (symboles noirs), **c1** (rouges), **c2** (bleus), **c3** (verts), **c4** (roses) and **c5** (violets). (b) Mobilité des trous en fonction de la concentration de $\mathbf{F_4TCNQ}$ en mésophases Sm_B (85 °C, noir) et Sm_A (115 °C, rouge).

mesures **TOF** pour tous les échantillons (Figure 18, (a)). Ces résultats montrent que la mobilité des trous augmente en Sm_B et diminue en Sm_A en fonction du taux de dopage.

Un prototype de transistor à effet de champ organique (OFET) a été réalisé par spin-coating afin d'obtenir une estimation des performances en vue d'une application potentielle dans les dispositifs électroniques à base de matériaux organiques (Figure 19).

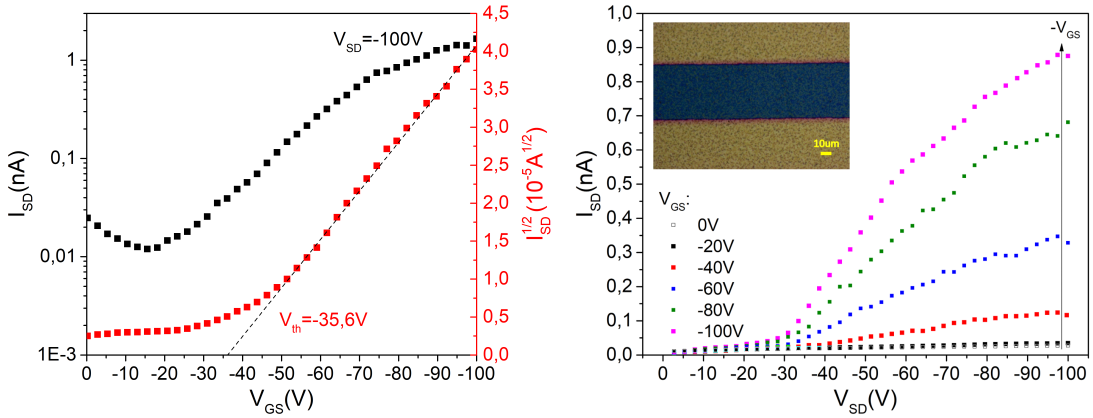

(a) (b)

Figure 19 – (a) Caractéristique de transfert et V_{th} d'un OFET (L = 50um, W=18mm) réalisé avec **c5**. (b) Caractéristique de sortie du même dispositif. Encart : photo de canal.

La mobilité extraite de la partie de courbe courant-tension correspondant au régime

de saturation était de $1.3 \times 10^{-8}\,\mathrm{cm}^2/(\mathrm{V\,s})$ avec un rapport ON/OFF de l'ordre de 10^2.

Stabilisation d'un matériau dopé par photo-polymérisation

La dernière partie de ce travail sur les matériaux à base de **8-PNP-O12** comprend une stabilisation d'un composite dopé par polymérisation *in situ*. Nous avons choisi la concentration de **RM82** de 3%, car elle nous offre une bonne densité de réseau polymère avec une mobilité de trous raisonnable (Figure 13, (b)). Trois mélanges ont été préparés contenant 0.1 (**gc1**), 0.5 (**gc2**) et 1 (**gc3**) % wt de **F_4TCNQ**. Les concentrations de **F_4TCNQ** supérieures à 1% empêchent la polymérisation du fait des propriétés d'accepteur d'électrons du dopant : les groupements fonctionnels de **RM82** (acryliques) font l'objet d'une attaque électrophile par la molécule dopante du **F_4TCNQ**.

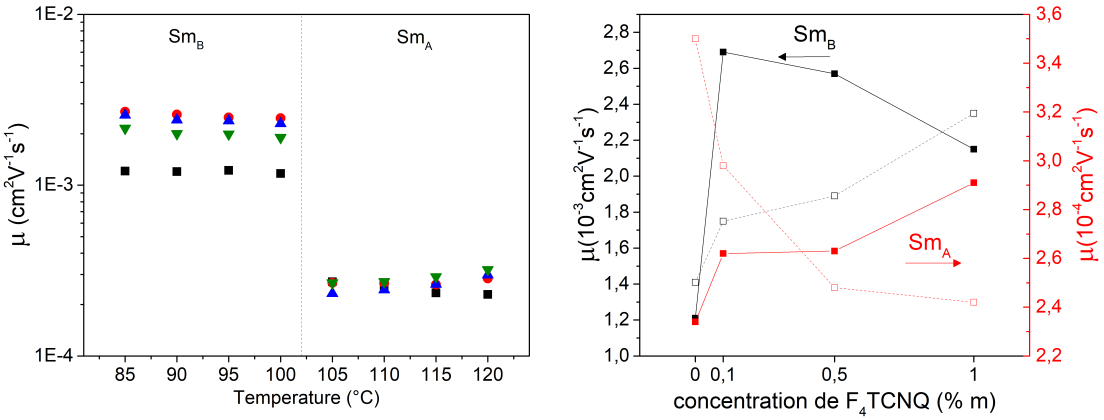

(a) (b)

Figure 20 – (a) Mobilité des trous en fonction de la température pour **g2** (symboles noirs), **gc1** (rouges), **gc2** (bleus), **gc3** (verts). (b) Mobilité des trous en fonction de la concentration de **F_4TCNQ** en mésophases Sm_B (85 °C, noir) et Sm_A (115 °C, rouge).

Les mesures **TOF** ont démontré les effets de stabilisation sur le comportement de la mobilité des trous en fonction de la température (Figure 20, (a)) par rapport au cas précédent où la mobilité a été thermiquement activée (Figure 18, (a)). Ce phénomène d'activation thermique est dû aux états pièges qui sont induits par les défauts structuraux dû à l'introduction d'une impureté (**F_4TCNQ**). Le réseau polymère sert à stabiliser la structure de mésophase est à diminuer la contribution de ces défauts, ce qui nous permet d'obtenir une mobilité de trous stable (Figure 20, (a)) et plus élevée (Figure 20, (b)).

Nouveaux matériaux à base de 2-amino-anthracène

La deuxième partie de cette thèse comprend la conception et la synthèse d'un nouveau semi-conducteur CL. Suite à l'observation de performances insatisfaisantes des composites de **8-PNP-O12** en couche active d'un transistor, nous avons développé une nouvelle

famille de SCOs à base de 2-amino-anthracène. Une attention particulière a été portée pour obtenir un matériau relativement facile à synthétiser et à faible coût. Cette molécule de (E)-N-(anthracen-2-yl)-1-(4-(decyloxy)-phenyl)methanimine (**10-OPIA**) contient un atome d'azote dans son système conjugué (Figure 21) afin d'éviter des voies de synthèse plus compliquées dédiés à l'obtention des liaisons C-C (couplage de Suzuki, par exemple). Les niveaux d'énergie moléculaire frontières sont étudiés par spectroscopie optique et

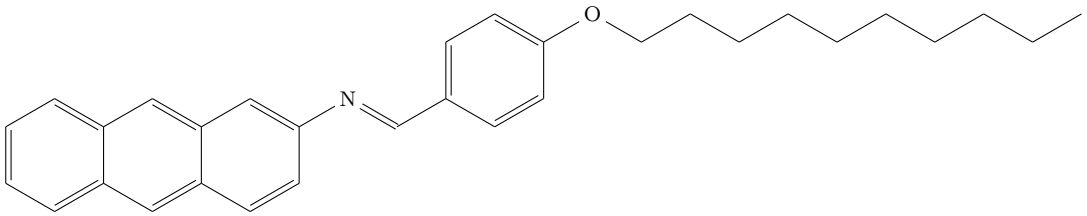

Figure 21 – Structure moléculaire du (E)-N-(anthracen-2-yl)-1-(4-(decyloxy)-phenyl)methanimine (**10-OPIA**)

voltamétrie cyclique (Figure 22, (b)) et comparés aux valeurs obtenues par calculs *ab initio* (Figure 22, (a)). Nous avons trouvé l'énergie de HOMO de −5.18 eV, ce qui nous a permis d'utiliser des contacts en or (travail d'extraction ϕ=−5.1 eV) afin d'avoir une barrière de potentiel faible pour injecter les trous dans HOMO de **10-OPIA** (transport de type p).

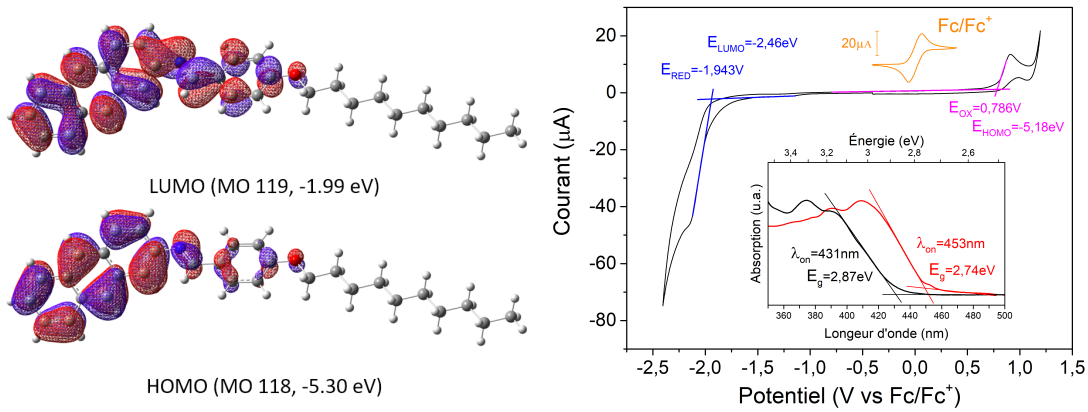

(a) (b)

Figure 22 – (a) HOMO et LUMO de **10-OPIA** calculées en niveau théorique de B3LYP/6-31G++(d,p). (b) Voltammogramme cyclique d' une solution 2mmol de **10-OPIA** avec 0.1M TBAPF6 en dichlorométhane versus Fc/Fc+. Encart : absorption optique en solution 10^{-5} M de **10-OPIA** en dichlorométhane (noir) et en couche mince (rouge).

Afin d'étudier la performance de cette molécule nouvellement synthétisée nous avons élaboré des transistors organiques par le dépôt d'une goutte de solution sur un substrat

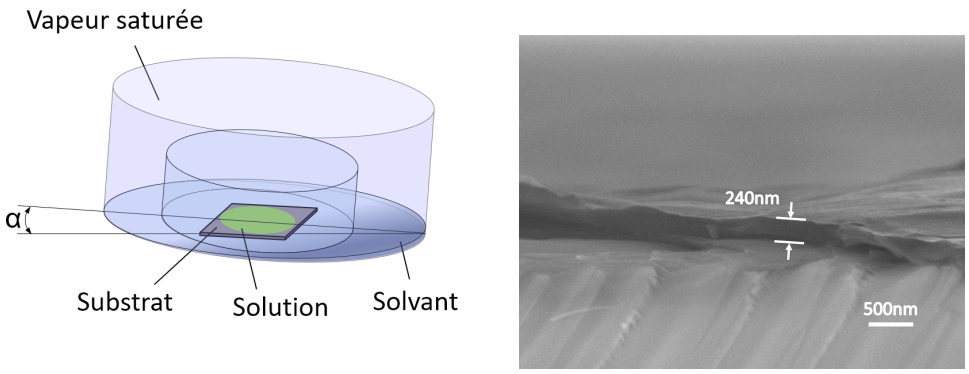

(a) (b)

Figure 23 – (a) Dépôt par goutte (*drop casting*) dans des conditions contrôlées. (b) Profil d'un film mince obtenu par le dépôt d'une goutte (0.5% m de **10-OPIA** en chlorobenzène) sur un substrat de verre.

incliné (Figure 23, (a)). Cette technique nous a permis de contrôler la direction de croissance des cristaux de **10-OPIA** assez facilement.

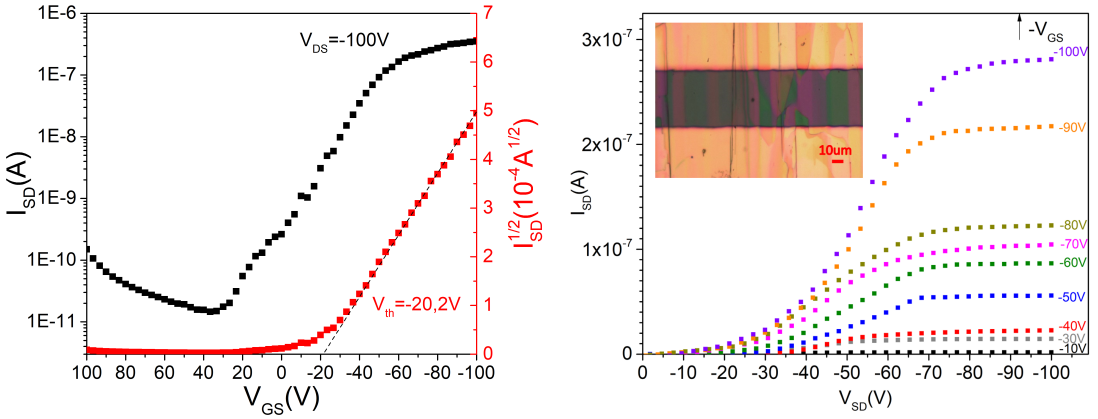

(a) (b)

Figure 24 – (a) Caractéristique de transfert et V_{th} d'un OFET (L = 50 µm, W=18mm) réalisé avec **10-OPIA**. (b) Caractéristique de sortie du même dispositif. Encart : photo de canal.

Nous avons obtenu des films d'épaisseur comprise entre 200 nm et 400 nm (Figure 23, (b)). Les dispositifs issus de cette méthode de dépôt ont été caractérisés afin d'extraire la mobilité des trous. Figure 24, (a) nous montre la caractéristique de transfert obtenue pour un des OFETs à base de **10-OPIA**. On peut remarquer une différence prononcée entre les états ON et OFF avec un rapport de 10^4 (contre 10^2 dans le cas d'un composite

de **8-PNP-O12** avec **F_4TCNQ**). La tension de seuil trouvée V_{th} est de -20.2 V, ce qui est raisonnable pour les OFETs préparés à partir d'une solution.

La caractéristique courant-tension est présente dans la Figure 24, (b). Nous voyons le comportement typique d'un transistor à effet de champ, où le courant I_{SD} est directement proportionnel à la tension de grille. Les courbes individuelles de I_{SD} montrent les parties distinctes des régimes linéaires et de saturation, nous permettant d'appliquer l'équation 3. La mobilité des trous à effet de champ a été calculée: $\mu = (2.6 \pm 1.2) \times 10^{-5}\,\mathrm{cm}^2/(\mathrm{V\,s})$.

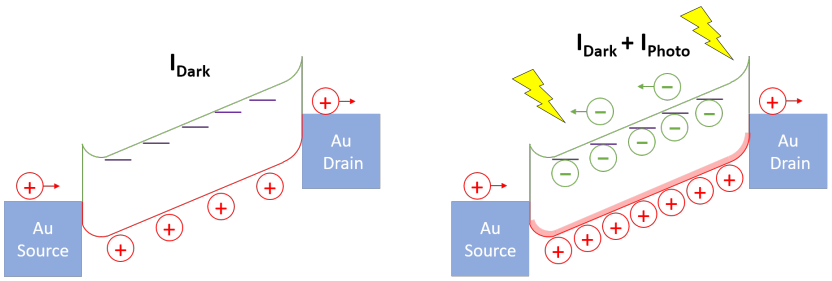

(a) (b)

Figure 25 – Diagramme des bandes d'énergie pour le canal d'un OFET (a) dans l'obscurité (b) sous illumination.

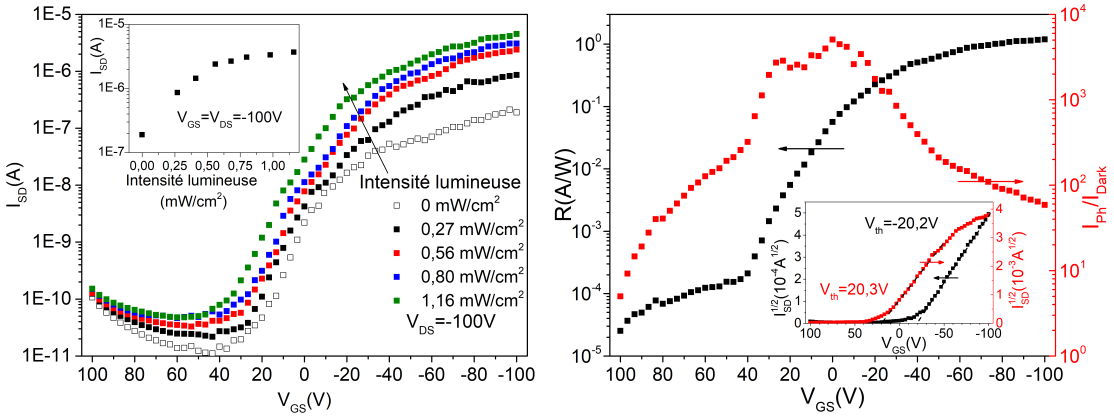

(a) (b)

Figure 26 – (a) Caractéristique de transfert d'un OFET (L = 50um, W=18mm) réalisé avec **10-OPIA** pour diverses puissances lumineuses. Encart : I_{Ph} de la partie de saturation en fonction de la puissance lumineuse. (b) Réponse normalisée (noir) et sensibilité (rouge) en fonction de V_{GS} pour $1.44\,\mathrm{mW/cm}^2$. Encart : caractéristiques V_{th} sans (noir) et avec (rouge) illumination.

Pendant l'étude de ce nouveau matériau, nous avons remarqué que le **10-OPIA**

possède des propriétés photo-conductrices. L'intensité du courant de canal I_{SD} est amplifiée par la lumière.

Cet effet est très prononcé et il est constitué de deux phénomènes assez proches: la photo-conductivité et le photo-*gating* (Figure 25, (b)). Dans le cas de la photo-conductivité, les charges additionnelles sont créées dans le matériau par excitation optique, ce qui donne lieu à l'augmentation du courant grâce à un nombre de porteurs de charge plus élevé. Dans le cas du photo-*gating*, des états ionisés sont créés au sein du matériau massif et notamment près de l'interface SCO/couche isolant de grille. La contribution au potentiel de matériau de ces états supplémentaires est vu comme une électrode de "grille", d'où l'appellation photo-*gating* [19]. Dans le cas d'un OFET préparé avec **10-OPIA**, le dispositif conserve le comportement d'un transistor sous illumination, c'est-à-dire présentant une différence distincte entre les états ON et OFF (Figure 26, (a)). La

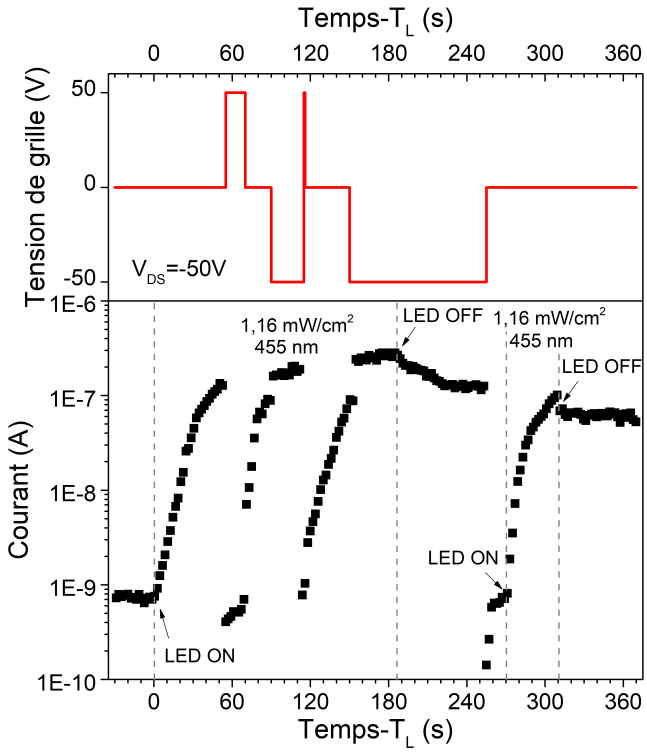

Figure 27 – Courant dans le canal d'un OFET (en sous) et tension de grille (au dessus) en fonction de temps. Puissance lumineuse de 1.16 mW/cm^2 à 455nm.

conductivité du canal est proportionnelle à la puissance lumineuse jusqu'à 0.5 mW/cm^2 à 455 nm, où elle commence à saturer. La majorité des photo-transistors est caractérisée par deux paramètres-clés : sensibilité P (rapport I_{Ph}/I_{Dark}) et réponse normalisée R (rapport de photo-courant et puissance lumineuse). Ces deux paramètres sont présentés dans la Figure 26, (b). On peut remarquer que la sensibilité atteint les valeurs maximales aux alentours de V_{GS} de -20 à 20V, ce qui correspond au décalage de la tension de seuil

V_{th} sous illumination (encart de Figure 26, (b)) dû à l'effet de photo-*gating*. La réponse normalisée possède le même profil qu'une caractéristique de transfert grâce au rapport ON/OFF élevé.

Nous avons également découvert que cet effet de photo-conductivité a une nature persistante, c'est-à-dire que la conductivité ne revient pas à la valeur initiale dans l'obscurité après illumination. D'autre part, cet effet peut être géré par application de la tension de grille V_{GS}: les tensions négatives augmentent la réponse de photo-conductivité, les valeurs positives effacent l'effet persistant. Nous avons effectué une simple démonstration de la flexibilité des propriétés de **10-OPIA** dans la Figure 27. Ces considérations nous suggèrent des applications photosensibles, ainsi que dans le domaine des dispositifs de mémoire ou des capteurs.

Conclusion

Dans cette thèse, nous avons exploré plusieurs aspects des matériaux semi-conducteurs organiques possédant des propriétés de cristaux liquides. Premièrement, **8-PNP-O12** étant un matériau connu, il nous a servi comme fondation solide afin d'aller plus loin pour explorer et améliorer ses propriétés de transport de charge. Les deux approches appliquées (stabilisation par un photo-polymère et dopage moléculaire) ont donné des résultats originaux et intéressants. La deuxième partie de ce travail a concerné la synthèse et la caractérisation d'une molécule nouvellement développée. Cette démarche nous a permis d'obtenir un matériau plus performant et de proposer quelques applications potentielles en relation avec ces propriétés photo-conductrices.

Mots-clés : semiconducteurs organiques, cristaux liquides, photopolyméres, dopage, temp de vol, transistors organiques à effet de champ

Bibliographie

[1] C. K. Chiang et al. “Electrical conductivity in doped polyacetylene”. In: *Physical Review Letters* 39.17 (1977), pp. 1098–1101. ISSN: 00319007. DOI: 10.1103/PhysRevLett.39.1098.

[2] Heinz Bässler and Anna Köhler. “Charge Transport in Organic Semiconductors”. In: vol. 35. 1. 2011, pp. 1–65. ISBN: 0002-9297. DOI: 10.1007/128_2011_218. arXiv: 15334406.

[3] Christopher A. Hunter and Jeremy K. M. Sanders. “The nature of .pi.-.pi. interactions”. In: *Journal of the American Chemical Society* 112.14 (July 1990), pp. 5525–5534. ISSN: 0002-7863. DOI: 10.1021/ja00170a016.

[4] K Ellmer. *Liquid Crystalline Semiconductors, Materials, Properties and Applications*. Vol. 169. 2013. ISBN: 9789048128723. DOI: 10.1007/978-3-642-33848-9.

[5] Ingo Salzmann et al. “Intermolecular hybridization governs molecular electrical doping”. In: *Physical Review Letters* 108.3 (2012), pp. 1–5. ISSN: 00319007. DOI: 10.1103/PhysRevLett.108.035502.

[6] James C. Blakesley et al. “Towards reliable charge-mobility benchmark measurements for organic semiconductors”. In: *Organic Electronics: physics, materials, applications* 15.6 (2014), pp. 1263–1272. ISSN: 15661199. DOI: 10.1016/j.orgel.2014.02.008.

[7] Sze. *Physics of Semiconductor Devices Physics of Semiconductor Devices*. Vol. 10. 1995, pp. 739–751. ISBN: 978-3-319-03001-2. DOI: 10.1007/978-3-319-03002-9. arXiv: 9809069v1 [arXiv:gr-qc].

[8] Masahiro Funahashi and Jun-ichi Hanna. “Fast ambipolar carrier transport in smectic phases of phenylnaphthalene liquid crystal”. In: *Applied Physics Letters* 71.5 (1997), pp. 602–604. ISSN: 0003-6951. DOI: 10.1063/1.119806.

[9] Naoki Yoshimoto and Jun-ichi Hanna. “Preparation of a novel organic semiconductor composite consisting of a liquid crystalline semiconductor and crosslinked polymer and characterization of its charge carrier transport properties”. In: *Journal of Materials Chemistry* 13.5 (2003), pp. 1004–1010. ISSN: 09599428. DOI: 10.1039/b209802d.

[10] Hiroaki Iino and Jun Ichi Hanna. “Electronic and ionic transports for negative charge carriers in smectic liquid crystalline photoconductor”. In: *Journal of Physical Chemistry B* 109.47 (2005), pp. 22120–22125. ISSN: 15206106. DOI: 10.1021/jp0507748.

[11] Tohru Toda, Jun-ichi Hanna, and Tadaaki Tani. “Electronic structure and charge injection at interface between electrode and liquid-crystalline semiconductor”. In: *Journal of Applied Physics* 101.2 (Jan. 2007), p. 024505. ISSN: 0021-8979. DOI: 10.1063/1.2424401.

[12] Sanjoy Paul et al. “Photogeneration and enhanced charge transport in aligned smectic liquid crystalline organic semiconductor”. In: *Journal of Applied Physics* 118.13 (Oct. 2015), p. 135702. ISSN: 0021-8979. DOI: 10.1063/1.4931913.

[13] Yi-Fei Wang, Hiroaki Iino, and Jun-ichi Hanna. “Fabrication of planarly-oriented polycrystalline thin films of smectic liquid crystalline organic semiconductors”. In: *Soft Matter* 13.37 (2017), pp. 6499–6505. ISSN: 1744-683X. DOI: 10.1039/C7SM01303E.

[14] Dirk J. Broer, Rifat A. M. Hikmet, and Ger Challa. “In-situ photopolymerization of oriented liquid-crystalline acrylates, 4 Influence of a lateral methyl substituent on monomer and oriented polymer network properties of a mesogenic diacrylate”. In: *Makromol. Chem.* 190 (1989), pp. 3201–3215. ISSN: 0025-116X. DOI: 10.1002/macp.1989.021901218.

[15] Jae Hyun Lee et al. “Effectiveness of p -dopants in an organic hole transporting material”. In: *Applied Physics Letters* 94.12 (2009), pp. 19–22. ISSN: 00036951. DOI: 10.1063/1.3107267.

[16] P. Pingel and D. Neher. “Comprehensive picture of p-type doping of P3HT with the molecular acceptor F4TCNQ”. In: *Physical Review B - Condensed Matter and Materials Physics* 87.11 (2013), pp. 1–9. ISSN: 10980121. DOI: 10.1103/PhysRevB.87.115209.

[17] Henry Méndez et al. “Charge-transfer crystallites as molecular electrical dopants”. In: *Nature Communications* 6 (2015), p. 8560. ISSN: 20411723. DOI: 10.1038/ncomms9560. arXiv: arXiv:1011.1669v3.

[18] M. J. Frisch et al. *Gaussian 16, Revision A.03*. 2016.

[19] Michele Buscema et al. “Photocurrent generation with two-dimensional van der Waals semiconductors”. In: *Chemical Society Reviews* 44.11 (2015), pp. 3691–3718. ISSN: 14604744. DOI: 10.1039/c5cs00106d.

Contents

General Introduction

The present work was conducted in the Unité de Dynamique et Structure des Matériaux Moléculaires (UDSMM) under the supervision of Professors Christian Legrand, Abdelylah Daoudi and Dr. Yahia Boussoualem. It deals with structural and electrical characterization of organic materials exhibiting mesogenic and semiconducting properties, as well as synthesis of new materials. This is the second thesis conducted on the organic semiconductors, and the first one dealing with organic field effect transistors in this laboratory.

This thesis in material science reunites different aspects of chemistry and physics, which means that we will have to address both in order to better explore our subject. In this manuscript, we have made an attempt to explore the vast domain of organic semiconductors, which deals with complex physical mechanisms of charge transport in condensed matter. To look for the electronic charge transport in organic matter may look quite counter-intuitive, especially for a stranger to this field of research. Indeed, when we hear about products of organic chemistry, we usually think « plastic », which a normal person would think of as an isolating material. However, not all organic materials are created equal. First experimental evidences of charge transport in organic materials date back to the beginning of XX century (more on the history of this subject in the beginning of Chapter 1). Significant research efforts conducted on the frontier of millennia have resulted in an apparition of the whole new class of organic materials - the organic semiconductors, which regroup all the benefits the organic chemistry has to offer (that is, the unprecedented flexibility of chemical structure and synthetic procedure, as well as great production scalability) with charge transporting properties. To date, it is indeed hard to underestimate the significance of these materials - their use in light-emitting applications becomes more and more ubiquitous, especially in the handheld devices and computer and TV screens. Other applications, such as photovoltaics, are still in the stage of development and are yet to become widely commercialized. This brings us to another potential application which we have envisioned for this work - the field effect transistors.

These devices are believed to find their place in fully organic circuits, which will make them solution processable, as well as enable flexible devices which may be produced "en masse" at low cost and high surface area.

In this work, we try to exploit the remarkable dependency of charge transporting properties on structural order of the material. To do so, we have looked into another mature and well-established field of material science - the liquid crystals. The first reports on this type of materials date to the end of the XIX century, when F. Reinitzer et al have discovered an unusual state of matter (which today we call mesophase) in a derivative of cholesterol. Since then, extraordinary progress has been made to this research field, which has resulted in numerous applications including but not limited to displays and light modulation. In this work, however, we are not going to disclose any light modulation-related properties. Instead, we are going to get interested in structural properties of these materials. The maturity of this research field benefits us in a sense of profound understanding of mesophase structure and the means to control their order and macroscopic orientation, which we are going to apply to study charge transporting properties of organic semiconductors.

In order to apply this expertise in liquid crystals to organic semiconductors, we need to focus our attention on a molecule which would combine these properties. It turns out that semiconducting, as well as mesogenic properties may be controlled by tuning the molecular structure. Large aromatic and π-conjugated structures are generally favorable for charge transport due to high delocalization degree of π-electrons. In turn, the overall shape of the molecule, as well as the presence of flexible lateral alkyl chains are believed to govern the mesogenic properties. It is then necessary to find a compromise between these two aspects, since large π-conjugated systems tend to have strong π-π intermolecular interactions, disrupting mesogenic properties and shifting melting temperatures higher. This makes the creation of a suitable material candidate a non-trivial task.

The experimental work of this thesis would be impossible without the solid understanding of basic physical principals (Chapter 1) as well as a vast array of experimental techniques (Chapter 2). We have put significant attention into the presentation of the most important concepts, including charge transport, doping, photopolymers and different aspects of the field-effect transistors. The experimental techniques cover the necessary structural, energetic as well as electrical properties of the studied materials. We also present the developed experimental procedure for sample preparation.

The experimental part of this thesis is divided in two parts. First part (Chapter 3) deals with a well-known liquid crystalline organic semiconductor based on phenyl naphthalene (**8-PNP-O12**). We have made attempts to improve its charge transporting

properties by preparing composite materials with it. The first approach is related to the liquid crystalline nature of **8-PNP-O12**: we employ a photo-polymeric reactive mesogen, which has good physical compatibility with host material in order to stabilize the structure of host's mesophase. The second approach is closely connected to the semiconducting properties of **8-PNP-O12**: we perform a process which is called P-doping by introducing an electron accepting impurity in the host material. This has allowed us to improve hole transport in the resulting composite as well as study the interconnection between the doping process and mesogenic nature of **8-PNP-O12**. Finally, we have made an attempt to combine these approaches and study the resulting material.

In the second part of this work (Chapter 4), we have created a novel molecule which exhibits semiconducting as well as liquid crystalline properties. This time, we have tried to improve upon the experience which we have obtained in the first part of this work conducted on **8-PNP-O12**. We fully characterize this molecule and propose several potential application for this new material.

To summarize, the principal aims of this work include:

- Understanding how the molecular structure influences mesogenic and semiconducting properties.
- Research of new ways to improve charge transport in liquid crystalline organic semiconductors.
- Investigation of multi-component systems in application to organic semiconductors (doping and polymer stabilization).
- Preparation of a novel mesogenic organic semiconductor, study of its potential applications.

Chapter 1

Organic semiconductors: concepts and theoretical basics

1.1 Introduction

The main objective of the first chapter is to briefly introduce the theoretical material relevant for the present study. It is designed to be accessible for wider public without a specific background in the organic electronics.

Firstly, the organic semiconductors are presented as a material class. Different classes of semiconducting molecules are presented as a function of their chemical structure. Further, the main theoretical aspects of the research subjects explored in the current thesis are covered, such as molecular doping and photo-activated polymers. The liquid crystals are also introduced, taking an important place in the present study. Finally, some information is given on the basic functioning of a field effect transistor, as well as recent progress in this field.

1.2 Organic semiconductors

1.2.1 History

The advent of semiconductor era has begun in the middle of last century, when the transistor has been invented. Solid state electronic devices based on inorganic semiconductor (**ISC**) materials such as silicon (Si) and germanium (Ge) have successively eliminated devices based on thermionic emission from almost all applications with rare exceptions. With overwhelming success of monocrystalline silicon and all the research facilities focused on **ISC** field, electronic properties of organic substances were somewhat neglected.

While organic materials were known to have dark and photo-conductivity for more than a century (one of the first studies of photoelectric properties of anthracene crystals date back to 1913 [1]), very little effort was initially put into the research of this material class. Some works on optical excitation and charge carrier transport in organic crystals [2] were inspired by the discovery of electroluminescence in 1960s, however practically viable parameters of samples were never attained (poor current density, quantum yield and excessively high operating voltage, notably due to high thickness of prepared samples [3]). It was not until 1977, when Heeger, MacDiarmid and Shirakawa (awarded with the Nobel Prize in Chemistry in 2000 for their contribution to organic electronics development) discovered conductivity in polyacetylene [4]. Synthesis and doping of π-conjugated polymers have lead to the production of conducting coatings and photo-detectors.

The demonstration of an efficient photovoltaic cell based on heterojunction of organic p- and n-type semiconductors [5], followed by working prototypes of thin film transistors based on π-conjugated polymers [6] [7], has revived the interest of scientific community

in intrinsic (undoped) organic semiconductors (**OSC**).

However, the real breakthrough in application of **OSC** has been induced by fabrication of electroluminiscent diodes (**OLED**) based on evaporated thin films of **OSC** [8] [9] and π-conjugated polymers [10]. **OLED** field has made significant progress over last twenty years, owing to combined academical and industrial research facilities and nowadays represent a significant market with growth perspectives, being in process of eliminating liquid crystal displays (LCDs) from the market, with Active-Matrix **OLED** (AMOLED) technology being one of the most widely employed. Organic photovoltaics (**OPV**) are on the brink of commercialization, induced by the development of deposition technologies (notably, **OSC** inks for printing). Logic circuits, based on **OFET**s are expected to follow in the nearest future.

1.2.2 Structure of organic semiconductors

By the term of organic semiconductors we usually mean solid substances constituted of π-conjugated organic molecules or polymer chains, presented in form of molecular crystals or thin amorphous films, depending on the method of processing. Their semiconducting properties show up upon chemical doping, charge injection or photoexcitation (in case of photovoltaics).

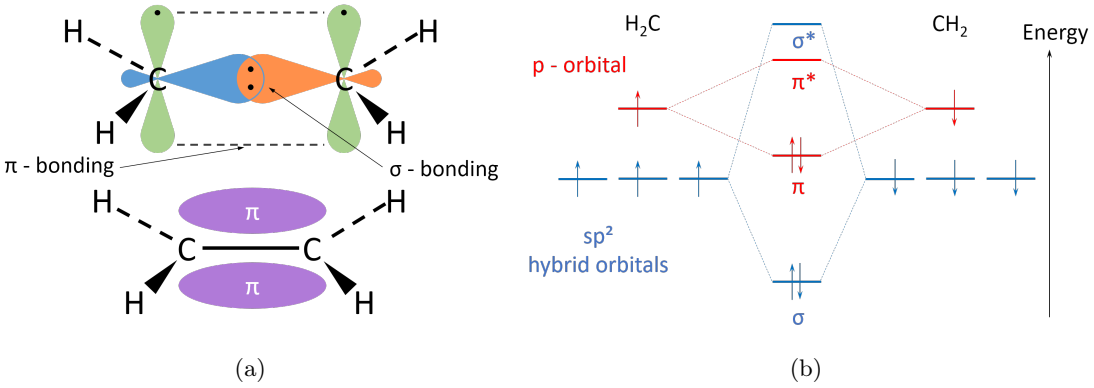

(a) (b)

Figure 1.1 – (a) Schematic representation of orbitals and σ - and π - bonds in ethylene. (b) Energy diagram of molecular orbitals in ethylene molecule demonstrates separation between σ - and π - energetic framework.

A system is called conjugated if it consists of alterating single and double/triple bonds formed by p_z orbitals in sp^2-hybridized carbon atoms (for example, ethylene, Figure 1.1, a) which makes electrons of conjugated π bonds "hop" between localized states over the system's backbone or even to a neighboring molecule. The σ bonds are significantly

stronger than π bonds (Figure 1.1, b), and as the excitations takes place in $\pi - \pi^*$ energetic domain, σ-bonded backbone of the molecule remains stable.

A good example of large-scale π-conjugated system is polyacetylene [4] (Figure 1.2), where entire polymer chain consists of sp^2-hybridized carbon atoms.

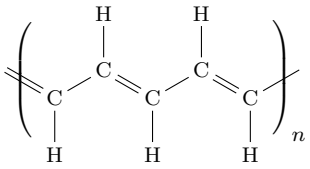

Figure 1.2 – Basic π-conjugated system, polyacetylene.

Conjugated π-system leads to band gap formation, which is the one of basic concepts in organic semiconductors physics. From the classic definition for **ISC**s, this is the energy range between the so-called valence and conduction bands where electron states do not exist. For semiconductors, and what comes from their definition, the band gap lies between 1.5 and 5 eV. Speaking of **OSC**, the terminology differs slightly. Their band gap energy range is between π (bonding) and π^* (antibonding) orbitals while electrons in strong σ carbon-carbon (or other heteroatom) bonds typically do not take part in excitation process, explaining the **OSC**' structural stability but also the ability to allow its π electrons to participate in charge transport.

The notions of valence and conductivity bands (which in fact comes from **ISC** domain) also differ: band gap energy being the difference between *highest occupied molecular orbital* (HOMO) and the *lowest unoccupied molecular orbital* (LUMO) which are analogous to conduction and valence bands in regular inorganic semiconductors. This emphasizes the attention to molecular nature of **OSC**: as the molecule or a monomer (in case of polymeric chains) is considered a basic unit of semiconducting substance, which is not necessarily of crystalline constitution, but very often presented in a form of amorphous solid, in contrast to conventional **ISC**s.

The band gap energy value, as being relative, is particularly important for such applications as LEDs and photovoltaics, since the wavelength of emitted/absorbed light depends on the energy difference between HOMO and LUMO levels (Figure 1.3).

However, for other applications (**OFET**), values of HOMO and LUMO could be regarded as key parameters as well: for example, a high HOMO level can pose potential barrier for charge injection on metal - **OSC** interface. Also, lowering HOMO level makes **OSC** molecule more chemically stable and less prone to oxidation under ambient conditions. For **OLED**s and **OPV**s the wavelength of emitted/absorbed light λ is reverse

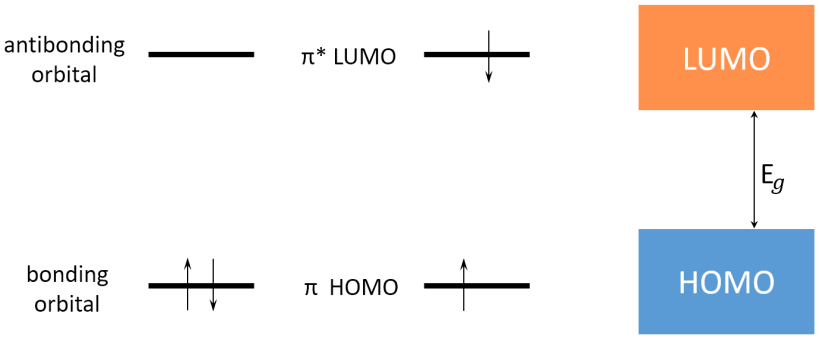

(a) Ground state (b) Excited state (c) Bulk semiconductor

Figure 1.3 – Diagrams for (a) ground state and (b) excited state of single **OSC** molecule; (c) representation of energy levels in bulk material.

proportional to band gap energy E_g:

$$\lambda \propto \frac{1}{E_g}. \tag{1.1}$$

Several methods may be used to determine HOMO and LUMO levels: X-ray and inverse photoelectron spectroscopy, optical spectroscopy with conjunction to cyclic voltammetry, with the latter being widely employed. The band gap energy depends on conjugation length, deviations from planarity, aromatic resonance energy (quinoid structure has lower band gap energy than aromatic), inductive* and mesomeric† effects and intermolecular or interchain interactions. All these factors are interrelated, which makes the band gap engineering not an easy task.

- Conjugation length is the size of double-single bond alternating backbone: increase of conjugation length reduces band gap energy level. Since the light absorption process is strongly related to band gap energy E_g value (equation 1.1), it is a very intuitive way to compare E_g by comparing light absorption characteristics. The family of oligoacenes (Table 1.1) illustrates this correlation well [11].

- Separate molecular orbitals do not exist for the material in bulk: the interactions between molecules smear HOMO and LUMO levels in more band-like structure (Figure 1.3), which once again lowers the band gap. This phenomena is related to

*The inductive effect is related to the difference of electronegativity between the atoms of host structure and substituent group, which manifests as a change in electron density of the molecule.

†The mesomeric effect is related to the interactions between the π-conjugated bonds through resonance stabilization, and helps to describe electron density distribution in the molecule.

Substance	Benzene	Naphthalene	Anthracene	Tetracene	Pentacene
Number of cycles	1	2	3	4	5
Absorption peak, nm	255	315	380	480	600

Table 1.1 – UV-Visible absorption characteristics of oligoacenes.

energetic disorder which is induced by intrinsic (crystalline grain boundaries and structural disorder) and extrinsic (impurities) trap states and low dielectric constant of material. For polymers, the repetition of monomer unit also rapidly reduces the band gap energy until certain effective conjugation length [12].

- The delocalization degree has direct impact on the band gap energy: the more electrons are delocalized, the more **OSC** behave similar to metals. This allows to tune the band gap by either localizing electron density in the monomer or delocalizing it across the polymer chain.

  Aromaticity lowers the delocalization degree across the chain and increases band gap [13]. Increase of torsion angle in the system decreases the interaction with neighboring π-orbitals with an angle of 90° disrupting the delocalization completely. This underlines the importance of steric factors for the performance of π-conjugated polymers.

- Various substituents of conjugated system induce their effects on HOMO/LUMO levels: electron acceptor groups lower HOMO and LUMO, simultaneously bringing LUMO level closer to HOMO, decreasing the band gap energy, contrary to electron donor groups. This defines the combination of functional groups as another way to tune the band gap energy.

1.2.3 Charge transport in organic semiconductors

The current which flows through the material on macroscopic scale may be expressed via following equation:

$$j = env = en\mu E, \tag{1.2}$$

where j is the current density, n is the number density of charge carriers and v is carrier drift velocity which is defined as a product of mobility μ and applied field E. Two of these parameters (n and μ) are intrinsic to the particular **OSC** substance. To date, charge carrier mobility μ of **OSC** at their best is comparable only with amorphous silicon (tenths of $\mathrm{cm}^2/(\mathrm{V\,s})$). Carrier density n also deserves a profound discussion.

The electronic properties of **OSC** are governed by these two parameters, which in turn depend on numerous factors. Basically, these factors have intra-molecular (or intra-chain in case of polymers) and intermolecular (or interchain) origins. Intra-molecular factors include the backbone structure, conjugation length, various functional groups, either providing or withdrawing electron density to the π-conjugated system, breaks in conjugation chain and other structural deviations. Intermolecular factors concerns larger scale - molecular packing (herringbone or lamellar pattern, see subsection 1.5.3) which influence $\pi - \pi$ stacking efficiency, chain length for polymers, phase nature for liquid crystal, etc.

Even in case of semiconducting polymer, there is never any chain crossing entire sample. But how in this case charge carrier is able to cross a long distance (compared to molecule length or chain size)? The possibility of effective charge transport between molecules and chains in the bulk is provided by π-π stacking interactions [14]: π-conjugated structures tend to aggregate in a sandwiched manner (Figure 1.4), bringing them close enough to allow charge hopping.

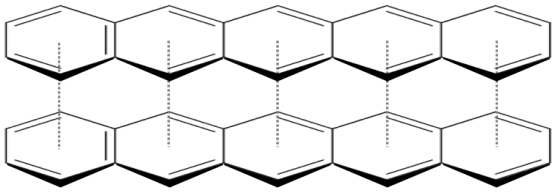

Figure 1.4 – Simplified representation of π-π stacking for two pentacene molecules.

Since **OSC**s consist of different types of materials, such as molecular crystals, amorphous films or glass-like polymers, there is no single generalized model to describe charge transport. Existing models are divided in three groups: band-like, disorder-based and polaronic transport, and their most important particularities are briefly stated below:

Band transport model is valid mostly for monocrystalline structures of high purity and on low temperatures, where scattering due to lattice vibrations is minimized. The interaction energy J (often called bandwidth or *transfer integral*) between neighboring sites of lattice is sufficiently high to overcome the effects of static and dynamic disorder which results in formation of conduction band. It is only true if the band is wider than energetic uncertainty of charge carrier (in case of metals, for example, $J \approx 1\,\mathrm{eV}$) [15]. Materials, studied in this work were not examined under conditions favorable for band transport.

Bässler's Gaussian disorder model explains the contrary case of *band transport* model. It describes charge carrier transport in disordered or amorphous solids, where excitations sites are localized on separate molecules, polymer chains or chain segments. This model introduces temperature dependence of mobility, since the charge carrier moves by "hopping" in the broad density of states, thus requiring thermal activation in order to overcome energy difference in different lattice sites [16]. Behavior of carrier mobility is described by following equation:

$$\mu = \mu_\infty \exp\left[-\left(\frac{2\sigma}{3kT}\right)^2\right] \exp\left\{C_0\left[\left(\frac{\sigma}{kT}\right)^2 - \Gamma^2\right]\sqrt{E}\right\}, \tag{1.3}$$

where E and T are applied field and temperature, respectively, μ_∞ is the value of mobility at infinite temperature and zero applied field, σ is energetic disorder, Γ is positional disorder (between neighboring "hopping" sites), C_0 is an empirical constant (which may be considered to be $2.9 \times 10^{-4}\,(\mathrm{cm/V})^{1/2}$ for a system with cubic lattice constant of 6 Å) and k is the Boltzmann constant.

Holstein's small polaron model describes the coupling of electron excitation to intramolecular or intermolecular vibrations [17]. In this model the charge is represented by a localized polaron with a hole-electron binding energy E_p, and the carrier mobility is described by the following equation:

$$\mu = \frac{1}{(kT)^{\frac{3}{2}}} \frac{ed^2}{\hbar} \left(\frac{\pi}{2E_p}\right)^{\frac{1}{2}} J^2 \exp\left(\frac{-E_p}{2kT}\right), \tag{1.4}$$

where d is the intermolecular distance, J is the transfer integral between neighboring sites and $\hbar$ is the reduced Planck's constant. The importance of this theoretical approach emerges more clearly in comparison to previously presented Gaussian disorder model of transport: since the equation contains both exponential and pre-exponential factors of temperature which provided with certain values of binding energy and *transfer integral* (as a more consistent way to describe intermolecular interactions, which also may be accessed through *ab initio* calculations) parameters will lead to weak temperature dependency of mobility in limits of a given mesophase, often encountered in pure liquid-crystalline **OSC** [18] [19].

The density of charge carriers can be expressed as [16]:

$$n = N_0 \exp\left(-\frac{E_g}{2kT}\right), \tag{1.5}$$

where N_0 is the effective density of states* (DOS). We may use the parameters corresponding to the Si (E_g=1.12 eV and $N_0 = 10^{19}/\text{cm}^3$) to obtain intrinsic carrier density $n_{Si} = 3.35 \times 10^9/\text{cm}^3$ at room temperature (298.15 K) and compare it to the value calculated for pentacene (E_g=1.9 eV and $N_0 = 7.5 \times 10^{16}/\text{cm}^3$[20]) which yields carrier density of about $n_{Pc} = 6.35/\text{cm}^3$ (this estimation provides lower border value, since any impurities will contribute to the resulting DOS). This estimation allows us to better understand the very low intrinsic conductivity of highly pure OSCs.

1.2.4 Doping in organic semiconductors

Since the intrinsic DOS of **OSC** is low, and their band gap energy is much larger than of their inorganic partners, intrinsic carrier density in organic substances is by orders of magnitude lower (equation 1.5). To obtain desirable charge transporting properties, it is often necessary to increase carrier density n by means of "doping". The conception of doping is very different for **OSC** (compared to traditional silicon-based materials) as it includes not only "classic" chemical doping, but any means of creating charge carriers in organic semiconducting system, for example, photoexcitation (photovoltaics and time-of-flight experiment), field-effect or direct charge injection from contacts (transistors and photoluminiscent diodes) which are also considered as doping. Chemical, or more correct to say, *molecular* doping in case of **OSC** is an effective way to increase charge carrier density, but is considerably more complicated compared to conventional processing of inorganic semiconductors due to the nature of **OSC**. Elemental doping (iodine doping of polyacetylene [21], alkaline metal doping [22]) of organic materials does not give desirable results due to diffusion of dopant species: migration of doping sites prevents from obtaining stable and reproducible composites. Next logical step in this direction is to use organic molecules with desired properties. However such substances are not easy to obtain. P-doping could be achieved by transferring an electron from HOMO of **OSC** to the LUMO of dopant. During n-doping the electron is transfered from HOMO of the dopant to LUMO of the **OSC** (Figure 1.5). In order to be efficient, a p-type dopant should have its LUMO close to the HOMO of the host semiconductor. This gives rise to another problem: since most of **OSC** have quite a large band gap, hence their HOMO lies quite deep (about −5 eV to −6 eV), implying the p-dopant to have very high LUMO providing pronounced electrophilic properties. The opposite is true for a n-type dopant,

*DOS describes the distribution of available energy states, which charge carriers may occupy ("populate") per unit volume. In relation to traditional **ISC**, this distribution is usually described via parabolic function, whereas for **OSC**s it is expressed by Gaussian distribution due to higher energetic disorder of the latter.

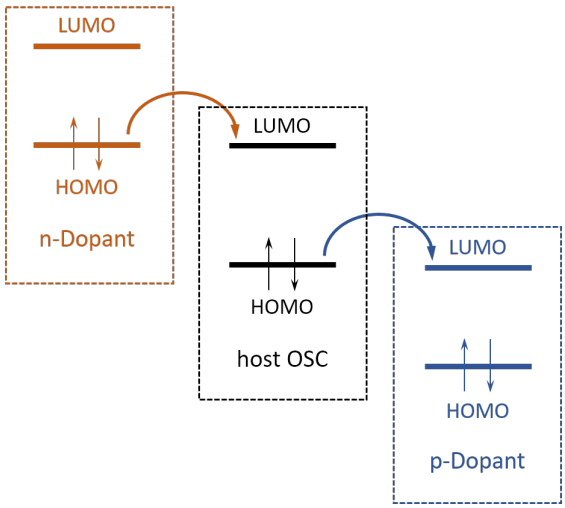

Figure 1.5 – Relation between molecular orbitals of host organic semiconductor and doping agents.

which molecule typically should have its HOMO above −2.5 eV to −3.5 eV. In addition, this makes it unstable in atmospheric conditions, because it would be readily oxidized. Doping also results in shift of HOMO and LUMO levels of composite material, as well as band gap reduction, which sometimes could be beneficial for applications in electronics, but is able to make final result hard to predict.

P-doping of the classic OSC materials such as polythiophenes [23] and pentacene [24, 25] has been thoroughly explored by numerous groups: it has been confirmed that introduction of strong electron acceptors, including the various substituted derivatives of tetracyanoquinodimethane (TCNQ) [26, 27, 28] and other molecules possesing deep LUMO levels [29, 30] results in substantial increase of the conductivity (sometimes even of several order magnitude [31]). These results have given rise to the profound interest in the closer inspection of intermolecular charge transfer (which is not a new subject by itself [32]) in application to organic electronics [33, 34, 35, 36].

Doping of some OSCs results in the apparition of ionized states within the bulk of the OSC. However, it has been recently demonstrated that this concept does not apply to every OSC. When an intermolecular charge transfer takes place, two possible options are usually considered [37]: so-called integral charge transfer (ICT) and partial charge transfer (PCT). The concept of ICT has dominated the field, particularly for classic OSCs with relatively shallow band gap and high lying HOMO, with poly(3-hexylthiophene) (P3HT) [38]. However, not every OSC with an appropriate level of HOMO will forcibly undergo an integral charge transfer. In fact, Mendez et al. [39] has confronted the ICT in

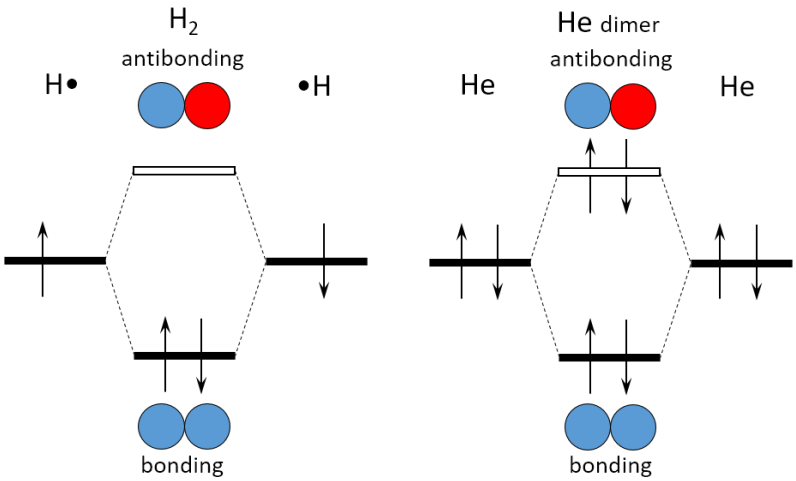

Figure 1.6 – (a) Energy splitting between MOs in a hydrogen molecule, (b) Splitting between bonding and antibonding MOs in a helium dimer.

P3HT - 2,3,5,6-tetrafluoro-7,7,8,8-tetracyanoquinodimethane (**F_4TCNQ**) system with the observable PCT signatures for the quaterthiophene (4T) oligomer. The charge transfer degree for 4T was only of 0.24 [39] as compared with that of fully ionized P3HT.

To better understand the concept of PCT, it is of interest to take a closer look into the nature of molecular orbitals (MOs). A classic example for this is the hydrogen molecule (Figure 1.6, a): each hydrogen atom possess one electron on its 1*s* atomic orbital (AO). The electronic interactions between two hydrogen atoms give rise to the splitting of two MO: a bonding MO (symmetric) and antibonding MO (antisymmetric). Since the H_2 molecule has only two electrons, which occupy the bonding MO in the ground state, the antibonding MO is left empty. The energy of newly formed bonding MO is lower than the individual energy of AOs, thus ensuring a stable covalent bond between the two hydrogen atoms. Another example, which allows us to better understand the interaction between the **OSC** molecules is helium (Figure 1.6, b). Each 1*s* AO of **He** atom is doubly occupied, thus, if two atoms are brought close enough for the MO splitting, it is clear that, as H_2 molecule, the system has the same 2 MOs, but four electrons for this time, which are expected to occupy both the bonding and antibonding orbitals. The overall energy of antibonding MO is higher than individual AOs of He, which explains why helium dimer may be held together only by Van der Waals forces, and no covalent bonding occurs [24].

The rudimentary example of **He** dimer allows to better understand the behavior of

OSC molecules, since most of them are closed-shell systems (HOMO is doubly occupied). In the case of good alignment between two adjacent molecules the MO splitting may arise, though the dimer is still held with only Van der Waals interactions (Figure 1.7a, a). This where the concept of PCT between the host **OSC** and the dopant applies a more elaborated approach. As discussed earlier, in case of good frontier MO energy alignment between the two molecules (donor and acceptor), they form a so-called charge transfer complex (**CTC**) which is regarded from the supramolecular point of view: the electron pair from the donor's HOMO is not entirely transferred to the LUMO of the acceptor, but is situated on a new *supramolecular* orbital which is hybridized during the complex "bonding" [30](Figure 1.7a, b). This MO has lower energy than initial HOMO of the donor and LUMO of the acceptor, which makes the complex state more beneficial and thermodynamically stable. Thus, the electron neither truly leaves the HOMO of the donor nor is fully transferred to the LUMO of acceptor, but is continuously "shared" between two molecular components [24].

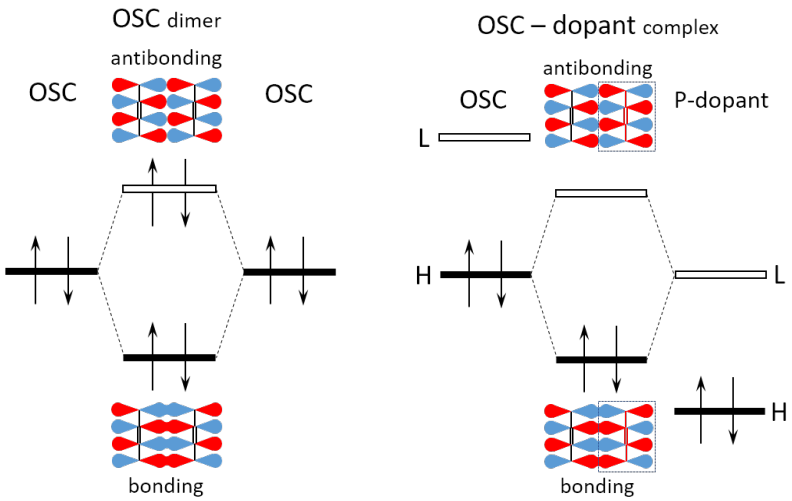

Figure 1.7 – (a) Splitting between bonding and antibonding MOs in **OSC** dimer, (b) Energy splitting between supramolecular MOs in a complex between the **OSC** and P-dopant.

It has been widely demonstrated for doped systems to exhibit an increase of charge carriers density [40, 23, 37]. However, further consequences of this process are not sufficiently addressed. It is expected that a change in electron arrangement of two neighboring molecules of the donor and acceptor substances may lead to the change in

their respective geometry, which may be further expressed as a change in their phase structure at higher scale [41, 42, 43, 44, 45]. For the OSCs, the molecular geometry and order are believed to be the ones of the key parameters governing their performance, notably, the charge carrier mobility [46].

One of the ways to explore the influence of the doping on these parameters is to utilize an OSC which order can be effectively controlled. Liquid crystalline **OSC**s (LC **OSC**s) provide a viable tool to govern the large and small scale order of the system by passing from one phase state to another on changing the temperature. Indeed, many groups have previously employed LC **OSC**s to explore the link between the molecular order and the performance of the material since the discovery of the photoconductivity in LC OSC [47].

1.2.5 Applications and processing

To date, two widely commercialized applications of **OSC** exist: **OLED**s and xerography. Xerography was invented in 1939 [48] and utilizes photoconductive properties of **OSC** to pattern the image by light. **OLED**s in turn are gaining popularity and effectively pushing out their inorganic counterparts out of market. Organic solar cells have also begun to enter the market. For example, danish startup InfinityPV (founded in 2014) offers flexible solar cells and mobile phone chargers. It is impossible for **OPV**s to compete with monocristalline Si or perovskite solar cells in terms of conversion rate, however they are significantly easier to produce. With the technology becoming more cost effective every year, it is possible for **OPV**s to become industrial standard for solar energy conversion. Since one of the main advantages of **OSC** is their unique flexibility in relation to industrial processing, huge efforts are being made in order to optimize production process. There are numerous ways to produce an **OSC** device, which choice would largely depend on physical and chemical properties of semiconductor molecule:

- **Drop casting**
  The most plain way to obtain an **OSC** film. The substance is dissolved in conventional organic solvents and then casted on previously prepared substrate, following with spontaneous solvent evaporation. The thickness of obtained film is directly proportional to the **OSC** concentration in working solution. This method is very simple and cost-efficient: no solution is lost. However, it possesses severe disadvantages: the area of coverage is limited, which in turn imposes difficulties in controlling film thickness. It is very hard to control film morphology,which is only possible via solvent combination and/or alteration of speed of evaporation by changing ambient conditions.

- **Spin coating**
  This method utilizes centrifugal force to control the thickness (get the limits of thickness) of obtained film and allows to achieve good uniformity and reproducibility of results. Thickness of deposited film is inversely proportional to the angular speed of spinning substrate and also depends on solvent choice and **OSC** concentration. While being much more advanced than simple drop casting, this method has some disadvantages related to its principle: the area of spinning substrate is limited due to high angular speed (speed limit) and significant quantity of solution is wasted during process while solvent on deposited part evaporates much faster, leaving less time for molecule ordering (some way to overcome this downside is to introduce post-deposition thermal annealing [49] and to use slower evaporating solvents [50]. This technique is going to be described in more details in the Chapter 2.

- **Blading**
  The basic principle of blading (and closely related screen printing) technique is to spread the working solution with a micrometer-controlled blade on moving or stationary substrate. This helps to attain high uniformity of film on relatively large surface without wasting solution. However, the dimensions of blade and the fact that it is controlled mechanically impose limit on attainable film thickness ($> 150 \div 200$nm)

The methods stated above are among the most popular ways of deposition of **OSC** films, though less common ways exist: dip coating (immersing the entire substrate in the working solution following its withdrawal with controlled speed), Langmuir-Blodgett film deposition (utilization of hydrophobicity and hydrophilicity of **OSC** molecules and substrate), spray coating (the substrate is sprayed by vaporised working solution) and inkjet printing (substance is deposited from the printer nozzle). All these methods are only applicable if **OSC** substance is soluble in conventional solvents.

However, a substantial ammount of small molecule **OSC** are insoluble (notably, non-substituted small molecule **OSC** which have high Van der Waals interactions). The following techniques are applied for deposition of insoluble **OSC** moieties:

- **Vacuum thermal evaporation**
  This method by far is used most often for deposition of insoluble **OSC**. Sublimation of organic molecules requires high vacuum (10^{-5}-10^{-7} torr) and high temperature (hundreds of °C) of resistively heated crucible, which negatively impacts the cost of equipment. However, good control over thickness and very high quality of order in thin films usually yields excellent reproducibility. Although this method

produces very good results (being one of the best techniques for small molecule **OSC** deposition) it has relatively low throughput and wastes considerable amount of high-purity material and lacks large surface area coverage.

- **Vapor Phase Deposition**
  To overcome the downsides of previous method, heated low pressure inert carrier gas (N_2, Ar) flow is used in a heated deposition chamber. This allows to enhance throughput by increasing deposition rate, lower material waste (since the walls of chamber are heated, no sublimation occurs). These factors allow to apply this technique to larger area of substrate.

- **Molecular beam epitaxy**
  One of the most advanced techniques in terms of attainable molecular order, which has even more restricted requirements than vacuum thermal evaporation (utra-high vacuum of 10^{-8}-10^{-12} torr) and extremely slow deposition rate which results in epitaxial crystal growth. These requirements make this technique very expensive to use.

Thermal evaporation methods are not the only ones for insoluble **OSC** deposition. It is possible to prepare an **OSC** film by using soluble precursor with any of solution processing techniques and then to transform the obtained film to the desired **OSC** by post-treatment (electropolymerization of pyrrole, for example).

1.3 Classification of organic semiconductors

This section does not attempt to fully cover all organic semiconductor types, but serves to demonstrate significant diversity which exists in the field of **OSC**. These organic compounds are usually divided in two large sub-groups: semiconducting polymers and so-called small molecules. This classification presents two distinct set of requirements, approaches to characterize and improve charge-transporting properties of these materials.

Polymeric semiconductors are historically the first regarded type of **OSC**, and their most notable feature is the ability to form amorphous films after being deposited from a solution. Charge transport in polymeric **OSC** films is carried out by two mechanisms: intra-chain (within the limits of a single chain) and interchain (on a larger scale, between different chains of polymer). Recent experiments with TRMC (time resolved microwave conductivity) show very high intra-chain mobility even for relatively low-perfoming **OSC**, for example poly[2-methoxy-5-(2-ethylhexyloxy)-1,4-phenylenevinylene] (MEH-PPV) [51].

This allows to propose that for polymeric **OSC** the interchain transport could be regarded as a bottleneck, postulating the need of its improvement. Numerous possibilities have been studied, including experimenting with polydispersity index, deposition process, post-annealing, introduction of aggregating agents and etc.

Small molecule semiconductors are the second family of **OSC**. These substances (notably, rubrene, pentacene and [1]benzothieno[3,2-b]benzothiophene) are capable of showing exceptionally high charge carrier mobility under laboratory conditions (single-crystal samples, under inert atmosphere and low temperature exhibit band transport), but however are not easily implemented in mass-production. Carefully grown by molecular beam epitaxy or thermal evaporation single crystals, which possess almost no crystalline defects, represent an ideal system for charge transport. However, for a more common case of polycrystalline film, band transport is no longer possible due to spatial disorder, and performance declines rapidly with increase of polycrystallinity. Possible ways to bypass these difficulties include improving long-range order, which could be attained with careful choice of solvent and deposition mode. This conclusion has sparked profound interest in small molecule **OSC**s which exhibit liquid crystalline properties, which enables greater control over molecule orientation and crystal domain size.

1.3.1 Polymeric OSCs

Members of this group are essentially polymers or co-polymers of various aromatic and π-conjugated structures, interconnected in a way which maintains π-π conjugation along the polymeric chain and may include different sidechain substituents, often alkyl chains with varying degree of ramification. These sidechains allow the polymeric structure to be readily solubilised in common solvents, effectively decreasing intermolecular Van der Waals interactions. Most widely employed monomer units include phenylene, fluorene, thiophene and other heterocycles (Figure 1.8).

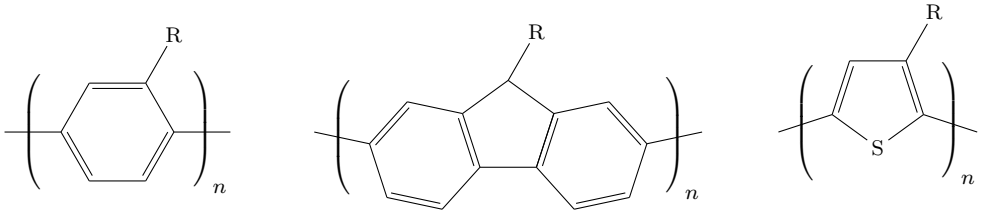

(a) (b) (c)

Figure 1.8 – Molecular structure of some polymeric **OSC**s: (a) polyparaphenylene, (b) polyfluorene, (c) polythiophene. R denotes optional alkyl sidechain.

Phenylene-based polymers are the most studied group of π-conjugated substances. Notable examples include polyparaphenylene (PPP, Figure 1.8, a), paraphenylenevinylene (PPV) as well as their alkyl substituted versions (for example, MEH-PPV with improved solubility). They are relatively simple and mass-produced **OSC**s, which have found their use in **OLED** industry [52] [53] [54] and exhibit low charge carrier mobility of order from $10^{-7}\,\mathrm{cm}^2/(\mathrm{V\,s})$ to $10^{-5}\,\mathrm{cm}^2/(\mathrm{V\,s})$ [55].

Fluorene-based polymers share the same light-emitting applications with phenylene-based materials. Studies of different substituents for fluorene moiety (Figure 1.8, b) has enabled first fabrication of blue organic light-emmiting diodes [56] [57]. Different copolymers of fluorene are capable of showing bulk hole mobility in the range from $10^{-5}\,\mathrm{cm}^2/(\mathrm{V\,s})$ to $10^{-3}\,\mathrm{cm}^2/(\mathrm{V\,s})$ [58].

Thiophene-based polymers (Figure 1.8, c) are the classic and most studied polymeric materials for charge transporting applications. Profound understanding of their electronic properties as well as good control over film morphology makes them the pinnacle of high-performing charge conducting polymers. This group makes a great example to illustrate the significance of structural planarity in π-conjugated systems. The remarkable comparison of poly(3-hexylthiophene) (P3HT) fractions with different degree of regioregularity*[59] shows carrier mobility spanning for almost four orders of magnitude from $2 \times 10^{-5}\,\mathrm{cm}^2/(\mathrm{V\,s})$ for 70% regioregular blend to extraordinary $0.1\,\mathrm{cm}^2/(\mathrm{V\,s})$ for sample with 96% of regioregularity.

N-type polymers are still relatively rare and present a growing field of interest. One of the most remarkable examples is the poly(benzobisimidazobenzophenanthroline) (BBL), a so-called ladder polymer, which is reported to have n-channel **OFET** mobility of $0.1\,\mathrm{cm}^2/(\mathrm{V\,s})$ [60]. Other examples are some fluorinated copolymers,naphthalene dicarboximide, pyridinium phenylene, etc.

1.3.2 Small molecule OSCs

The concept of small molecule **OSC**s consists of relatively large π-conjugated core with optional substituents enhancing its solubility. Building blocks for core structures usually include but not limited to mono- or polycyclic aromatic hydrocarbons (benzene, naphthalene, other oligoacenes and their structural isomers), heterocycles (thiophene, pyrrole,

*This property describes a polymer chain where all the repeating units are derived from the same isomer. In relation to poly(3-alkylthiophene), the alkyl chains are attached to the *same* side of the thiophene heterocycles, which makes them aligned in the *same* direction.

imidazole) and their fused variations as well as their combinations with unsaturated aliphatic groups (olefinic and acetylenic). Similar to conventional **ISC**s, their organic incarnations can favor either p- or n-type transport:

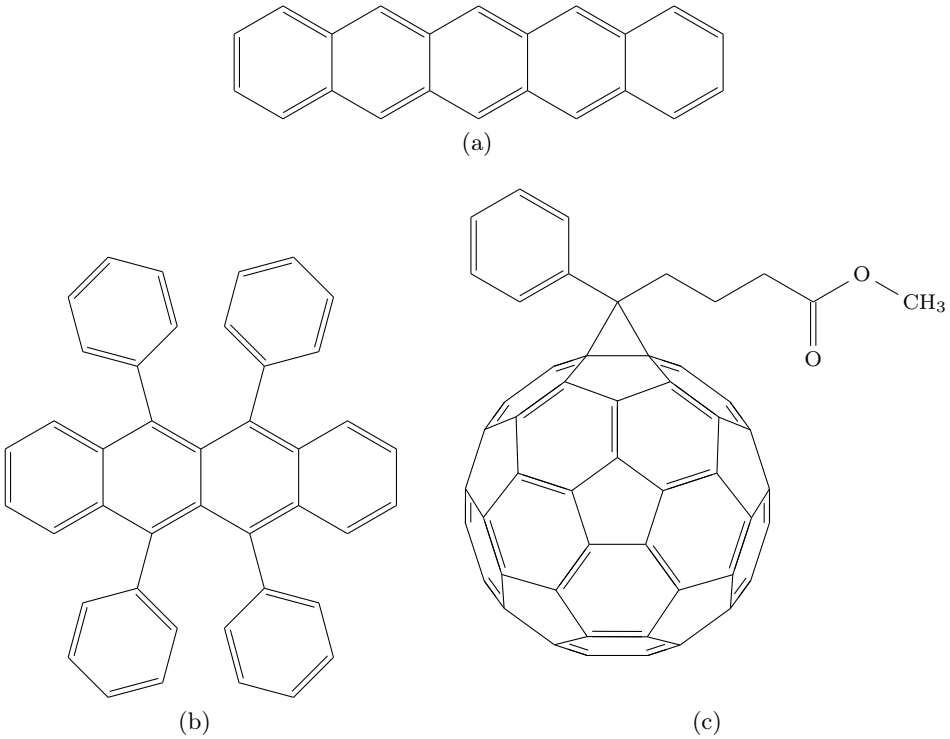

Figure 1.9 – Molecular structure of some small molecule **OSC**s: (a) pentacene, (b) rubrene, (c) phenyl-C61-butyric acid methyl ester (PCBM).

P-type small molecule OSC are mostly represented by polycyclic aromatic hydrocarbons (for example, tetracene and pentacene (up to $5\,cm^2/(V\,s)$ [61]) (Figure 1.9, a)), their isomers (pyrene and perylene) and derivatives (rubrene ($13\,cm^2/(V\,s)$ [62], Figure 1.9, b) and (triisopropylsilyl)ethynyl (TIPS) functionalized pentacene, $2.4\,cm^2/(V\,s)$ [63]) and are able to compete with amorphous Si in terms of mobility (tenths of $cm^2/(V\,s)$). Heterocyclic molecules have also proven their place in this class of materials: significant amount of studies was conducted on oligothiophenes [64], derivatives of tetrathiafulvalene [65] and other thienoacenes [66]. Molecules which contain nitrogen atoms are also not rare and include phtalocyanine [67] and porphyrin[68] derivatives with their organometallic complexes [69].

N-type small molecule OSC are less numerous than P-type ones, similarly to conjugated polymers. Compounds based on fullerene C_{60}, which have high electron

affinity (LUMO about 4 eV) have attracted the most attention and have been thoroughly studied in application to **OPV**s [70] and **OFET**s [71]: for example, phenyl-C61-butyric acid methyl ester (PCBM, Figure 1.9, c) has demonstrated good solubility and very high field effect electron mobility up to $6\,\mathrm{cm}^2/(\mathrm{V\,s})$. Other more exotic subtypes of N-type small molecule **OSC** include fluorinated derivatives of acenes or compounds incorporating cyano- and carbonyl functional groups.

1.3.3 Liquid crystalline OSCs

The majority of liquid crystalline **OSC**s may be regarded as small molecule **OSC** which exhibit mesogenic behavior (though some examples of lyotropic behavior in conjugated polymers have been reported [72]). This concept is particularly attractive since liquid-crystalline properties offer exceptional control over intermolecular order. However, in-depth review of **LC**s is not an objective of this thesis, and detailed physical and thermodynamical properties are not going to be covered here [73], but only the properties which are relevant to charge transport.

Calamitic organic semiconductors

This type of **LC**s consists of rod-like molecules with π-conjugated core with one or more often two aliphatic side chains which are responsible for their solubility and mesogenic properties. They form relatively fluid mesophases which still retain different degrees of order for their molecular long-axes (*directors*).

The most common and primitive case of mesophase is nematic (N) phase [73]. In this phase the molecules have only one degree of order: the *directors* of molecules stay more or less parallel over a significant (for a microscopic scale) distance. Molecules are free to move along their molecular axes and therefore their mass centers are randomly distributed (Figure 1.10). Generally, nematic phase has low viscosity and is easily aligned by moderate electric or magnetic field and spontaneously align on pre-treated surfaces. Another subtype of nematic phase is a so-called *twisted nematic* phase which is formed by chiral molecules and produces helix-like structures, however, this phase is not covered in this section.

Next step in mesophase ordering is the family of smectic phases. Smectic mesophases have two-dimensional order: in addition to *director* collinearity, the molecules are organised in layer structures. For smectic A (Sm_A) phase, the molecules are aligned mostly parallel to the layer plane normal, when for the more-ordered smectic B (Sm_B) phase the molecules tend be more strictly ordered and to form hexagonal pattern within the layer plane

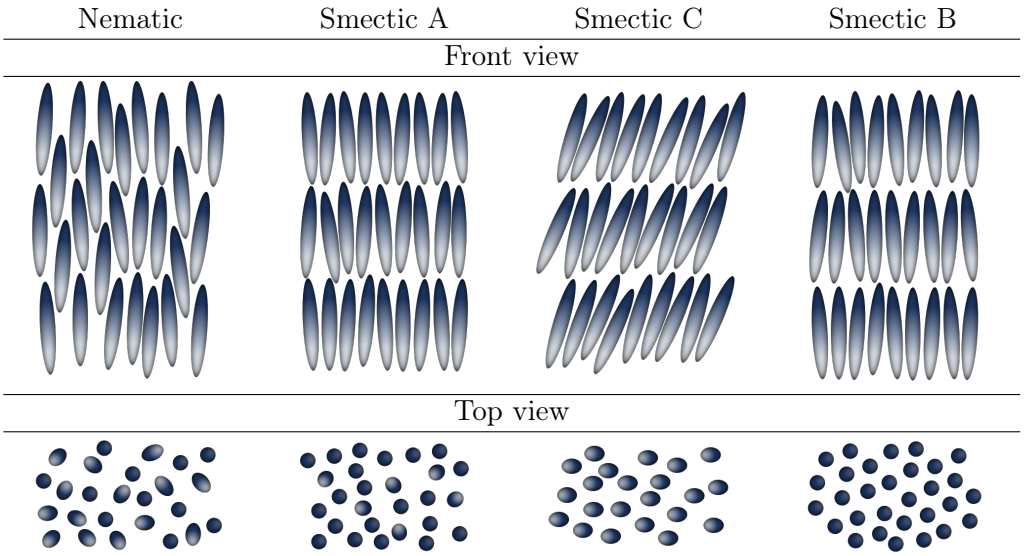

Figure 1.10 – Schematic representation of most common calamitic mesophases: nematic (N), smectic A (Sm_A), smectic C (Sm_C) and smectic B (Sm_B).

(Figure 1.10), however this pattern lacks long range order. Smectic C is essentialy the Sm_A phase with molecules tilted to a certain angle in respect to layer normal. There are other types of smectic phases with different combinations of short- and long-range ordering, labeled by letters of alphabet and have their chiral counterparts, similar to the case of nematic mesophase.

These smectic phases exhibit long range orientational order and short range positional order. The phases with both long-range orientational and positional order are often called *smectic crystals* and are outside of the subject of this study. Generally speaking, improved order of a mesophase is induced by higher interaction between molecules, which in turn renders this mesophase less susceptible to alignment control.

Figure 1.11 illustrates by means of a generic calamitic smectic mesogen the relation between charge carrier mobility and structural order of system. Further in this section we are going to describe two types of **LC**s: calamitic and discotic **OSC**s with relevant examples.

Typical core structures for semiconducting calamitic **LC**s include oligothiophenes (bisphenyl bithiophene, quarterthiophene), carbazole, benzothiadiazole, fused acenes (naphthalene and anthracene) or thiophenes (thienothiophene and dithienothiophene), fluorene, or less common pyridine and their various combinations (benzothienobenzothiophene, thienonaphthalene, etc.). Some notable examples are assembled in the Figure 1.12.

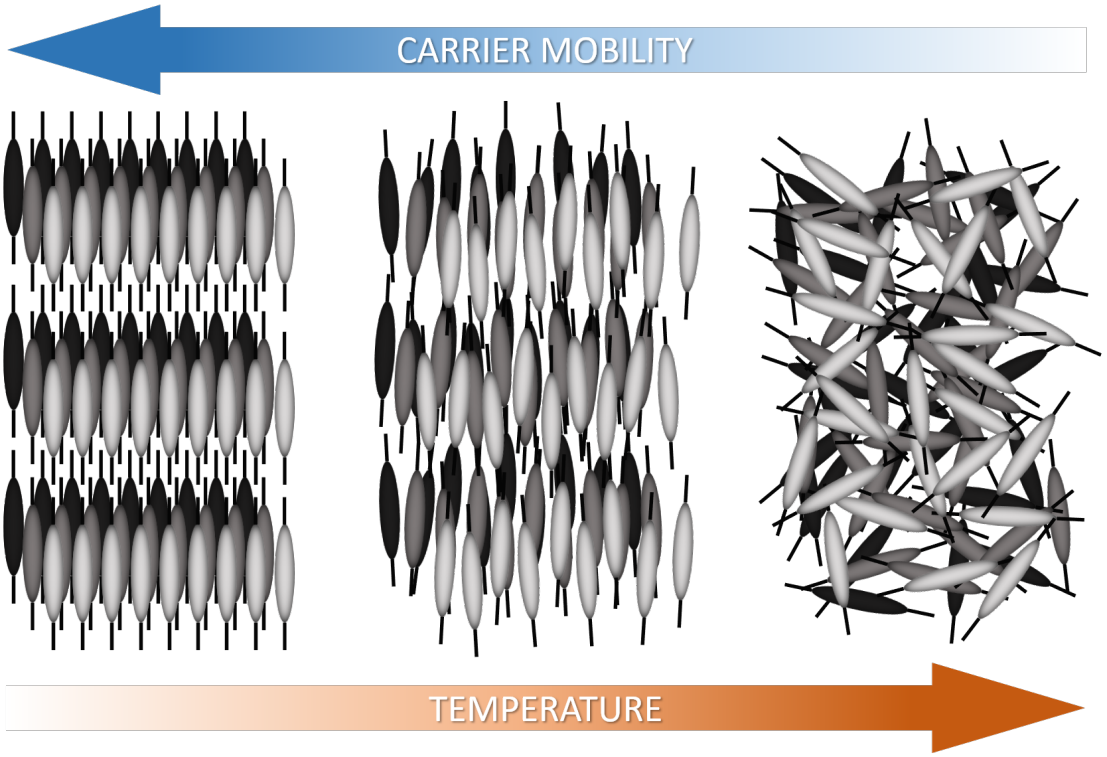

Figure 1.11 – Relation between phase state (from left to right: crystalline, liquid-crystalline, isotropic liquid) and charge carrier mobility.

Evidence of charge transport in calamitic liquid crystals begin to emerge as early as of 1993, with the works on photoconductivity of oxadiazole- and thiadiazole-based smectogens [47]. Later, phenyl naphthalene-based (Figure 1.12, (d)) liquid crystal (2-(4'-octylphenyl)-6-dodecyloxynaphthalene, **8-PNP-O12**) [74] was prepared by M.Funahashi and J.Hanna in 1997 and became one of the first calamitic **LC OSC** to receive significant attention and revive interest to liquid crystals. It possesses moderate mobility of $1.6 \times 10^{-3}\,\mathrm{cm}^2/(\mathrm{V\,s})$ in Sm_B mesophase and $2.5 \times 10^{-4}\,\mathrm{cm}^2/(\mathrm{V\,s})$ in Sm_A mesophases, but for last years has became de-facto a model liquid crystal organic semiconductor due to numerous works published [75] [76] [77] [78].

Oligothiophene (Figure 1.12, (b))- and phenylthiophene(Figure 1.12, (a))-based liquid crystals were extensively studied by groups of M. Funahashi [79], J. Hanna [80] I. McCulloch and T. Kreouzis [81] [82], yielding hole mobility values in their most ordered mesophase up to $0.1\,\mathrm{cm}^2/(\mathrm{V\,s})$ [80] for quaterthiophene, $0.02\,\mathrm{cm}^2/(\mathrm{V\,s})$ for phenyl trithiophene [79] and $0.044\,\mathrm{cm}^2/(\mathrm{V\,s})$[81] bisphenyl bithiophene-based molecules. **LC OSC**s tend to exhibit smectic phases with an exception for thienylethynyl terthiophene (Fig-

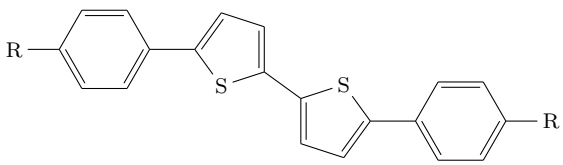

(a) Bisphenyl bithiophene

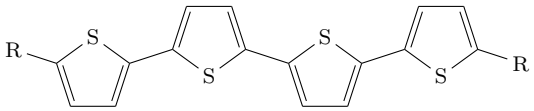

(b) Quaterthiophene

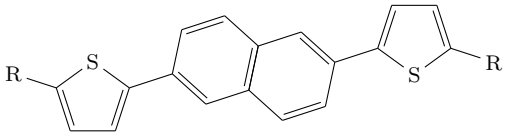

(c) Bisthienyl naphthalene

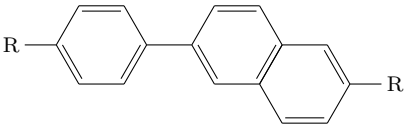

(d) Phenyl naphthalene

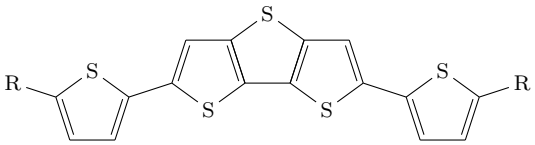

(e) Bisthienyl bisthienothiophene

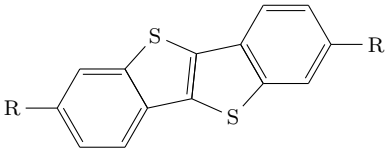

(f) Benzothieno-benzothiophene

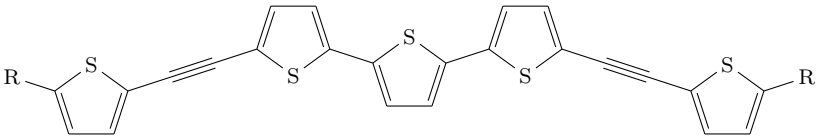

(g) Thienylethynyl terthiophene

Figure 1.12 – Examples of calamitic **LC OSC** cores, where R is the lateral alkyl chain.

ure 1.12, (g))-based molecule, posessing also a nematic phase and showing relatively high mobility of $0.02\,\mathrm{cm}^2/(\mathrm{V\,s})$ [83] for the hexyl-substituted derivative. Fused core structures tend to possess higher mobility values (which can be explained by improved conjugation), however that is not always true. For instance, bisubstituted derivatives of bisthienyl-bisthienothiophene (Figure 1.12, (e)) attain mobility up to $0.02\,\mathrm{cm}^2/(\mathrm{V\,s})$ [84], and for octyl-substituted 2,5-bisthiophene thieno[3,2b]thiophene values up to $0.07\,\mathrm{cm}^2/(\mathrm{V\,s})$ [85] were obtained. Bisthienyl-benzene with $0.1\,\mathrm{cm}^2/(\mathrm{V\,s})$ [86], -naphthalene (Figure 1.12, (c)) with $0.14\,\mathrm{cm}^2/(\mathrm{V\,s})$ [87], -anthracene with $0.48\,\mathrm{cm}^2/(\mathrm{V\,s})$ [88] show, however, a remarkable succession in dependency of mobility on the core conjugation length.

One of the most interesting groups to date are the derivatives of [1]benzothieno[3,2-b]-[1]benzothiophene (Figure 1.12, (f)) which have outstanding charge carrier mobility. In particular, 2,7-dioctyl[1]benzothieno[3,2-b][1]benzothiophene [89] prepared by Ebata et al. in 2007 has record mobility up to $43\,\mathrm{cm}^2/(\mathrm{V\,s})$ [90] measured in a highly-aligned film.

Discotic organic semiconductors

Discotic **LC**s represent another concept of mesogenic compound, notably a disc-shaped molecule. In relation to **OSC**, they usually have a large aromatic core with radial symmetry and several alkyl chains attached to perimeter of the core. Thereby, their structure is more adapted to be used as a high-performance **OSC**: large conjugated core allows to attain higher levels of π-interaction and is possibly more effective as a charge transporting moiety.

Figure 1.13 – Schematic representation of most common discotic mesophases: discotic nematic N_D, columnar nematic N_{Col} and columnar hexagonal Col_H

The least-ordered phase of discotic **LC**s is the discotic nematic (N_D, Figure 1.13) which is in some way analogous to calamitic nematic: the planes of molecules are ordered in a more or less parallel disposition. Another subtype of nematic family is the columnar nematic (N_{Col}, Figure 1.13) phase. Here, the elementary unit of system is not a single

molecule (encountered in N_D case) but a relatively short column of stacked molecules [91]. These units form a nematic "array", in a similar way with calamitic nematics. Both of these cases are rare among the discotics, proving the nematic ordering to be not largely inherent for this family of **LC**s.

Columnar mesophases occur more frequently. In columnar phases stacks of molecules are arranged in parallel structures, but they also have a certain degree of pattern-like ordering, which in turn is labeled by letters (in fact, very similar to the classification of smectic mesophases). As an example, the columnar hexagonal phase Col_H (Figure 1.13) strongly resembles Sm_B mesophase by means of its hexagonal pattern. The degree of order inside of a column also varies from substance to substance, and for same phases the molecules can possess significant tilt.

Most notable examples of π-conjugated structures of discotic **LC OSC** are perylene (often in a form of diimide), triphenylene, coronene (or other fused arenes), porphyrins, phtalocyanines and sometimes organometallic complexes. Perylene diimide (Figure 1.14, (a)) is a well-known n-type **OSC**, exhibiting π-stacking columnar properties [92], its derivatives are capable of high electron mobilities ($0.6\,\mathrm{cm^2/(V\,s)}$ [93]). Another similar structure, pyrene is well-known for its high fluorescent properties, discotics based on this core have interesting perspectives in light-emitting applications [94]. Pyrene is also often used as a substitutent for discotic dendritic structures [95]. However, one of the most interesting groups of discotic **OSC** are triphenylenes (Figure 1.14, (b)). A whole family of alkyl-substituted triphenylene derivatives exhibit hole mobility in order of $1 \times 10^{-3}\,\mathrm{cm^2/(V\,s)}$ for pentyl (R=C_5H_{11}) lateral chain [94] and up to $0.018\,\mathrm{cm^2/(V\,s)}$ in case of shorter butyl (R=C_4H_9) substituents [96]. Structures which possess bigger π-conjugated core such as hexabenzocoronene (Figure 1.14, (d)) exhibit much higher mobility, however it is very difficult to control the sample alignment. For decyl (R=$C_{10}H_{21}$) substituted hexabenzocoronene, an extremely high mobility of $0.5\,\mathrm{cm^2/(V\,s)}$ [97] was observed on single-column scale, attaining however only $1 \times 10^{-3}\,\mathrm{cm^2/(V\,s)}$ [98] in the bulk. Phthalocyanines (Figure 1.14, (c)) and porphyrines were also extensively studied [99] [100] [101], yielding hole mobility of about $0.2\,\mathrm{cm^2/(V\,s)}$ in the bulk. These examples allow us to estimate the orders of carrier mobility value, typically obtainable for this class of materials. To conclude, liquid crystalline semiconductors show best mobility values at their most ordered mesophase. But, for seemingly the most ordered crystalline phase, grain boundaries are significantly limiting their performance. Numerous studies have been conducted on this subject, and it is safe to say that there is a lot to be done in order to understand and take into account all the factors which influence semiconducting properties of organic molecules.

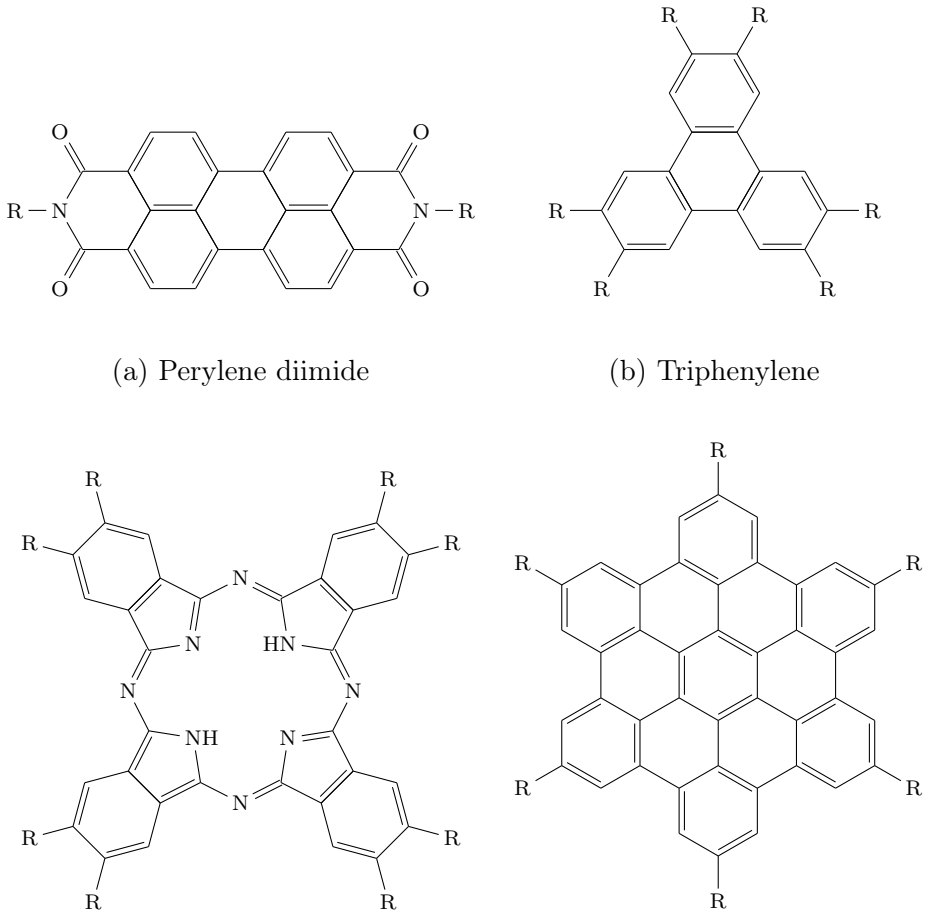

(a) Perylene diimide

(b) Triphenylene

(c) Phthalocyanine

(d) Hexabenzocoronene

Figure 1.14 – Examples of discotic **LC OSC** cores, where R is the lateral alkyl chain.

1.4 Photopolymers

Photopolymer is a composite of monomer and corresponding photoinitiator, which undergoes structural changes (construction of polymeric network, so-called curing) induced by light irradiation. The photopolymerisation process is followed by significant change of physical properties (hardening, formation of resins) which has a wide variety of applications: varnishes, enamels, glues and photoresists, etc.

In application to **OSC** one should not confuse polymeric semiconductors with photopolymers, as for polymeric **OSC** the monomer units are $\pi-$conjugated with each other along the whole backbone of polymeric chain, but for now no method exist to create a π-π conjugated bond via conventional photopolymerizable groups. Photopolymerizable

OSC could be a small semiconductor molecule, often of liquid crystal type and carry their functional groups on the end of an aliphatic chain.

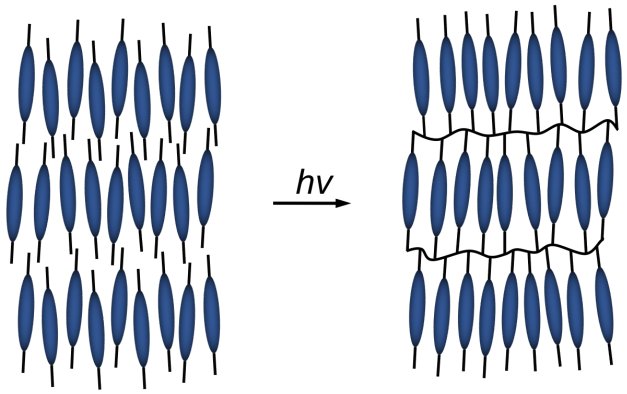

Figure 1.15 – Cross-linking of a smectic reactive mesogens.

The main interest of creating such substances is to "freeze" liquid crystal **OSC** in the most ordered mesophase by photocuring (Figure 1.15) [102], [103] [104]. Potentially this would help to attain thermal stability with retaining valuable properties of chosen mesophase. Other benefits are improving mechanical properties of **OSC** film, gaining of insolubility and blocking or significantly hampering movement of ionic impurities (these impurities in turn could act as charge traps), almost always present in **OSC**. Also, retaining **LC** structure will, in theory, help to overcome grain boundary defects of crystalline phase. Some applications, as light-emitting diodes, could also benefit from the opportunity to pattern the semiconductors with light. However, great care should be taken with introducing photopolymerizable functional groups in the molecule. Alteration of chemical structure could cause unpredictable results: loss or weakening of mesogenic properties, lowering of charge carrier mobility because of increased intermolecular distance hampering charge hopping rate, and undesired shifts in HOMO & LUMO levels. Polymerization also alters intermolecular spacing, bringing it from Van der Waals interactions distance to a covalent bond, which sometimes can improve π-π interactions, or induce more boundary defects, rendering the result quite unpredictable and difficult to interpret[105].

Excess of photoinitiator left after curing can also become a source of defects in liquid crystalline media and result in charge trapping [104]. For applications where light absorption or emission is required, excessive use of photoinitiator may cause unwanted shifts in spectrum. Together, these issues make a preparation of a polymer formulation with favorable properties a non-trivial task.

In fact, the idea of applying photopolymers to **OSC**, notably liquid crystal **OSC**, is not new by itself, as some attempts have already been made to functionalise calamitic and discotic semiconductors. A very comprehensive work was conducted by the group of Theo Kreozis to functionalise phenylnaphthalene (Figure 1.12, (d))- and quaterthiophene (Figure 1.12, (b))- based liquid crystals with different types of photo-crosslinkable groups of free-radical and cationic process [105]. However, it is still difficult to estimate the contribution of polymeric groups to charge carrier transport. Discotic semiconductors can also undergo chemical functionalization [106] [107] [108] in order to form crosslinked structures, effectively stabilizing charge-transporting properties of their mesophases at room temperature. Design and synthesis of molecules which combine these properties (semiconducting, mesogenic and photopolymeric) is a non-trivial task and often leads to fairly unpredictable results.

Such problems give rise to a more simple solution: creating a bi-component system, consisting of a conventional liquid crystalline semiconductor and a so-called reactive mesogen: a bi- or monofunctionalised liquid crystal, usually of calamitic nature (Figure 1.16).

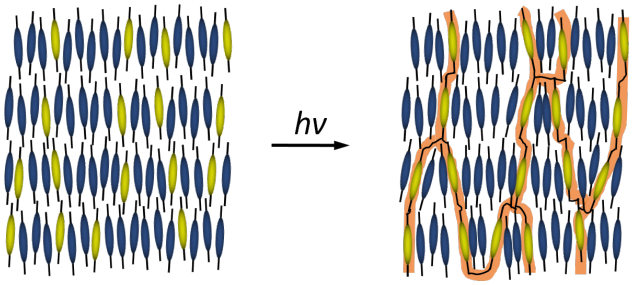

Figure 1.16 – *In situ* creation of polymeric backbone within **OSC** host by introduction of a reactive mesogen.

Most of liquid crystalline **OSC** are limited by their π-interacting nature and usually exhibit highly-ordered smectic or plastic crystalline phases. These materials have excellent short-range order but stay poorly oriented on higher scale, exhibiting polydomain structure. Reactive mesogens in turn are mostly nematic liquid crystals and their orientation is easily controlled. Combining both types of compounds in theory allows to increase the size of domains and render them more ordered, thus improving interdomain charge transport. Most promising works in this direction were conducted on discotic semiconductors by preparation of physical (hydrogen-bonded) gels [109] [110] [111], improving mechanical

properties and alignment of mesophases. Considerable amount of such works do not benefit from possible liquid-crystalline properties of a gelator [112].

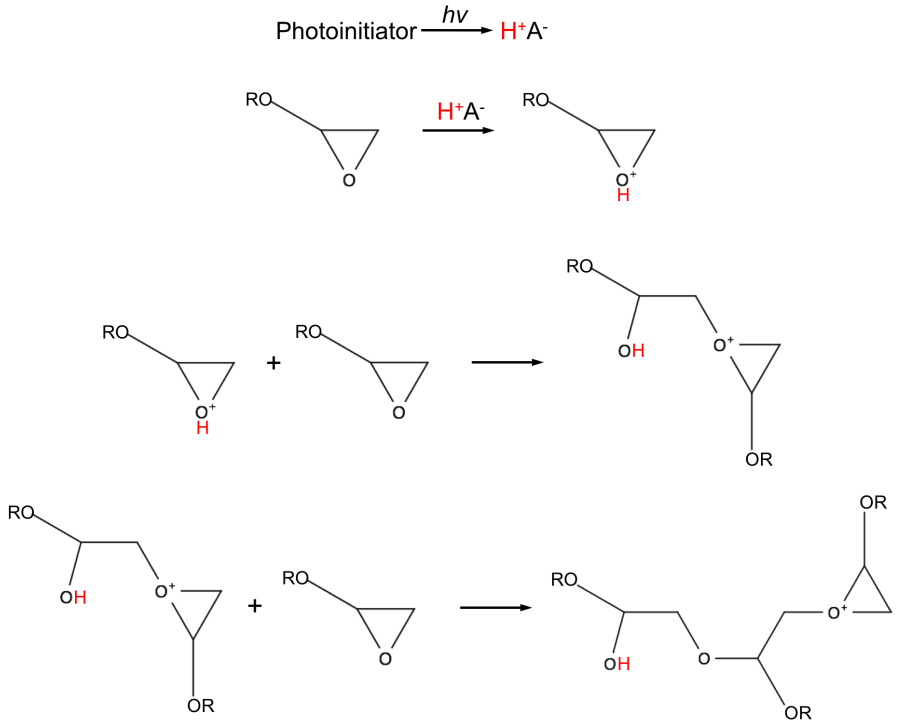

Figure 1.17 – Possible mechanism for cationic polymerization on the example of epoxide functional group.

1.4.1 Functional groups

Two methods of photopolymerization exist: cationic (anionic photoinitiators are considerably less investigated and are almost not present in commercial use) and free-radical.

Epoxide, vinylether and oxetane groups can be cross-linked with a cationic photoinitiator. One particular advantage of cationic process is its indifference to oxygen level, so it may be conducted under ambient conditions. Most popular choices of cationic curing agent include sulfonium, iodonium and pyridinium salts. The process itself is being initiated by a strong photo-acid (Brønsted or Lewis-type) which is formed after the photoinitiator absorbs light. The cationic photoinitiators got their name for the light-absorbing part of the molecule: the cation is being light-sensitive, and the anion becomes a photo-acid. Though the exact mechanism of cationic photopolymerization is

yet to be understood, generalized schematic could be observed on the Figure 1.17 by the example of epoxide group. After the protonation by photo-acid, the charge transfers from one chain member to the next.

Free-radical process is usually applied to acrylate and methacrylate functional groups, and could be significantly hampered by presence of oxygen and requires inert gas environment, usually nitrogen. Also, functional groups of this type are shown to be much more sensible to high temperature and are prone to spontaneous polymerization, thus requiring some thermal stabilizers (for example, butylated hydroxytoluene or BHT). However, one of the most significant advantages compared to cationic process is the sensibility of photoinitiator. Contrary to cationic curing, it is the radical which is being transferred along the polymer chain (Figure 1.18). Salt which are used for cationic process mostly have their absorption maxima in deep UV ($<$250 nm), when free-radical photoinitiators possess more user-friendly absorption region (often above 300 nm). In fact, sometimes some free-radical sensitizer is used to assist a cationic curing process in order to use more convenient wavelength of irradiation [113].

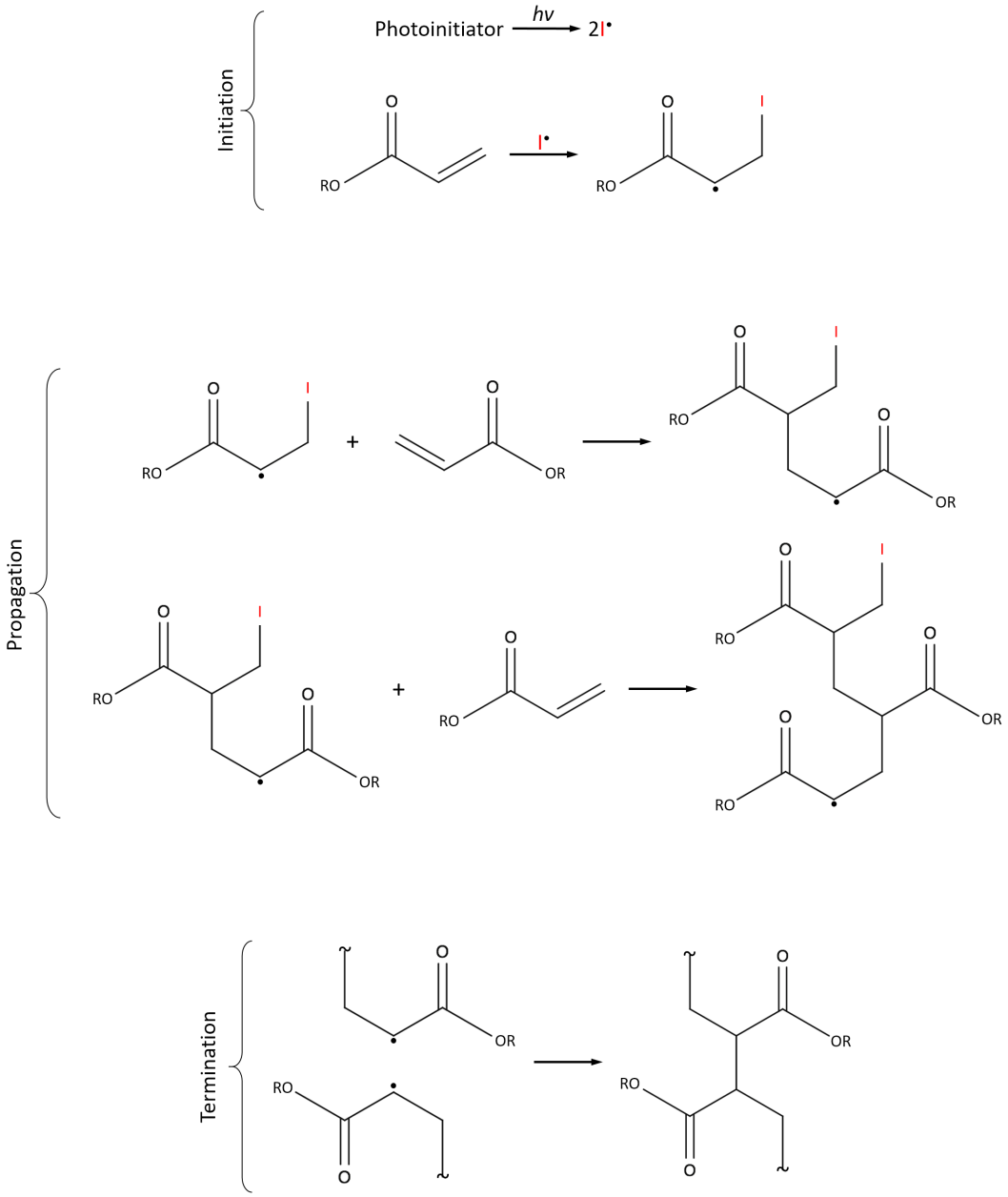

Figure 1.18 – Possible mechanism for free-radical polymerization process.

1.5 Organic Field Effect Transistor

1.5.1 Introduction

Transistor is an electronic device based on a semiconductor material and is used to switch or amplify electrical signal. Today, transistor is the main building block of computer logic and is an indispensable component of many circuit concepts, employed either as a standalone component, or as a part of integrated circuit. There are two most popular basic types of transistors: bipolar junction transistor (BJT) and field effect transistor (FET). In this thesis the attention would be focused on the FET family of devices. The FET group in turn divides in two sub-types, insulated-gate FETs (notable examples are metal-oxide-semiconductor FET (**MOSFET**) and organic FET (**OFET**)) and junction-gate FETs. **MOSFET** devices usually operate in depletion or enhancement mode, when most of **OFET**s works in accumulation mode except for some rare examples [33]). Inorganic semiconductor devices are not covered in this study.

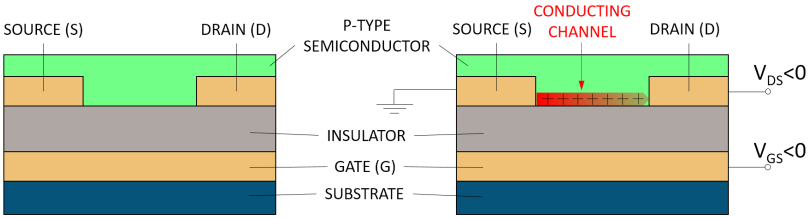

(a) No voltage applied to gate terminal (b) Negative voltage applied between source and gate terminals

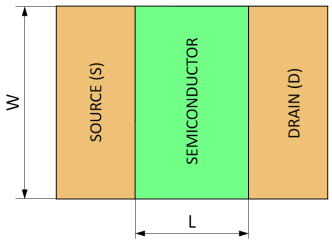

(c) Channel geometry

Figure 1.19 – Schematic structure of **OFET**: (a) device is switched off; (b) current is driven by voltage V_{DS} while **OFET** is swiched on by negative gate voltage V_{GS}; (c) geometry of **OFET** channel: **L** is the channel length, **W** is the channel width.

Basically, the geometry of an **OFET** strongly resembles one of a capacitor (Figure 1.19) with one conventional electrode (*gate*) separated with a dielectric layer from the second

electrode, which consists of two conducting parts (*source* and *drain*) and semiconductor (*channel*).

In fact, the undoped **OSC** by itself behaves similarly to an insulator: the number of free charge carriers is significantly lower (orders of magnitude) than in its inorganic counterparts [114]. For example, in p-type **OFET** (since most of the **OSC** are p-type) under applied negative gate field, holes are being injected in the channel from the source electrode (which has an appropriate work function value in order to ensure ohmic contact with **OSC**), increasing charge carrier density. After injection, charge carriers accumulate in the **OSC**-insulator interface region called conducting channel(Figure 1.19, (b)). This phenomena is called "field-effect", hence the name of the device. Assuming the insulator

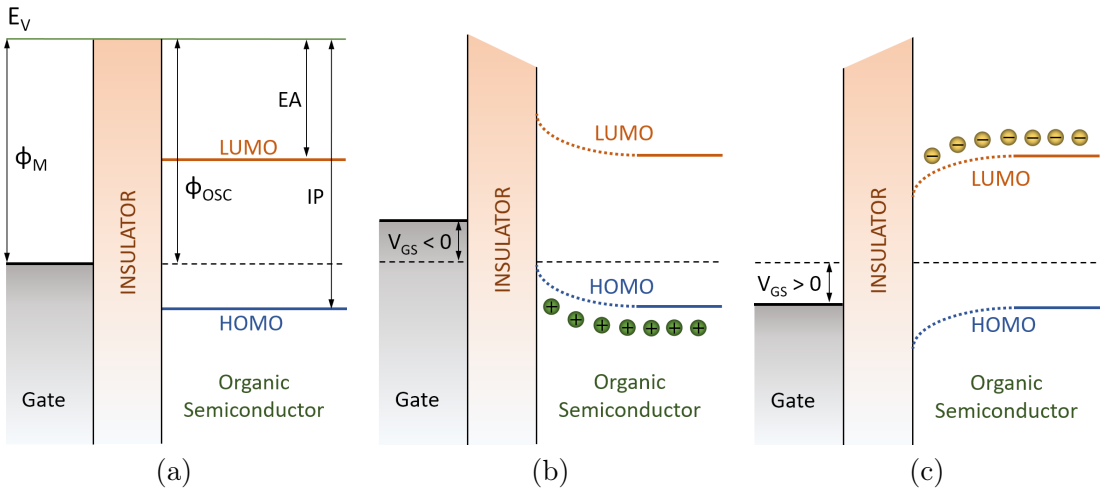

Figure 1.20 – Energy band diagram of gate - insulator - p-type **OSC** interface: (a) zero gate voltage, (b) negative gate voltage and (c) positive gate voltage. E_V is the vacuum level, Φ_M is the work function of gate material, Φ_{OSC} is the work function of **OSC**, EA is the electron affinity, IP is the ionization potential and V_{GS} is gate voltage.

does not conduct and there is no band bending without applied field (i.e. Fermi levels of gate material and **OSC** are aligned), Figure 1.20 allows us to take a closer look at gate - insulator - **OSC** interface from band energy point of view.

Upon application of negative voltage V_{GS} to gate of a p-type **OFET**, the bands bend upward and HOMO edge shifts closer to Fermi level, which results in increase of hole density near insulator/**OSC** interface region. In opposite case (positive V_{GS}), the bands bend downward and the channel of transistor becomes depleted of free charge carriers which resembles the case of **MOSFET** depletion mode. When the transistor is turned ON ($|V_{GS}| > |V_{th}|$), hole population of insulator/**OSC** interface is sufficient to create a

conductive channel from source to drain contacts. If negative voltage is applied between these terminals (V_{DS}), accumulated holes will cross the channel which will result in electric current. For a given value of V_{GS}, channel current I_{DS} is proportional to V_{DS} (Figure 1.21, a) until the electrical field between source and drain terminals becomes comparable to the field between gate and source, which will result in a gradual slow down of current increase. At $|V_{DS}| = |V_{GS} - V_{th}|$ the channel is "pinched-off" (Figure 1.21, b): further increase of V_{DS} will not change carrier concentration near drain electrode (Figure 1.21, c).

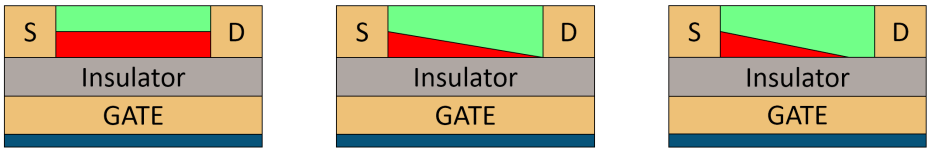

(a) $|V_{DS}| < |V_{GS} - V_{th}|$ (b) $|V_{DS}| = |V_{GS} - V_{th}|$ (c) $|V_{DS}| > |V_{GS} - V_{th}|$

Figure 1.21 – Charge carrier density in **OFET** channel: (a) in linear regime; (b) pinch-off; (c) in saturation regime.

Figure 1.22 represents characteristics of a p-type **OFET** in respect of gate voltage V_{GS}. Transfer characteristic represents the dependency of channel current I_{DS} for a fixed V_{DS} as a function of V_{GS} (Figure 1.22, a): it is often plotted in logarithmic scale and demonstrates distinct difference between the ON and OFF states of **OFET**. By tracing the square root of I_{DS} as a function of V_{GS}, we may extract the threshold voltage V_{th} of **OFET**: the intersection of linear fit of $\sqrt{I_{DS}}$ with x-axis ($I_{DS} = 0$) affords us this parameter. Output characteristic is obtained by plotting I_{DS} for different values of V_{GS} as a function of V_{DS} (Figure 1.22, b). The current I_{DS} is proportional to charge carrier density accumulated in the conducting channel and hence to the value of V_{GS}. Typical output characteristic of an **OFET** can be divided in two regimes: so-called "*linear*" regime with a non-linear region close to higher V_{DS} values and *saturation* regime. The "*linear*" regime is observed when $|V_{DS}| < |V_{GS} - V_{th}|$ (Figure 1.21, a): the current I_{DS} increases proportionally to V_{DS} in almost linear manner.Channel current is described by the model of Sze [115]. In "*linear*" regime I_{DS} may be described by the following equation:

$$I_{DS} = \left(\frac{W}{L}\right) \mu_F C_i \left(V_{GS} - V_{th} - \frac{V_{DS}}{2}\right) V_{DS}, \tag{1.6}$$

where W is the channel width and L is the channel length, C_i is the capacitance per unit area of the gate dielectric, μ_F is the field-effect mobility and V_{th} is the threshold voltage.

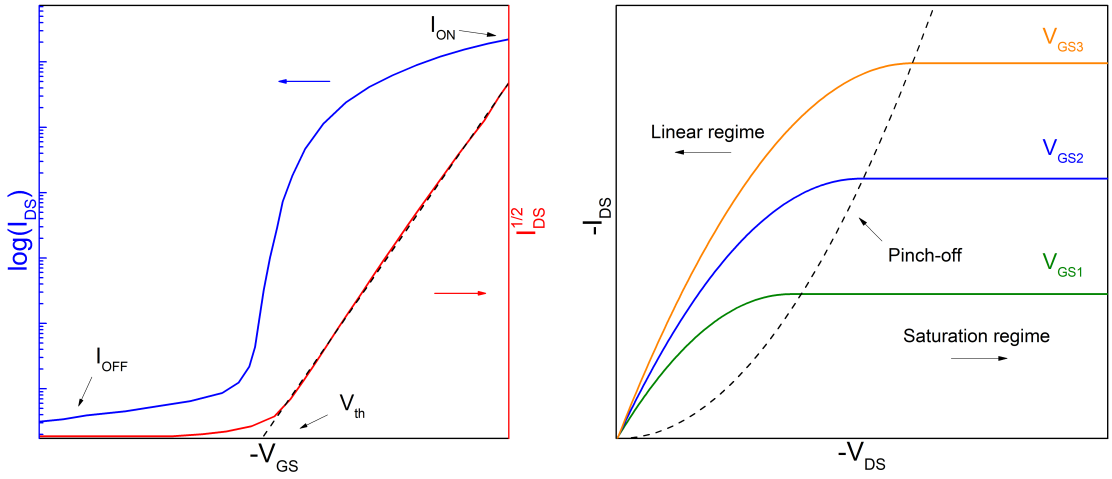

Figure 1.22 – Examples of characteristic plots for a generic p-type **OFET**: (a) transfer characteristic in logarithmic scale (in blue) and threshold voltage V_{th} (in red) characteristic (b) output characteristic for various gate voltage values ($|V_{G3}| > |V_{G2}| > |V_{G1}|$).

As we discussed previously, in *saturation* regime the current I_{DS} no longer depends on drain voltage when $|V_{DS}| > |V_{GS} - V_{th}|$ (Figure 1.21, c) and in this case is described by means of the following equation:

$$I_{DS} = \left(\frac{W}{2L}\right) \mu_F C_i \left(V_{GS} - V_{th}\right)^2 . \tag{1.7}$$

Another important parameter of **OFET** is its ON/OFF ratio, which is the ratio of I_{DS} recorded for values of V_{GS} below threshold and I_{DS} in saturation regime at a given V_{DS} (Figure 1.22, a). ON/OFF ratio is directly connected to the intrinsic conductivity of **OSC** and is heavily influenced by doping (several orders of magnitude [36]), which means that great care should be taken upon choosing appropriate doping concentration.

1.5.2 Architecture

Four types of **OFET** architecture are presented in the Figure 1.23. Each of these types has its own requirements for manufacturing process. For example, those types which presume deposition on **OSC** layer impose additional requirements to surface quality, thus favoring thermal evaporation methods. *Bottom gate - bottom contact* configuration (Figure 1.23, (a)) is the most forgiving in terms of deposition techniques and is one of the most widely employed. In fact, it is even possible to find some commercially distributed

substrates which require only **OSC** deposition and are very easy to use.

Apart from layered sequence, different types of contacts exist, notably simple linear (Figure 1.24, (b)) and interdigitated (Figure 1.24, (a)). The latter one possesses significant advantage over former, since the drain current I_D is directly proportional to width/length of channel ratio $\frac{W}{L}$ (Figure 1.24, in red). This approach allows to drastically increase channel width without substantial difference in geometrical size of device. However, it is generally more expensive to produce and the channel length is limited conventional photolithography (electron beam lithography is hardly applicable, if one opts for low-cost production). The linear configuration does not allow to obtain high current, but is significantly cheaper and less demanding for **OSC** layer uniformity. Doped silicon substrates are usually used as a laboratory standard. The gate is formed by heavily doped region of silicon, whether the dielectric layer consists of silicon dioxide. Flexible substrates (plastic with ITO or PEDOT:PSS electrodes) occur quite frequently in publications, which opens a path to study mechanical stability of **OSC**.

1.5.3 Device performance

This subsection is intended to give some information about numerous factors which may influence the performance of a complete device. The technological process of **OFET** production includes numerous steps, for example the most abundant device based on silicon substrate with bottom gate - bottom contact layout has to undergo the dielectric layer by thermal grow of silicon oxide or deposition of dedicated insulating material, thermal evaporation or sputtering of electrodes, sometimes followed by surfactant treatment and at last, the semiconducting layer. All these processes are sensible to preparation conditions (temperature, presence of oxygen, pressure, moist, dust) as well as to choice of materials. For example, polymeric dielectrics (PMMA, poly(methyl methacrylate)) and organic electrodes (conducting polymers as PEDOT:PSS) have naturally higher affinity to organic nature of **OSC**, thus improving the performance. This postulates the need of careful choice of materials and severe control over production conditions if repeatability is required.

Packing of semiconductor molecules

Apart from intrinsic **OSC** properties as mobility and carrier density, device performance is also influenced by intermolecular order of semiconducting layer. Several kinds of intermolecular packing are known for **OSC** molecules (Figure 1.25). The brick-wall (Figure 1.25, (d); example: TIPS-pentacene [116]) type stacking being believed to be

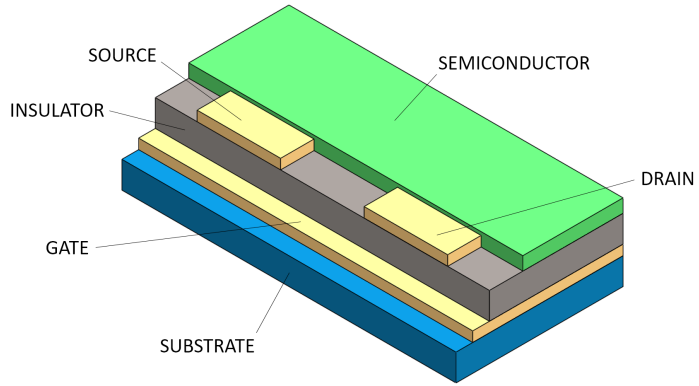

(a) Bottom gate - bottom contact

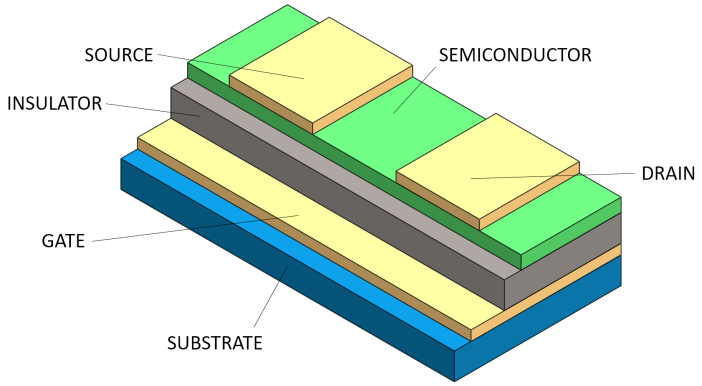

(b) Bottom gate - top contact

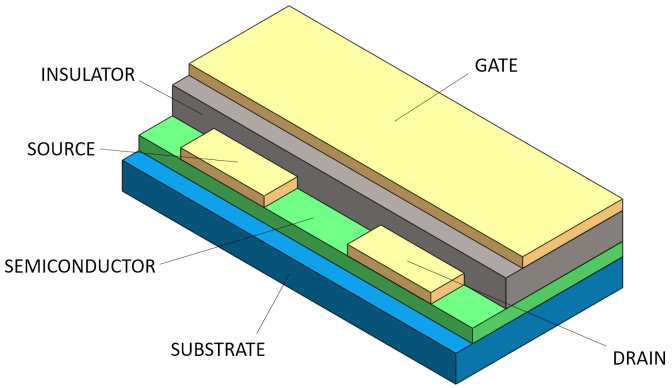

(c) Top gate - top contact

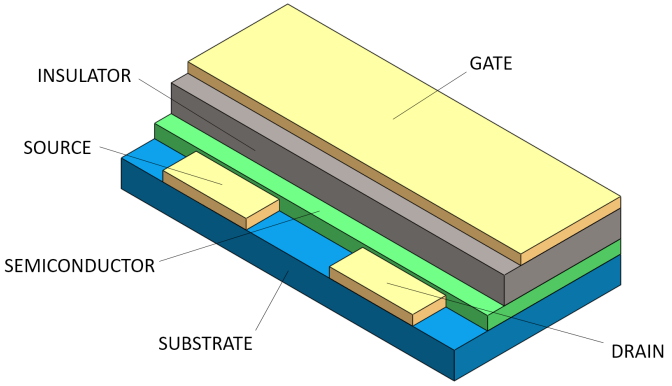

(d) Top gate - bottom contact

Figure 1.23 – Four types of **OFET** architecture.

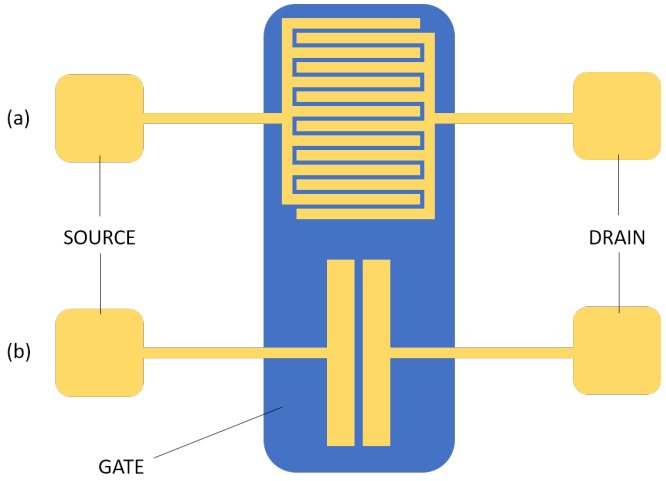

Figure 1.24 – Top view on two geometry types of **OFET** contacts with common gate electrode: (a) interdigitated; (b) linear.

the most efficient as it allows 2D-transport. Most of **OSC** have herringbone pattern with face-to-edge stacking (Figure 1.25, (a)) which does not have any significant $\pi - \pi$ overlap and does not promote good intermolecular charge transporting properties. Some efforts were made to alter the chemical structure of **OSC** by introducing heteroatoms and functional groups to induce intermolecular interactions which favor more effective stacking.

Figure 1.25 – Four types of intermolecular packing in bulk material: (a) herringbone with face-to-edge stacking; (b) herringbone with face-to-face stacking; (c) lamellar; (d) brick wall.

In addition to these packing types, the alignment of **OSC** relatively to substrate can also be different. Such applications as transistor can benefit from the so-called "edge-on" conformation (Figure 1.26, (b)), which is optimal for charge transport in the direction

parallel to substrate due to the $\pi - \pi$ stacking of molecules (since drain and source electrodes of the transistor are situated in the same plane). "Face-on" alignment is useful for **OLED**s and **OPV**s, since in these applications the charge carriers usually move perpendicularly to the substrate plane.

Since **LC**s possess extraordinary alignment and self-organizing properties, this class of substances is of particular interest in **OFET** application. Hydrophobic coating, such as OTS-18 (octadecyltrichlorosilane), can induce the homeotropic orientation of molecules, which corresponds to edge-on alignment. Recent studies of semiconducting **LC** deposition show the possibility to induce in-plane (in other words, face-on) alignment by coating of an additional layer of poly(vinyl alcohol) (PVA, one of the classic alignment layer material in **LC** field) over semiconductor layer [117].

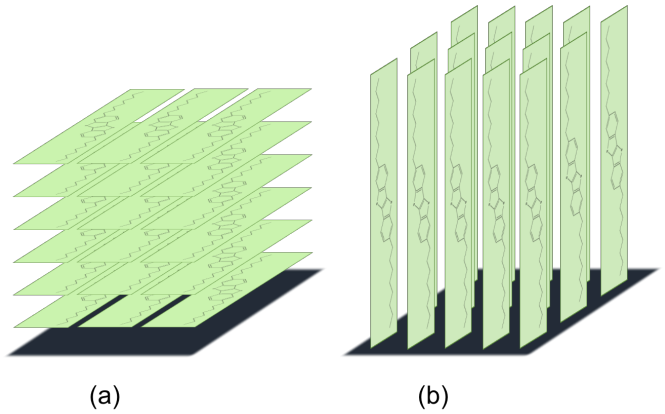

Figure 1.26 – Possible orientations of **OSC** molecules (dioctyl-substituted benzothieno-benzothiophene as an example) on a substrate: (a) face-on; (b) edge-on.

Device production

As mentioned before in subsection 1.2.5, an organic transistor can be prepared by either solution, either vacuum deposition methods. Thermal evaporation allows to obtain a uniform film of very high quality with intermolecular assembly "on-the-go", as well as tune the thickness by order of monolayers. However, solution processes are gaining popularity, as they are expected to enable low production costs of organic electronics. Significant efforts are being made just for the sake of optimizing the deposition process by improving already existing techniques or using new combinations of solvents or deposition parameters.

Gate - dielectric - semiconductor interface

Expand its role in performance, and, in particular, its interaction with LC **OSC**. Since intermolecular interactions in organic semiconductors are much weaker than in conventional inorganic solids, substrate properties such as roughness may significantly affect **OSC** molecular alignment and hence, performance of the device. For example, pronounced surface roughness is able to impede the formation of large-size crystalline domain and increase the number of charge traps, or even to induce undesirable interface energy states in organic semiconductor. Capacitance of insulator layer is directly responsible for threshold and operating voltage, thus reduction of dielectric layer thickness results in a drop of the latter [118]. Polarity of dielectric also plays an important role, as high-k dielectrics can broaden the distribution of site energies close to dielectric interface, which results in different behavior compared to bulk of **OSC**. Use of dielectrics with low polarity yields mobility values closer to intrinsic properties of **OSC**(measured by Time-of-Flight, for example [119]).

One of the first dielectric materials applied in this scope was silicon dioxide SiO_2. A very convenient way is to use a heavily doped Si wafer as gate electrode with thermally grown SiO_2 on it as an insulator, which comes from inorganic semiconductor industry and is well-optimized. Similarly, other oxides with higher dielectric constant ϵ, for example, Al_2O_3 ($\epsilon = 8.4$) and TiO_2 ($\epsilon = 41$) could be used in order to decrease operating voltage [120]. However, the main quest of **OFET** suggest flexibility of the device, and the number of published works on polymeric gate insulators is substantial. Organic dielectrics generally produce more smooth surface and can be solution-processed, which combines well with general **OFET** agenda. This class of substances also enables top gate architecture, since any surface treatment of conventional inorganic oxides could be troublesome. Use of such substances as PMMA (poly(methyl methacrylate)), PET (polyethylene terephthalate) and polyimide results in higher mobilities than that with SiO_2 [121] [122].

Electrode - semiconductor interface

As mentioned in subsection 1.2.2, the intrinsic density of charge carriers of **OSC** is low, and in order to conduct current, these carriers are injected from metal electrodes. Together with previous subsection this makes the performance of such a device as **OFET** highly dependent on interfaces between functional materials. Large contact resistance in **OFET** may result in non-negligible voltage drop on the interface and is often cased by uneven crystallinity of **OSC** in contact region, surface dipole and high potential barrier between metal and semiconductor. Due to the presence of substantial charge

carrier injection barrier on metal - **OSC** interface (Figure 1.27), the contact demonstrates Schottky-type behavior. In fact, the nature of **OSC** (p- or n-type) is mostly determined by the height of potential barrier, favoring the injection of corresponding charge carrier type. When these materials are placed in intimate contact, Fermi level of semiconductor

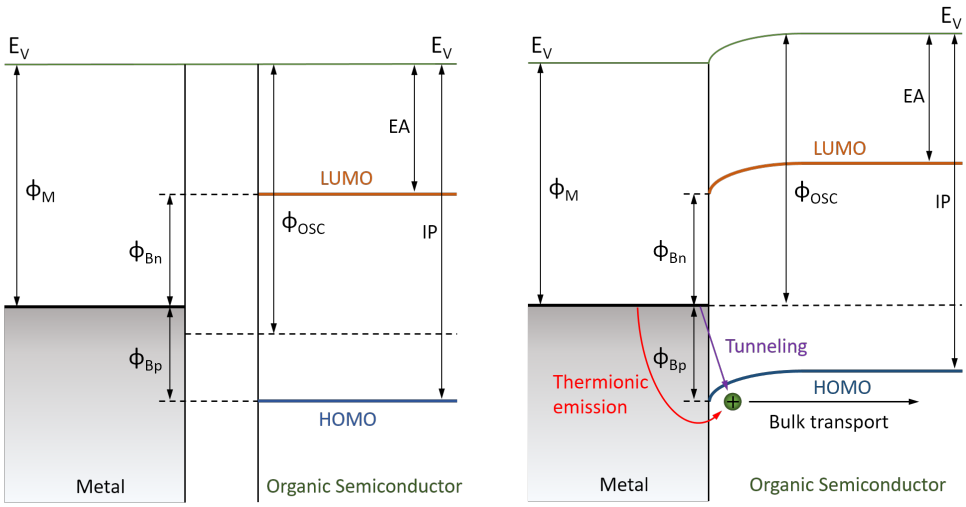

(a) (b)

Figure 1.27 – Energy band diagram of metal - p-type **OSC** interface: (a) before and (b) after contact. E_V is the vacuum level, Φ_M is the work function of metal, Φ_{OSC} is the work function of **OSC**, Φ_{Bn} is the barrier height for electrons, Φ_{Bp} is the barrier height for holes, EA is the electron affinity and IP is the ionization potential

Φ_{OSC} aligns with that of metal, and semiconductor's energy bands undergo bending (Figure 1.27, (b)) expressed as $\Delta\Phi = \Phi_{OSC} - \Phi_M$. For example, in **OFET** prepared with pentacene ($E_{HOMO} \approx 4.9\,\text{eV}$) and gold ($\Phi_{\text{Au}} = 5.2\,\text{eV}$) the barrier height due to energy level misalignment can reach significant values up to 0.85 eV [123]. To overcome this difficulty, great care should be take to surface properties of contact material to reduce roughness or to gain control over surface dipole [124]. Traditional solution for **MOSFET** is to employ contact doping (ion beam implantation, for example). These methods do not work in case of **OFET** due to molecular nature of **OSC**, however some attempts to dope contacts by co-evaporation of molecular dopants were published [33] [25].

1.6 Conclusion

To summarize, Chapter 1 is composed with a purpose to give the reader an idea of the complexity of subject in scope: basic principles of organic semiconductors are introduced from the perspective of chemical structure and basic electronic properties, as well as from bulk charge transport standpoint. A connection to liquid crystal subject is made, and most interesting examples are presented. We have also presented different ways of improving the transporting properties of OSCs. These sections are highly relevant for the subject of present thesis: molecular doping serves as a one way to improve weak intrinsic conductivity of the OSCs by increasing charge carrier density, while dispersion and *in situ* formation of polymer network is aimed to improve structure and order of semiconductor, which is another key element on the way to better performance. Finally, we have introduced the field-effect transistor as one of potential applications: we have exposed numerous factors which are closely related to the choice of materials, molecular structure of semiconductor as well as the preparation procedure.

Bibliography of the current chapter

[1] Max Volmer. "Die verschiedenen lichtelektrischen Erscheinungen am Anthracen, ihre Beziehungen zueinander, zur Fluoreszenz und Dianthracenbildung". In: *Annalen der Physik* 345.4 (1913), pp. 775–796. ISSN: 15213889. DOI: 10.1002/andp.19133450411.

[2] M. Pope, H. P. Kallmann, and P. Magnante. "Electroluminescence in Organic Crystals". In: *The Journal of Chemical Physics* 38.8 (Apr. 1963), pp. 2042–2043. ISSN: 0021-9606. DOI: 10.1063/1.1733929. arXiv: /dx.doi.org/10.1063/1.343409 [http:].

[3] W. Helfrich and W. G. Schneider. "Recombination Radiation in Anthracene Crystals". In: *Physical Review Letters* 14.7 (Feb. 1965), pp. 229–231. ISSN: 0031-9007. DOI: 10.1103/PhysRevLett.14.229.

[4] C. K. Chiang et al. "Electrical conductivity in doped polyacetylene". In: *Physical Review Letters* 39.17 (1977), pp. 1098–1101. ISSN: 00319007. DOI: 10.1103/PhysRevLett.39.1098.

[5] C. W. Tang. "Two-layer organic photovoltaic cell". In: *Applied Physics Letters* 48.2 (Jan. 1986), pp. 183–185. ISSN: 0003-6951. DOI: 10.1063/1.96937.

[6] H. Koezuka and A. Tsumura. "Field-effect transistor utilizing conducting polymers". In: *Synthetic Metals* 28.1-2 (Jan. 1989), pp. 753–760. ISSN: 03796779. DOI: 10.1016/0379-6779(89)90600-0.

[7] J. H. Burroughes, C. A. Jones, and R. H. Friend. "New semiconductor device physics in polymer diodes and transistors". In: *Nature* 335.6186 (Sept. 1988), pp. 137–141. ISSN: 0028-0836. DOI: 10.1038/335137a0.

[8] C. W. Tang and S. A. VanSlyke. "Organic electroluminescent diodes". In: *Applied Physics Letters* 51.12 (Sept. 1987), pp. 913–915. ISSN: 0003-6951. DOI: 10.1063/1.98799.

[9] C. W. Tang, S. A. VanSlyke, and C. H. Chen. "Electroluminescence of doped organic thin films". In: *Journal of Applied Physics* 65.9 (May 1989), pp. 3610–3616. ISSN: 0021-8979. DOI: 10.1063/1.343409.

[10] J. H. Burroughes et al. "Light-emitting diodes based on conjugated polymers". In: *Nature* 347.6293 (Oct. 1990), pp. 539–541. ISSN: 0028-0836. DOI: 10.1038/347539a0.

[11] R. Rieger and K. Müllen. "Forever young: Polycyclic aromatic hydrocarbons as model cases for structural and optical studies". In: *Journal of Physical Organic Chemistry* 23.4 (2010), pp. 315–325. ISSN: 08943230. DOI: 10.1002/poc.1644.

[12] Michael Wykes, Begoña Milián-Medina, and Johannes Gierschner. "Computational engineering of low bandgap copolymers". In: *Frontiers in Chemistry* 1.December (2013), pp. 1–12. ISSN: 22962646. DOI: 10.3389/fchem.2013.00035.

[13] H.A.M. van Mullekom. "Developments in the chemistry and band gap engineering of donor–acceptor substituted conjugated polymers". In: *Materials Science and Engineering: R: Reports* 32.1 (Feb. 2001), pp. 1–40. ISSN: 0927796X. DOI: 10.1016/S0927-796X(00)00029-2.

[14] Christopher A. Hunter and Jeremy K. M. Sanders. "The nature of .pi.-.pi. interactions". In: *Journal of the American Chemical Society* 112.14 (July 1990), pp. 5525–5534. ISSN: 0002-7863. DOI: 10.1021/ja00170a016.

[15] Martin Pope and Charles E. Swenberg. *Electronic processes in organic crystals and polymers*. Oxford University Press, 1999, p. 1328. ISBN: 9780195129632.

[16] Heinz Bässler and Anna Köhler. "Charge Transport in Organic Semiconductors". In: vol. 35. 1. 2011, pp. 1–65. ISBN: 0002-9297. DOI: 10.1007/128_2011_218. arXiv: 15334406.

[17] T. Holstein. "Studies of polaron motion". In: *Annals of Physics* 8.3 (Nov. 1959), pp. 343–389. ISSN: 00034916. DOI: 10.1016/0003-4916(59)90003-X.

[18] T. Kreouzis et al. "Temperature-independent hole mobility in discotic liquid crystals". In: *The Journal of Chemical Physics* 114.4 (Jan. 2001), pp. 1797–1802. ISSN: 0021-9606. DOI: 10.1063/1.1334958.

[19] I. Shiyanovskaya et al. "Charge transport in hexagonal columnar liquid crystals self-organized from supramolecular cylinders based on acene-functionalized dendrons". In: *Physical Review B* 67.3 (Jan. 2003), p. 035204. ISSN: 0163-1829. DOI: 10.1103/PhysRevB.67.035204.

[20] J. Puigdollers et al. "Density-of-states in pentacene from the electrical characteristics of thin-film transistors". In: *Organic Electronics: physics, materials, applications* 11.8 (2010), pp. 1333–1337. ISSN: 15661199. DOI: 10.1016/j.orgel.2010.05.007.

[21] F. Beniere et al. "Doping of polyacetylene by diffusion of iodine". In: *Journal of Physics and Chemistry of Solids* 42.8 (Jan. 1981), pp. 649–654. ISSN: 00223697. DOI: 10.1016/0022-3697(81)90117-7.

[22] Huanjun Ding and Yongli Gao. "Alkali metal doping and energy level shift in organic semiconductors". In: *Applied Surface Science* 252.11 (Mar. 2006), pp. 3943–3947. ISSN: 01694332. DOI: 10.1016/j.apsusc.2005.09.071.

[23] P Pingel, R Schwarzl, and D Neher. "Effect of molecular p-doping on hole density and mobility in poly (3- hexylthiophene) Effect of molecular p-doping on hole density and mobility". In: *Appl. Phys. Lett.* 100 (2012), p. 143303. ISSN: 00036951. DOI: 10.1063/1.3701729.

[24] Georg Heimel, Ingo Salzmann, and Norbert Koch. "On the fundamental processes in molecular electrical doping of organic semiconductors". In: *AIP Conference Proceedings* 1456.June (2012), pp. 148–156. ISSN: 15517616. DOI: 10.1063/1.4730654.

[25] Ching-Lin Fan et al. "Effects of the F4TCNQ-Doped Pentacene Interlayers on Performance Improvement of Top-Contact Pentacene-Based Organic Thin-Film Transistors". In: *Materials* 9.1 (Jan. 2016), p. 46. ISSN: 1996-1944. DOI: 10.3390/ma9010046.

[26] M. Pfeiffer et al. "Controlled p-doping of pigment layers by cosublimation: basic mechanisms and implications for their use in organic photovoltaic cells". In: *Solar Energy Materials and Solar Cells* 63.1 (2000), pp. 83–99. ISSN: 09270248. DOI: 10.1016/S0927-0248(00)00022-2.

[27] Igor Avilov, Victor Geskin, and Jérôme Cornil. "Quantum-Chemical Characterization of the Origin of Dipole Formation at Molecular Organic/Organic Interfaces". In: *Advanced Functional Materials* 19.4 (Feb. 2009), pp. 624–633. ISSN: 1616301X. DOI: 10.1002/adfm.200800632.

[28] Manisha Bajpai et al. "p-Type doping of tetrafluorotetracynoquinodimethane (F4TCNQ) in poly(para-phenylene vinylene) (PPV) derivative "Super Yellow" (SY)". In: *RSC Adv.* 4.88 (2014), pp. 47899–47905. ISSN: 2046-2069. DOI: 10.1039/C4RA08880H.

[29] M. Pfeiffer et al. "Doped organic semiconductors: Physics and application in light emitting diodes". In: *Organic Electronics: physics, materials, applications* 4.2-3 (2003), pp. 89–103. ISSN: 15661199. DOI: 10.1016/j.orgel.2003.08.004.

[30] Ingo Salzmann et al. "Intermolecular hybridization governs molecular electrical doping". In: *Physical Review Letters* 108.3 (2012), pp. 1–5. ISSN: 00319007. DOI: 10.1103/PhysRevLett.108.035502.

[31] Renee Kroon et al. “Polar Side Chains Enhance Processability, Electrical Conductivity, and Thermal Stability of a Molecularly p-Doped Polythiophene”. In: *Advanced Materials* 29.24 (June 2017), p. 1700930. ISSN: 09359648. DOI: 10.1002/adma.201700930.

[32] R.S. Mulliken and Willis B. Person. “DONOR-ACCEPTOR COMPLEXES”. In: *Annu. Rev. Phys. Chem* 13.November (1962), pp. 107–126.

[33] Bjorn Lussem et al. “Doped organic transistors operating in the inversion and depletion regime”. In: *Nature Communications* 4 (2013), pp. 1–6. ISSN: 20411723. DOI: 10.1038/ncomms3775.

[34] Binrui Xu et al. “Functional solid additive modified PEDOT:PSS as an anode buffer layer for enhanced photovoltaic performance and stability in polymer solar cells”. In: *Scientific Reports* 7.October 2016 (2017), pp. 1–12. ISSN: 20452322. DOI: 10.1038/srep45079.

[35] Chunyu Liu et al. “Improving the charge carrier transport of organic solar cells by incorporating a deep energy level molecule”. In: *Phys. Chem. Chem. Phys.* 19.1 (2017), pp. 245–250. ISSN: 1463-9076. DOI: 10.1039/C6CP07344A.

[36] Ryonosuke Sato et al. “Charge-Transfer Complexes of Benzothienobenzothiophene with Tetracyanoquinodimethane and the n-Channel Organic Field-Effect Transistors”. In: *Journal of Physical Chemistry C* 121.12 (2017), pp. 6561–6568. ISSN: 19327455. DOI: 10.1021/acs.jpcc.7b00902.

[37] P. Pingel and D. Neher. “Comprehensive picture of p-type doping of P3HT with the molecular acceptor F4TCNQ”. In: *Physical Review B - Condensed Matter and Materials Physics* 87.11 (2013), pp. 1–9. ISSN: 10980121. DOI: 10.1103/PhysRevB.87.115209.

[38] Daisuke Tadaki et al. “Molecular doping of regioregular poly(3-hexylthiophene) layers by 2,3,5,6-tetrafluoro-7,7,8,8-tetracyanoquinodimethane investigated by infrared spectroscopy and electrical measurements”. In: *Japanese Journal of Applied Physics* 54.9 (Sept. 2015), p. 091602. ISSN: 0021-4922. DOI: 10.7567/JJAP.54.091602.

[39] Henry Méndez et al. “Charge-transfer crystallites as molecular electrical dopants”. In: *Nature Communications* 6 (2015), p. 8560. ISSN: 20411723. DOI: 10.1038/ncomms9560. arXiv: arXiv:1011.1669v3.

[40] Karsten Walzer et al. “Highly efficient organic devices based on electrically doped transport layers”. In: *Chemical Reviews* 107.4 (2007), pp. 1233–1271. ISSN: 00092665. DOI: 10.1021/cr050156n.

[41] Canbin Ouyang et al. "Tuning morphologies and field-emission properties of CuTCNQF AgTCNQF nanostructures". In: *Journal of Physical Chemistry C* 113.17 (2009), pp. 7044–7051. ISSN: 19327447. DOI: 10.1021/jp8113545.

[42] Kai Xiao et al. "Growth, patterning, and one-dimensional electron -Transport properties of self-assembled Ag-TCNQF4 organic nanowires". In: *Chemistry of Materials* 21.18 (2009), pp. 4275–4281. ISSN: 08974756. DOI: 10.1021/cm901431f.

[43] Goudappagouda et al. "Seeded on-surface supramolecular growth for large area conductive donor-acceptor assembly". In: *Chemical Communications* 51.52 (2015), pp. 10439–10442. ISSN: 1364548X. DOI: 10.1039/c5cc03091a. arXiv: 1101.5171.

[44] Alan K. Thomas et al. "Charge Transfer Doping Induced Conformational Ordering of a Non-Crystalline Conjugated Polymer". In: *Journal of Physical Chemistry C* 121.42 (2017), pp. 23817–23826. ISSN: 19327455. DOI: 10.1021/acs.jpcc.7b08773.

[45] Sheshanath V. Bhosale et al. "The sensitivity of donor - Acceptor charge transfer to molecular geometry in DAN - NDI based supramolecular flower-like self-assemblies". In: *Scientific Reports* 7.1 (2017), pp. 1–11. ISSN: 20452322. DOI: 10.1038/s41598-017-15599-9.

[46] Veaceslav Coropceanu et al. "Charge transport in organic semiconductors". In: *Chemical Reviews* 107.4 (2007), pp. 926–952. ISSN: 00092665. DOI: 10.1021/cr050140x. arXiv: 0810.3534.

[47] F. Closs et al. "Liquid crystalline photoconductors". In: *Liquid Crystals* 14.3 (Jan. 1993), pp. 629–634. ISSN: 0267-8292. DOI: 10.1080/02678299308027741.

[48] Chester F Carlson. *Electrophotography*. Apr. 1939.

[49] Iain McCulloch et al. "Liquid-crystalline semiconducting polymers with high charge-carrier mobility". In: *Nature Materials* 5.4 (Apr. 2006), pp. 328–333. ISSN: 1476-1122. DOI: 10.1038/nmat1612.

[50] Jui-fen Chang et al. "Enhanced mobility of poly (3-hexylthiophene) transistors by spin-coating from high boiling point solvents". In: *Chem. Mater.* 16.7 (2004), pp. 4772–4776. ISSN: 0897-4756. DOI: 10.1021/cm049617w.

[51] Ferdinand C. Grozema et al. "Intramolecular charge transport along isolated chains of conjugated polymers: Effect of torsional disorder and polymerization defects". In: *Journal of Physical Chemistry B* 106.32 (2002), pp. 7791–7795. ISSN: 10895647. DOI: 10.1021/jp021114v.

[52] Gabriele Grem et al. “Realization of a blue-light-emitting device using poly(p-phenylene)”. In: *Advanced Materials* 4.1 (Jan. 1992), pp. 36–37. ISSN: 0935-9648. DOI: 10.1002/adma.19920040107.

[53] Nir Tessler et al. “Efficient near-infrared polymer nanocrystal light-emitting diodes”. In: *Science* 295.5559 (2002), pp. 1506–1508. ISSN: 00368075. DOI: 10.1126/science.1068153.

[54] Y. Yang, Q. Pei, and A. J. Heeger. “Efficient blue polymer light-emitting diodes from a series of soluble poly(paraphenylene)s”. In: *Journal of Applied Physics* 79.2 (1996), p. 934. ISSN: 00218979. DOI: 10.1063/1.360875.

[55] I. H. Campbell et al. “Consistent time-of-flight mobility measurements and polymer light-emitting diode current-voltage characteristics”. In: *Applied Physics Letters* 74.19 (1999), pp. 2809–2811. ISSN: 00036951. DOI: 10.1063/1.124021.

[56] Dirk Marsitzky et al. “Self-Encapsulation of Poly-2,7-fluorenes in a Dendrimer Matrix”. In: *Journal of the American Chemical Society* 123.29 (July 2001), pp. 6965–6972. ISSN: 0002-7863. DOI: 10.1021/ja010020g.

[57] U. Scherf and E.J.W. List. “Semiconducting Polyfluorenes—Towards Reliable Structure-Property Relationships”. In: *Advanced Materials* 14.7 (Apr. 2002), pp. 477–487. ISSN: 0935-9648. DOI: 10.1002/1521-4095(20020404)14:7<477::AID-ADMA477>3.0.CO;2-9.

[58] Ruth Rawcliffe, Donal D. C. Bradley, and Alasdair J. Campbell. “Comparison between bulk and field effect mobility in polyfluorene copolymer field effect transistors”. In: *Organic Field Effect Transistors II* 5217 (2003), p. 25. DOI: 10.1117/12.506038.

[59] H. Sirringhaus et al. “Two-dimensional charge transport in self-organized, high-mobility conjugated polymers”. In: *Nature* 401.6754 (1999), pp. 685–688. ISSN: 00280836. DOI: 10.1038/44359. arXiv: arXiv:1011.1669v3.

[60] Amit Babel and Samson A. Jenekhe. “High Electron Mobility in Ladder Polymer Field-Effect Transistors”. In: *Journal of the American Chemical Society* 125.45 (Nov. 2003), pp. 13656–13657. ISSN: 0002-7863. DOI: 10.1021/ja0371810.

[61] Tommie W Kelley et al. “High Performance Organic Thin Film Transistors”. In: *MRS Proceedings* 771 (Feb. 2003), p. L6.5. ISSN: 0272-9172. DOI: 10.1557/PROC-771-L6.5.

[62] Roswitha Zeis et al. “Field Effect Studies on Rubrene and Impurities of Rubrene”. In: *Chemistry of Materials* 18.2 (Jan. 2006), pp. 244–248. ISSN: 0897-4756. DOI: 10.1021/cm0502626.

[63] Richard Hamilton et al. "High-Performance Polymer-Small Molecule Blend Organic Transistors". In: *Advanced Materials* 21.10-11 (Mar. 2009), pp. 1166–1171. ISSN: 09359648. DOI: 10.1002/adma.200801725.

[64] Francis Garnier et al. "Molecular engineering of organic semiconductors: design of self-assembly properties in conjugated thiophene oligomers". In: *Journal of the American Chemical Society* 115.19 (Sept. 1993), pp. 8716–8721. ISSN: 0002-7863. DOI: 10.1021/ja00072a026.

[65] Jin Sun Kim et al. "A charge-transfer phenomenon between 2,3,5,6-tetrafluoro-7,7,8,8- tetracyanop-quinodimethane (F4TCNQ) and a tetrathiafulvalene-based self-assembled monolayer using an indium-tin oxide electrode". In: *Bulletin of the Korean Chemical Society* 31.5 (2010), pp. 1415–1418. ISSN: 02532964. DOI: 10.5012/bkcs.2010.31.5.1415.

[66] Yaowu He et al. "Molecular phase engineering of organic semiconductors based on a [1]benzothieno[3,2-b][1]benzothiophene core". In: *RSC Adv.* 6.97 (2016), pp. 95149–95155. ISSN: 2046-2069. DOI: 10.1039/C6RA22999A.

[67] Wenping Hu et al. "The application of Langmuir–Blodgett films of a new asymmetrically substituted phthalocyanine, amino-tri-tert-butyl-phthalocyanine, in diodes and in all organic field-effect-transistors". In: *Synthetic Metals* 104.1 (June 1999), pp. 19–26. ISSN: 03796779. DOI: 10.1016/S0379-6779(99)00036-3.

[68] Chi-Ming Che et al. "A High-Performance Organic Field-Effect Transistor Based on Platinum(II) Porphyrin: Peripheral Substituents on Porphyrin Ligand Significantly Affect Film Structure and Charge Mobility". In: *Chemistry – An Asian Journal* 3.7 (July 2008), pp. 1092–1103. ISSN: 18614728. DOI: 10.1002/asia.200800011.

[69] Chengliang Wang et al. "Semiconducting π-conjugated systems in field-effect transistors: A material odyssey of organic electronics". In: *Chemical Reviews* 112.4 (2012), pp. 2208–2267. ISSN: 00092665. DOI: 10.1021/cr100380z. arXiv: 0702472 [cond-mat].

[70] Chang-Zhi Li, Hin-Lap Yip, and Alex K.-Y. Jen. "Functional fullerenes for organic photovoltaics". In: *Journal of Materials Chemistry* 22.10 (Feb. 2012), p. 4161. ISSN: 0959-9428. DOI: 10.1039/c2jm15126j.

[71] Thomas D. Anthopoulos et al. "High performance n-channel organic field-effect transistors and ring oscillators based on C60 fullerene films". In: *Applied Physics Letters* 89.21 (Nov. 2006), p. 213504. ISSN: 0003-6951. DOI: 10.1063/1.2387892.

[72] Bong Gi Kim et al. "A molecular design principle of lyotropic liquid-crystalline conjugated polymers with directed alignment capability for plastic electronics". In: *Nature Materials* 12.7 (2013), pp. 659–664. ISSN: 14761122. DOI: 10.1038/nmat3595.

[73] K Ellmer. *Liquid Crystalline Semiconductors, Materials, Properties and Applications*. Vol. 169. 2013. ISBN: 9789048128723. DOI: 10.1007/978-3-642-33848-9.

[74] Masahiro Funahashi and Jun-ichi Hanna. "Fast ambipolar carrier transport in smectic phases of phenylnaphthalene liquid crystal". In: *Applied Physics Letters* 71.5 (1997), pp. 602–604. ISSN: 0003-6951. DOI: 10.1063/1.119806.

[75] Tohru Toda, Jun-ichi Hanna, and Tadaaki Tani. "Electronic structure and charge injection at interface between electrode and liquid-crystalline semiconductor". In: *Journal of Applied Physics* 101.2 (Jan. 2007), p. 024505. ISSN: 0021-8979. DOI: 10.1063/1.2424401.

[76] Hong Zhang, Masahiro Funahashi, and Jun-ichi Hanna. "Photosensitization of smectic photoconductive liquid crystal by C 70 doping". In: ed. by Donal D. C. Bradley and Bernard Kippelen. Vol. 3939. International Society for Optics and Photonics, May 2000, p. 126. DOI: 10.1117/12.386367.

[77] Kyohei Nakano et al. "Charge injection enhanced by guest material in molecularly doped liquid crystalline thin films". In: *Japanese Journal of Applied Physics* 51.1 (2012). ISSN: 00214922. DOI: 10.1143/JJAP.51.011701.

[78] Sanjoy Paul et al. "Photogeneration and enhanced charge transport in aligned smectic liquid crystalline organic semiconductor". In: *Journal of Applied Physics* 118.13 (Oct. 2015), p. 135702. ISSN: 0021-8979. DOI: 10.1063/1.4931913.

[79] Masahiro Funahashi, Fapei Zhang, and Nobuyuki Tamaoki. "High ambipolar mobility in a highly ordered smectic phase of a dialkylphenylterthiophene derivative that can be applied to solution-processed organic field-effect transistors". In: *Advanced Materials* 19.3 (2007), pp. 353–358. ISSN: 09359648. DOI: 10.1002/adma.200602319.

[80] Masahiro Funahashi and Jun Ichi Hanna. "High carrier mobility up to 0.1 cm2 V-1 s -1 at ambient temperatures in thiophene-based smectic liquid crystals". In: *Advanced Materials* 17.5 (2005), pp. 594–598. ISSN: 09359648. DOI: 10.1002/adma.200401274.

[81] Iain Mcculloch et al. "Electrical properties of reactive liquid crystal semiconductors". In: *Japanese Journal of Applied Physics* 47.1 PART 2 (2008), pp. 488–491. ISSN: 00214922. DOI: 10.1143/JJAP.47.488.

[82] Iain McCulloch et al. "Polymerizable liquid crystalline organic semiconductors and their fabrication in organic field effect transistors." In: *Journal of Materials Chemistry* 13.10 (2003), p. 2436. ISSN: 0959-9428. DOI: 10.1039/b307764k.

[83] Albert J J M Van Breemen et al. "Large area liquid crystal monodomain field-effect transistors". In: *Journal of the American Chemical Society* 128.7 (2006), pp. 2336–2345. ISSN: 00027863. DOI: 10.1021/ja055337l.

[84] Manuela Melucci et al. "Liquid-crystalline rigid-core semiconductor oligothiophenes: influence of molecular structure on phase behaviour and thin-film properties". In: *Chemistry - A European Journal* 13.36 (2007), pp. 10046–10054. ISSN: 09476539. DOI: 10.1002/chem.200701368.

[85] Leszek Mazur et al. "Charge carrier mobility study of a mesogenic thienothiophene derivative in bulk and thin films". In: *Organic Electronics: physics, materials, applications* 15.4 (2014), pp. 943–953. ISSN: 15661199. DOI: 10.1016/j.orgel.2014.01.017.

[86] Kazuma Oikawa et al. "A novel calamitic mesophase semiconductor with the fastest mobility of charged carriers: 1,4-di(5'-octyl-2'-thienyl)benzene." In: *Chemical communications (Cambridge, England)* 42 (2005), pp. 5337–5339. ISSN: 1359-7345. DOI: 10.1039/b509512n.

[87] Y Shimizu et al. "Mesophase semiconductors: The alignment control and self-assembling nature for transistor applications". In: *Molecular Crystals and Liquid Crystals* 509.1 (2009), pp. 206–212. ISSN: 15421406. DOI: 10.1080/15421400903054519.

[88] Hiroko Yamada et al. "FET performance and substitution effect on 2,6-dithienylanthracene devices prepared by photoirradiation of their diketone precursors." In: *Chemical communications (Cambridge, England)* 48.90 (2012), pp. 11136–8. ISSN: 1364-548X. DOI: 10.1039/c2cc35439j.

[89] Hideaki Ebata et al. "Highly soluble [1]benzothieno[3,2-b]benzothiophene (BTBT) derivatives for high-performance, solution-processed organic field-effect transistors". In: *Journal of the American Chemical Society* 129.51 (2007), pp. 15732–15733. ISSN: 00027863. DOI: 10.1021/ja074841i.

[90] Yongbo Yuan et al. "Ultra-high mobility transparent organic thin film transistors grown by an off-centre spin-coating method". In: *Nature Communications* 5 (Jan. 2014), pp. 1–9. ISSN: 2041-1723. DOI: 10.1038/ncomms4005.

[91] Tobias Wöhrle et al. "Discotic Liquid Crystals". In: *Chemical Reviews* 116.3 (2016), pp. 1139–1241. ISSN: 15206890. DOI: 10.1021/acs.chemrev.5b00190.

[92] Sheng Gao Liu et al. "Self-organizing liquid crystal perylene diimide thin films: Spectroscopy, crystallinity, and molecular orientation". In: *Journal of Physical Chemistry B* 106.6 (2002), pp. 1307–1315. ISSN: 10895647. DOI: 10.1021/jp013254v.

[93] Si Guang Chen, Paul Stradins, and Brian A. Gregg. "Doping highly ordered organic semiconductors: Experimental results and fits to a self-consistent model of excitonic processes, doping, and transport". In: *Journal of Physical Chemistry B* 109.28 (2005), pp. 13451–13460. ISSN: 15206106. DOI: 10.1021/jp0506080.

[94] Anna Hayer et al. "Highly Fluorescent Crystalline and Liquid Crystalline Columnar Phases of Pyrene-Based Structures". In: *The Journal of Physical Chemistry B* 110.15 (Apr. 2006), pp. 7653–7659. ISSN: 1520-6106. DOI: 10.1021/jp0573689.

[95] Teresa M. Figueira-Duarte and Klaus Müllen. "Pyrene-Based Materials for Organic Electronics". In: *Chemical Reviews* 111.11 (Nov. 2011), pp. 7260–7314. ISSN: 0009-2665. DOI: 10.1021/cr100428a.

[96] Jürgen Simmerer et al. "Transient photoconductivity in a discotic hexagonal plastic crystal". In: *Advanced Materials* 8.10 (Oct. 1996), pp. 815–819. ISSN: 09359648. DOI: 10.1002/adma.19960081010.

[97] A L Atwood et al. "Record Charge Carrier Mobility in a Room- Temperature Discotic Liquid-Crystalline Derivative of Hexabenzocoronene". In: *Advanced Materials* 634.9 (1996), pp. 7640–905. ISSN: 0935-9648. DOI: 10.1002/(SICI)1521-4095(199912)11:17<1469::AID-ADMA1469>3.0.CO;2-K.

[98] Marcel Kastler et al. "Room-temperature nondispersive hole transport in a discotic liquid crystal". In: *Applied Physics Letters* 89.25 (Dec. 2006), p. 252103. ISSN: 0003-6951. DOI: 10.1063/1.2408654.

[99] Hideo Fujikake et al. "Time-of-flight analysis of charge mobility in a Cu-phthalocyanine-based discotic liquid crystal semiconductor". In: *Applied Physics Letters* 85.16 (Oct. 2004), pp. 3474–3476. ISSN: 0003-6951. DOI: 10.1063/1.1805178.

[100] Hiroaki Iino et al. "Very high time-of-flight mobility in the columnar phases of a discotic liquid crystal". In: *Applied Physics Letters* 87.13 (Sept. 2005), p. 132102. ISSN: 0003-6951. DOI: 10.1063/1.2056608.

[101] Pieter G. Schouten et al. "Charge migration in supramolecular stacks of peripherally substituted porphyrins". In: *Nature* 353.6346 (Oct. 1991), pp. 736–737. ISSN: 0028-0836. DOI: 10.1038/353736a0.

[102] Andreas Bacher et al. "Synthesis and characterisation of a conjugated reactive mesogen". In: *Journal of Materials Chemistry* 9.12 (Jan. 1999), pp. 2985–2989. ISSN: 09599428. DOI: 10.1039/a906371d.

[103] A Bacher et al. "Conjugated reactive mesogens". In: *Synthetic Metals* 111-112 (June 2000), pp. 413–415. ISSN: 03796779. DOI: 10.1016/S0379-6779(99)00385-9.

[104] Dirk J. Broer, Gregory P. Crawford, and Slobodan Zumer. *Cross-Linked Liquid Crystaline Systems*. 2011. ISBN: 9781420046229.

[105] R. J. Baldwin et al. "A comprehensive study of the effect of reactive end groups on the charge carrier transport within polymerized and nonpolymerized liquid crystals". In: *Journal of Applied Physics* 101.2 (2007). ISSN: 00218979. DOI: 10.1063/1.2432045.

[106] I. Bleyl et al. "Photopolymerization and Transport Properties of Liquid Crystalline Triphenylenes". In: *Molecular Crystals and Liquid Crystals Science and Technology. Section A. Molecular Crystals and Liquid Crystals* 299.1 (June 1997), pp. 149–155. ISSN: 1058-725X. DOI: 10.1080/10587259708041987.

[107] Marcel Kastler et al. "Nanostructuring with a Crosslinkable Discotic Material". In: *Small* 3.8 (Aug. 2007), pp. 1438–1444. ISSN: 16136810. DOI: 10.1002/smll.200700109.

[108] Masaaki Inoue et al. "Effect of Photopolymerization on Photoconductive Behavior in Triphenylene Discotic Liquid Crystals". In: *Molecular Crystals and Liquid Crystals Science and Technology. Section A. Molecular Crystals and Liquid Crystals* 365.1 (July 2001), pp. 439–446. ISSN: 1058-725X. DOI: 10.1080/10587250108025323.

[109] Yuki Hirai et al. "Enhanced hole-transporting behavior of discotic liquid-crystalline physical gels". In: *Advanced Functional Materials* 18.11 (2008), pp. 1668–1675. ISSN: 1616301X. DOI: 10.1002/adfm.200701313.

[110] Masaya Moriyama, Norihiro Mizoshita, and Takashi Kato. "Photopatterning of Discotic Liquid-Crystalline Gels". In: *Polymer Journal* 36.8 (2004), pp. 661–664. ISSN: 0032-3896. DOI: 10.1295/polymj.36.661.

[111] Sukumaran Santhosh Babu, Vakayil K Praveen, and Ayyappanpillai Ajayaghosh. "Functional π - Gelators and Their Applications". In: (2013).

[112] Naoki Yoshimoto and Jun-ichi Hanna. "Preparation of a novel organic semiconductor composite consisting of a liquid crystalline semiconductor and crosslinked polymer and characterization of its charge carrier transport properties". In: *Journal of Materials Chemistry* 13.5 (2003), pp. 1004–1010. ISSN: 09599428. DOI: 10.1039/b209802d.

[113] Yasemin Yuksel Durmaz, Norbert Moszner, and Yusuf Yagci. "Visible Light Initiated Free Radical Promoted Cationic Polymerization Using Acylgermane Based Photoinitiator in the Presence of Onium Salts". In: *Macromolecules* 41.18 (Sept. 2008), pp. 6714–6718. ISSN: 0024-9297. DOI: 10.1021/ma801208n.

[114] J Zaumseil and H Sirringhaus. "Electron and Ambipolar Transport in Organic Field-Effect Transistors". In: *Chemical Reviews* 107 (2007), pp. 1296–1323. ISSN: 0009-2665. DOI: 10.1021/cr0501543.

[115] Sze. *Physics of Semiconductor Devices Physics of Semiconductor Devices*. Vol. 10. 1995, pp. 739–751. ISBN: 978-3-319-03001-2. DOI: 10.1007/978-3-319-03002-9. arXiv: 9809069v1 [arXiv:gr-qc].

[116] T. Tokumoto et al. "Persistent photo-excited conducting states in functionalized pentacene". In: *Synthetic Metals* 152.1-3 (2005), pp. 449–452. ISSN: 03796779. DOI: 10.1016/j.synthmet.2005.07.179.

[117] Yi-Fei Wang, Hiroaki Iino, and Jun-ichi Hanna. "Fabrication of planarly-oriented polycrystalline thin films of smectic liquid crystalline organic semiconductors". In: *Soft Matter* 13.37 (2017), pp. 6499–6505. ISSN: 1744-683X. DOI: 10.1039/C7SM01303E.

[118] Janos Veres et al. "Gate Insulators in Organic Field-Effect Transistors". In: *Chemistry of Materials* 16.23 (Nov. 2004), pp. 4543–4555. ISSN: 0897-4756. DOI: 10.1021/cm049598q.

[119] J. Veres et al. "Low-k Insulators as the Choice of Dielectrics in Organic Field-Effect Transistors". In: *Advanced Functional Materials* 13.3 (Mar. 2003), pp. 199–204. ISSN: 1616301X. DOI: 10.1002/adfm.200390030.

[120] Guangming Wang et al. "Poly(3-hexylthiophene) field-effect transistors with high dielectric constant gate insulator". In: *Journal of Applied Physics* 95.1 (Jan. 2004), pp. 316–322. ISSN: 0021-8979. DOI: 10.1063/1.1630693.

[121] F Garnier et al. "All-Polymer Field-Effect Transistor Realized by Printing Techniques". In: *Science* 265.5179 (Sept. 1994), pp. 1684–1686. ISSN: 0036-8075. DOI: 10.1126/science.265.5179.1684.

[122] Gilles Horowitz. "Organic Field-Effect Transistors". In: *Advanced Materials* 10.5 (Mar. 1998), pp. 365–377. ISSN: 0935-9648. DOI: 10.1002/(SICI)1521-4095(199803)10:5<365::AID-ADMA365>3.0.CO;2-U.

[123] Raoul Schroeder, Leszek A. Majewski, and Martin Grell. "Improving organic transistor performance with Schottky contacts". In: *Applied Physics Letters* 84.6 (Feb. 2004), pp. 1004–1006. ISSN: 0003-6951. DOI: 10.1063/1.1645993.

[124] Mélanie Devynck et al. "Cumulative effects of electrode and dielectric surface modifications on pentacene-based transistors". In: *Applied Physics Letters* 100.5 (2012). ISSN: 00036951. DOI: 10.1063/1.3681791.

Chapter 2

Experimental methods and techniques

2.1 Introduction

This chapter describes the array of experimental methods used in this work. An attempt is made to briefly introduce the most significant techniques, with an emphasis on the type of obtained data and potential impact on the present study.

These techniques can be approximately divided in several groups: more generalized characterization of materials which includes morphological and structural study, spectroscopic techniques, and more application-specific methods: study of bulk charge transporting properties and preparation - characterization of the **OFET**, as well as electrochemical and optical bandgap estimation.

This work also includes several techniques more appropriate for a chemist, and their brief introduction is nonetheless included in order to lower the interdisciplinary barrier. Protocols of some procedures are included, which details may help those who decide to pursuit their studies in this field.

Detailed explanation of software used in this work and computer programs elaborated during the course of this thesis is omitted in order to restrain the volume of this section.

2.2 Structural and morphological characterization techniques

2.2.1 Polarized optical microscopy

Optical microscopy is a relatively simple, accessible yet effective method of material study. Polarized optical microscopy (**POM**) has become one of the most widely employed techniques for optically anisotropic (birefringent) materials, notably liquid crystals. In a typical experimental setup, the **LC** sample is placed in a special cell of so-called "sandwich-type", where it is held between two glass surfaces. The **LC** orientation could be controlled by the means of surface interactions, thickness of the cell gap and magnetic or electric field. The **LC** could be spontaneously oriented in the case of an untreated cell surface (discotic mesogenes are especially prone to it) or aligned at different angles, depending on the nature and treatment (rubbing force and direction) of alignment layer, which is often pre-deposited during the process of cell fabrication.

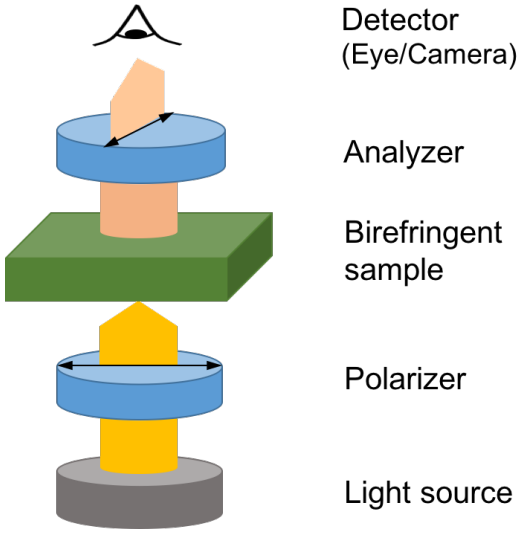

Figure 2.1 – Schematic representation of light path throug a polarizing optical microscope with an angle $\Theta = 90^\circ$ between the analyzer/polarizer.

The **LC** cell is filled by capillary action in isotropic phase of studied sample and then placed inside of a heating stage which is mounted on a microscope. Polarizer and analyzer are aligned with an angle $\Theta = 90^\circ$ between them, while the light is shined perpendicularly to the sample surface in transmission mode of optical microscope (Figure 2.1). If the **LC** is in the isotropic phase, no change in the polarized light occurs, as it goes through an optically isotropic sample unchanged and the **LC**s appear black under the microscope (Figure 2.2, c), since the analyzer blocks all the light. However, the light going through a

mesophase splits in two different components due to the two distinct refractive indexes, and when exiting the sample, it recombines with different polarization that can than go through the analyzer. The resulting color and intensity of the obtained image depends on the LC orientation, birefringence index and cell thickness.

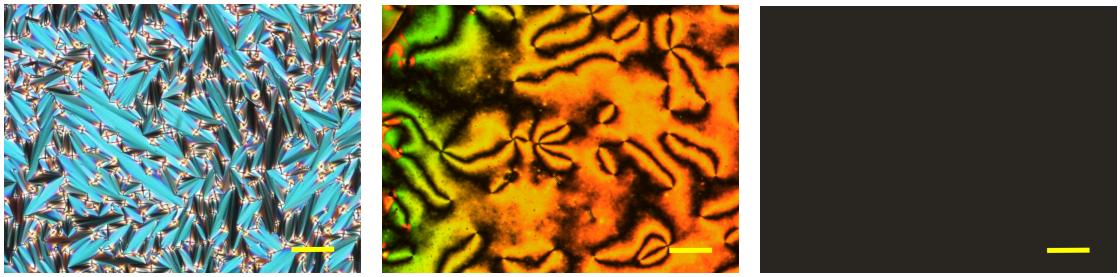

(a) Smectic A (b) Nematic (c) Isotropic

Figure 2.2 – Examples of sample texture in various phases: (a) smectic A, (b) nematic and (c) isotropic. Scale bar represents 50 µm.

The **LC** texture observed by polarized optical microscopy could be used to identify the type of mesophase. Nematic **LC**s usually have a distinct *Schlieren* texture (Figure 2.2, b) when placed between untreated glass surfaces that promote the parallel alignment of *directors* to the surface. It is characterized by dark brushes corresponding to the extinction position of the nematic *director* field of the **LC** where *directors* are parallel to the polarizer or analyzer. The area where these brushes meet is a disclination point with topological defects. Smectic **LC**s typically form a fan-like texture (Figure 2.2, a) with so-called focal cone domains, which are observable when the **LC** *directors* and layers are parallel and perpendicular to the glass surface, respectively. These layers are organized into circular domains where the layer's normal direction points towards the center of the focal cone[125].

Optical microscope used in present study is the Olympus BX60F5 alongside with Linkam LTS 350 hotstage (−196 °C to 350 °C) and Linkam TMS 93 controller.

2.2.2 Scanning Electron Microscopy (SEM)

In SEM, the imaging is performed by scanning the sample area with a narrow beam of the electrons in X-Y plane. The wavelength of electrons is much smaller (in the order of pm) than that of photons and depend on the accelerating voltage. This allows to obtain high resolution images on a scale of several nanometers, which is unattainable by conventional light microscopy due to optical diffraction phenomena.

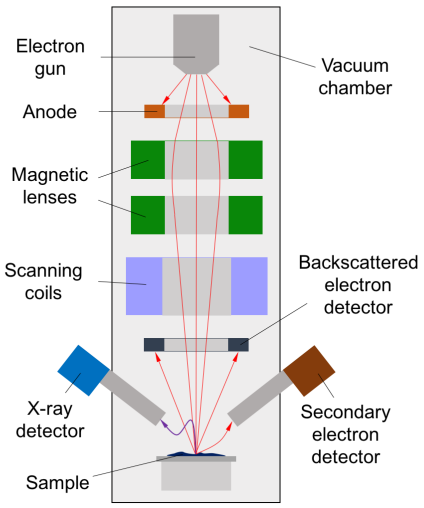

Figure 2.3 – Schematic representation of a SEM instrument.

A SEM instrument is built in a vacuum chamber in order to avoid the scattering of the electrons of the gas molecules. The electrons are emitted from cathode ("electron gun") and accelerated by a voltage applied between the gun and anode. The magnetic lens serve to narrow down, i.e. "focus" the electron beam to the sample surface. Beam displacement in X-Y plane is performed by scanning coils which are able to deflect electrons to the desired spot of the sample. Topographical information is obtained by detecting the secondary electrons which are emitted from the sample surface. Another imaging mode is relied upon detecting the electrons which undergo elastic scattering from the sample atoms, often providing contrast related to the elemental composition of the sample (Figure 2.3).

This imaging technique imposes some additional requirements to the sample which should be vacuum-stable: outgassing could compromise the experimental conditions, contaminate the chamber and/or damage the pump. The sample is also required to be able to evacuate the electrons, which are rapidly delivered to its surface by the beam. Failing to do so often results in severe contrast degradation and beam instability due

to the repulsion forces, especially on higher accelerating voltages. Samples are covered with a thin layer of conductive material (gold, carbon, etc.) during the preparation by sputtering prior to SEM analysis.

Energy-Dispersive X-ray analysis

An X-ray detector is often bundled with a SEM instrument, which allows to perform Energy-Dispersive Analysis (EDX). This method is based on the detection of the characteristic X-ray emission, which may occur upon absorbing an incoming electron by atoms of the sample. The energy of these X-ray photons is an intrinsic property of the chemical element, which allows to obtain an elemental composition for a desired spot under the electron beam, or perform a full elemental mapping of the scanned area.

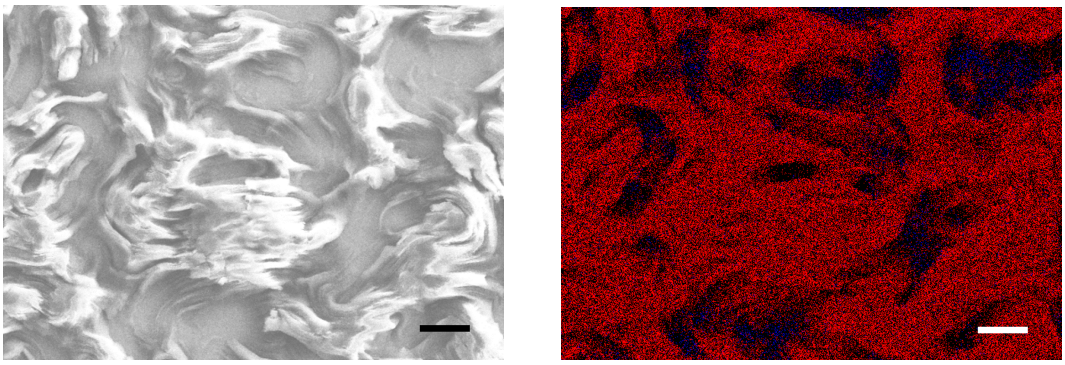

(a) (b)

Figure 2.4 – Example of elemental mapping: (a) SEM image of an organic compound on a glass substrate and (b) corresponding carbon (red) and oxygen (blue) element map. Scale bar represents 10 µm.

SEM images in this work were obtained using JEOL JSM-7100F Scanning Electron Microscope with 15 kV (otherwise explicitly cited) accelerating voltage. EDX analysis was performed by using Bruker QUANTAX (3x XFLASH 6130) detector system.

2.2.3 Atomic Force Microscopy (AFM)

This technique is a part of a wider family of scanning probe microscopy. Despite its name, it does not use lenses or sample irradiation to obtain an image, thus excluding optical limitations of wave optics and aberrations which may be introduced by lens. Instead, it is based on direct interaction of the probe tip (5 nm to 10 nm diameter) with the surface of sample, which allows to overcome diffraction limit imposed by conventional optical microscopy and attain resolution on a nanometric scale.

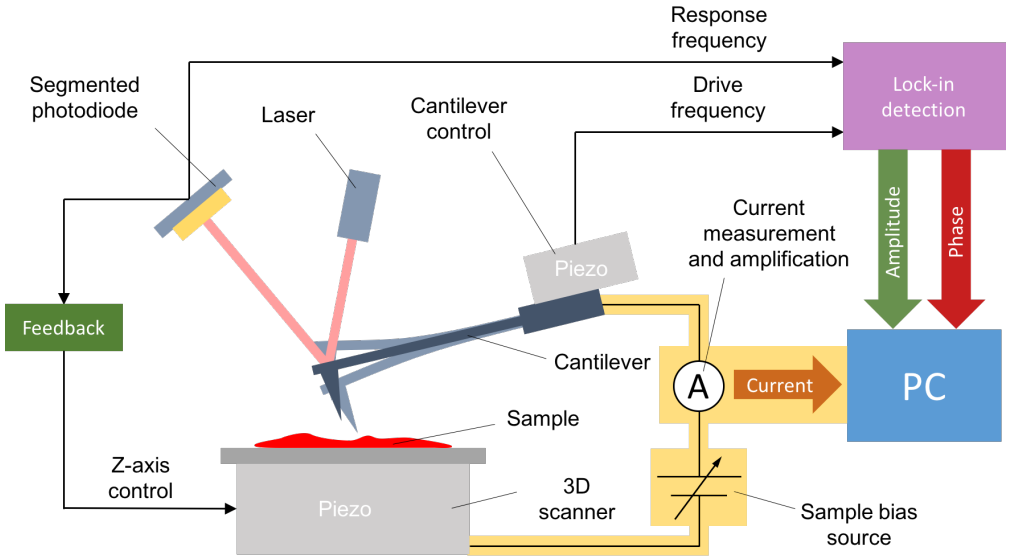

Figure 2.5 – Schematic representation of an **AFM** instrument. The conductive module is highlighted in yellow.

A typical **AFM** instrument (Figure 2.5) consists of a cantilever with a sharp tip, which serves to probe the surface of the sample. The backside of this cantilever is made reflective in order to allow a laser beam to be reflected on a segmented photo-diode, which in turn enables readout of the cantilever deflection. The in-plane scanning, as well as Z-axis adjustment is performed with a piezoelectric element under the sample substrate. Depending on the measurement mode, the probe tip may be kept in contact with the sample surface, or oscillate with a predefined frequency.

During the contact scan, the cantilever deflection creates an input for a feedback loop, which is employed to keep the deflection - distance between the tip apex and the sample constant (defined by a setpoint) by adjusting the Z-axis travel. The adjustment of Z-axis (sample topography) is coupled to the X-Y travel of the probe in order to form a pseudo-colored 2D image, where color represents the height.

Conductive AFM (C-AFM)

This technique was derived from the parental AFM in the nineties as a tool for semiconducting material science. It is based on measuring the current flowing through the sample at a given applied voltage and enables the user to obtain local conductivity data. This data can be represented as a current-voltage characteristic curve of a certain contact area of a sample, or as a conductivity "mapping", usually performed at a constant bias and coupled to the topographic information of the sample surface (Figure 2.6) [126]. The basic facilities for the topography imaging are the same as for the aforementioned **AFM**. However, this technique imposes some additional requirements to the probe tip and the sample. C-AFM usually utilizes specially fabricated conductive probe tips. The sample itself has to be reasonably thin and conductive in order to obtain a measurable signal amplitude.

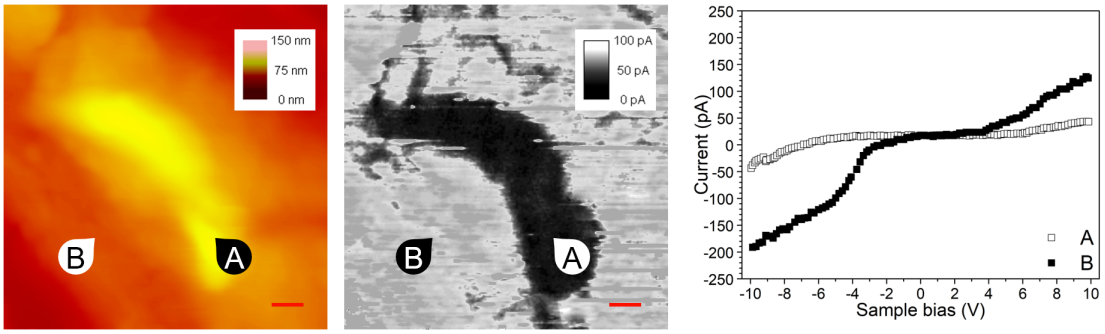

Figure 2.6 – Example of C-AFM mapping, sample demonstrates some non-conductive agglomerate in the organic semiconductor thin film deposited on gold. Left to right: sample topography, current mapping (-5V sample bias), local current-voltage characteristics. Scale bar represents 100 nm.

AFM images in this work were obtained with the help of Veeco (Bruker) Multimode III with an optional C-AFM module. Samples used for conductive measurements were deposited on gold and ITO coated substrates. Small near-edge area of the conductive surface of these substrates was masked with a tape prior to coating. A small silver wire was attached by means of silver paste to make electrical contact of the conductive substrate layer and AFM sample holder in order to enable electrical field application between the aforementioned layer and conductive tip apex of the AFM instrument. Slow scanning speed (1.5 µm/s) was employed, as well as minimal contact force (deflection setpoint was adjusted prior to each image capture) was utilized in order to reduce tip wear and enhance reliability of conductivity data collected during measurements. An average of two conductive tips (Bruker^{TM} SCM-PIC-V2) was utilized for each sample.

2.2.4 Differential scanning calorimetry (DSC)

DSC is the most widely used technique among different types of analysis methods to study thermal properties of materials. It helps to establish a connection between the temperature and particular thermodynamic properties which are characteristic for substances such as polymers, metallic glasses, liquid crystals, pharmaceutical substances and etc.

The **DSC** is an instrument of thermal analysis which is able to measure the heat flow between twin pans (reference and sample, Figure 2.7) as well as the sample temperature. During a physical or chemical transformation (chemical reaction or phase transition) of the sample, requiring energy exchange, the **DSC** measures a heat quantity emitted (exothermic process) or absorbed (endothermic process) by the sample.

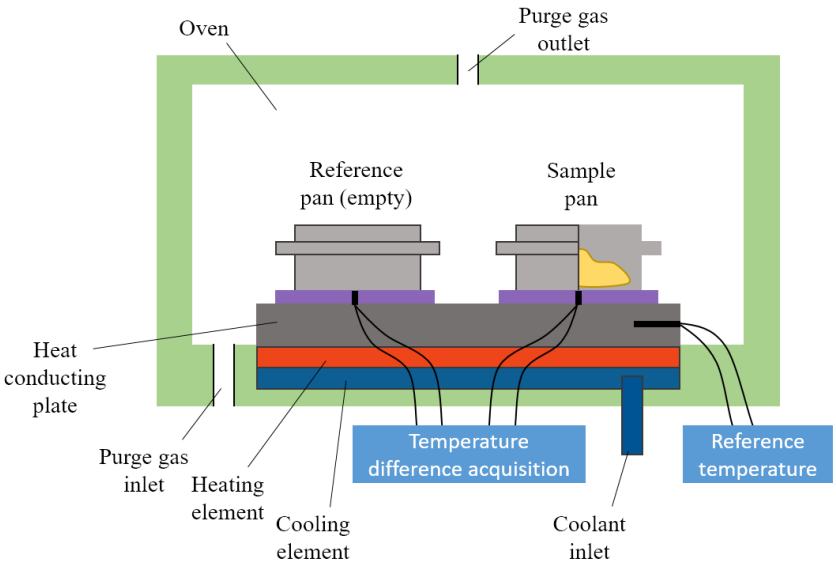

Figure 2.7 – Schematic representation of heat flux **DSC** setup.

The output of a **DSC** experiment, called thermogram, is a plot of the difference of heat delivered to the sample and to reference pans as a function of the sample temperature (or time) (Figure 2.8).

Typical **DSC** setup (Figure 2.7) is built around a well-insulated oven, where two crucibles (sample and reference) are placed on special stands incorporating high precision thermocouples to determine difference in heat flow. The oven itself has a dedicated thermocouple for temperature control. Heating is usually implemented by a heating resistor, and liquid nitrogen is often used as a coolant agent. To avoid sample oxidation,

an inert purge gas (helium, argon, or more commonly, nitrogen) is constantly fed into the oven.

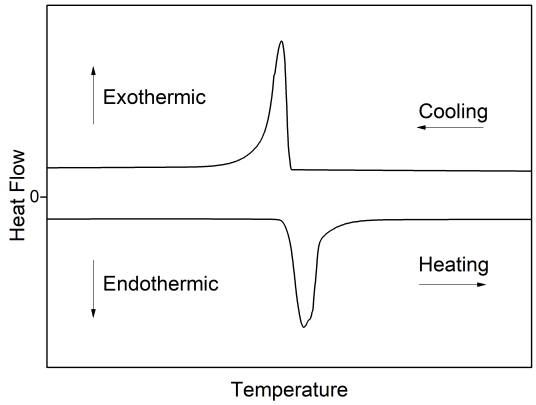

Figure 2.8 – Example of a **DSC** output curve (thermogram) - bottom for an endothermic phase transition (melting) and top for an exothermic (crystallization).

Example of typical thermograms obtained by **DSC** is illustrated in Figure 2.8). If on heating a melting (endothermic process) phase transition occurs, in order to maintain the same temperature of the both pans, more heat flux must be transferred to the sample pan than to reference pan: a peak is then observed in the thermogram. The energy consumed as heat for this process (enthalpy change) is related to the area of the observed peak and can be easily calculated from the integral. In contrary, the sample is going to emit heat upon cooling during the crystallization. In this case more heat flux is delivered to the reference pan than the sample pan. This transition is going to appear in thermogram as an exothermic peak in the opposite direction.

The calorimetric studies in this work were made by a TA Instruments Q1000 Differential Scanning Calorimeter (−180 °C to 725 °C).

2.2.5 X-Ray Scattering

X-ray scattering techniques have proven themselves to become an indispensable tool in the fields of solid and condensed matter, macromolecular chemistry and nanoscience. This technique is based on the elastic interaction of X-rays with the matter, and allows the user to obtain information on structural properties of the material under study, i.e. intermolecular distance, crystalline lattice type, etc.

In application to liquid crystals, Wide-Angle/Small-Angle X-ray Scattering has been historically utilized in order to identify and characterize the mesophase structure.

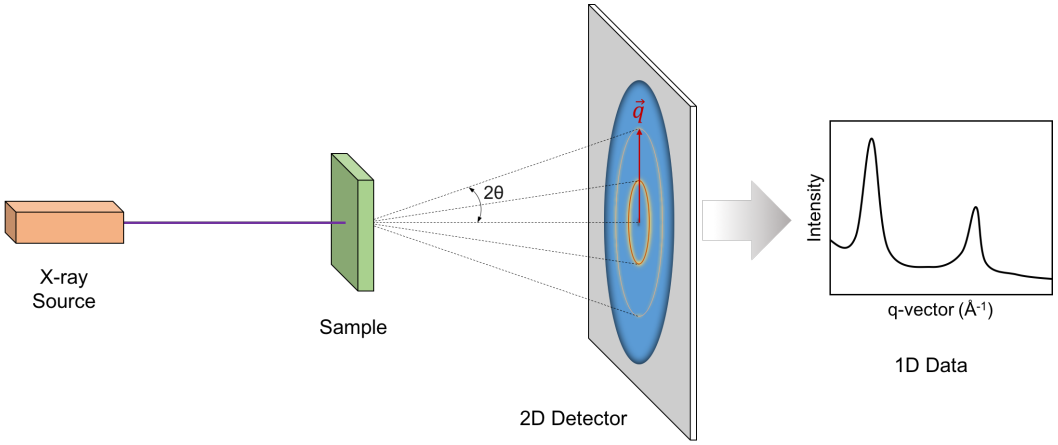

Figure 2.9 – Schematic representation of the X-ray scattering experiment.

The experimental data is often represented as a 2D detector image, which is further reduced to the 1D scattering profile. The d-spacing corresponds to the scattering vector q:

$$q = \frac{4\pi \sin\theta}{\lambda}, \tag{2.1}$$

where θ is the scattering angle and λ is the wavelength of X-rays. In order to extract the d-spacing l out of the scattering vector, a following ratio is used:

$$l = \frac{2\pi}{q}. \tag{2.2}$$

X-ray scattering data in this work was obtained with Forvis Technologies instrument. The x-ray source was 30 W Genix 3D (Cu anode, $\lambda = 1.5405$ Å and $E = 8.050\,92$ keV), the detector was Dectris Eiger R 1M. The beam size was $0.8 \times 0.8\text{mm}^2$, the x-ray flux was 4×10^7 photons/s and sample-to-detector distance was 190 mm. Wide-Angle X-ray scattering experiments were performed during the course of collaboration with University of Colorado, Boulder, USA. The contributions of Rayshan Visvanathan, Alexandra E. Duncan and Noel A. Clark are greatly acknowledged.

2.3 Spectroscopic techniques

2.3.1 Optical Spectroscopy

UV-Vis-NIR Absorption Spectroscopy

This technique relies on measuring the absorption of light by the sample as a function of it wavelength. A typical result of an experiment is an absorption spectrum. For the case of visible radiation (UV-Vis-NIR spectroscopy), the absorption of incident light photons is correlated to the change in the electronic state of the molecule, which makes it ubiquitous in the field of material science.

The absorbance (A) follows the Beer-Lambert law (for one absorbing moiety):

$$A = \epsilon c l, \tag{2.3}$$

where ϵ is the molar extinction coefficient, c is the molar concentration of the absorbing moiety and l is the optical path. This law implies that the absorption is directly proportional to the concentration of the molecule of interest.

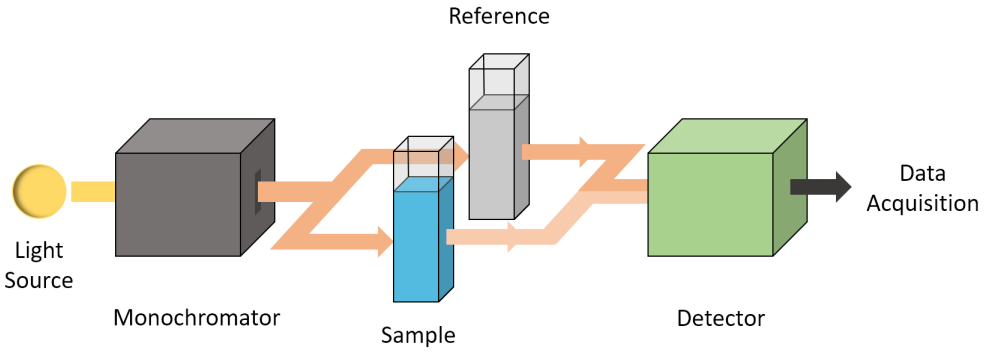

Figure 2.10 – Schematic representation of UV-Visible absorption experimental setup.

A typical UV-Vis-NIR spectrometer consists of a light source followed by a monochromator, sample/reference compartment and a detection device (Figure 2.10). The monochromator allows to perform a sweep in a wavelength range (typically between 190 nm to 1100 nm). The monochromatic light then passes through the sample and/or reference and is collected by the detector, which calculates the optical absorbance by using the following equation:

$$A = -\log_{10} \frac{I}{I_0}, \tag{2.4}$$

where I is the transmitted light intensity and I_0 is the intensity before entering the sample.

As mentioned before, UV/Vis light absorption process is connected to the electronic transitions in the atoms and molecules. In application to the **OSC**, this technique allows to probe the transition of an electron from HOMO to LUMO, thus allowing to obtain the band gap energy. The energy of a photon corresponding to the onset of the optical absorption enables the calculation of the optical bandgap (E_{Gopt}) using the following relation:

$$E_{Gopt} = \frac{hc}{\lambda_{on}}, \tag{2.5}$$

where h is the Planck's constant, c is the speed of light and λ_{on} is the onset of the optical absorption.

The instruments used in this work were Varian (Agilent) Cary 100 and Perkin Elmer Lambda 2 spectrometers with a standard 1 cm fused quartz cuvette.

Fluorescence Spectroscopy

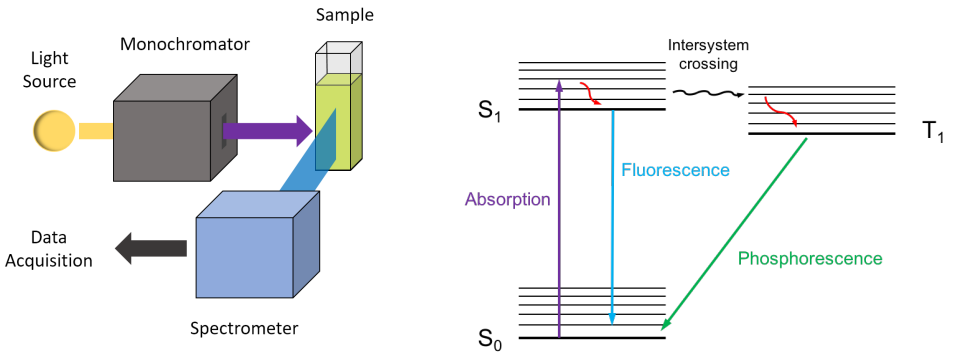

(a) (b)

Figure 2.11 – (a) Schematic representation of Fluorescence spectrometer. (b) Simplified Jablonsky diagram: S_0 and S_1 are ground and first excited singlet states, T_1 is the first triplet state.

This technique is often complementary to the UV-Vis-NIR absorption spectroscopy. While the absorption spectroscopy allows us to obtain the energy of the electron transitions from ground state S_0 to the excited state S_1, fluorescence spectroscopy studies the inverse process. In this technique (Figure 2.11, a), the sample is irradiated with a light which photons have sufficient energy to excite the molecule (for this, knowledge of absorption maxima is mandatory). The molecule further reverts to its ground state S_0 through

internal conversion (vibrational relaxation, where the energy is finally transformed into heat), often followed by a photon emission (Figure 2.11, b). Sometimes it is possible for the excited molecule to transit to a state with a different spin multiplicity (triplet state T_1), whose lifetime is much longer when compared to the excited singlet state of the molecule. The emission intensity is then recorded for the desired energy range with a spectrometer, which is placed at the 90° angle with excitation source in order to avoid its saturation by elastically scattered light.

Fluorescence spectra in this work were recorded on Cary Eclipse Fluorescence Spectrophotometer in a 1 cm fused quartz cuvette.

Time Resolved Fluorescence Lifetime

This techniques operates by the same phenomena as the aforementioned fluorescence spectroscopy, however it provides data in time domain, and the principal experimental setup is similar. The sample is excited by a short pulse of monochromatic light (by a laser

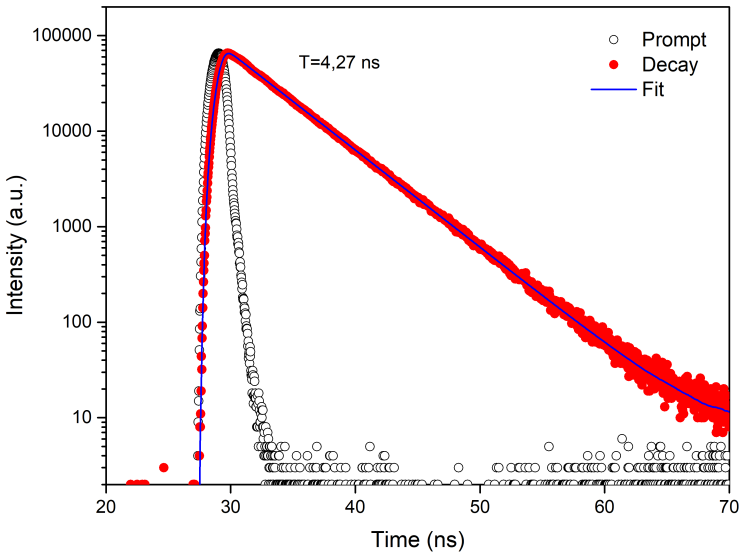

Figure 2.12 – Fluorescence decay of dilute (10^{-5} M) anthracene solution in acetone (degassed with argon): empty circles: instrument response function (recorded with 1% wt LUDOX^{TM} HS-40 colloidal silica in deionized water), red circles: experimental data for anthracene solution, blue line: data fit.

or a LED), but the measurement is performed at a single emission wavelength instead of a whole spectrum. The fluorescence intensity is plotted as a function of time elapsed after the excitation pulse (example of anthracene fluorescence lifetime measurement (τ=4.27 ns)

is presented in Figure 2.12) and fitted with an exponential decay function, which allows to extract fluorescence lifetime. This may give additional information on molecular structure of organic semiconductors, as well as potential relevance for light emitting applications.

Fluorescence Lifetime spectra were recorded on Horiba DeltaFlex TCSPC system with 370 nm laser diode as an excitation source, colloidal silica was used for prompting.

2.3.2 Raman Spectroscopy

Raman spectroscopy is an analytical technique used to observe low frequency modes of vibration, rotation and others in a molecular system. Raman spectroscopy is commonly used in chemistry to identify various substances or to study chemical transformations.

The method is based on inelastic scattering, or Raman scattering by the sample of monochromatic light from a laser source in the near-ultraviolet, near-infrared, or visible range. Laser light interacts with molecular vibrations or other excitations in the system, which results in a positive or negative change of scattered photons. This shift gives information on the vibrational modes of the molecular system.

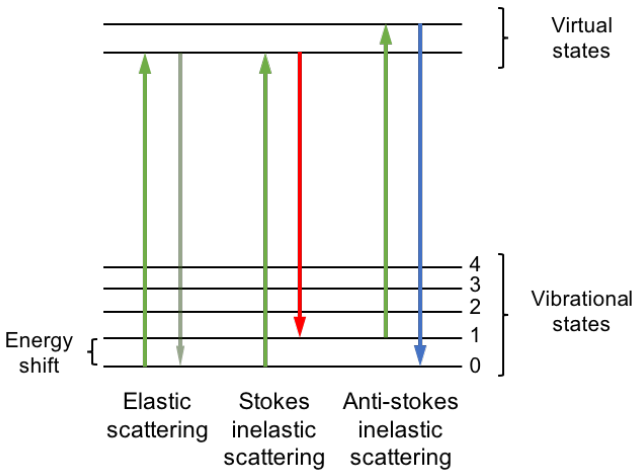

Figure 2.13 – Schematic energy diagram of elastic and inelastic scattering.

The molecule under study absorbs a photon from the excitation source, which results in transition from its initial state to a so-called *virtual* energetic state (Figure 2.13). The molecule then rapidly decays by emitting another photon of light. If the end vibrational state of the molecule is more energetic than the initial vibrational state, the inelastically scattered photon will shift to a lower frequency of the total energy of the system to remain balanced. This frequency change is referred to as a Stokes shift. If the final vibration state is less energetic than the initial state, then the inelastically scattered

photon will be shifted to a higher frequency, which is referred to as an anti-Stokes shift (Figure 2.13). This defines the Raman scattering as a two-photon process and an example of inelastic scattering due to the transfer of energy and motion between photons and molecules during interaction. The Fourier-transform infrared spectroscopy (FTIR), which is a complementary technique of Raman spectroscopy relies on a one-photon process: elastic scattering, or Rayleigh scattering. The energy of photons is dispersed at the same frequency (wavelength) as incoming electromagnetic radiation.

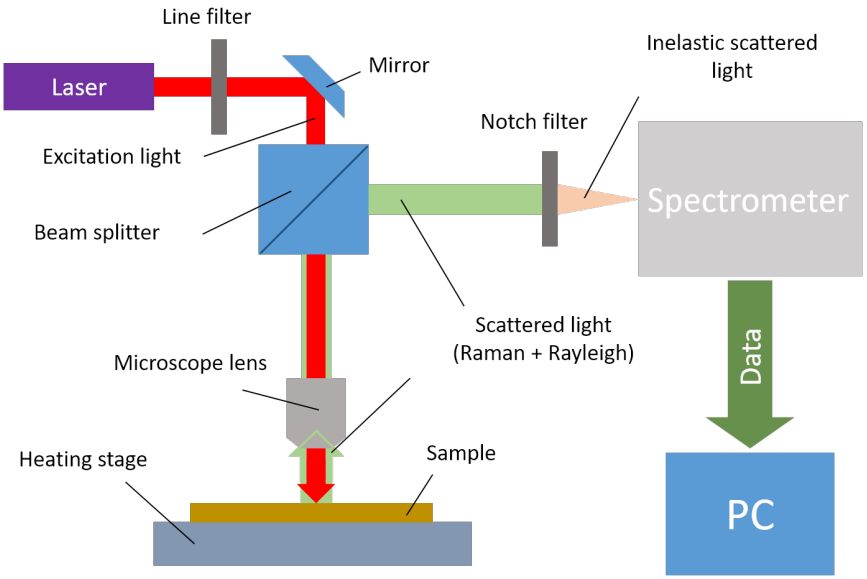

Figure 2.14 – Schematic representation of Raman spectrometer.

In a typical Raman spectroscopy experiment, a sample is illuminated by a laser beam (excitation light). The electromagnetic radiation scattered by the sample is collected with a microscope lens and sent through a spectrometer. Elastic scattered radiation at the wavelength corresponding to the excitation laser line (Rayleigh scattering) is filtered by a notch filter, while the rest of the collected light is passed to a detector (Figure 2.14).

Raman scattering amplitude is usually very small. So the main challenge of Raman spectroscopy is to reduce the intense Rayleigh scattered light of the excitation source in order to record the small amplitude light which is inelastically scattered from the sample. First Raman spectrometers used multiple monochromators with holographic gratings and dispersion stages in order to obtain a reasonable degree of laser light suppression. Photomultiplier tube detectors were also widely employed for their high sensitivity, which however imposed very long acquisition times. Modern instrumentation employs

almost universally notch filters for laser rejection and Peltier or liquid nitrogen cooled charge-coupled device (CCD) detectors.

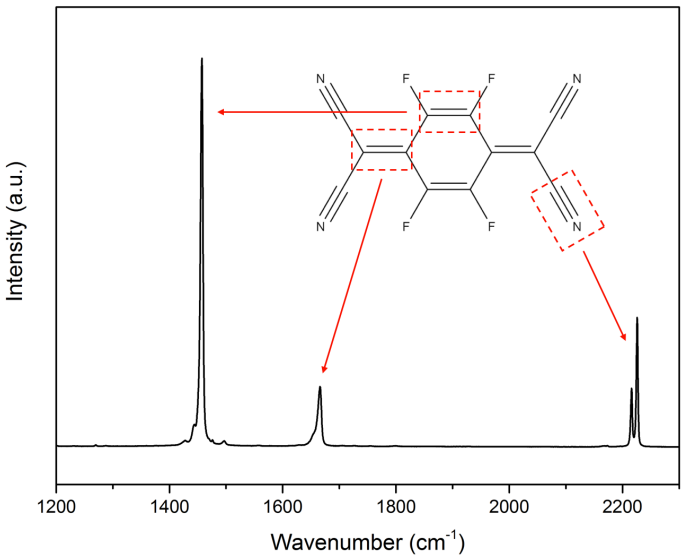

Figure 2.15 – Example of Raman spectrum of $\mathbf{F_4TCNQ}$ molecule (recorded with 785 nm excitation wavelength), the corresponding vibrational modes are referred to the parts of molecular structure.

A typical experimental spectrum of a Raman-active substance is plotted as a function of energy shift relative to the excitation line (often expressed in 1/cm). Figure 2.15 demonstrates a portion of a Raman spectrum of 2,3,5,6-tetrafluoro-7,7,8,8-tetracyanoquinodimethane ($\mathbf{F_4TCNQ}$). The three groups of peaks in this spectrum correspond to the different molecular vibrations associated with separate parts of molecular structure. The large peak at about 1450/cm corresponds to symmetric stretching of C=C double bound in the ring of quinoid structure, when a smaller peak around 1670/cm is related to the stretching of C=C conjugated lateral bond. The peaks around 2200/cm correspond to the vibrations of the nitrile groups. The positions of these peaks are heavily influenced by molecular structure, as well as intermolecular interactions, which allows us to probe relatively fine changes in the electron density of the molecule by this technique.

Raman spectra in this work were recorded with Horiba LabRAM HR spectrometer with 4 m W power and 785 nm excitation wavelength, the temperature was controlled with Linkam TMS 600 hotstage (−196 °C to 600 °C).

2.4 Charge transport characterization techniques

2.4.1 Time Of Flight (TOF) mobility measurment

Generalities on charge carrier mobility measurement

Electronic charge carrier (essentially, any charged particle: electron, hole or ion) mobility μ ($m^2\,V^{-1}\,s^{-1}$, for simplicity very often expressed in $cm^2\,V^{-1}\,s^{-1}$) is defined as:

$$\mu = \frac{v}{E}, \tag{2.6}$$

where v is charge carrier velocity ($m\,s^{-1}$) and E is applied electric field ($V\,m^{-1}$). There are many techniques which allow to estimate charge carrier mobility[127, 128]. The most widely employed are: time-of-flight [129] (**TOF**), space-charge-limited current [130] (SCLC), carrier extraction by linearly increasing voltage [131] (CELIV), **OFET** I-V characterization [132] and time-resolved microwave conductivity [133] (TRMC) as recently emerged but quickly gaining popularity. Each of these techniques has its own advantages and limitations. However their detailed overview is out of scope of this thesis. Hereby we are going to describe **TOF** method which was widely utilized during present research work.

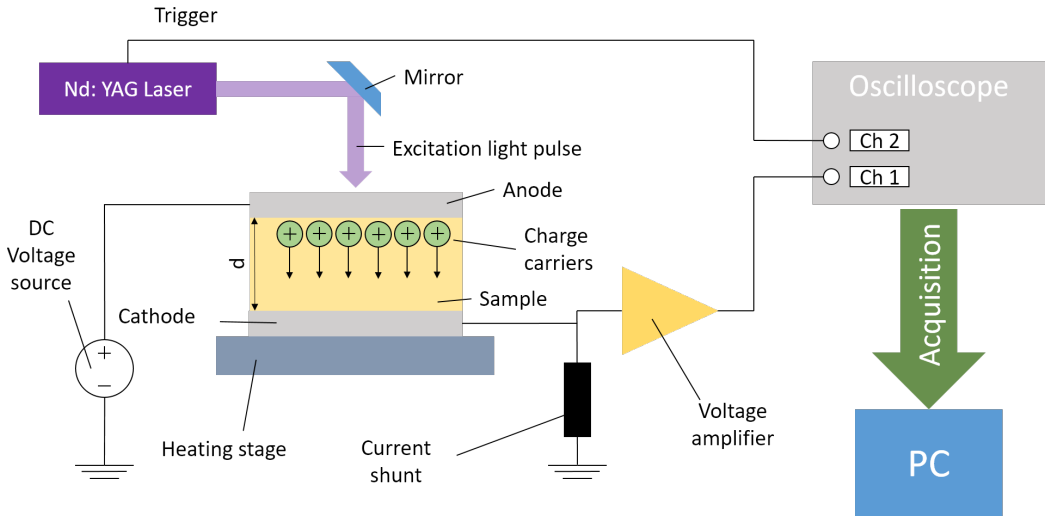

Figure 2.16 – Schematic representation of **TOF** experiment in case of hole transport.

The so-called "time-of-flight" technique of charge carrier mobility measurement is based on photoexcitation of the sample of **OSC** material sandwiched between two electrodes, at least one of them should be semi-transparent for excitation light. Fermi level of electrode

material should be between HOMO and LUMO levels of **OSC** in order to block charge injection, which in turn under high applied field will result in space charge and affect electric field uniformity.

The principle of transient current measurement is relatively straightforward: light pulse creates an electron-hole pair in fine layer of **OSC** near to the electrode surface. This pair is separated by applied electric field. In case of hole transport study, electrons are almost immediately recombined at anode (Figure 2.16), when holes have to cross all the sample thickness d in order to recombine on cathode.

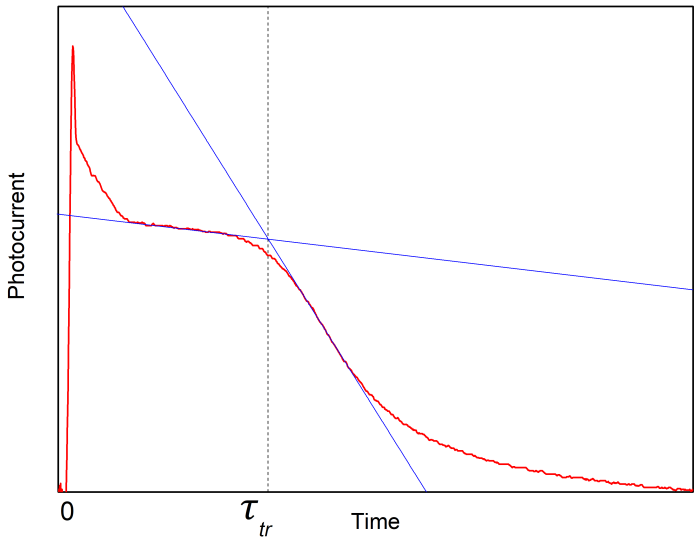

Figure 2.17 – Generalized transient photocurrent curve for non-dispersive charge transport in linear scale.

This process gives rise to a transient photocurrent (Figure 2.17) which can be visualized on oscilloscope after current-voltage conversion. For non-dispersive charge transport regime, one typically obtains a sharp peak followed by a plateau with an inflexion point, from where photocurrent begins to decline rapidly. This plateau represents constant current attained in thermal equilibrium, and inflexion point shows arrival time of fastest charge carriers. The angle of post-inflexion current curve region reflects the diffusion of charge carriers during their transit, i.e. the sharper it is, the more uniform is the distribution of charge carriers velocity. The intersection of linear fits of plateau and current decay regions yields charge carrier transit time τ_{tr} (Figure 2.17).

However, for some samples or under certain experimental conditions, the charge transport is dispersive and it is impossible to extract transit time from conventional

photocurrent plot (Figure 2.18, (a)). To resolve this problem, the data has to be plotted in double logarithmic scale, and only then linearly fitted. Intersection of fitted straight lines allows us to extract τ_{tr} of fastest charge carriers.

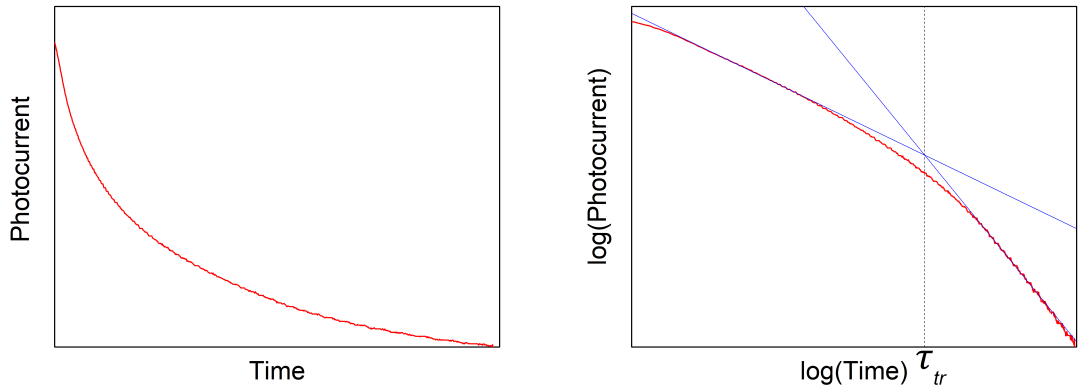

(a)Linear scale (b) Double logarithmic scale

Figure 2.18 – Generalized transient photocurrent curves for dispersive charge transport.

In order to obtain mobility value from extracted time of transit, expanded version of equation 2.6 is usually used:

$$\mu = \frac{d^2}{\tau_{tr} V}, \tag{2.7}$$

since $v = \frac{d}{\tau_{tr}}$ and $E = \frac{V}{d}$. In this equation d is the thickness of sample, and V is the applied voltage.

Experimental setup description

A basic **TOF** setup includes an excitation source (laser of excitating wavelength), DC voltage source, measurement cell or deposited electrodes in parallel configuration, current-to-voltage conversion stage (current amplifier or current shunting resistor) and an oscilloscope (Figure 2.16).

The experimental setup consists of Quantel (USA) Ultra Nd:YAG (neodymium-doped yttrium aluminium garnet) laser with frequency-tripled output (λ=355 nm, pulse duration = 5 ns), Keithley (USA) 6487 Picoammeter/Voltage Source, commercially available liquid crystal cells (Figure 2.19) by AWAT (Poland) with ITO electrodes (1 Ω/□) and custom made PID-controlled holder/heating stage, 1 kΩ potentiometer, Stanford Research (USA) SR560 voltage amplifier and Keysight (USA) DSO-X3022T oscilloscope. Experimental parameter control and data acquisition is performed via a custom-made Labview program.

Oscilloscope is triggered into laser's Q-Switch output on channel 2 to obtain transient signal and filtering of amplifier is switched off in order to benefit from the maximum of available bandwidth.

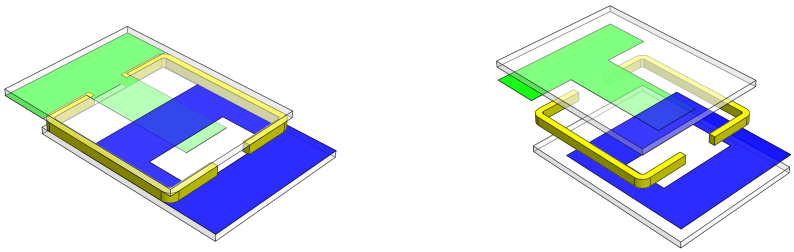

(a) Assembled view (b) Exploded view

Figure 2.19 – 3D model of sample cell: two ITO electrodes, top (green, T-shaped) and bottom (blue, O-shaped) are deposited on glass slides and glued together with a precision spacer (yellow). The active area of 5x5 mm is situated in the center of the cell where top electrode crosses the bottom one.

Despite being seemingly simple, **TOF** technique requires considerable attention to experimental parameters and conditions. While performing **TOF** experiments, one should not forget that the **TOF** setup is particularly sensible to circuit components which modify its response time. As we have mentioned earlier, the generated photocurrent needs to be converted into voltage in order to be visualized by an oscilloscope. Two possible ways to perform this conversion may be employed (Figure 2.20). We may either use a shunt resistor(Figure 2.20, a), or a current-voltage (transimpedance) amplifier (Figure 2.20, b). The latter is preferred for some applications, since it offers superior noise performance, stability, and simplicity of circuit layout. In our case, the noise do not pose a significant problem due to low repetition rate of Q-Switch (10 Hz), which enables us to use extensive signal averaging. Relatively large gains are required for acceptable signal-to-noise ratio (about 10^4-10^5), which means feedback components of a typical current amplifier (Keithley 428) significantly limit the signal bandwidth (bandwidth is inversely proportional to the gain). Since the ability to measure short (in order of µs) transient times is essential for TOF experiment, a better solution must be employed which does not reduce the signal bandwidth (and the rise time t_r) as strongly as in the case of a single stage transimpedance amplifier.

It was proposed to utilize a relatively small value shunt resistor to convert the current to voltage, which will be further amplified by a second stage non-inverting voltage amplifier.

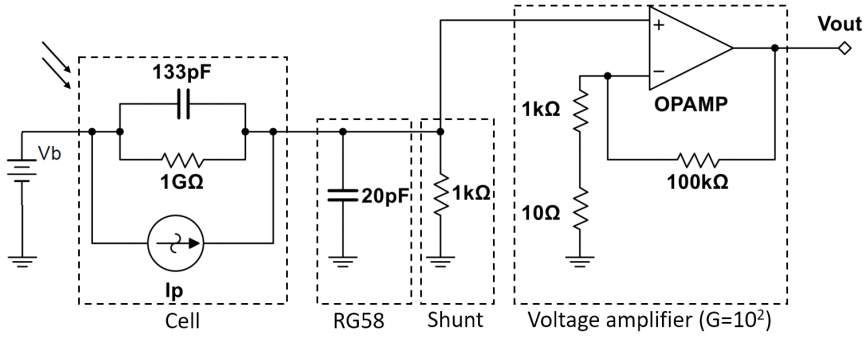

(a) Cascaded configuration

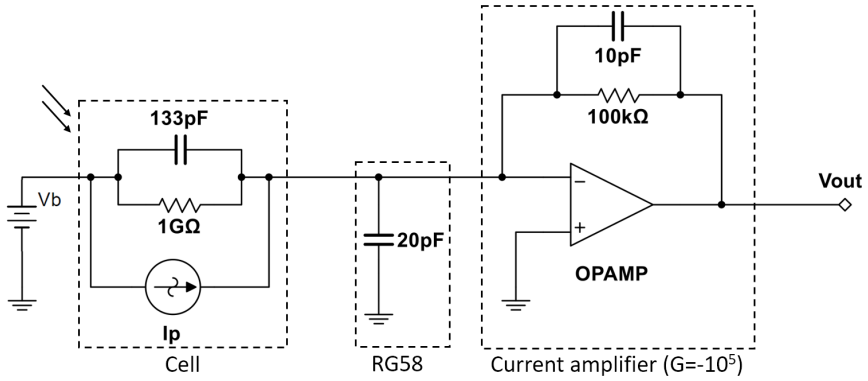

(b) One stage configuration

Figure 2.20 – Basic electric circuit of **TOF** which includes the DC voltage source **Vb**, sample cell which is represented by a photocurrent source in parallel with a resistor and a capacitor (typical values are presented), coaxial cable and current conversion stage: shunt resistor followed by voltage amplifier (a) or transimpedance amplifier (b). The resulting voltage V_{out} is fed into oscilloscope.

The resulting RC time constant τ of the current conversion circuit is

$$\tau = RC,$$

where R is value of shunt resistor and C is the capacitance of sample cell. This means employing large R values or using very thin samples will result in increase of τ and decrease the available resolution in time domain. For example, if we take a sample (typical dielectric constant ϵ about 3 for organic materials) in a cell (Figure 2.19) with 5 µm spacer d and 5×5 mm active area A, we may calculate its capacitance with the parallel plate

capacitor formula:

$$C = \frac{\epsilon\epsilon_0 A}{d},$$

where ϵ_0 is the vacuum permittivity, which yields us C=133 pF. By taking into account a typical value of shunt resistor of 1 kΩ, the time constant of the circuit is found to be of 0.133 µs. The signal is then amplified in a cascade sequence with bandwidth of about 1 MHz.

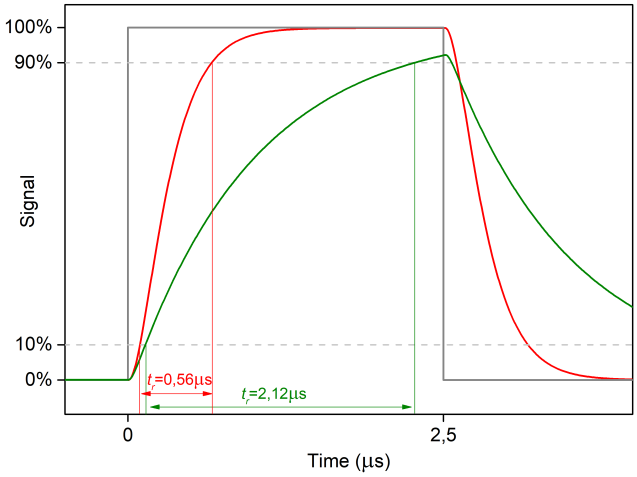

Figure 2.21 – Transient signals obtained from circuit simulation: current pulse (1 µA amplitude, in gray), cascade configuration (1 kΩ shunt × 100 non-inverting gain, in red) and one stage configuration (inverted, 100 kΩ+10 pF feedback, in green) and their corresponding rise times.

Figure 2.21 demonstrates transient voltage output for the circuits presented in the Figure 2.20 (simulated in NI Multisim 14.0). We have included typical cell parameters (capacitance C=133 pF and resistance R=1 GΩ), as well as cable capacitance (20 cm of RG58 coaxial cable account for about 20 pF) in the simulation. An idealized operational amplifier (unity gain bandwidth 100 MHz, open loop gain 2×10^5, input resistance 10 MΩ) was used in both cases. The value of feedback capacitor (10 pF) in Figure 2.20, (b) corresponds to that in Keithley 428 schematic for 10^5 gain. The results of this simulation allow us to compare time response of two current conversion approaches with the same gain value and confront it with the initial 1 µA amplitude and 2.5 µs duration current pulse (Figure 2.21, gray line). We have calculated the rise time t_r which is defined as a period of time required for output signal to go from 10% to 90% of its final value in response to ideal square wave input. In our case, the resulting t_r for cascaded conversion scheme was

almost four times lower than for single stage conversion (0.56 µs versus 2.12 µs).

Our experimental observations have confirmed the results of this simulation: use of cascaded scheme resulted in typical signal rise time t_r of less than 1 µs, when for one stage current conversion via Keithley 428 we have obtained t_r of about 5 µs (which is in good agreement with its specifications) for similar 10^5 gain, which has determined our choice of cascaded conversion scheme for better resolution in time domain.

This consideration also imposes its limits on μ values which can be measured by TOF setup: higher mobilities will necessitate use of low voltages to extend transit time. This will require further signal amplification, and, as a consequence, bandwidth reduction. It is also necessary to choose appropriate excitation wavelength and intensity, in order to have most of the light absorbed very close to electrode surface. The irradiation intensity should be high enough to provide reasonable amplitude of signal, but in the same time low enough to avoid charge carrier generation in the bulk of sample. Absorption in the bulk of material leads to curve distortion due to space-charge and inconsistency of transit time measurement.

2.4.2 Transistor I-V characterization

In this work we have used commercial **OFET** substrates (Figure 2.22) in bottom gate/bottom contact configuration provided by Ossila (Sheffield, UK), following information on manufacturing process and electrical characteristics are provided by the supplier. Each substrate had 20 source/drain electrode pairs with a common gate. The size is 20×15 mm, thickness is (725 ± 25) µm.

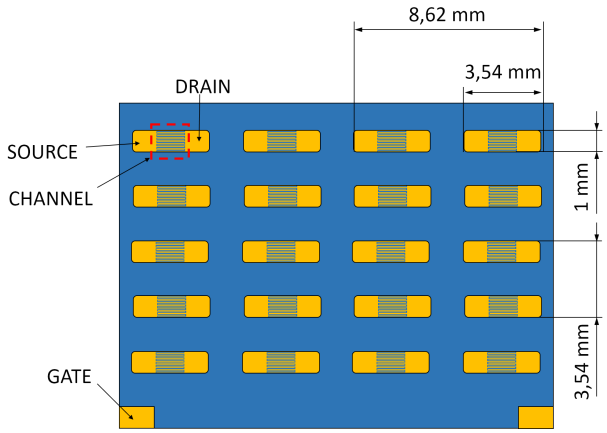

Figure 2.22 – Schematic representation of **OFET** substrate.

The substrate is manufactured on a heavily p-doped (Boron) Si wafer (resistivity

$5 \times 10^{-4}\,\Omega/\mathrm{cm}$ to $10^{-2}\,\Omega/\mathrm{cm}$) which also functions as gate electrode. The wafer is then coated with SiO_2 (300 nm, capacitance $1.09 \times 10^{-8}\,\mathrm{F/cm^2}$) on both sides, and source/drain electrodes are thermally evaporated on the polished side of the wafer through the shadow mask: 2 nm of chromium adhesion layer, then 70 nm of gold. After **OSC** is deposited on the substrate (deposition techniques are covered in further sections), the surface of source/drain contact pads is wiped with clean room swabs in order to allow electrical contact with probe tip.

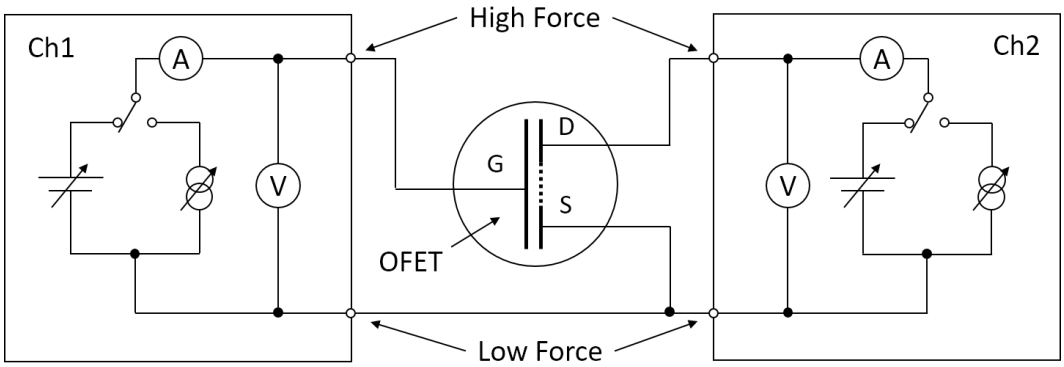

Figure 2.23 – Schematic representation of transistor test setup.

The experimental setup of evaluation of key performance parameters of **OFET**s is built around a wafer inspection station which is modified to accommodate micromanipulators. The station is equipped with a binocular magnifier and a Carl Zeiss KL2500 Halogen Cold Light source. Electrical connections with the on-substrate contact pads were made by employing three micromanipulators (Everbeing EB700) equipped with CuBe and W low leakage triaxial probes. All the electrical connections between the manipulators and measuring equipment were made with triaxial leads in order to minimize leakage currents. The measurements were performed with two Keysight B2901 precision source measuring units (100 fA resolution), operated via LAN interface (Figure 2.23). The first SMU (denoted as Channel 1) was utilized to drive gate voltage and measure the leakage current across the gate dielectric. The second SMU (Channel 2) was intended to apply voltage between the source and drain terminals, while measuring the resulting current. Photoconductivity measurements were enabled by Thorlabs M455L4 LED (455nm, bandwidth FWHM=18nm), powered by DC2100 driver. This setup allowed quick and easy low-noise collection of the output and transfer characteristics of OFETs.

2.5 Complimentary techniques

2.5.1 Molecular structure characterization techniques

The present manuscript contains a section dedicated to an entirely new material, synthesized during the course of this PhD thesis. This section assembles the techniques used to determine the molecular structure of the substance in scope. Due to the novelty of the material, basic analytical characterization is required in order to ensure the conformity to the expected molecular structure and validate the proposed synthetic route. However, these techniques are only briefly introduced, since the detailed chemical investigation is out of scope of this study.

Nuclear magnetic resonance spectroscopy

This technique is used primarily to assess the quality control of a substance, i.e. purity and conformity to a proposed molecular structure. There are many subtypes of this technique which are related to the nuclei type of interest. In this work, two primary sub-techniques were employed: ^{1}H and ^{13}C.

The sample is dissolved in a suitable solvent (deuterated solvents are used in order to avoid the contribution of its protons in ^{1}H) in a thin walled glass tube. The tube is then placed in a strong magnetic field, where the phenomena of the nuclear magnetic resonance is observed. The data is usually obtained in a form of the chemical shift spectrum. The chemical shift is a value between the measured resonance frequency and the reference frequency; being extremely small, it is often expressed in parts per million (**ppm**).

Chemical shift is directly related to the local electron environment of a given nucleus: for example, electron-withdrawing environment will actively contribute to the nucleus de-shielding, which will result in a stronger chemical shift. This technique makes possible to quantify unique nucleus environments of ^{1}H and ^{13}C in the molecule and compare them to the expected numbers, as well as to directly correlate these environments with each other (2D-techniques).

The instrument used in this work was Bruker Avance III 400 MHz spectrometer. The spectra were obtained in chloroform-d, which was passed over dry alumina powder in order to remove acid and water traces prior to sample preparation.

High-resolution mass spectroscopy

This technique allows the detection of molecules with a respect to their mass with a 0.001 atomic mass unit precision. An actual mass spectrometer measures a mass-to-charge

ratio, m/z, since only charged particles can be used as a subject of mass spectrometry.

A typical mass spectrometer includes three main components: ion source, mass analyzer and detector. The type of an ion source depends largely on the substance under study. In this work, an instrument with an electrospray-type source was used, since it is considered to be a "soft" ionization method, usually resulting in little fragmentation and often employed for macromolecules and polymers.

The mass analyzer is utilized to separate the ions or molecular pseudoions by their m/z ratio. One of the most popular mass analyzer types for organic substances include time-of-flight (TOF) and quadrupole analyzers. The TOF analyzer accelerates the ions by applying an electric field: for the ions of the same charge, their velocity will solely depend on their mass. Thus, it is possible to extract the ion's mass from its arrival time. The quadrupole analyzer is capable to separate the ions by a RF quadrupole field created between four parallel rods. This type of analyzer is often used in fragmentation studies.

In application to organic molecules, ions are often created by addition of a proton or another cation, and the expected mass must be calculated as $\mathbf{[M+H^+]}$.

High resolution mass spectrum (HRMS) in this work was recorded in positive mode using an Agilent 6540 Accurate-Mass Quadrupole Time-of-Flight (Q-TOF) LC/MS system equipped with an Agilent Jet Stream dual electrospray source. Analysis parameters were as follows: Gas temperature (150 °C, 5 L/min), Nebulizer (35 psig), Sheath gas (375 °C, 12 L/min) Vcap (3500 V), nozzle voltage (2000 V), fragmentor (100 V), skimmer (65 V) OCT1RFVpp (750 V).

2.5.2 Cyclic voltammetry

Cyclic voltammetry is an experimental technique which is purposed to study the process of electrochemical oxidation or reduction of molecules. Since theses processes are directly related to addition or withdrawal of an electron from a molecule, this technique is widely applied to the field of organic semiconductor characterization.It allows to extract the information about the frontier molecular orbitals, which is crucial for understanding of the charge transporting properties [134, 135].

The experimental setup (Figure 2.24) consists of an electrochemical cell which is connected to the potentiostat (Metrohm AUTOLAB PGSTAT302). The electrochemical cell is composed of the electrolyte containment vessel with three electrodes: a working electrode (WE), a counter electrode (CE, sometimes called an auxiliary electrode) and a reference electrode (RE). The RE, as its name suggest, provides a potential reference, which remains constant during the experiment, while the current flows between the WE

and CE. The WE used in this work is represented by a platinum disc of 3 mm diameter (Ø), platinum wire was used as the CE. Two REs were used in this work - a silver wire pseudoreference and an Ag/Ag^+ RE, which was filled with an electrolyte for non-aqueous measurements ([NEt_4Br]=0.4 M in ethylene glycol). Both the WE and Ag/Ag^+ RE were provided by Metrohm, while the CE was purchased from Radiometer Analytical, the pseudoreference was custom-made.

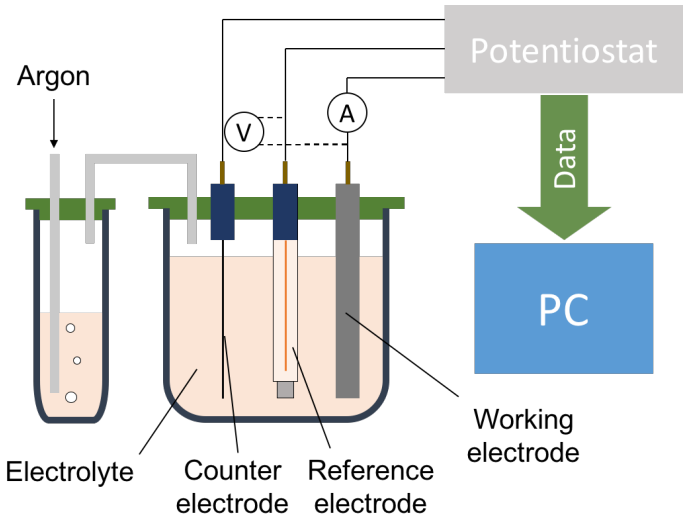

Figure 2.24 – Schematic representation of cyclic voltammetry setup.

The experiment involves measuring the current at the WE while performing a voltage sweep (in respect to RE potential). The voltage is ramped linearly with a selected scan rate, and upon reaching a certain value (formal potential of redox-active molecule) the electrical current is observed, which corresponds to the redox event. If the voltage is swept in the positive direction, the molecule is oxidized and a positive current is measured. On the contrary, sweeping in the negative direction results in a reduction, which is expressed as a negative current.

In a typical experiment, the voltage is scanned up to a certain limit which is determined by the so-called electrochemical window (this potential range is imposed by the solvent and supporting electrolyte in order to avoid their reduction/oxidation). Upon reaching the limiting potential (also called vertex potential), the scanning direction is reversed. For example, in the case of oxidation event (Figure 2.25), the molecules situated near the WE loose one electron; when the scan direction is reversed, these molecules obtain an electron and revert to their initial neutral state (become de-oxidized). An increase in the scanning rate results in rise of the current. The ferrocene from this example exhibits

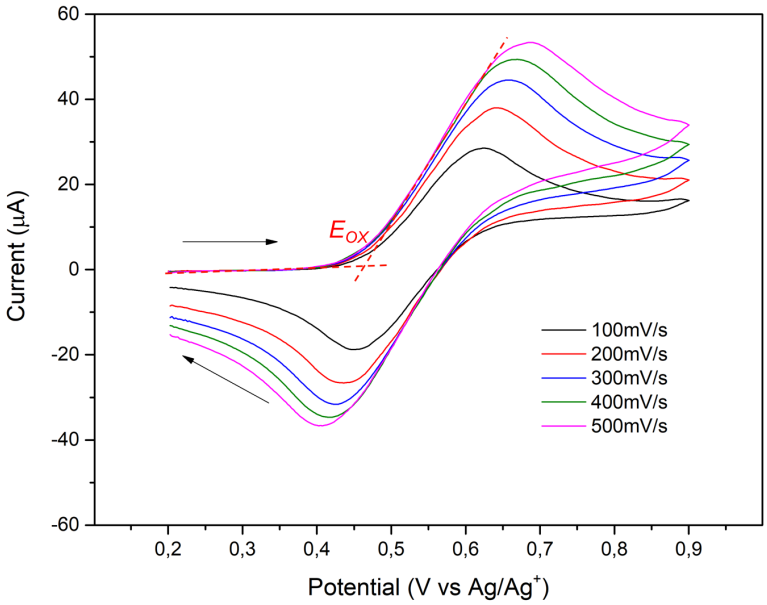

Figure 2.25 – Cyclic voltammetry of 2 mmol/L ferrocene in dichloromethane ($[NBu_4PF_6]$=0.1 M) on Pt electrode (Ø=3 mm). Color corresponds to the scanning rate.

quasi-reversible behavior in dichloromethane, given the separation of oxidation and de-oxidation potentials. Most of **OSC** molecules exhibit similar or non-reversible behavior, where it is required to apply further potential to revert the molecule in its original state. This behavior is directly connected to the rate of the electron exchange, which depends on the solvent used in the experiment, as well as the stability of oxidized/reduced molecule. By tracing a tangent of the current corresponding to the oxidizing event (Figure 2.25, in red), we may extract the onset of oxidation for a given molecule, i.e. the energy which is required to extract an electron from its HOMO. By carefully referencing this energy to a known potential (reference electrode or internal reference substance with known oxidation/reduction potential, such as ferrocene), we may obtain an absolute energy value of its HOMO. In the case of reduction process, the same applies to calculation of the LUMO energy.

It is possible to carry out the experiment for the substance of interest in dissolved and solid state (deposited on the working electrode). The latter method enables the study of deposition and processing methods contribution to the potential landscape of the material, as well as study of insoluble substances. In this work however, the experiments were performed in a solution of dichloromethane, given the soluble nature of the studied

substances. It is worth noting that the presence of oxygen interferes with the experiment (the molecule of oxygen, while being redox-active, undergoes a reduction, which manifests itself in the negative range of voltage sweep). The assembled cell was bubbled with the argon gas (saturated with dichloromethane vapors) prior to the experiment.

2.5.3 Self-Assembled Mono-layer (SAM) coating

Numerous failed attempts to spin-coat **OSC** on bare (and thoroughly cleaned) glass/ITO substrates have showed poor compatibility with utilized solvents (toluene, anisole, THF and chloroform). Both types of substrates used in this work, glass and Si wafers are covered with a layer of SiO_2. In order to overcome excessive hydrophilicity, it was proposed to use octadecyltrichlorosilane (OTS-18, Figure 2.26) as a well-known self-assembled mono-layer adhesion promoter[136].

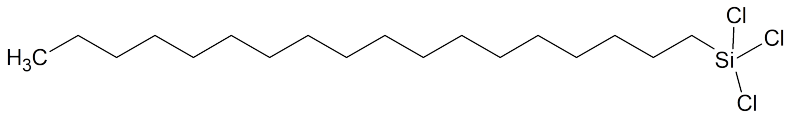

Figure 2.26 – Molecular structure of OTS-18.

The coating process involves creation of covalent bonds with Si atoms of OTS-18 trichlorosilane end group and Si-O groups of the substrate. First, the substrate is meticulously cleaned and treated with an oxidizing agent in order to break Si-O-Si bonds on the surface and attach a hydroxyl groups in their place. The substrate then is reacted with the SAM solution through the following scheme:

$$CH_3(CH_2)_{17}SiCl_3 + 3\,H_2O \longrightarrow CH_3(CH_2)_{17}Si(OH)_3 + 3\,HCl$$
$$CH_3(CH_2)_{17}Si(OH)_3 + 3\,SiOH_{(solid)} \longrightarrow CH_3(CH_2)_{17}Si(OSi)_{3(solid)} + 3\,H_2O$$

The presence of trace amounts of water is necessary for the first step of the reaction, however excessive moisture will result in uncontrollable SAM polymerization in solution. The solution should be used only if it is transparent, and any cloudy deposits should be skimmed from the surface prior to substrate introduction.

The resulting SAM monolayer (Figure 2.27) is covalently bonded to the substrate and can withstand following ambient air handling and cleaning.

Coating with trichlorosilane-based SAMs is a delicate and moisture-sensitive process, which includes handling of highly corrosive, potentially explosive and carcinogenic sub-

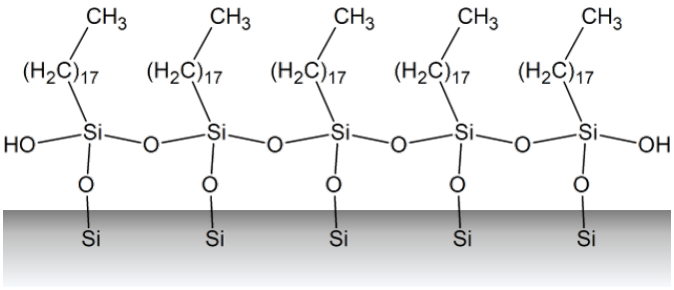

Figure 2.27 – Schematic representation of OTS-18 mono-layer grafted on the substrate.

stances. Safety protocols must be in place. The SAM coating solution container, as well as reaction vessel and handling tools (tweezers and stirring bars) should be made out of hydrophobic material (preferably PTFE), great attention and care should be exercised while working with "piranha" solution: overheating or introducing a large amount of organic material poses a significant foaming or explosion risk. The following protocol of OTS-18 coating was elaborated:

- Preliminary substrate cleaning - sonicate for 15 minutes in the following solutions:
  - 5% Decon^{TM} 90 solution in deionized water
  - Deionized water
  - Acetone
  - Isopropyl alcohol
- Substrate drying - 2h at 50 °C in a closed Petri dish in the oven
- Substrate oxidation (always ensure the substrate is completely dry before proceeding to the next step)
  - "Piranha" bath for 15 minutes at 50 °C: 50/50% mixture of concentrated sulfuric acid and 30% H_2O_2 (prepared by slowly adding hydrogen peroxide to the acid)
  - Deionized water - sonicate for 15 minutes at 50 °C, 2 times
- Substrate drying - 2h at 50 °C in a closed Petri dish in the oven
- SAM solution preparation: 20 ml of hexadecane is mixed with 5 µL of chloroform and 50 µL of OTS-18 (Alfa Aesar, 98%), stored in the cold while the substrate is in the oven.

- SAM coating: the substrate is immersed in the SAM solution and left undisturbed for 30 minutes
- Final cleaning - sonicating for 15 minutes in the following solutions:
  - Chloroform
  - Acetone
  - Isopropyl alcohol
- Substrate drying - 2h at 50 °C in a closed Petri dish in the oven

This protocol was successfully used to coat soda lime glass slides, as well as prefabricated Si OFET substrates. No sign of gold electrode degradation was found.

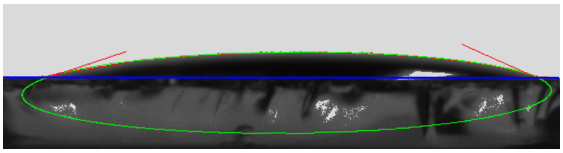

Figure 2.28 – Droplet (V = 5 µL) profile of toluene (non-polar solvent) on OTS-18 coated glass substrate. Average contact angle calculated to be about 21.3° after 4 measurements.

Figure 2.28 demonstrates superior wetting properties of a soda lime glass slide coated with a OTS-18 monolayer: the contact angle (measured wit KRUSS DSA100 Drop Shape Analyzer) of toluene drop is close to 20° which indicates hydrophobic properties of the functionalized surface.

2.5.4 Spin-coating

Spin coating principle is based on utilizing of the centrifugal forces created by spinning the substrate with controlled speed. When the work solution is placed in the center of the substrate, the centrifugal forces make the liquid spread evenly on the surface of the substrate.

Often a so-called dynamic disperse method is employed, when the solution is placed on a relatively slowly spinning (about several hundred RPM) substrate, which ensures its complete and homogeneous coverage. The substrate is then ramped to the next high-speed step to obtain the desired coating thickness (Figure 2.29). There are many parameters which influence the thickness of resulting film including but not limited to: spin velocity, duration and acceleration, viscosity of the solvent, its evaporation rate, solution concentration, substrate wettability and the interfacial interactions between the

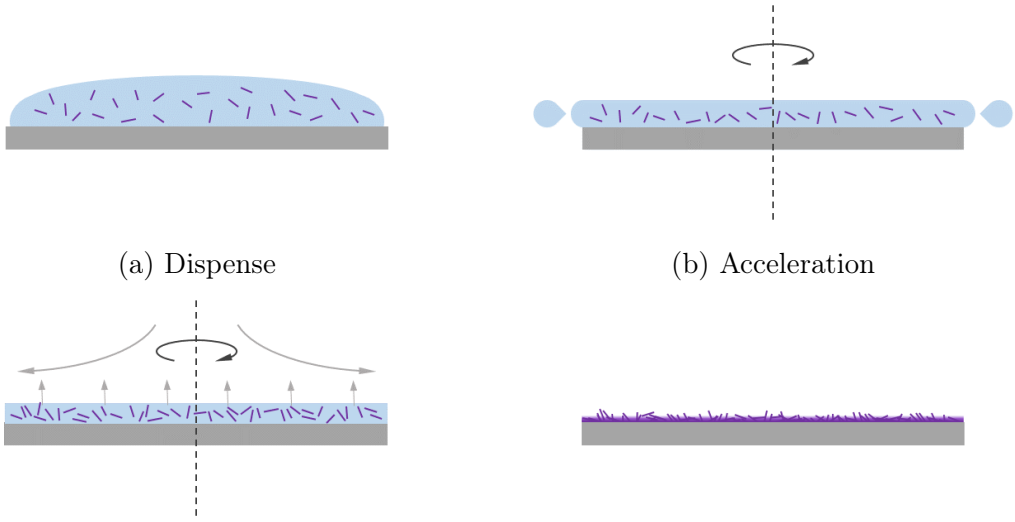

(a) Dispense (b) Acceleration

(c) Drying (d) Polycrystalline film

Figure 2.29 – Diagram of spin-coating procedure. Size of the solute molecules is greatly exaggerated.

substrate and the dissolved substance. These factors make the obtaining of a high-quality thin film a non trivial task, requiring trial and error method. Substrate quality also plays crucial role, with a rigorous cleaning being mandatory.

Prior to spin-coating, all the substrates were sonicated in a Decon^{TM} 90 solution, distilled water, acetone, isopropanol, with subsequent drying in the oven at 50 °C. The finishing touch was a UV-Ozone cleaning step for 20 minutes in Ossila UV Ozone cleaner; substrates were immediately processed after the final step to avoid possible contamination. Thin films in this work were prepared with Laurell WS-650 spin processor in a vertical laminar air flow workbench equipped with a high efficiency particulate filter (HEPA), removing 99.97% of all particles 0.3 µm or larger.

2.5.5 Drop-casting

This deposition method is very fast, simple and easily accessible, however it should not be overlooked. It is based on direct deposition of the solution on the substrate surface and requires no special equipment, however, it is difficult to control the resulting film quality.

In this work, this method was combined with solvent vapor annealing, which means it was performed in a controlled environment of saturated solvent vapor on a heatplate (about 50 °C). The substrate was placed in a small Petri dish cover, which in turn was

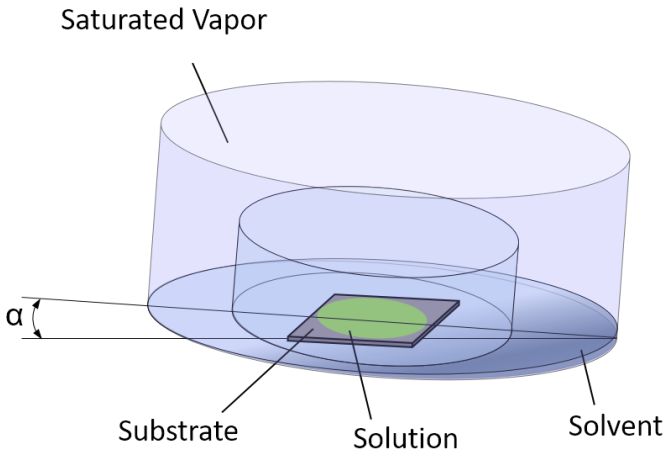

Figure 2.30 – Schematic representation of drop-casting setup. α is the substrate inclination angle.

placed in a bigger Petri dish to trap the solvent vapors. This dish itself was placed on a heatplate with a small inclination of about 2-3°) (Figure 2.30). This inclination is created in a direction perpendicular to the transistor channel width, and helps to orient the crystal growth in the direction favorable for the charge transport. Substrate preparation steps were identical to the aforementioned spin-coating procedure.

2.6 Conclusion

This chapter briefly describes the techniques and methods used during the course of present PhD thesis. It also demonstrates, in conjunction with Chapter 1, the vast complexity of the studied subject. These techniques are utilized in order to characterize the elaborated materials in the course of Chapters 3&4. In addition to description of some standard techniques, we have also included a short description of our work conducted on optimization of the **TOF** setup. We hope that the reader will find this chapter useful, and it will allow to better understand the experimental results which we are going to present further.

Bibliography of the current chapter

[125] Ingo Dierking. *Textures of Liquid Crystals*. Vol. 301. 1. Weinheim, FRG: Wiley-VCH Verlag GmbH & Co. KGaA, May 2003, pp. 15–45. ISBN: 3527307257. DOI: 10.1002/3527602054.

[126] Chiara Musumeci et al. "Electronic characterization of supramolecular materials at the nanoscale by Conductive Atomic Force and Kelvin Probe Force microscopies". In: *Materials Today* 17.10 (2014), pp. 504–517. ISSN: 13697021. DOI: 10.1016/j.mattod.2014.05.010.

[127] Jason U Wallace. "Carrier Mobility in Organic Charge Transport Materials: Methods of Measurement, Analysis, and Modulation". In: *Thesis* (2009), p. 188.

[128] Akshay Kokil, Ke Yang, and Jayant Kumar. "Techniques for characterization of charge carrier mobility in organic semiconductors". In: *Journal of Polymer Science, Part B: Polymer Physics* 50.15 (2012), pp. 1130–1144. ISSN: 08876266. DOI: 10.1002/polb.23103.

[129] James C. Blakesley et al. "Towards reliable charge-mobility benchmark measurements for organic semiconductors". In: *Organic Electronics: physics, materials, applications* 15.6 (2014), pp. 1263–1272. ISSN: 15661199. DOI: 10.1016/j.orgel.2014.02.008.

[130] Ammar A. Khan et al. "Homologous binary mixtures and improved hole conduction of self-assembled discotic liquid crystals". In: *Organic Electronics: physics, materials, applications* 36 (2016), pp. 35–44. ISSN: 15661199. DOI: 10.1016/j.orgel.2016.05.027.

[131] Steve Albrecht et al. "On the Field Dependence of Free Charge Carrier Generation and Recombination of PCPDTBT/PC70BM: Influence of Solvent Additives". In: *The Journal of Physical Chemistry Letters* 3.5 (2012), pp. 640–645. ISSN: 1948-7185. DOI: dx.doi.org/10.1021/jz3000849.

[132] Yulan Huang et al. "Controllable thin-film morphology and structure for 2,7-dioctyl[1]benzothieno[3,2-b][1]benzothiophene (C8BTBT) based organic field-effect transistors". In: *Organic Electronics: physics, materials, applications* 36.March (2016), pp. 73–81. ISSN: 15661199. DOI: 10.1016/j.orgel.2016.05.019.

[133] Gerald Dicker et al. "Electrodeless time-resolved microwave conductivity study of charge-carrier photogeneration in regioregular poly(3-hexylthiophene) thin films".

In: *Physical Review B - Condensed Matter and Materials Physics* 70.4 (2004), pp. 1–8. ISSN: 01631829. DOI: 10.1103/PhysRevB.70.045203.

[134] Christian Ruzié et al. "Design, synthesis, chemical stability, packing, cyclic voltammetry, ionisation potential, and charge transport of [1]benzothieno[3,2-b][1]benzothiophene derivatives". In: *Journal of Materials Chemistry C* 4.22 (2016), pp. 4863–4879. ISSN: 2050-7526. DOI: 10.1039/C6TC01409G.

[135] Ji Eun Park, Sunga Song, and Ik Soo Shin. "Voltammetric investigation for electron-transfer characteristics of organic semiconductors". In: *International Journal of Electrochemical Science* 11.7 (2016), pp. 5891–5899. ISSN: 14523981. DOI: 10.20964/2016.07.14.

[136] M. Lessel et al. "Self-assembled silane monolayers: An efficient step-by-step recipe for high-quality, low energy surfaces". In: *Surface and Interface Analysis* 47.5 (2015), pp. 557–564. ISSN: 10969918. DOI: 10.1002/sia.5729. arXiv: 1212.0998.

Chapter 3

Composite materials based on 2-dodecyloxy-6-(4-octylphenyl)-naphthalene

3.1 General introduction

This chapter describes physical properties of various composites based on 2-dodecyloxy-6-(4-octylphenyl)- naphthalene (**8-PNP-O12**). This molecule is a well-known liquid crystalline semiconductor which exhibits two smectic mesophases on moderate temperatures [74].

First, the composite materials which contain a dispersed polymer network are studied. We have thoroughly investigated the influence of reactive mesogen on thermophysical as well as alignment properties of the **8-PNP-O12**, followed by characterization of hole transport in the mesophase. This section also serves as an introduction to the **8-PNP-O12** material and prepares the reader for the upcoming sections.

The next stage was the study of effects of chemical p-doping on the structural properties and charge transport performance. Extensive preliminary work was performed by employing *ab initio* (*Gaussian 16*, Rev. A03 software[137]) calculations in order to anticipate the charge transfer between the host and the dopant and to further correlate it with experimental data obtained by spectroscopic techniques. We have prepared a comprehensive range of dispersion concentrations, and studied their charge transporting properties in the mesophase by TOF technique. The next step of this section was to find favorable conditions to prepare a thin film of doped **8-PNP-O12**, which has allowed us to prepare a field effect transistor.

The final stage is the investigation of a polymer stabilized p-doped system: we have investigated the feasibility of composites, where a reactive mesogen undergoes a light-activated polymerization in a presence of doping impurity. This section concludes the research effort carried out on **8-PNP-O12** material.

3.2 Cross-linked "gel"-type composites

Composites of smectic OSC and nematic reactive mesogen undergo UV-activated polymerization in Sm_B phase which yields the formation of chemical gels. The structure of resulting composites is characterized by means of optical and electronic microscopies. The influence of polymer network on hole transport in smectic OSC is investigated by the time of flight charge carrier mobility measurements. This subsection summarizes the studies conducted on the composite materials.

3.2.1 Materials

One of the most widely known LC OSC is the 2-dodecyloxy-6-(4-octylphenyl)-naphthalene (**8-PNP-O12**, Figure 3.1) which exhibits two mesophases: Smectic B (Sm_B, 66 °C to 101 °C) in which the molecules are organized in layered structure and possess pronounced intra-layer short range scale in a hexagonal motive (see Section 1.3.3) and Smectic A (Sm_A, 101 °C to 121 °C) mesophase which occurs on higher temperature and has similar layered organization, but the short-range hexagonal pattern is no longer relevant for this mesophase, the molecules are organized more randomly within the same smectic layer (see Section 1.3.3). This difference of intermolecular order within the layers is well reflected by the order of charge carrier mobility μ in the two smectic phases: μ of the order of $1 \times 10^{-3}\,\mathrm{cm}^2/(\mathrm{V\,s})$ in the Sm_B mesophase whereas it is almost one order lower in the Sm_A mesophase. This molecule can be regarded as a model for rod-like LC OSCs [74, 112, 138, 75, 78, 117]. It was employed as the host OSC material in the current study and was used as supplied by SYNTHON Chemicals GmbH & Co. KG (Chemie Park Bitterfeld Wolfen, Germany), 99% purity.

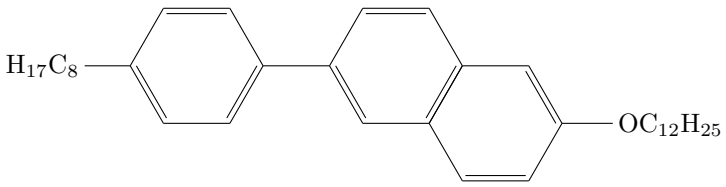

Figure 3.1 – Molecular structure of 2-dodecyloxy-6-(4-octylphenyl)- naphthalene (**8-PNP-O12**). The phase sequence on cooling: $Cr \xleftarrow{66\,^\circ\mathrm{C}} Sm_B \xleftarrow{101\,^\circ\mathrm{C}} Sm_A \xleftarrow{121\,^\circ\mathrm{C}} Iso.$

A diacrylate reactive mesogen (**RM82**, Figure 3.2, a) is commercially available from Merck as RM82. The molecule of 2-methyl-1,4-phenylene bis(4-((6-(acryloyloxy)hexyl)oxy)benzoate)

Figure 3.2 – Molecular structure of the components of reactive mesogene precursor mixture: monomer (a) 2-methyl-1,4-phenylene bis(4-((6-(acryloyloxy)hexyl)oxy)benzoate) (**RM82**), photoinitiator (b) 2-benzyl-2-(dimethylamino)-1-[4-(4-morpholinyl)phenyl]-1-butanone (**Irgacure 369**) and thermal stabilizer (c) 2,6-di-tert-butyl-4-methylphenol (**BHT**).

[139] contains acrylate functional groups and has a nematic (N) mesophase in a range from 86 °C to 116 °C ($Cr \xleftarrow{86\,°C} N \xleftarrow{116\,°C} Iso$).

In order to make **RM82** UV-cross-linkable, free-radical photoinitiator 2-benzyl-2-(dimethylamino)-1-[4-(4-morpholinyl)phenyl]-1-butanone (**Irgacure 369**, Figure 3.2, b) (Ciba) and thermal stabilizer 2,6-di-tert-butyl-4-methylphenol (**BHT**, Figure 3.2, c) were added to pure **RM82** by 0.5% and 1% of total RM mixture mass, respectively.

The photoinitiator has a pronounced absorption in UV part of optical spectra (Figure 3.3), which has enabled the use of a UV LED with emission wavelength of 365 nm for UV-initiated polymerization process.

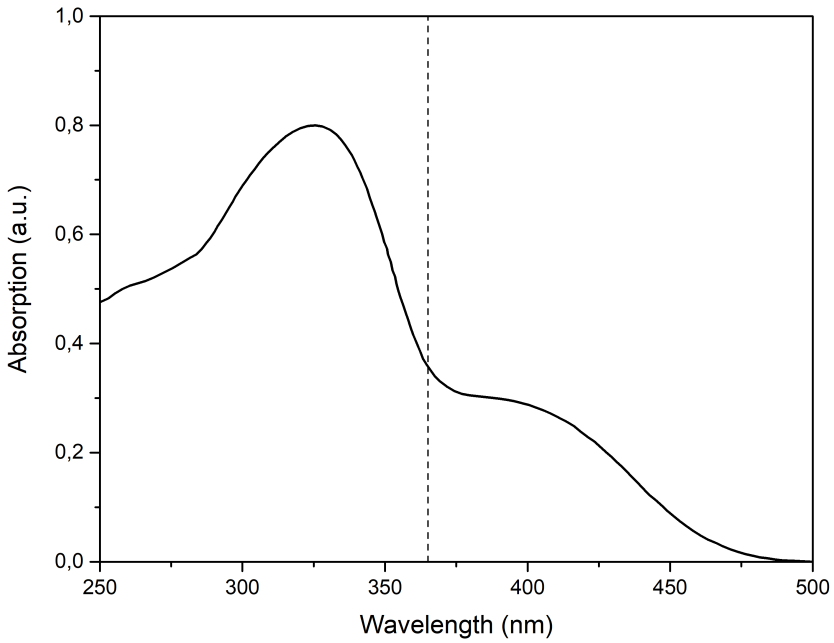

Figure 3.3 – Optical absorption spectrum of the **Irgacure 369** in acetonitrile. Vertical black dashed line corresponds to the wavelength of emission peak of the LED used for curing.

3.2.2 Sample preparation

Optical microscopy and hole mobility measurements were carried out in a prefabricated commercial liquid crystal cells (predeposited ITO electrodes, homogeneous alignment layer and 5 µm spacer by AWAT, Poland).

The sample preparation procedure was as follows: first, the precursor mixtures (LC OSC and reactive mesogene) were prepared by dissolving the components for a desired

weight concentrations in the chloroform and further magnetic stirring of the mixture in dark glass vial for one hour at 50 °C. After the stirring has ensured the sample homogeneity, the vials were kept open in dark area for 24 hours to attain complete solvent evaporation. Sample in dry powder form was placed on the edge of the cell. It was then was placed in a light tight hotstage, and was further heated to the isotropic temperature of the composite (about 130 °C), where it was maintained for about 20 min. This procedure has made possible to avoid curing at undesirable temperature due to significant sensibility of the **RM82** precursor mixture at elevated temperatures. After the cell has been filled by capillary force, the hotstage was slowly (0.5 °C/min) cooled to 90 °C which would correspond to the Sm_B phase of the composite. After the temperature was stabilized, the curing LED was introduced. Curing was performed at 1 mW/cm^2 power density of 365 nm wavelength radiation for 15 min.

3.2.3 Thermophysical, mesogenic and structural properties

Four composites have been prepared with the following mass fraction of **RM82** in the mixture: 1% (**g1**), 3% (**g2**), 5% (**g3**) and 10% (**g4**). The DSC plots for cooling of the samples of prepared composites exhibit (Figure 3.4) some shift in the phase transitions to a lower temperature, as compared with that of pure **8-PNP-O12**. This shift is merely explained by the mixture effect, and demonstrates that **RM82** and **8-PNP-O12** molecules are miscible for the here studied concentrations range.

Adding **RM82** to **8-PNP-O12** does not alter the texture of the host material: the mesogenic behavior of **8-PNP-O12** is preserved. The observed shift in phase transitions temperatures however is only valid for the precursor mixtures. Once the mixtures undergo polymerization, the obtained composites demonstrate the phase stability equivalent to the pure **8-PNP-O12**, which is going to be addressed further.

Texture of the mesophases was observed under polarizing optical microscope. Figure 3.5 assembles the texture of the cross-linked composites in Sm_B, Sm_A and I phases. One can notice that the similar focal conic pattern, which is characteristic for the smectic phase, is present in the corresponding smectic states of the prepared composites. It is also of interest to underline that the transition temperatures for cross-linked samples are almost similar to those of the pure **8-PNP-O12**. It is proposed that the polymer network becomes micro-phase-separated from the host **8-PNP-O12**, and it no longer interferes with the stability of the mesophases of host material.

The texture of the composites demonstrates a noticeable change in alignment: the smectic domains seem to be oriented in a preferred direction, as compared to the pure

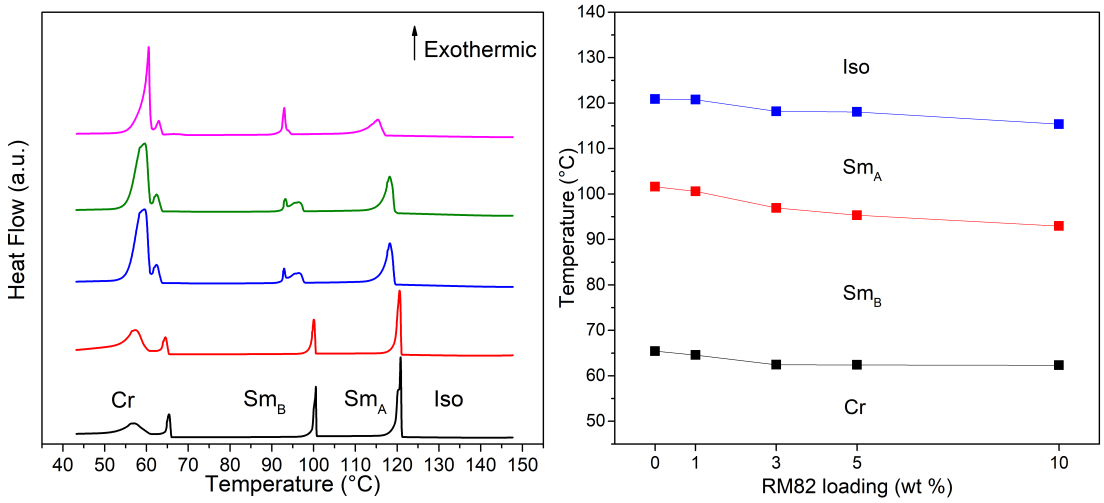

(a) (b)

Figure 3.4 – (a) DSC plots for pure **8-PNP-O12** (black), **g1** (red), **g2** (blue), **g3** (green) and **g4** (pink) composites obtained with 10 °C/min cooling program. (b) Phase transition temperatures of precursor composites as a function of **RM82** concentration: Cr to Sm_B (black squares), Sm_B to Sm_A (red squares) and Sm_A to I (blue squares).

8-PNP-O12, where these domains are distributed randomly. This can be explained by the nematogenic nature of **RM82**: the directors in the nematic phase are aligned unidirectionally on surfaces with homogeneous anchoring. The good compatibility between **RM82** and **8-PNP-O12** allows the nematic mesogene to "lead" otherwise difficult-to-align smectic host material, creating the observed alignment effect. A similar system based on the same host material and a conventional (non-mesogenic) cross-linker was studied by Hanna et al. [140, 141] and it does not exhibit any alignment effect, thus allowing to conclude that it solely the properties of **RM82** which are responsible for the alignment and not the degradation of the smectic order. Moreover, the studies carried out with the same reactive mesogene, but a completely different host material with a mesophase of discotic nature [142] demonstrates similar strong effects on long-scale order. These facts reveal that despite the relatively low order of the nematogenic **RM82**, it is however capable to significantly influence the long range order of much higher ordered mesophases.

The transition from the Sm_A mesophase to the isotropic liquid phase allows to observe the polymeric network, which is formed *in situ* during the cross-linking process (right column of the Figure 3.5). Its thermal stability signifies that the curing under applied

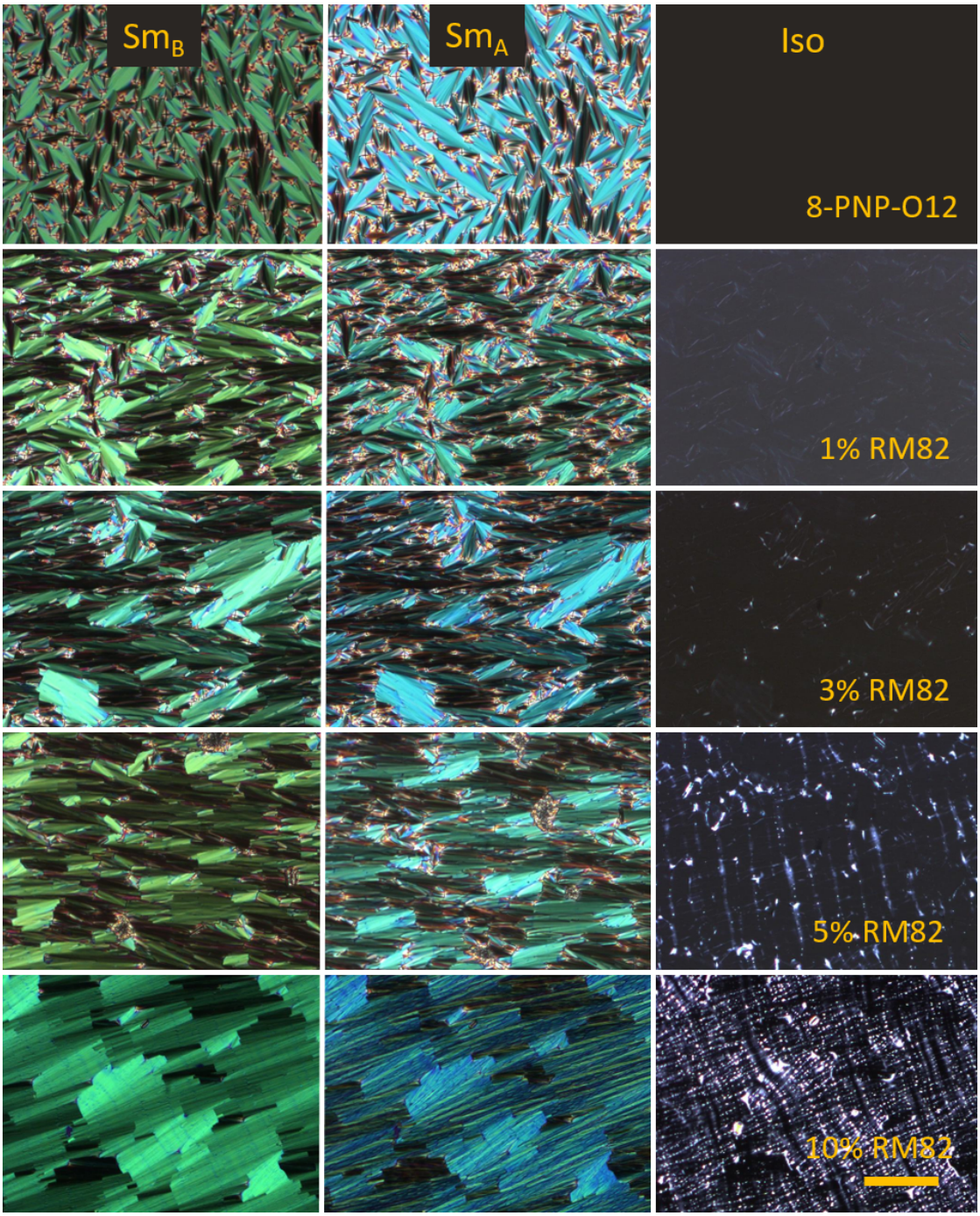

Figure 3.5 – Sample texture under crossed analyzer-polarizer: for pure **8-PNP-O12** and cross-linked mixtures **g1**, **g2**, **g3** and **g4** (in Sm_B at 85 °C, Sm_A mesophase at 115 °C and isotropic phase at 130 °C). Scale bar represents 100 µm.

conditions was successful. The density of polymer network increases with the weight fraction of **RM82**. It is also possible to notice that the network looks like a very close imprint of the texture observed in the mesophase, which could be regarded as a sign of intimate contact between this network and host material. The reverse transition to the Sm_A mesophase from the liquid phase, the resulting texture looks very similar to that before the melting to the liquid phase. The network acts as a "skeleton" for the mesophase, it stabilizes the liquid crystal order and preserves the alignment of the samples upon heating-cooling cycles.

The optically observed polymer network demands a closer structure inspection. Another set of "sacrificial" cells was prepared for SEM analysis in order to replicate the anchoring conditions which lead to the previously observed alignment effects. The prepared cells were then opened, and the host **8-PNP-O12** was washed out several times with acetone. The substrates (one "face" of the cell) were dried in the oven to ensure complete evaporation of the solvent (to prevent the swelling of polymer) prior to loading in the SEM.

SEM captures are assembled in Figure 3.6. Higher magnification reveals that this network is in fact composed of fiber-like shapes, which seem to follow the imprint of a smectic domain. The density of the observed network is in good agreement with the content of **RM82**. However, it should be underlined that due to the destructive method of sample preparation (the sample is cross-linked *in situ* while confined between two cell faces, which are further forced apart, thus tearing the sample in process), the density of an intact sample is going to be higher.

The sample of **g2** exhibits some round shaped inclusions, which could be assigned as some signs of aggregation during the polymerization process, since the sample of **g3** demonstrates an even higher content of these aggregates. This leads to a conclusion that despite seemingly good aligning properties of the **RM82** and absence of any visible separation under POM, the host **8-PNP-O12** is unable to accommodate high quantity of the monomer.

Figure 3.7 contains a higher magnification SEM image of **g2**, which allows us to gain insight of the fibrillar nature of the polymer network. As previously demonstrated, the network consists of fibers of about one micron diameter (insets of Figure 3.6, b and c), which are in turn composed of smaller fibers, as demonstrated by the inset of the Figure 3.7 on nanometric scale. Taking into account the strength of the optically observed aligning effects, it is possible to conclude that the host **8-PNP-O12** is densely inter-penetrated by the **RM82** fibers. This observation is in contrast with the system based on discotic host OSC (2,3,6,7,10,11 - hexapentyloxytriphenylene, HAT-5) [142], where the polymer

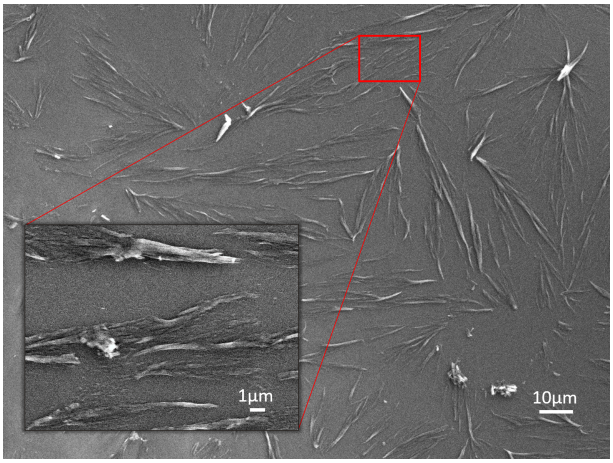

(a)

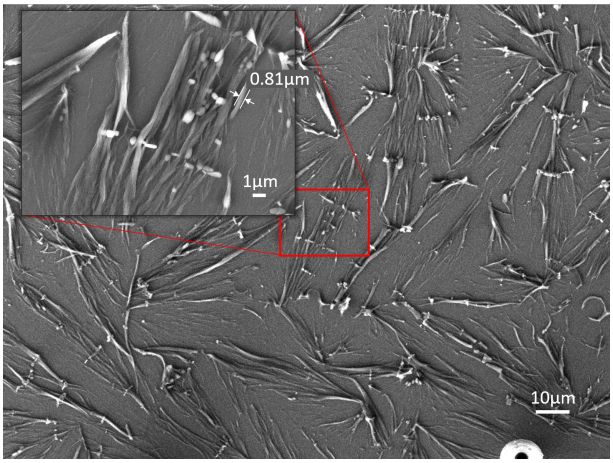

(b)

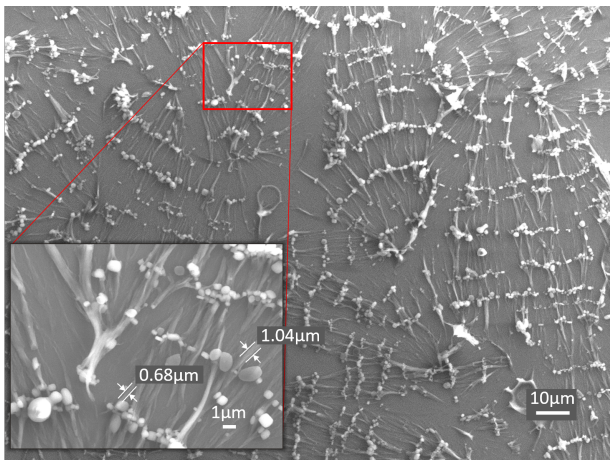

(c)

Figure 3.6 – SEM images of the polymer backbone: (a) **g1**, (b) **g2** and (c) **g3**.

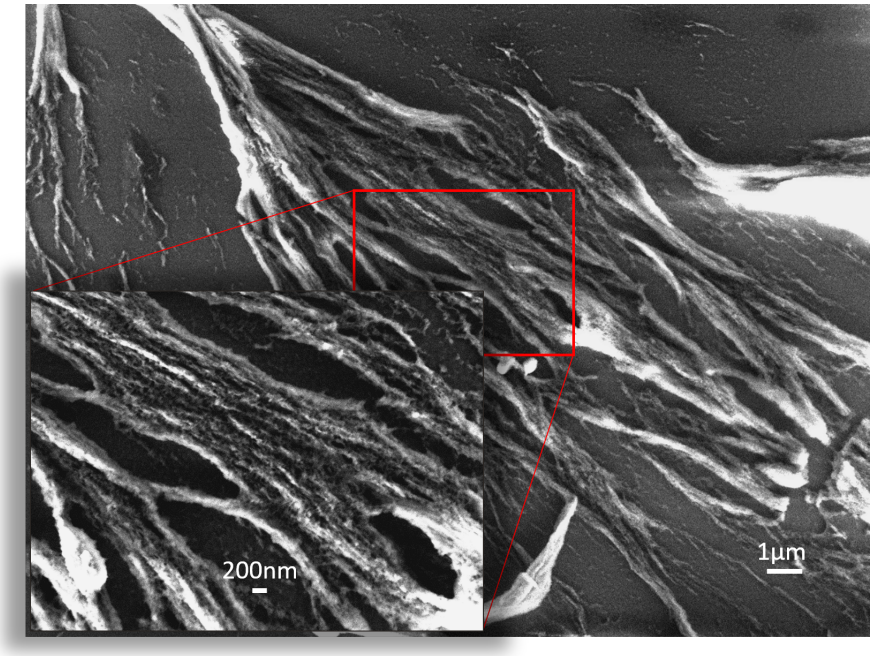

Figure 3.7 – High magnification SEM image of the polymer backbone of **g2**.

structures comprised of the same **RM82** tended to form sponge-like porous network.

3.2.4 Charge transporting properties in the mesophase

Hole transporting properties were studied with the time-of-flight technique previously described in the Chapter 2. Measurements were performed for the range of applied electric field ,E, from 20 kV/cm to 44 kV/cm with a step of 4 kV/cm at Sm_B mesophase and from 32 kV/cm to 60 kV/cm with the same step. Higher values of electric field are necessary to be applied in the Sm_A mesophase in order to obtain a reasonable signal-to-noise ratio due to the lower carrier mobility intrinsic to this mesophase. Homogeneous alignment sample cells with the spacer thickness d=5 µm were used for these measurements.

Figures 3.8 and 3.9 demonstrate the dependency of the calculated hole velocity ($v = \frac{d}{\tau_{tr}}$). The distribution of the calculated values is found to be linear, which means that the hole mobility is field-independent for the range of utilized electric fields. This behavior is in good agreement with the results previously reported for the **8-PNP-O12** and is not uncommon for this class of materials. The composites exhibit the same characteristic as the pure **8-PNP-O12**: linear distribution of the hole velocity, but with smaller slope allows to suggest lower hole mobility for these samples. The data for hole mobility of **g4**

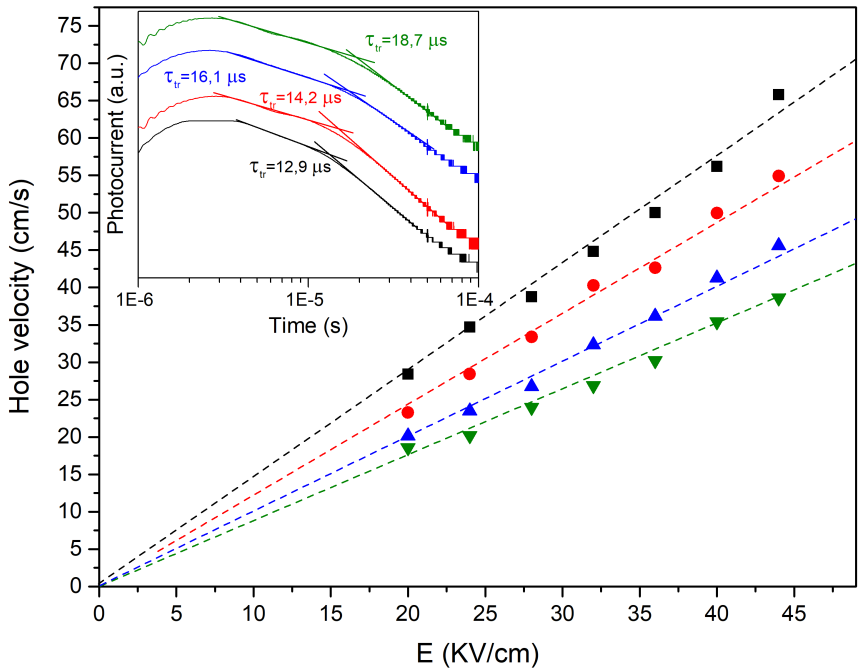

Figure 3.8 – Plot of the hole velocity as a function of applied electric field for pure **8-PNP-O12** (black squares), **g1** (red circles), **g2** (blue triangles) and **g3** (green triangles) in Sm_B mesophase at 85 °C. Inset: Transient photocurrent plots for pure **8-PNP-O12** (black), **g1** (red), **g2** (blue) and **g3** (green) in Sm_B mesophase at 28 kV/cm and 85 °C.

sample in the Sm_B mesophase is missing due to the dispersive photocurrent profile, thus making it impossible to extract the transit time τ_{tr}.

Transient photocurrent plots are grouped in the insets of the Figures 3.8 and 3.9 (sharp spike at 50 µs is related to measurement setup artifact). It could be noticed that the profile of photocurrent decay for composites remains unchanged when compared to that of the pure **8-PNP-O12**.

This demonstrates that the polymer network does not contribute to significant trapping of the photo-generated holes or impede their withdrawal at electrode interface [75]: the transport mechanism of the pure **8-PNP-O12** is preserved for the composites.

The influence of the polymer network on the hole mobility is illustrated by the Figure 3.10. It is clear that the polymeric network has somewhat negative effect on the hole mobility and the magnitude of this effect is depends on the order of mesophase. As the Figure 3.10 (a) suggests, the hole mobility drops for about 15% upon adding 1% of the **RM82**, and then stays almost invariable for higher concentrations of **RM82**. However,

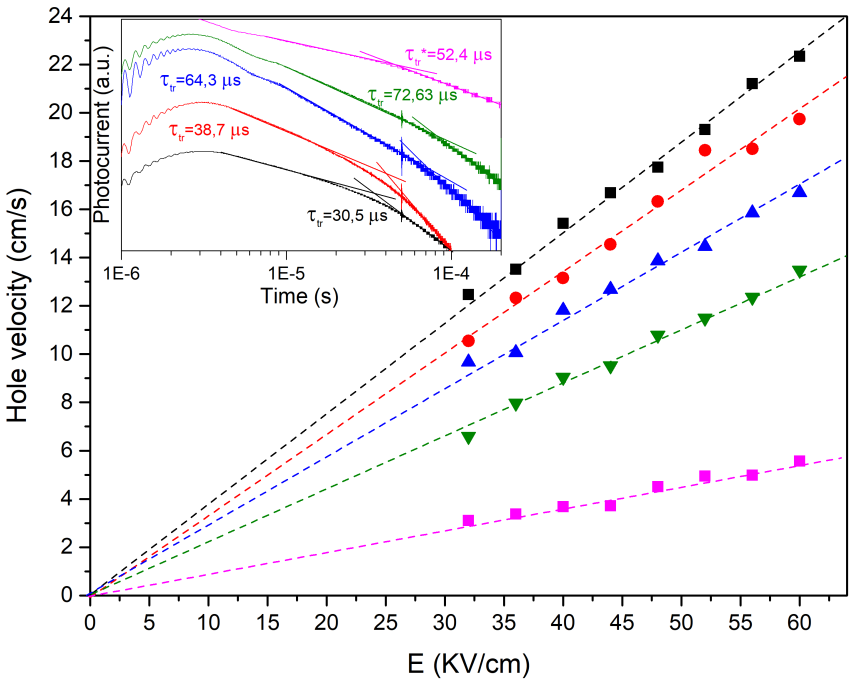

Figure 3.9 – Plot of the hole velocity as a function of applied electric field for pure **8-PNP-O12** (black squares), **g1** (red circles), **g2** (blue triangles), **g3** (green triangles) and **g4** (magenta squares) in Sm_A mesophase at 115 °C. Inset: Transient photocurrent plots for pure **8-PNP-O12** (black), **g1** (red), **g2** (blue), **g3** (green) and **g4** (magenta) in Sm_A mesophase at 40 kV/cm (80 kV/cm for the **g4**, marked with asterisk) and 115 °C.

in the Sm_A mesophase the mobility degrades much more rapidly and proportionally to the density of the polymeric network, demonstrating almost linear behavior.

We may propose that polymer network is able to introduce some trap states for charge carriers in the bulk of the composite. It is of interest ot compare these composites with the system of the same **RM82** and the discotic OSC (HAT-5) [142], mentioned previously. Discotic LCs are notorious for having poor compatibility with calamitic materials, which results on a phase separation on a higher scale (i.e. the host mesophase is less permeable to the polymeric network, thus making it less possible to interfere with its short range positional order). That system exhibited enhanced mobility with a similar-looking alignment effect, showing a clear positive contribution of **RM82** network [142]. In the case of **8-PNP-O12** as a host material, the compatibility between the two components of the precursor mixture is higher, which results in a significant penetration of the smectic domains of the host material by the polymer, which negates the positive

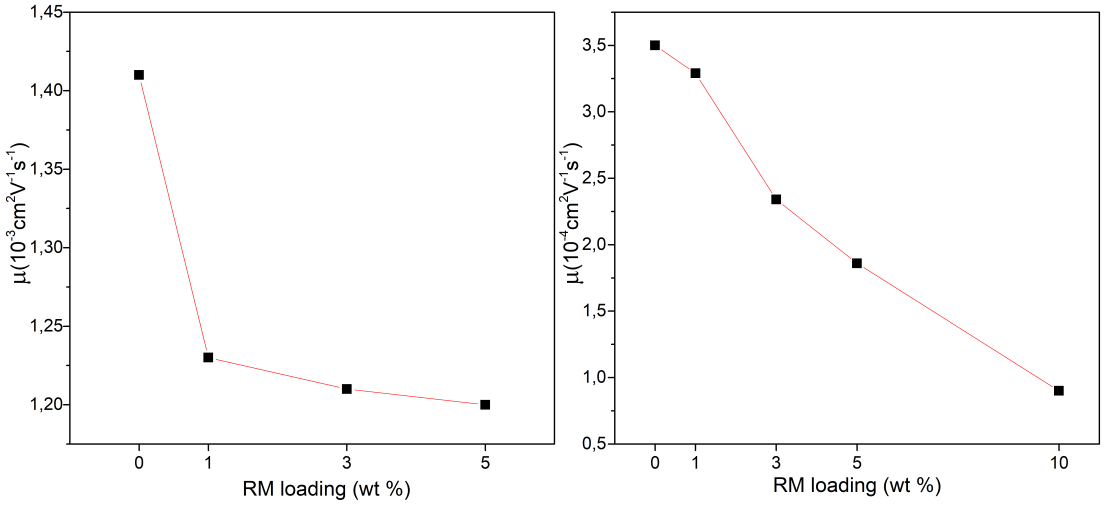

(a) (b)

Figure 3.10 – Plots of the hole mobility as a function of **RM82** content in Sm_B mesophase at 85 °C (a) and Sm_A mesophase at 115 °C (b).

effects of the long-range alignment.

The dependency of hole mobility on the temperature is plotted in the Figure 3.11. This plot demonstrates that the charge carrier mobility does not depend on temperature in a range of single mesophase. One can also notice that the transition temperatures of the composites closely resemble those of the pure **8-PNP-O12**. It is found that the pure **8-PNP-O12** and composites have comparable behavior: hole mobility is almost invariable within the limits of the mesophase, which is commonly seen in the LC OSCs. The polymeric network does not disturb the thermodynamic nature of the charge transport. A similar cross-linked system studied earlier [112] shows signs of thermal activation of carrier mobility, which is related to the increased disorder (structural and energetic) in the system. Temperature increase helps to overcome potential barriers related to system disorder, which further results in mobility increase [46]. For our system, it is possible to explain the stability of hole mobility by the improvement and stabilization of long range order of **8-PNP-O12** mesophase. All of the studied samples exhibit photocurrent in the isotropic phase, where the positive charge carrier mobility is found to be of the order of $1 \times 10^{-5}\,\mathrm{cm}^2/(\mathrm{V\,s})$, which is typically attributed to the ionic transport [143, 144].

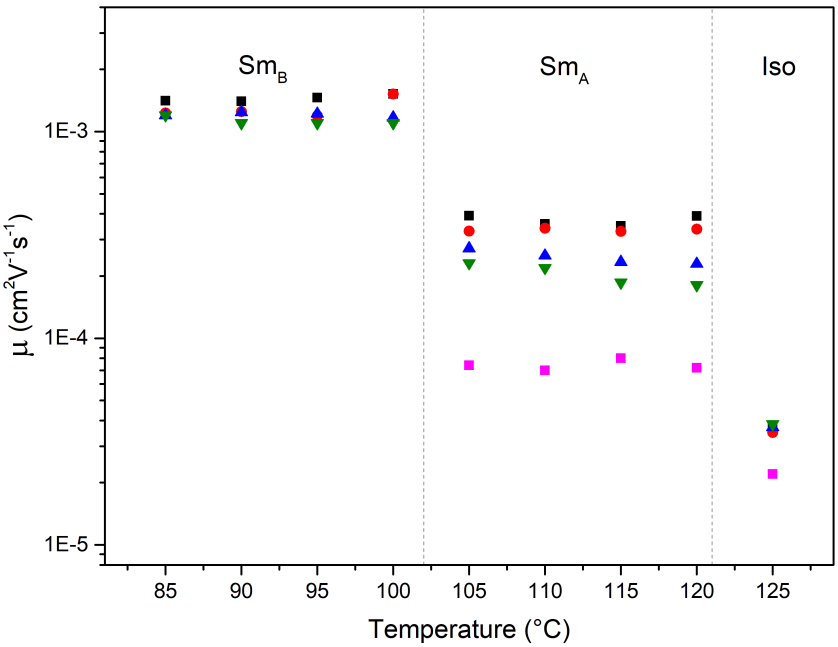

Figure 3.11 – Plot of the hole mobility as a function of temperature for pure **8-PNP-O12** (black squares), **g1** (red circles), **g2** (blue triangles), **g3** (green triangles) and **g4** (magenta squares). Vertical dashed lines indicate the transition temperatures of pure **8-PNP-O12**.

3.2.5 Conclusion

The preparation of LC OSC - photopolymer composites has resulted in the apparition of a novel material which combines the beneficial properties of its both components. The *in situ* cured polymer network shows a fibrillar structure, which allowed to evaluate its influence on the charge transporting properties of the studied composites. The experimental data was confronted with results obtained on discotic LC - photopolymer composite, which has made possible to estimate the role of compatibility of the components in their contribution to the electrical properties of resulting composites.

The studies conducted on pure **8-PNP-O12** and composites have revealed a remarkable alignment effect of **RM82** material in the conditions of homogeneous orientation of the composites. The hole mobility was found to be slightly lower for the composites than for pure **8-PNP-O12**, this result may be correlated with minor trapping induced by the guest polymeric structures. By taking into account the temperature stability of prepared composites in the presence of *in situ* formed polymeric network, we may conclude that it does not provide significant contribution to the structural and energetic disorder of the resulting composites.

3.3 P-doped LC OSC

We have decided to apply another approach in an attempt to enhance hole transport in the LC OSC, since the preparation of LC OSC/polymer composites did not result in an increase of hole mobility. We explore the molecular nature of doping in OSC by employing the aforementioned phenyl naphthalene-based liquid crystalline organic semiconductor as a model substance.

The main idea of this research effort revolves around the so-called charge transfer complex (**CTC**), which is initially presumed to be formed between the host organic semiconductor (**8-PNP-O12**) and the introduced doping impurity, an electron acceptor (**F_4TCNQ**). Firstly, the density functional theory (DFT) calculations were performed in order to predict the electronic properties of the **CTC**, which allowed us to anticipate its characteristic behavior, further uncovered by spectroscopy. The basic thermodynamic properties and the mesophase nature of resulting system has been investigated by means of differential scanning calorimetry, polarized optical microscopy and x-ray scattering. Optical and vibrational spectroscopies allowed us to estimate the amount of charge transfer for **CTC** and expose some properties which appear only in complexed stateand validate the geometry predicted by DFT.

These preliminary studies have enabled us to further investigate the influence of dopant introduction on the bulk hole mobility of **8-PNP-O12** and understand how the presence of **CTC** interacts with the hole transport in Smectic B and less ordered Smectic A mesophases. The results are confronted with local conductivity mapping via conductive atomic force microscopy.

3.3.1 Materials

For doping **8-PNP-O12**, a fluorinated derivative of tetracyanoquinodimethane (TCNQ), the 2,3,5,6-tetrafluoro-7,7,8,8-tetracyanoquinodimethane (**F_4TCNQ**, Figure 3.12) was used as the electron acceptor. This dopant was provided by Apollo Scientific (Bredbury, United Kingdom), 97% purity. The molecules from tetracyanoquinodimethane family are well-known for their relevance in the field of OSCs and have been previously used in discotic semiconducting liquid crystals [130] in an attempt to improve hole transport. Their effects on optoelectronic properties were also studied in nematic [145] and ferroelectric LCs [146].

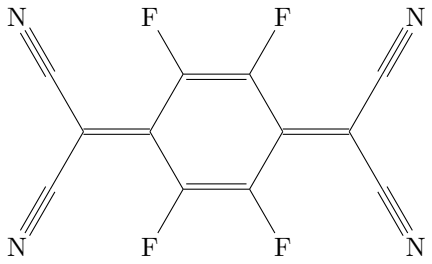

Figure 3.12 – Molecular structure of 2,3,5,6-tetrafluoro-7,7,8,8-tetracyanoquinodimethane (**F_4TCNQ**).

3.3.2 Spectroscopic tools for studying of charge transfer

As we have discussed in Chapter 1 (Section 1.2.4), both cases of charge transfer between the host and dopant (integral and partial charge transfer (ICT and PCT)) result in noticeable change of electronic configuration of the host OSC moiety. It is possible to observe such changes by conventional spectroscopic methods. Furthermore, by the means of *ab initio* calculations it is possible to predict the character of this charge transfer [45]. In our study, the experimental results obtained from spectroscopy are confronted to the values deduced from *ab initio* calculations. This comparison provides us the basis to validate the predicted geometry for the **CTC** and utilize it to explain its effect on the charge transporting properties.

Computational study

Geometries of pristine **8-PNP-O12**, **F_4TCNQ** and the **CTC** were firstly optimized by semi-empirical methods with further DFT optimisation on B3LYP/6-31++G(d,p) level with additional empirical dispersion corrections (GD2) for the **CTC**. This have proven itself to significantly enhance [147] the accuracy of systems which involve intermolecular charge transfer. Optimized geometry had zero imaginary frequencies.

The molecular orbital diagram for **CTC** and its isolated components (Figure 3.13) shows successful hybridisation of the HOMO of the **8-PNP-O12** and the LUMO of the **F_4TCNQ** into a novel *intra*molecular bonding orbital at −6.29 eV.

As a result of complex "bonding", the geometry of its components undergoes some noticeable change. **F_4TCNQ** molecule now exhibits some deviation of planarity (minor longitudinal torsion). For the **8-PNP-O12**, a quite significant point is the change of the dihedral angle between the phenyl and naphthalene moieties of **8-PNP-O12** molecule, which changes from 141.57 to 155.83°. This angle is of particular importance, since the planarity of molecule enhances the delocalization degree of electron density over the

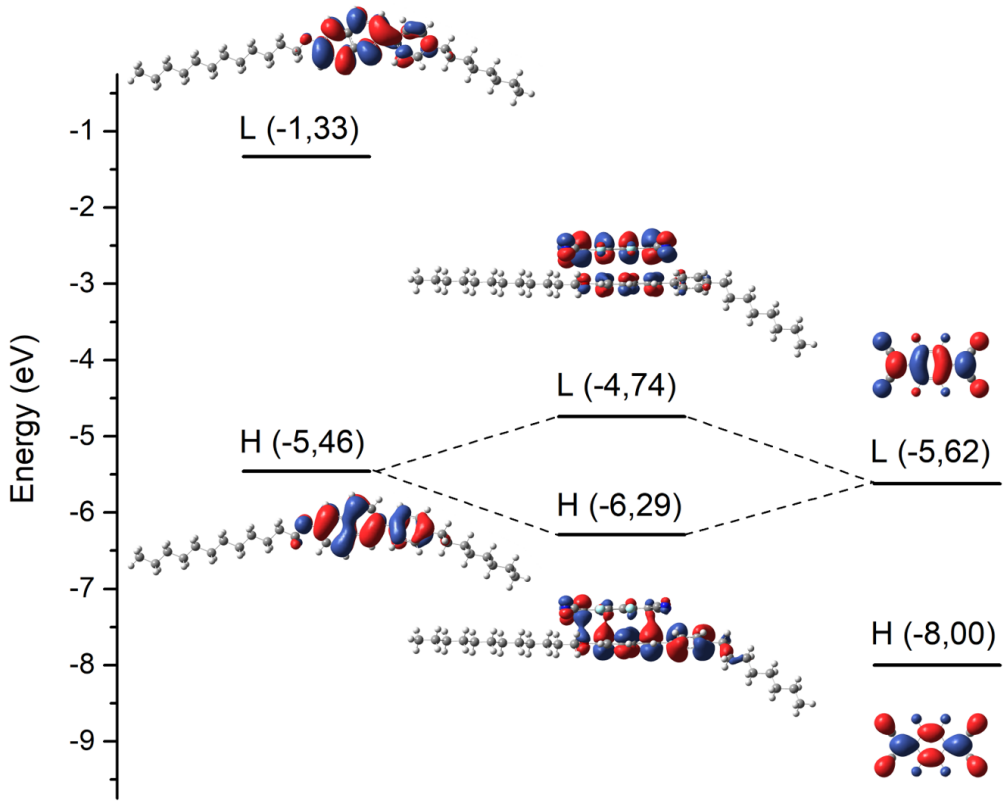

Figure 3.13 – Energy diagram of frontier molecular orbital levels for **CTC** and isolated molecules of **8-PNP-O12** and **F_4TCNQ**. MO energy levels of **CTC** and pristine substances are calculated on B3LYP/6-31++G(d,p) level.

π-conjugated core.

The top view on the optimized geometry (Figure 3.14) demonstrates good alignment of the quinoid ring of the **F_4TCNQ** with one of the naphthalene rings of **8-PNP-O12**, which enables the hybridisaton of frontier molecular orbitals. In order to better explore the relocation fo electron density in the **CTC**, we have assembled the lengths of chemical bonds for the isolated molecules of **8-PNP-O12** and **F_4TCNQ**, as well as their charged species (Figure 3.15). The bond lengths of quinoid ring and naphthalene in the **CTC** undergo expected change in the case of integral charge transfer through resonance stabilization. Quinoid system approaches aromaticity upon allocation of the transferred electron, which means that the length of bonds 6 and 7 of electron-deficient cycle become more similar to that of benzene ring, as well as the lateral double bond 5 becomes longer (Figure 3.15, b). The opposite is true for the aromatic system of the

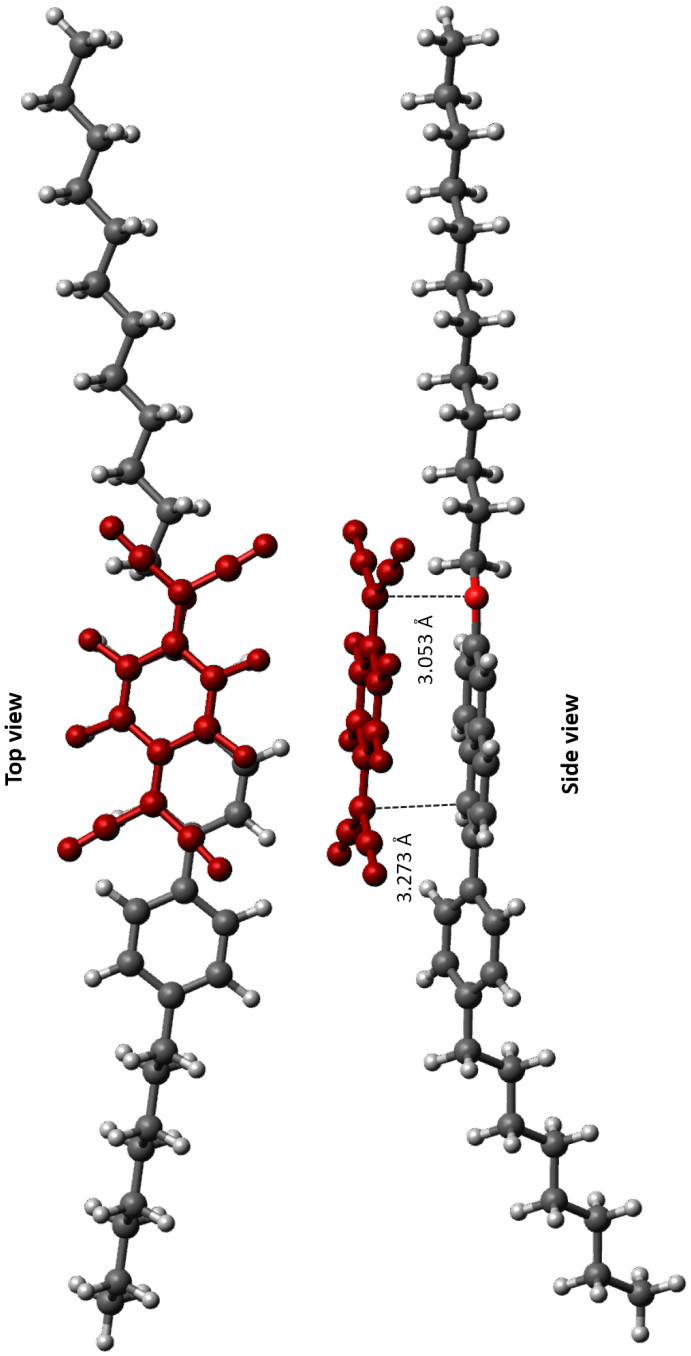

Figure 3.14 – Molecular structure of the (**CTC** of **8-PNP-O12** and $\mathbf{F_4TCNQ}$, geometry optimized on B3LYP-D/6-31++G(d,p) level.

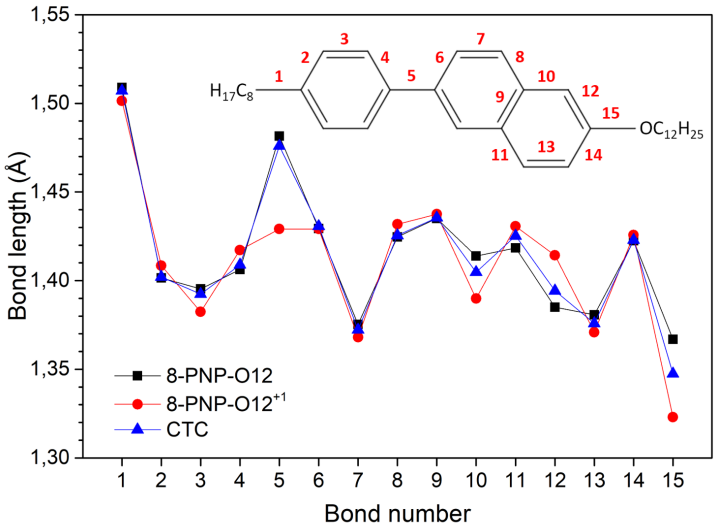

(a)

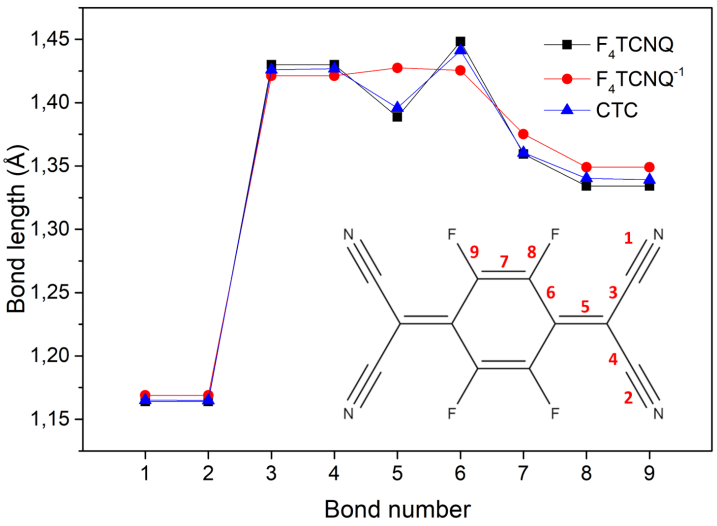

(b)

Figure 3.15 – Bond lengths calculated on B3LYP/6-31++G(d,p) level of theory for (a) the isolated neutral **8-PNP-O12**, the cation **8-PNP-O12**$^{+1}$ and the charge-transfer complex with **F$_4$TCNQ**; for (b) the isolated neutral **F$_4$TCNQ**, the anion **F$_4$TCNQ**$^{-1}$ and the charge-transfer complex with **8-PNP-O12** (**CTC**).

naphthalene: difference between bonds 10 to 13 increases, the same is true for bonds 2 to 4 in the phenyl moiety. The bond 5 between the two aromatic structures becomes shorter and approaches a C=C double bond (Figure 3.15, a). It is of interest to compare

this data with bond lengths obtained for **CTC**: it is clear that the chemical structure of its components lies in between the neutral and charged states, which suggests some relocation of electron density from the **8-PNP-O12** molecule to **F_4TCNQ**.

The geometry of neutral **8-PNP-O12** is not planar, since it has some noticeable torsion angle between phenyl and naphthalene parts. Due to this fact, the **F_4TCNQ** molecule is not able to align itself completely parallel to the aromatic system of **8-PNP-O12**, which results in the intermolecular distance between **8-PNP-O12** and **F_4TCNQ** to be found in a range between 3.273 and 3.053 Å (Figure 3.14, side view). This fact presumably contributes to the significant asymmetry (Figure 3.13) of the shape of the HOMO of **CTC** as compared to that of more planar donor substances [39].

The **CTC** is calculated to have a bandgap of about 1.55 eV (Figure 3.13). Thus, it is then expected for the **CTC** to exhibit optical absorption in near infrared (NIR) part of the spectrum. UV-Visible-NIR spectroscopy is a suitable tool to investigate the character of newly formed **CTC**, given the absence of any electron transitions for initial products [148, 39] in the NIR range.

3.3.3 Phase behavior, structural and optical properties

Five mixtures were prepared by mixing selected weight fraction of dopant of 0.1 (**c1**), 0.5 (**c2**), 1 (**c3**), 3 (**c4**), 5 (**c5**) %wt. with host material in chloroform solvent in glass vial at 50 °C for 1 hour. Vials then were left open for 24 hours under vent hood to ensure complete solvent evaporation.

As a first step, we have performed DSC over the whole sample sequence in order to ensure mesophase stability over its temperature range. The thermograms of DSC analysis for all studied concentrations are presented in Figure 3.16. Interestingly, the mixtures exhibit relatively minor changes in melting and clarification ($Sm_A \rightarrow Iso$) temperatures (Figure 3.17,b). Figure 3.17, (a) allows us to observe the transition temperature between Sm_A and Sm_B of the mixtures and compare it to pure **8-PNP-O12**. This transition is affected the most by the presence of **F_4TCNQ** and its temperature is inversely proportional to its concentration.

POM allowed us to observe the texture change as a function of temperature of mixtures (Figure 3.18). The presence of **F_4TCNQ** appears to have little effect on the texture of both Sm_B and Sm_A mesophases. The characteristic focal conic pattern is preserved for all mixtures and the size of liquid crystalline monodomains decreases as the **F_4TCNQ** content is increased. Thermodynamic data and optical observations demonstrate good overall compatibility between the **8-PNP-O12** and **F_4TCNQ** for the

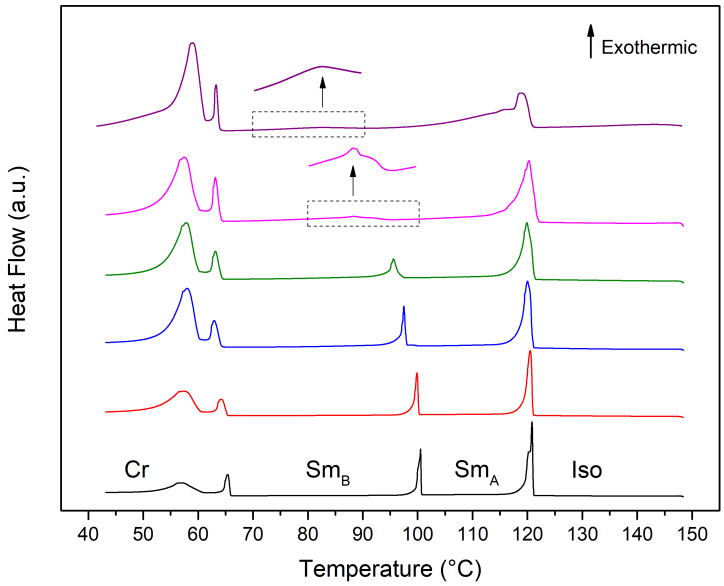

Figure 3.16 – DSC plots for pure **8-PNP-O12** (black), **c1** (red), **c2** (blue), **c3** (green), **c4** (pink) mixtures obtained with 10 °C/min cooling program and **c5** (purple) samples obtained with 5 °C/min cooling program. Dashed rectangles denote the scaled part of the thermogram.

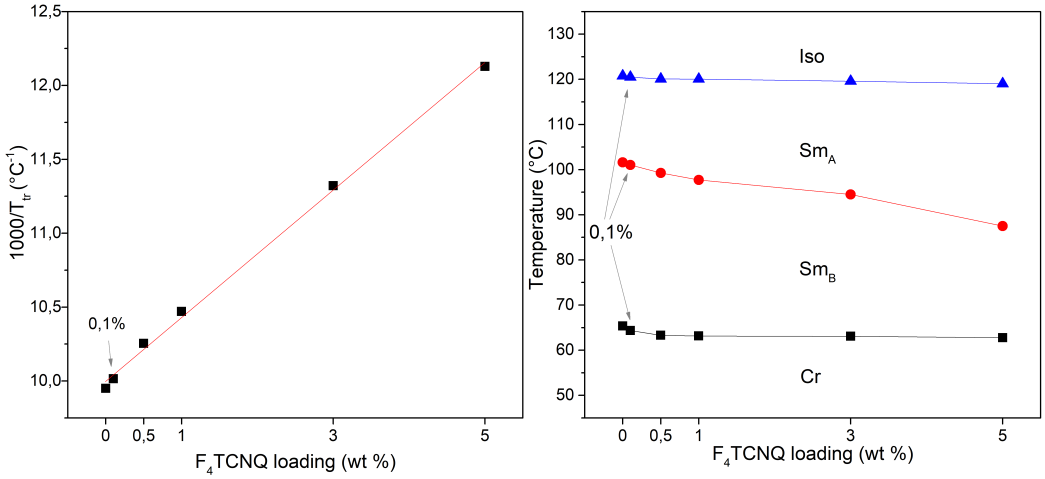

(a) (b)

Figure 3.17 – (a) Plot for inverse temperature (1000/T) of the Sm_A to Sm_B phase transition as a function of $\mathbf{F_4TCNQ}$ concentration. (b) Phase transition temperatures of **8-PNP-O12**/$\mathbf{F_4TCNQ}$ mixtures as a function of $\mathbf{F_4TCNQ}$ concentration: Cr to Sm_B (black squares), Sm_B to Sm_A (red circles) and Sm_A to I (blue triangles).

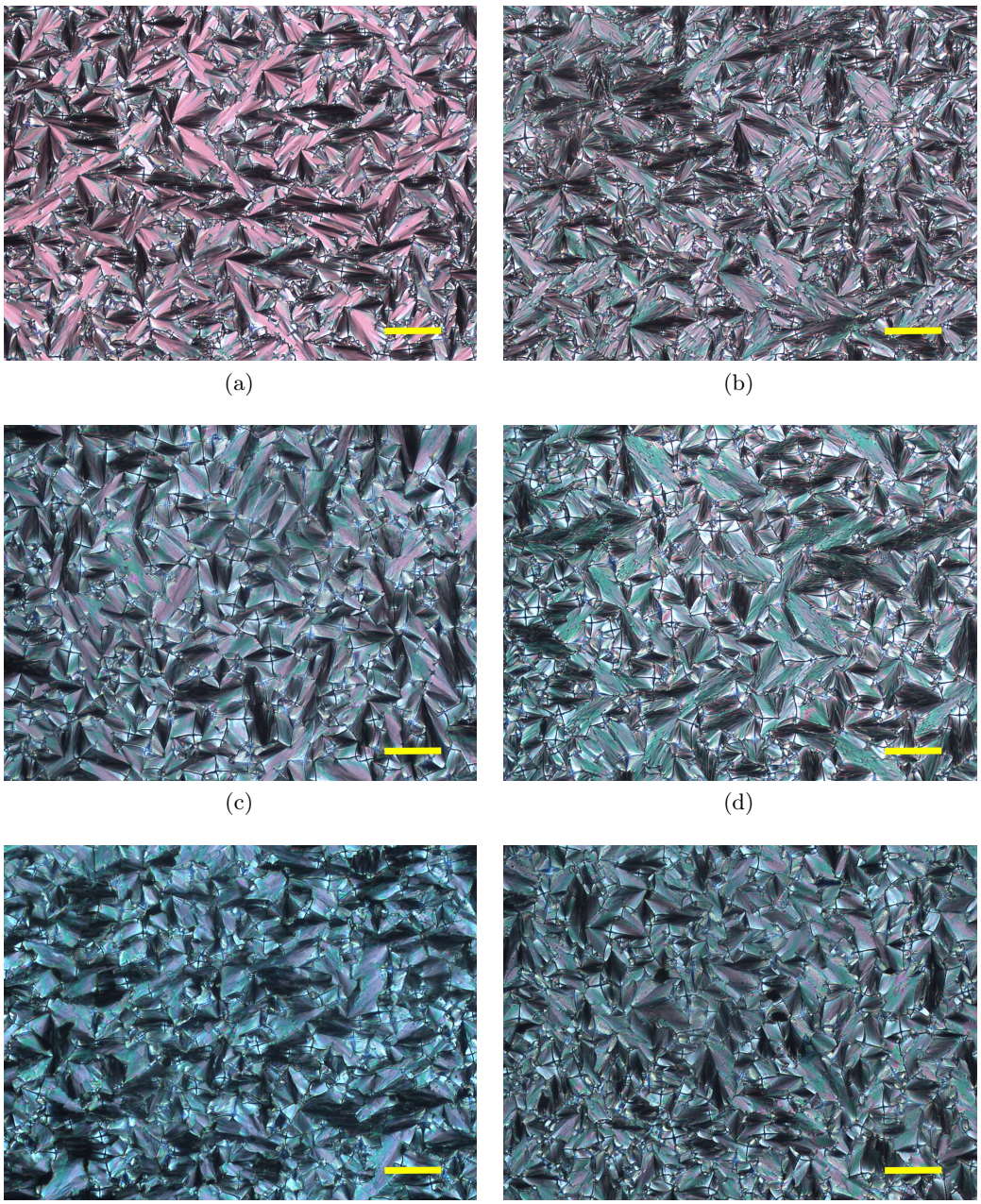

(a) (b) (c) (d) (e) (f)

Figure 3.18 – Sample texture under crossed analyzer-polarizer: for pure **8-PNP-O12** (in Sm_B (a) and Sm_A (b) mesophase), **c3** (in Sm_B (c) and Sm_A (d) mesophase), and **c5** (in Sm_B (e) and Sm_A (f) mesophase). Scale bar represents 100 µm.

here studied concentration range.

One can notice the color change, which becomes more apparent on higher concentrations (Figure 3.18, c - f). The color of the cells filled with the mixtures itself exhibits notable shift towards blue, though neither of initial products has this color. This coloration can be regarded as a result of interaction between **8-PNP-O12** and **F_4TCNQ**. To better explore this, we have performed UV-Vis-NIR optical spectroscopy, which is going to be covered in the corresponding section.

3.3.4 Structural studies by wide angle X-ray scattering (WAXS)

1D data extracted from wide-angle x-ray scattering images (inset of Figure 3.19, (a)) shows the characteristic peaks corresponding to the Sm_B and Sm_A mesophases: the first peak labeled b corresponds to the pseudo-hexagonal order inside of the smectic layer at about q=1.39/Å ($d = 4.56$ Å), and the second peak labeled a corresponds to the layered structure of smectic phases around q=0.17/Å ($d = 36.96$ Å). The latter appears in both

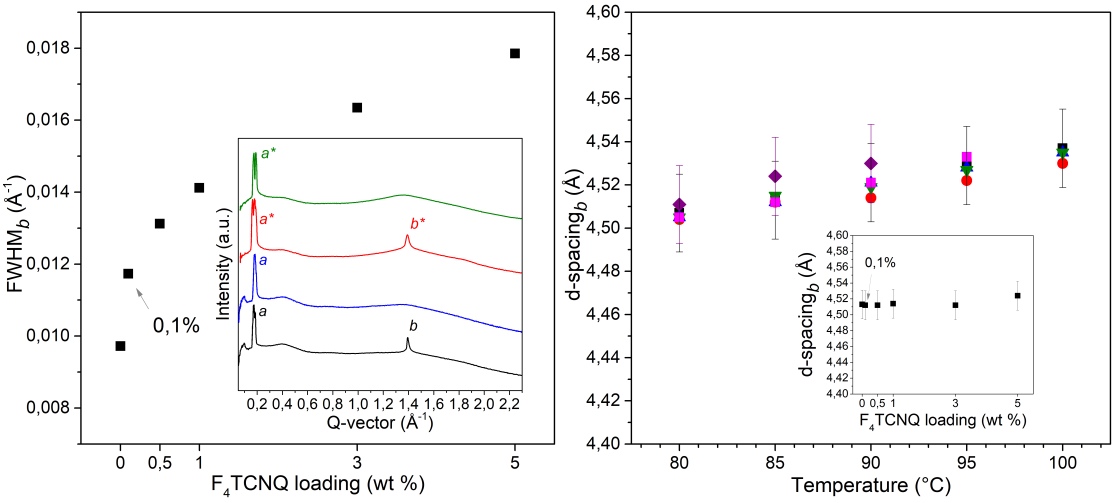

(a) (b)

Figure 3.19 – (a)Plot for FWHM of Sm_B in-layer order (peak b) as a function of **F_4TCNQ** content. Inset: 1D WAXS data for pure **8-PNP-O12** in Sm_B at 85 °C (black line), in Sm_A mesophase at 115 °C (blue line) and for **c5** in Sm_B at 85 °C (red line), in Sm_A at 115 °C (green line). (b) Pseudo-hexagonal order spacing in Sm_B as a function of temperature: black squares correspond to pure **8-PNP-O12** (black squares), **c1** (red circles), **c2** (blue triangles), **c3** (green triangles), **c4** (magenta squares) and **c5** (purple diamonds). Inset: intermolecular Sm_B spacing as a function of **F_4TCNQ** content at 85 °C.

the Sm_B and Sm_A mesophases. The calculated length of the **8-PNP-O12** molecule (35.58 Å) allows us to suggest mono-layer structure for these mesophases.

The in-layer positional order distance (peak b) in the Sm_B (Figure 3.19, (b)) feebly increases with temperature. However, it is found to be indifferent to the $\mathbf{F_4TCNQ}$ content (inset of Figure 3.19, (b)). We have also evaluated the values of the full width at half maximum (FWHM) of peak b, which correspond to the distribution of the intermolecular distance inside the Sm_B layer. Figure 3.19, (a) shows the dependency of FWHM of peak b as a function of $\mathbf{F_4TCNQ}$ content. It is found that FWHM increases with the concentration of $\mathbf{F_4TCNQ}$, which signifies that intermolecular distances are more widely distributed around the characteristic value of $d = 4.56$ Å in bulk of the sample. One can conclude that the presence of $\mathbf{F_4TCNQ}$ acts as an impurity leading to a decrease of the in-plane order within the Sm_B layer.

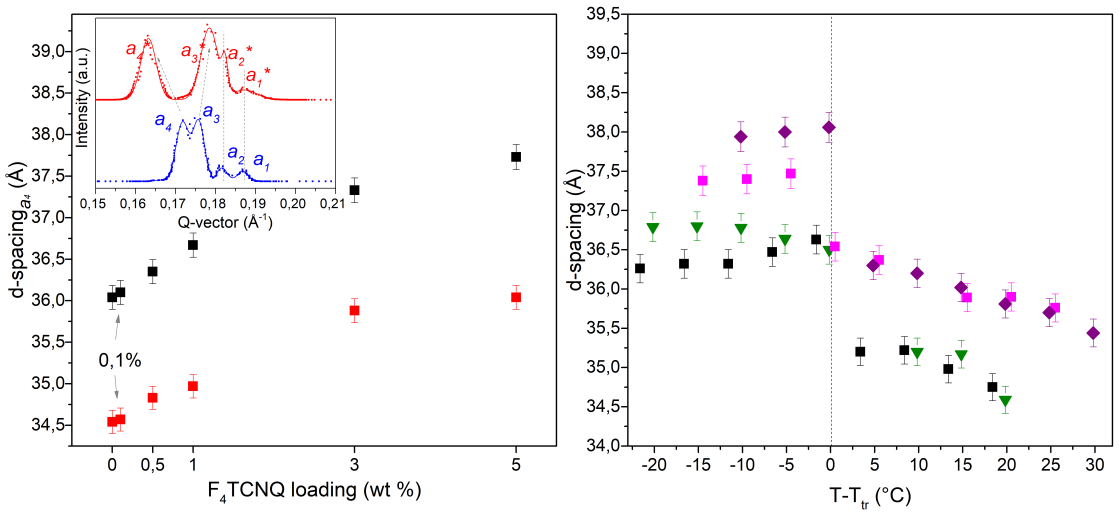

(a) (b)

Figure 3.20 – (a)Plot for smectic layer spacing as a function of $\mathbf{F_4TCNQ}$ content in Sm_B at 85 °C (black squares) and in Sm_A mesophase at 115 °C (red circles). Inset: small-angle part of 1D WAXS data at 85 °C (Sm_B) for pure **8-PNP-O12** (in blue, layer spacing $d = 36.12$ Å) and **c5** (in red, layer spacing $d = 37.73$ Å). (b) Smectic layer spacing as a function of relative temperature in respect to transition temperature (T_{tr}) from Sm_B to Sm_A mesophases. Black squares correspond to pure **8-PNP-O12**, green triangles – **c3**, magenta squares – **c4**, purple diamonds – **c5**, respectively.

The small-angle part of the data demonstrates a more complex picture of the 2D-layered structure of the smectic mesophases (inset of Figure 3.20, (a)). Multiple peaks appearing in the 1D data could be attributed to the "ripple" in plane of the smectic

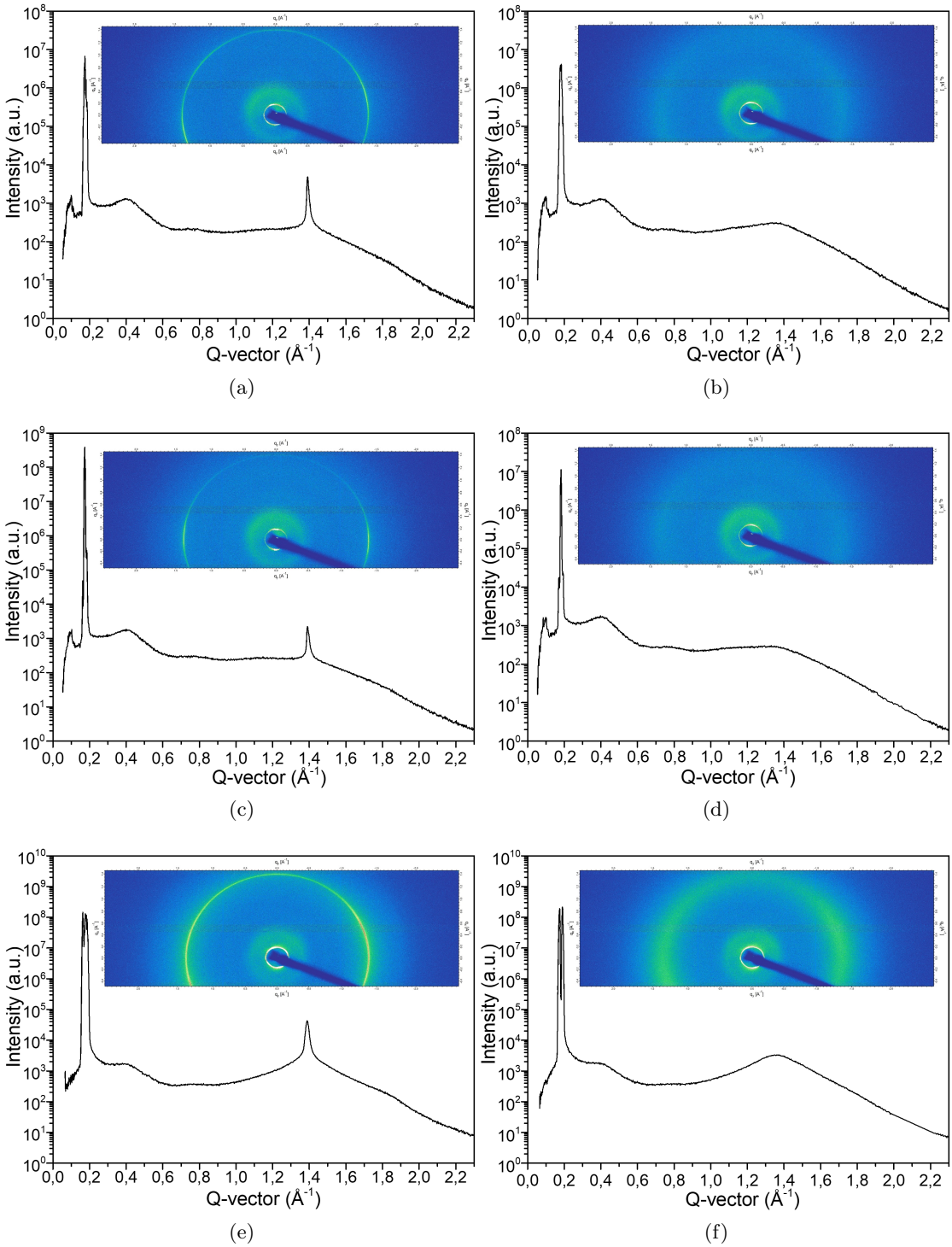

Figure 3.21 – 1D and 2D (detector image) WAXS data: for pure **8-PNP-O12** (in Sm_B (a) and Sm_A (b) mesophase), **c3** (in Sm_B (c) and Sm_A (d) mesophase), and **c5** (in Sm_B (e) and Sm_A (f) mesophase).

layer which results in a so-called modulated smectic mesophase [149]. Such structures are encountered in lyotropic [150] as well as thermotropic [151, 152] LCs and are not uncommon for assymetric molecules exhibiting longitudinal torsion [153]. The leftmost intense peaks (a_4 and a_4^*, inset of Figure 3.20, (a)) are attributed to the direction orthogonal to the layer plane and can be utilized to extract the smectic interlayer distance, when the satellite peaks (a_1-a_3 and a_1^*-a_3^*, inset of Figure 3.20) correspond to the layer modulation. Figure 3.20 allows us to compare the smectic layer separation distance for pure **8-PNP-O12** with the studied mixtures. The value of interlayer distance is found to be slightly greater than the **8-PNP-O12** molecule length in Sm_B, whereas it is found to be slightly smaller in Sm_A, indicating some interpenetration of layers. The layer spacing is found to be proportional to the content of **F_4TCNQ** (as for the intermolecular distance distribution, Figure 3.19), the layers become less condensed as the doping ratio increases, which promotes greater layer flexibility and subsequently decreases the overall order of the mixtures [154]. The observed behavior is encountered in all samples containing **F_4TCNQ** (Figure 3.21).

Optical spectroscopy

Since the **CTC** forms new supramolecular orbitals with their own energy levels and bandgap, there should exist dedicated electron transition energy levels. In theory, it should be possible to observe the signature of **CTC** in the UV/Vis spectrum. Previous works, conducted on P3HT [37, 39] have shown that it is indeed possible to observe the sharp peaks of fully ionized **F_4TCNQ$^-$** in case of ICT. P-doping of discotic LC HAT-6 with **F_4TCNQ** has also demonstrated distinctive absorption features in both crystalline phase and columnar mesophase [130].

Pure **8-PNP-O12** exhibits optical absorption in UV region, which is explained by its wide optical bandgap [75]. **F_4TCNQ** in turn, has it absorption onset at 2.6 eV, which leaves the remaining part of optical spectrum isolated and allows comfortable observation of their interaction product (**CTC**). The absorption spectra of initial products are assembled in Figure 3.22.

We have performed time-dependent DFT (TD-DFT) calculations in order to gain insight on the observed results. Observations of calculated optical absorption spectra (Figure 3.23) allows us to assign observed peaks in near infrared (peak at 1.45 eV with a sharp shoulder around 1.75 eV) and visible (two peaks at 2.27 eV and 2.57 eV) parts of spectrum (Figure 3.24) to the presence of **CTC** in the solution.

We are able to observe neutral **F_4TCNQ** signatures on higher concentrations, however

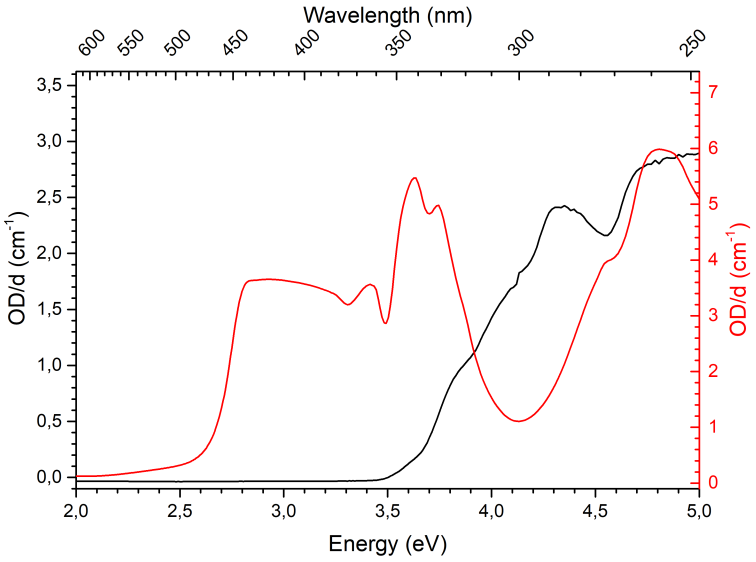

Figure 3.22 – UV-Vis spectra for starting products: pure **8-PNP-O12** (black) and **F_4TCNQ** (red), 2 mg/ml chloroform solution.

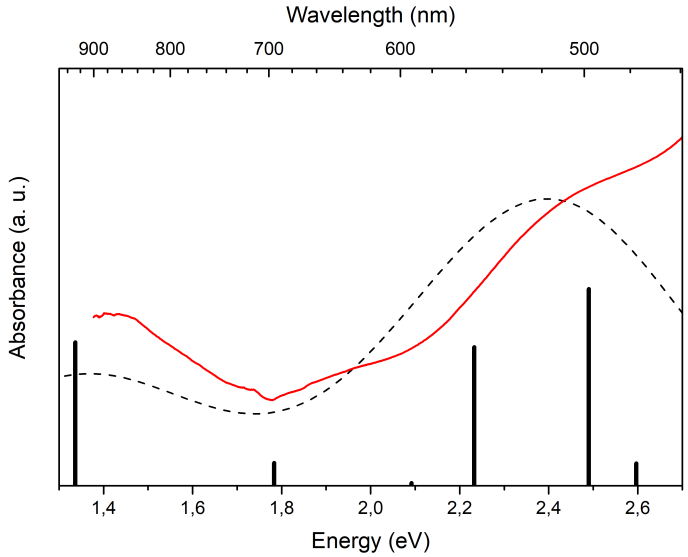

Figure 3.23 – UV-Vis spectrum of **c5** sample (solid red line) and the result of TD-DFT calculation of **CTC** (dashed black line). Black vertical lines denote transition energies and corresponding oscillator strengths.

it is possible to notice some new absorption peaks situated in the near infrared part of the spectra which are not present for the initial materials. The absorption intensity of these new peaks seems to be in good agreement with the content of **F_4TCNQ**.

The anion of **F_4TCNQ** has optical absorption bands at 1.45 eV, 1.65 eV and 3 eV [155, 156]. Sharp features observed on these energy levels would propose the ICT mechanism. It is possible to observe one peak at 1.45 eV, however the other peaks at 1.65 eV and around 3 eV (expected in case of ICT) are absent. Instead, we observe a shoulder at 1.72 eV, as well as some new features in the visible part (two distinct absorption bands at 2.27 eV and 2.57 eV are observed on low concentrations and further convolute in a shoulder at larger dopant load). As illustrated by Mendez et al. [39], for PCT case the absorption peaks of **CTC** may be situated on different photon energy values.

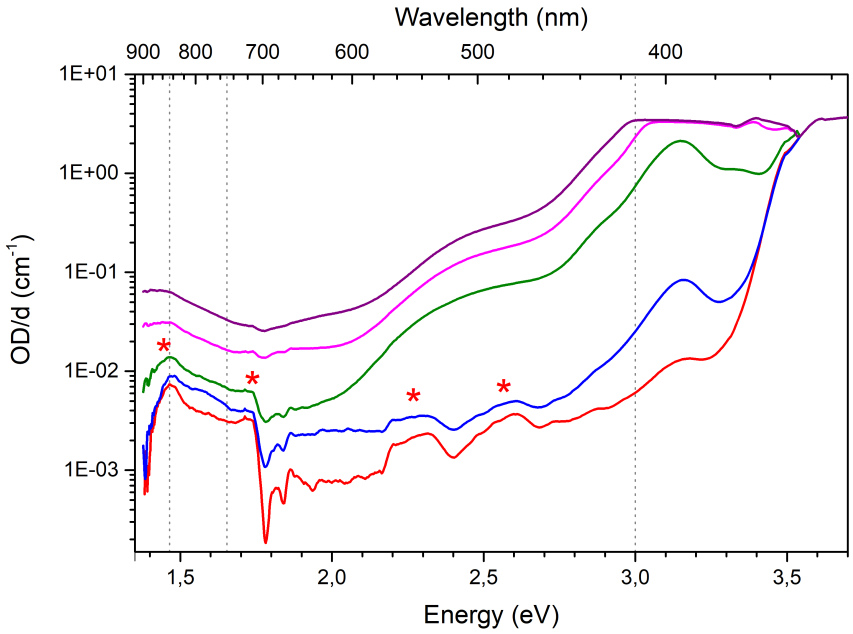

Figure 3.24 – UV-Vis spectra for prepared samples taken in 2 mg/ml chloroform solution: **c1** (red), **c2** (blue), **c3** (green), **c4** (pink) and **c5** (purple) samples. Gray vertical dotted lines correspond to the expected energies of the anion **F_4TCNQ$^-$** absorption peaks [39][155]. Peaks assigned to **CTC** are marked with red asterisks.

These observations allow us to confirm the partial charge transfer between the **8-PNP-O12** and **F_4TCNQ**. However, the optical signatures of pristine **F_4TCNQ** are still present in the mixture. It suggests a possible solvation effect, which may somewhat hinder the process of charge transfer, or the resulting **CTC** has lower solubility in chloroform

than initial products.

3.3.5 Vibrational spectroscopy

Preliminary investigations

In order to investigate the possible contribution of structural order to the electron transfer in **8-PNP-O12**/**F_4TCNQ** system, we have carried out Raman spectroscopy in all phases displayed by this system. The first spectrum was recorded in crystalline phase **Cr**, then the sample was heated to isotropic phase **Iso**, where it was maintained for 30 minutes. After annealing, each sample was slowly cooled back to crystalline phase through Smectic A (**SmA**) and Smectic B (**SmB**) mesophases. Raman spectra were recorded in every phase state, as well as two times in crystalline phase (before and after annealing). This was done in order to confirm the charge transfer and to investigate the thermal stability and possible influence of mesophase on the **CTC**. Pure **8-PNP-O12** does not exhibit any Raman vibrational frequency variation as a function of its phase state. This is not surprising, as the molecule itself is stable and does not undergo any structural change. Presented experimental spectra are accompanied by the quantum DFT calculations of presumed molecular moiety, performed with Gaussian 16 package on B3LYP level of theory with 6-31G++(d,p) basis set. Raman intensities for 785nm excitation wavelength were computed with GaussSum 3.0 software. Here, we would like to illustrate how the

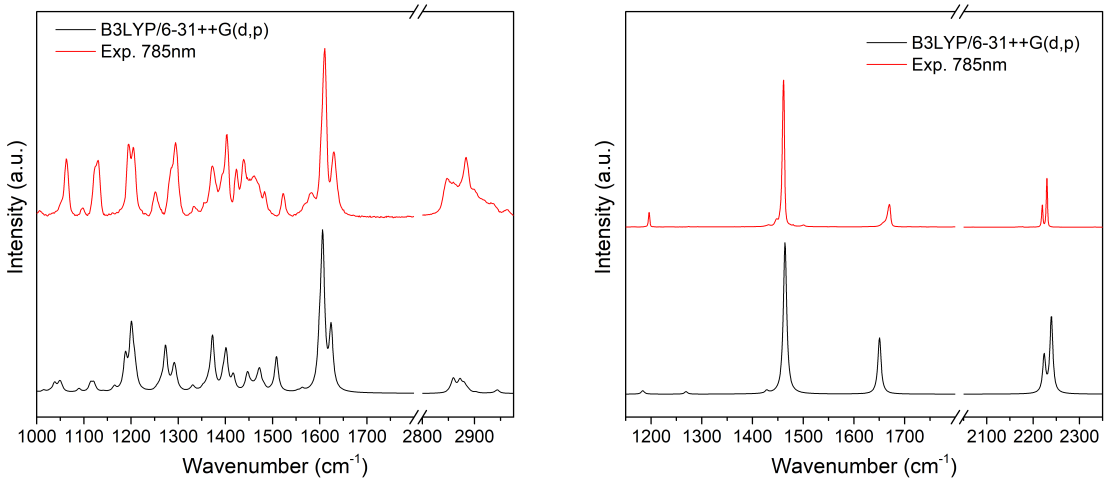

Figure 3.25 – Raman spectra for (a) pure **8-PNP-O12** and (b) pure **F_4TCNQ**: black for calculated (scaling factor of 0.9626 [157, 158]) and red for experimental spectra. Intensity is normalized for highest peak.

experimental Raman spectra comply to a calculated one (after application of a scaling parameter [158]): Figure 3.25a shows us good matching of experimental and calculated spectra, especially for the aromatic carbon region around 1600 1/cm, which is particularly interesting for us, since it is the part which contains the HOMO of **8-PNP-O12** molecule (Figure 3.26, calculated on B3LYP/6-31++G(d,p) level).

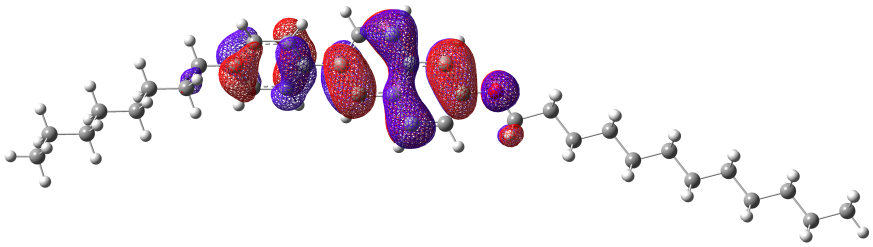

Figure 3.26 – HOMO of neutral **8-PNP-O12** molecule.

Simulated spectrum of dopant exhibit slight mismatch of vibrational frequencies (Figure 3.25b). Possible reasons may include strong anharmonic interactions between different Raman modes, as well as the fact that dopant molecule contains heavier atoms (nitrogen and fluorine), which are less precisely defined with used calculation theory method and basis set. The largest error is exhibited by the stretching of conjugated lateral double bond (3-4 in Figure 3.27, (b)).

In order to model the products of charge transfer between the dopant and host molecules, we have also performed calculation of vibrational spectra of charged molecules (charge **-1** for **F_4TCNQ** and **+1** for **8-PNP-O12**) which allows us to identify the frequency change in case of charge transfer (Figures 3.28a and 3.28b).

It is clear that for both substances a transition to the charged state ends up with a shift in Raman bands towards lower wavenumber (Figures 3.28a and 3.28b). For **8-PNP-O12**, the most important change takes place in the aromatic carbon area: the peaks of 1605 1/cm (phenyl ring C-stretching, 1-6 in Figure 3.27, (a)) and 1630 1/cm (naphthalene conjugated ring C-stretching, 7-16 in Figure 3.27, (a)) shift towards 1592 1/cm and 1597 1/cm, respectively. In turn, the molecule of **F_4TCNQ** undergoes similar changes: it has pronounced bands of cyano group (asymmetric C≡N stretching, 1-2 in Figure 3.27, (a)) at 2225 1/cm and 2240 1/cm which shift towards 2169 1/cm and 2203 1/cm, as well as bands related to quinoid system: double C=C ring bonds stretching (5-6 in Figure 3.27, (b), it shifts from 1650 to 1630 1/cm) and conjugated lateral double bond C=C stretching (3-4 in Figure 3.27, (b), it shifts from 1462 to 1416 1/cm).

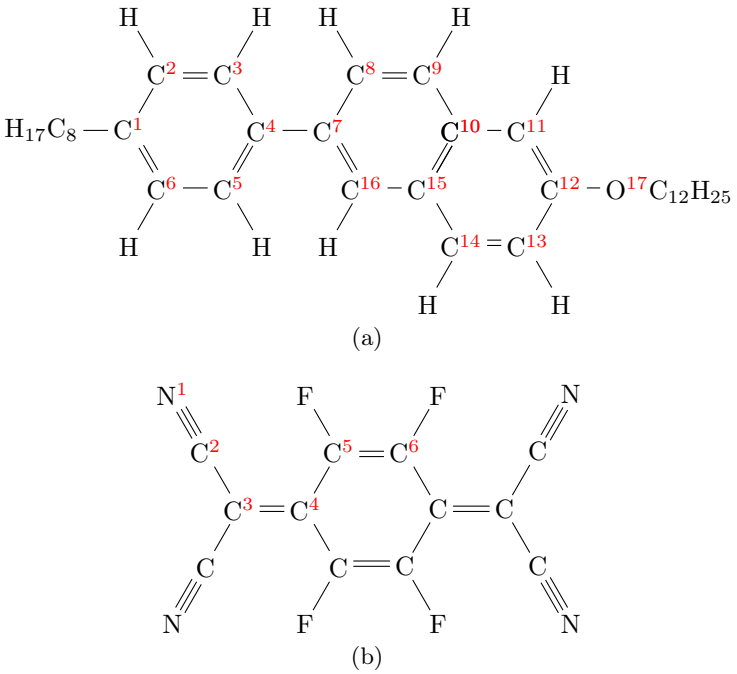

Figure 3.27 – Atom indexing of molecular structure of (a) 2-dodecyloxy-6-(4-octylphenyl)-naphthalene (**8-PNP-O12**) and (b) 2,3,5,6-tetrafluoro-7,7,8,8-tetracyanoquinodimethane (**F_4TCNQ**).

We should also point out certain limits of this preliminary approach of integral charge transfer: it is not aimed to quantitatively evaluate the Raman band shift (instead, experimental data on **F_4TCNQ^{-1}** is used [39, 38]) in comparison between experimental and calculated spectra for all of the observable vibrational modes, but to give an idea of the changes in vibrational spectra of a mixture which exhibit evidence of successful charge transfer (i.e. the presence of binded complex between host and dopant) at this stage.

We begin with the comparison of different doping concentrations in the form of as-prepared powder, as shown in the Figure 3.29. The spectra are normalized in respect of intensity of the peak at about 1300 1/cm. Pronounced peak at 1450 1/cm comes from the conjugated lateral double bond C=C stretching of the dopant and it is clear that its intensity is proportional to the dopant concentration. That is also true for the peak at 1667 1/cm previously assigned to quinoid ring C=C stretching. The cyano (C≡N) bands are not observed until high concentrations, but then still follow the observed dependency on **F_4TCNQ** content. One can notice the apparition of new peak, clearly visible at 1655 1/cm, which is connected to the dopant molecule after charge transfer (highlighted with arrow in Figure 3.29).

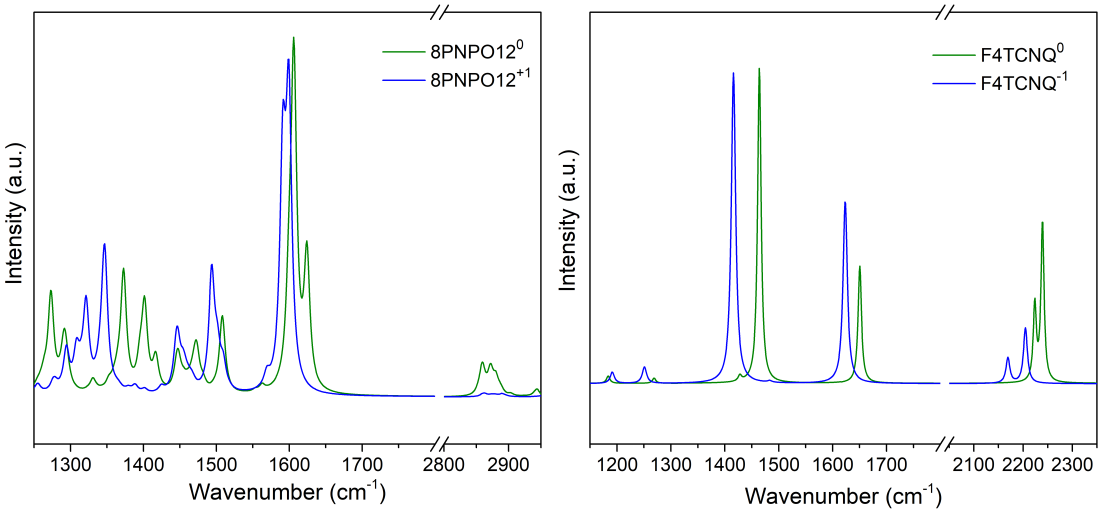

(a) (b)

Figure 3.28 – Calculated Raman spectra for (a) **8-PNP-O12** and (b) **F_4TCNQ**: green for neutral and blue for charged molecule. Intensity is normalized for highest peak, scaling factor of 0.9626[157, 158] is applied

Nevertheless, the most interesting results have been obtained upon annealing doped **8-PNP-O12** samples. An example to illustrate this effect is presented in the Figure 3.30. This figure shows the data obtained for **c5** sample at the same temperature sequence as for pure **8-PNP-O12**. The only signs of formation of charge transfer complex which are present in as-prepared sample are the previously mentioned peak of charged dopant's quinoid ring (1655 1/cm) and cyano group (around 2200 1/cm), which coexist with relatively strong signature of initial neutral products. Almost all the peaks of each component of the mixture match with neutral state molecules (Figures 3.25a and 3.25b).

Firstly, we would like to discuss the case of the freshly prepared mixture in the **Cr** phase (Figure 3.30, **Cr**). The spectrum exhibit strong signatures of pristine **F_4TCNQ**, notably the isolated vibrational bands of nitrile group (symmetric and assymetric stretching of 1-2 bond, Figure 3.27, b) at 2220 and 2228/cm, as well as quinoid part (lateral double bond 3-4 and ring 5-6, Figure 3.27, b at 1458 and 1668/cm, respectively). The only new feature noticeable in this spectrum is a new band at 1654/cm between the aforementioned quinoid ring stretch band and naphthalene ring (bonds 7-16 at Figure 3.27, a) stretching at 1634/cm.

The situation changes significantly upon heating to isotropic phase (Figure 3.30, **Iso**). The nitrile group peak is shifted to the left 2212/cm and broadened. The quinoid ring

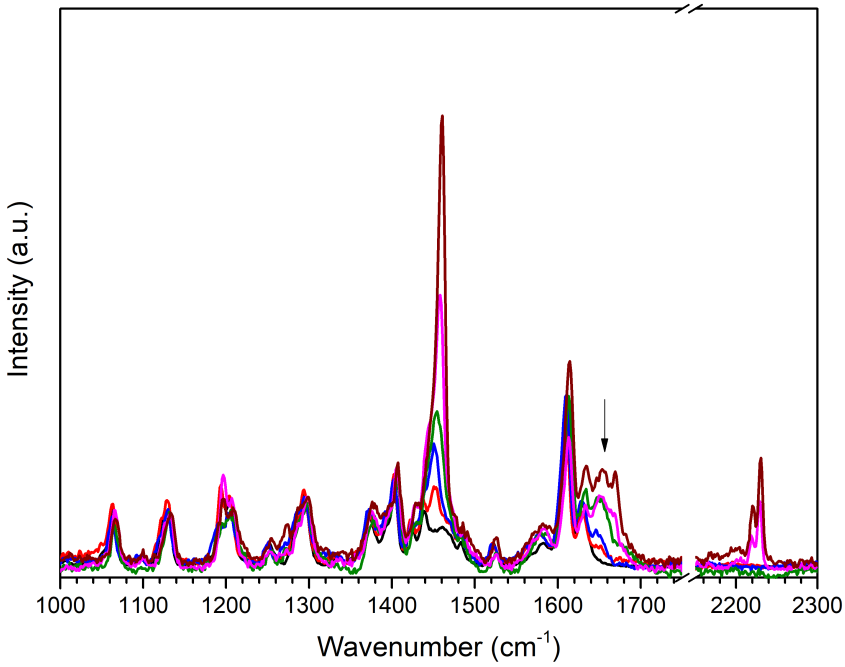

Figure 3.29 – Raman spectra for mixtures in as-prepared powder: black for pure **8-PNP-O12**, red for 0.1%, blue for 0.5%, green for 1%, magenta for 3% and brown for 5% **F_4TCNQ** content. Black arrow highlights new band apparition. Intensity is normalized for peak at around 1300/cm.

stretching band disappears, and stretching of lateral double bond shifts to the left (1437 1/cm). Peaks, related to the aromatic system (phenyl and naphthalene rings stretching) of **8-PNP-O12** also undergo noticeable shift to the left (1606 and 1624 1/cm, respectively). Interestingly, the spectra recorded in SmA and SmB phases (Figure 3.30) seem to bear no difference with each other.

Finally, after crystallizing from Sm_B mesophase, the annealed crystalline sample shows (Figure 3.30, **Cr**$*$) correlation to the spectra, previously observed during annealing as we can notice in more pronounced peaks of aromatic system of **8-PNP-O12** (1600 and 1619 1/cm), as well as the reappeared shifted band connected to the quinoid ring (1650 1/cm). Samples of the other concentrations, as can be noticed in Figure 3.31, exhibit similar behavior: the other concentrations with less pronounced effects due to strong contribution of the initial components. The general trend observed for all of these mixtures allows us to attest successful formation of charge transfer complex between the host and the dopant.

In previous section, we have noticed that **CTC** has optical absorption in near-infrared

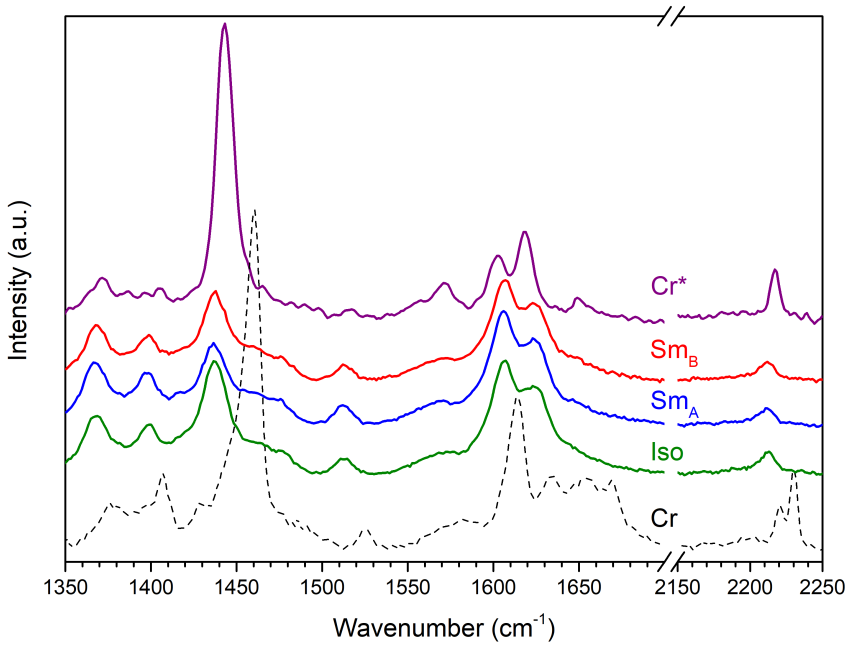

Figure 3.30 – Example of Raman spectra recorded for **c5** sample in different phase: black dashed for as-prepared powder, green for I, blue for Sm_A, red for Sm_B and purple for annealed Cr. Intensity is normalized for naphthalene ring stretch band (1635/cm before annealing, 1624/cm in liquid and liquid crystalline phase and 1618/cm after annealing).

part of the spectrum (Figure 3.24). The energy of laser excitation (785 nm or 1.58 eV) seems to be in resonance with one of the electron transition energies of **CTC**. This can explain little to no signature of initial products in the spectra recorded during annealing, as well as for the annealed samples (Figure 3.30 for **c5**), despite the huge excess of pristine **8-PNP-O12** which is expected to contribute to the Raman spectrum.

These experimental Raman spectra suggest that the formed **CTC** is thermodynamically stable within applied temperature range of 50 °C to 130 °C, i.e. for all phase states displayed by the **8-PNP-O12**/**F$_4$TCNQ** mixtures. This result is in good agreement with the observations of Khan et al [130]: their system was based on HAT-5 and **F$_4$TCNQ**. The optical absorption spectra recorded in isotropic phase of their mixtures looked similarly to other phase states exhibited by their samples. Moreover, for our system, there seems to be no observable influence of the structural order on the quantity of the charge transfer between **8-PNP-O12** and **F$_4$TCNQ**. In fact, the vibrational bands positions do not change between Sm_B and Sm_A mesophases. It is of interest to compare this observation to the case of PTCBI derivative [92, 159], where a phase transition introduces

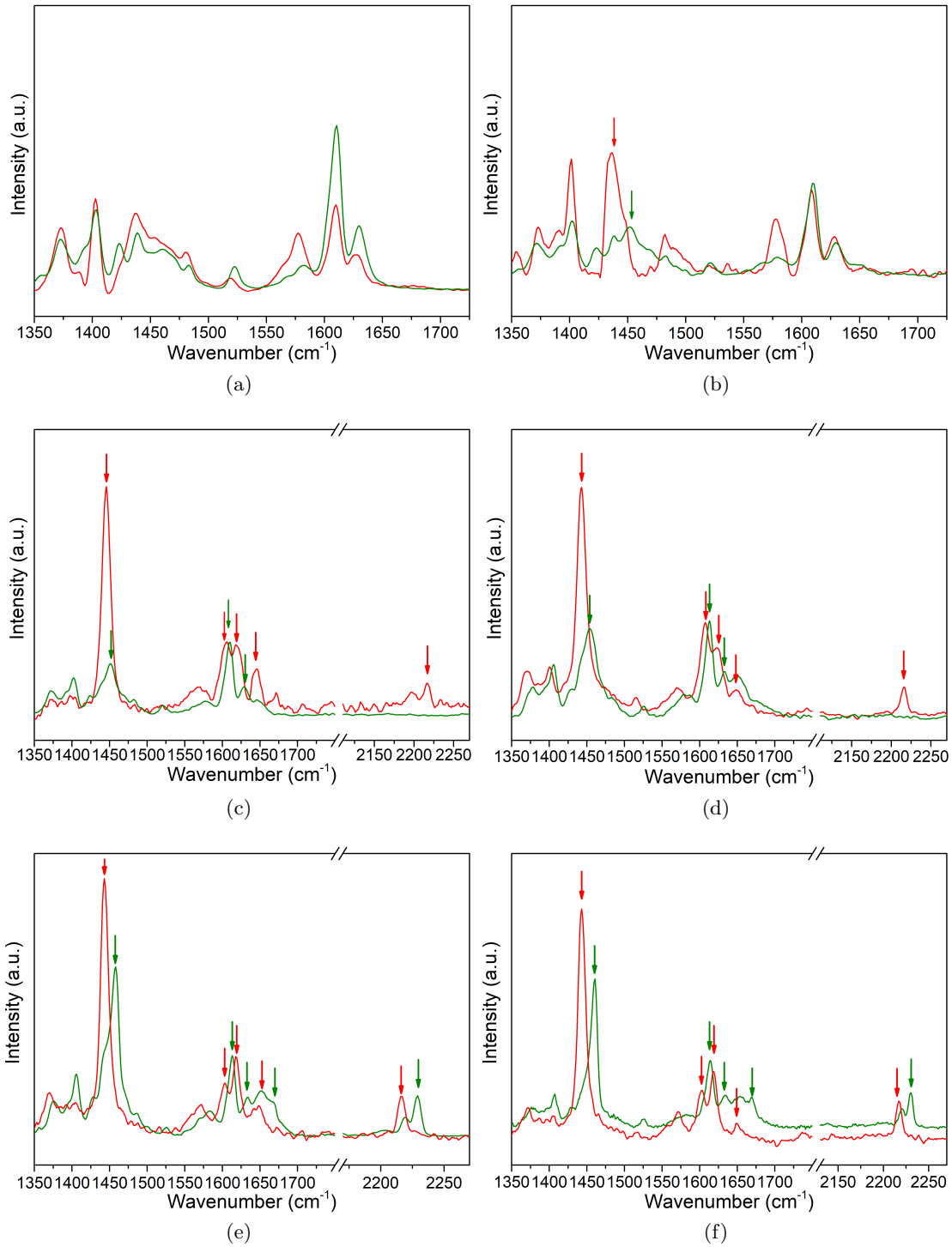

Figure 3.31 – Raman spectra for as-prepared (green) and annealed (red) samples (a) pure **8-PNP-O12**, (b) for 0.1%, (c) for 0.5%, (d) for 1%, (e) for 3% and (f) for 5% **F_4TCNQ** content. Green and red arrows indicate Raman bands shifts after annealing.

a striking change in spectroscopic properties of the material. The authors have attributed this change to the shift in π-π overlap between the neighboring molecules due to the intermolecular longitudinal offset, which is induced on the phase transition. In our case, the transition from Sm_B to Sm_A mostly affects the positional order within the smectic layers and does not induce any significant inter-layer change, thus the formed **CTC** remains undisturbed. Weak signatures of **CTC** in pre-annealed samples allow us to emphasize the role of annealing in preparing of such type of mixtures. Simple dissolution of the initial components of the mixture in a solvent seems to be not quite efficient, and melting of host **8-PNP-O12** is able to provide more intimate contact between two components of **CTC**, which is necessary for "bonding".

The b_{1u} vibrational mode

The role of vibrational spectroscopy in the study of charge transfer related to $\mathbf{F_4TCNQ}$ and its homologues is undeniable [155, 160, 148, 147, 39, 161]. The vibrational analysis

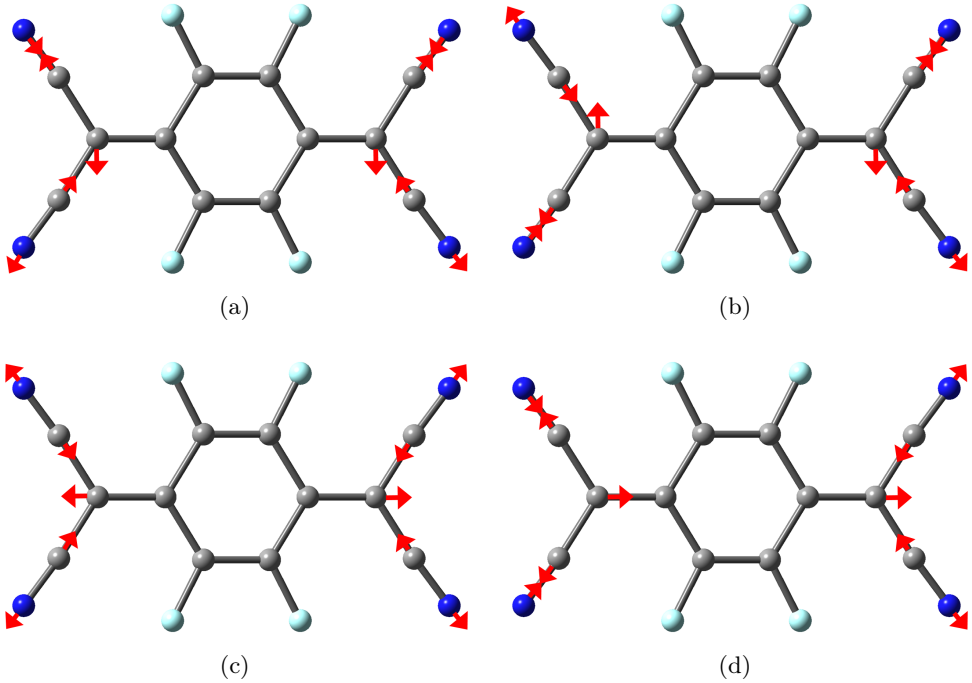

Figure 3.32 – Vibrations of $\mathbf{F_4TCNQ}$ molecule : IR-active b_{2u} (a) and b_{1u} (d); Raman-active b_{3g} (b) and a_g (c).

of the charge transfer is based on the shift of nitrile band, since this vibrational band is situated in the part of the spectrum which is usually isolated: it does not contain any other

vibrational modes of initial products. It seems that a vast number of research groups favor IR spectroscopy over Raman [65, 162, 28]. In fact, pristine **F_4TCNQ** molecule exhibits 4 vibrational modes in this region of the spectrum (2100/cm to 2300/cm), with two of them being IR active (b_{2u} and b_{1u} at 2213/cm and 2227/cm [147], respectively), and the other two - Raman active (b_{3g} and a_g at 2219/cm and 2227/cm [160], respectively). These vibrational modes are illustrated in the Figure 3.32. Zhu et al. have provided a detailed theoretical study on vibrational spectroscopic properties of **F_4TCNQ** molecule in case of charge transfer [147]. In their work, they have predicted possible change in vibrational activity of **F_4TCNQ** and proposed that deviations in molecular geometry due to electron density relocation will allow to break the mutual exclusion rule, i.e. make all the modes of molecular vibration Raman and IR active.

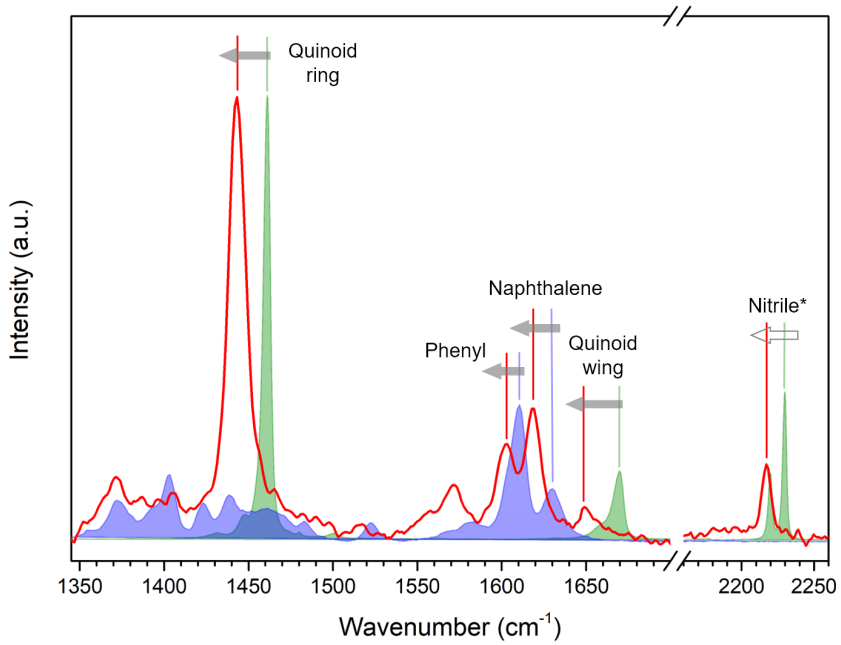

Figure 3.33 – Raman spectra for **Cr*** of **c5** sample (red solid line), pure **8-PNP-O12** (dark blue filled plot) and pure **F_4TCNQ** (green filled plot) recorded at room temperature. The Raman bands of interest are labeled with the corresponding color.

The analysis in our work demonstrates that Raman spectroscopy is able to provide us useful information in case PCT and in the meantime allows to choose an excitation wavelength for potential resonant effects. Figure 3.33 presents an example of comparison between the Raman spectra of annealed **Cr*** of **c5** mixture with initial products (pure **8-PNP-O12** and **F_4TCNQ**). Some noticeable red shift occurs to the bands assigned to

the aromatic system of **8-PNP-O12** and quinoid as well as nitrile parts of the **F_4TCNQ** molecule. However, it is difficult to estimate the individual contribution of lower frequency vibrational bands, since they are located in tighter groups, and their intensity is relatively low.

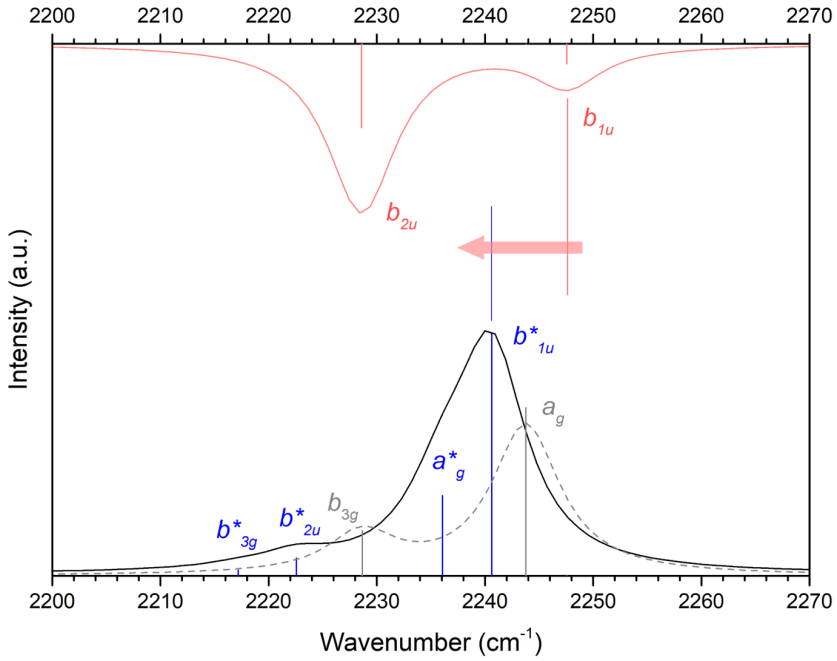

Figure 3.34 – Calculated vibrational spectra (scaling factor of 0.9626 [157, 158]) for pure **F_4TCNQ** (Raman in dashed gray and IR in solid red) and **CTC** (Raman in solid black and vibrational frequencies in blue). The corresponding vibrations are assigned respectively.

In fact, due to previously discussed change in molecular geometry, the mutual exclusion rule which is valid for **F_4TCNQ** and **F_4TCNQ$^-$** (they belong to D_2h symmetry group [155]) does no longer apply to the vibrational modes exhibited by **CTC** (as predicted by Zhu and coworkers [147]). DFT frequency calculations performed on **CTC** show significant polarizability change (in fact, of higher magnitude than inherent Raman modes b_{3g} and a_g) which occurs on vibrational mode previously attributed to b_{1u} mode for symmetrical molecules (for convenience labeled b^*_{1u}). The resulting Raman intensity at 785 nm excitation of the b^*_{1u} band (around 2241/cm in Figure 3.34 is even greater than of normally expected a^*_g. This fact allows to assign the peak observed at 2217/cm (Figure 3.33) to the Raman-active (in case of **CTC**) vibrational mode b^*_{1u}.

This conclusion also enables us to directly compare the observed vibrational mode b^*_{1u}

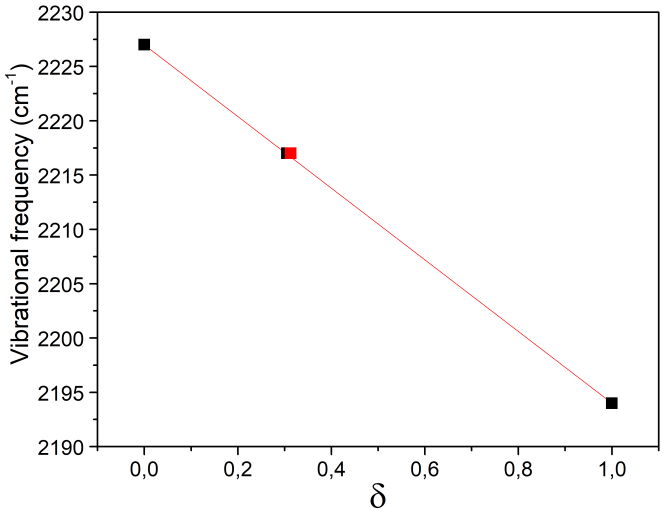

Figure 3.35 – Graphical representation of b_{1u} vibrational frequency as a function of charge transfer degree. Black points corresponding to $\mathbf{F_4TCNQ}$ and $\mathbf{F_4TCNQ^-}$ indicate frequencies extracted from IR spectroscopy [39, 38]. Frequency corresponding to partial charge transfer is extracted from Raman spectrum. The point in red represents the expected amount of charge transfer from the DFT calculations.

to frequencies of those b_{1u} modes which are only IR-active in $\mathbf{F_4TCNQ}$ and $\mathbf{F_4TCNQ^-}$ (since it no longer posses a center of symmetry). It is possible to perform a quantitative estimation of the charge transfer degree δ between **8-PNP-O12** and $\mathbf{F_4TCNQ}$ using the following equation [163]:

$$\delta = \frac{2\Delta\nu}{\nu_0}\left[1 - \frac{\nu_1^2}{\nu_0^2}\right]^{-1}, \tag{3.1}$$

where the observed shift in vibrational frequency ($\Delta\nu$) is compared to the position of the same band in pure $\mathbf{F_4TCNQ}$ (ν_0) and the anion $\mathbf{F_4TCNQ^-}$ (ν_1).

The value for frequency of b_{1u} mode for $\mathbf{F_4TCNQ^-}$ is taken to be 2194/cm [39, 38]. The observable red shift of this band (2227→22171/cm, Figure 3.33) yields a charge transfer degree δ of **0.31** (equation 3.1), which is in excellent agreement with DFT calculations (value of 0.31 obtained as an average of electrostatic potential (**ESP**, 0.33), natural bond orbital (**NBO**, 0.32) and Hirshfeld population (**CM5**, 0.29) analysis schemes). Figure 3.35 allows us to compare the calculated value (red) with the one extracted from the Raman spectrum (black).

To summarize, the spectroscopic studies have allowed us to confirm the predicted by *ab initio* calculations charge transfer between the **8-PNP-O12** and $\mathbf{F_4TCNQ}$ and

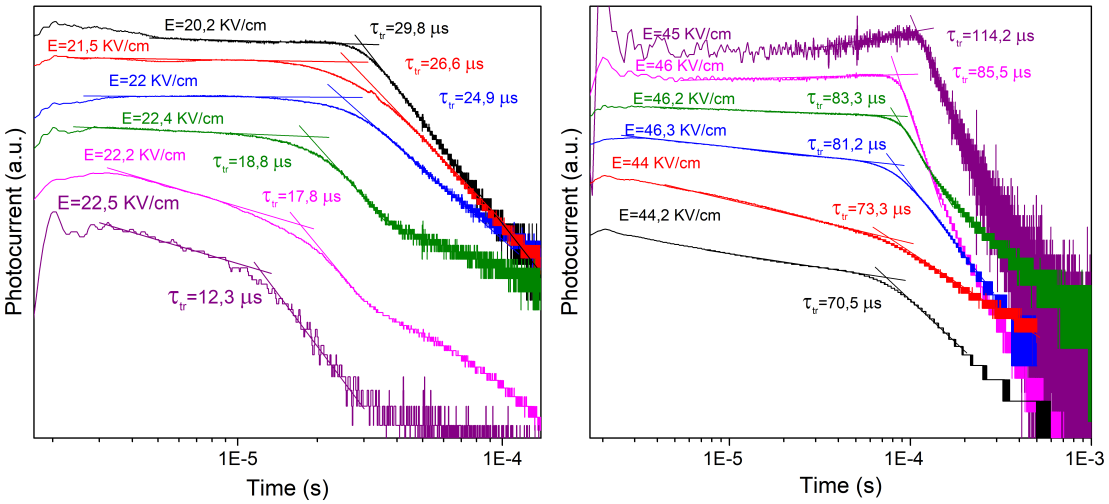

(a) (b)

Figure 3.36 – Plots of the photocurrent as a function of $\mathbf{F_4TCNQ}$ content in Sm_B at 85 °C (a) and Sm_A at 115 °C (b): : pure **8-PNP-O12** (black), **c1** (red), **c2** (blue), **c3** (green), **c4** (magenta) and **c5** (purple).

determine its character (partial charge transfer, PCT). The Raman spectroscopy has allowed us to quantify the amount of transferred charge, as well as to confirm the stability of the **CTC** in the phase states exhibited by the prepared mixtures. These results are going to help us in the investigations of their charge transporting properties, which are covered in the next section.

3.3.6 Charge transporting properties in the mesophase

It is usually assumed that introduction of dopant results in increase of notoriously weak intrinsic "free" charge carrier density in organic substances, though its effects on bulk mobility need to be addressed more profusely. In this section we have made an attempt to disclose the influence of charge transfer complex on bulk hole mobility of **8-PNP-O12** by utilizing the TOF technique [164, 165, 91, 166, 142].

Due to the nature of this technique, the obtained results are decoupled from the absolute number of charge carriers which participate in the transport (quantity of carriers impacts the amplitude of signal and not the photocurrent decay profile). Mobility (μ) is calculated by using the equation 2.6 [128].

Hole mobility values are measured for the range of applied electric field E from 10 kV/cm to 50 kV/cm in Sm_B mesophase and 25 kV/cm to 60 kV/cm in Sm_A mesophase,

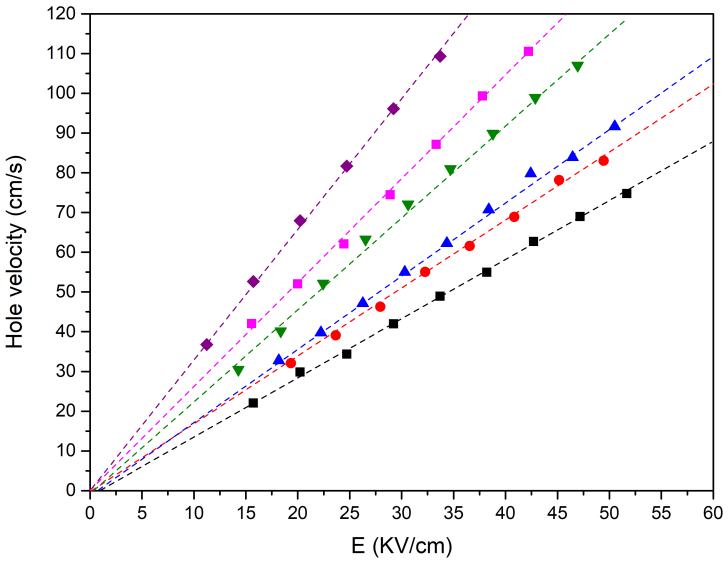

(a)

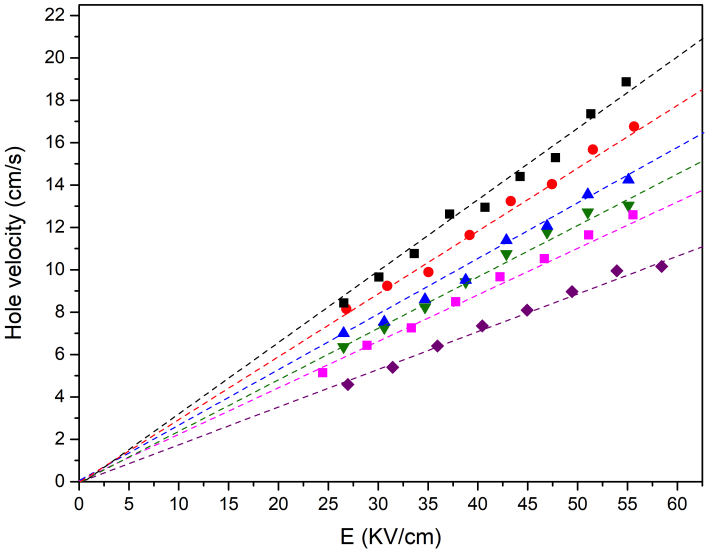

(b)

Figure 3.37 – Plot of the hole velocity as a function of applied electric field for pure **8-PNP-O12** (black squares), **c1** (red circles), **c2** (blue triangles), **c3** (green triangles), **c4** (magenta squares) and **c5** (purple diamonds) in Sm_B at 85 °C (a) and Sm_A at 115 °C (b).

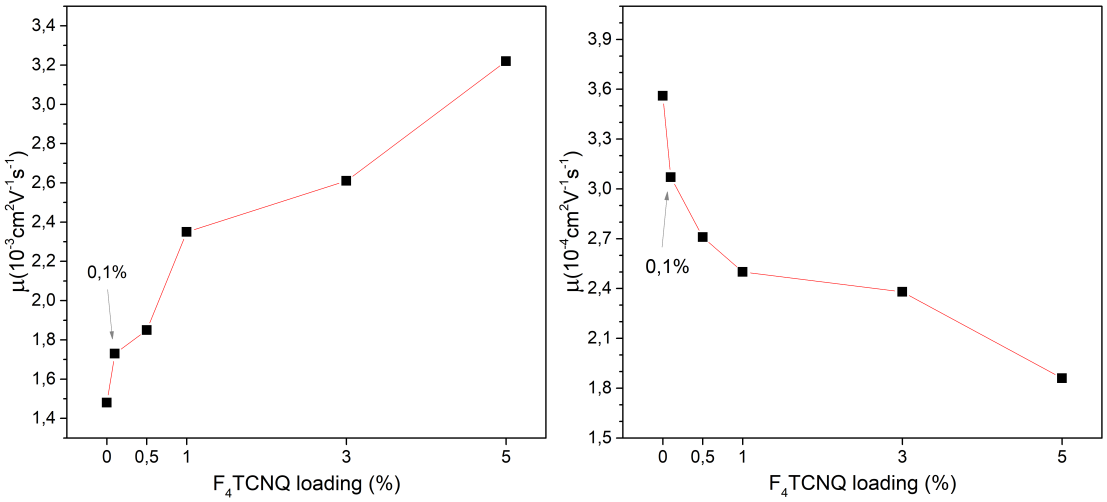

(a) (b)

Figure 3.38 – Plots of the hole mobility as a function of **F_4TCNQ** content in Sm_B mesophase at 85 °C (a) and Sm_A mesophase at 115 °C (b).

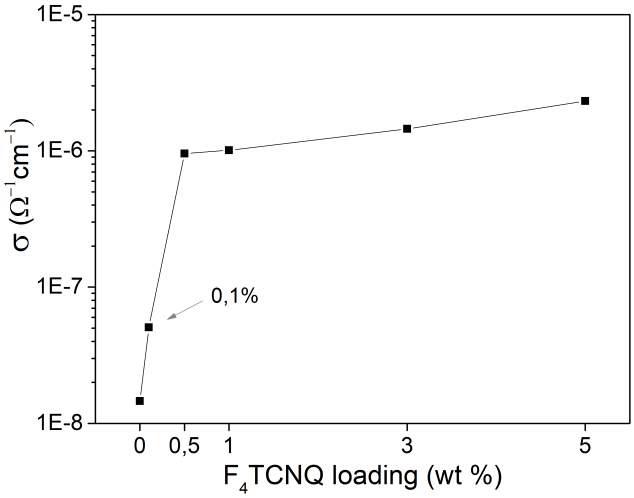

Figure 3.39 – Conductivity of samples extracted from current-voltage plot in Sm_B at 85 °C as afunction of **F_4TCNQ** content. Sample was placed in Au/ITO measurement cell with gap of 12 µm and 5×5 mm active area.

the sample thickness was about 9 µm (sample cells were individually calibrated prior to filling by means of an impedance analyzer).

Figure 3.36 assembles examples of photocurrent transient plots obtained by TOF measurements as a function of **F_4TCNQ** content in the two smectic mesophases. The

hole transit time, extracted from these measurements has allowed us to calculate carrier velocity (Figure 3.37) as a function of applied electric field E. It should be noted that for all the mixtures the linear dependency of carrier velocity is observed, as for the pure **8-PNP-O12**.

Interestingly, the prepared mixtures exhibit different trends in each mesophase. In Sm_B, the hole velocity increases with the content of introduced **F_4TCNQ**, whereas in the Sm_A the situation is opposite. Since we have previously demonstrated the thermal stability of the CTC (Figure 3.30), it is reasonable to correlate this observed behavior to structural changes in the mesophases and not to the interaction between the **8-PNP-O12** and **F_4TCNQ**.

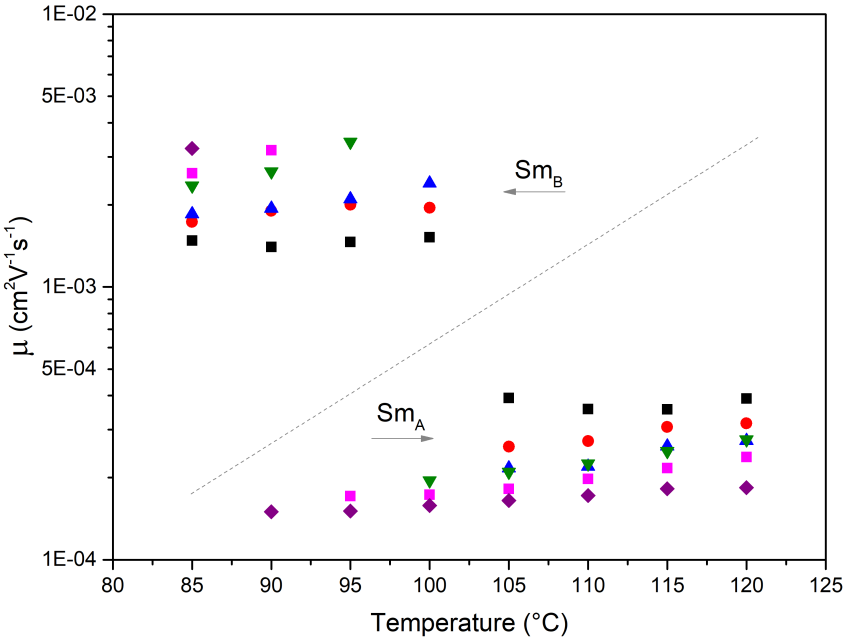

Figure 3.40 – Plot of the hole mobility as a function of temperature for pure **8-PNP-O12** (black squares), **c1** (red circles), **c2** (blue triangles), **c3** (green triangles), **c4** (magenta squares) and **c5** (purple diamonds).

It seems that **CTC** is able to promote hole transport in Sm_B mesophase (Figure 3.38, a) and impede it in Sm_A (Figure 3.38, b). It is also noteworthy to mention that with increasing of dopant content, the signal-to-noise ratio of TOF transient current is deteriorating (Figure 3.36). This can be explained by the shift of frontier molecular orbital energy level of the sample due to the presence of **CTC** moieties closer to the work function of the electrode material (ITO) [167], which results in easier charge injection and

subsequent rise of the DC conductivity (Figure 3.39). One of the basic requirements for TOF measurements is injection-blocking contacts, since under high applied field (often used in TOF measurements) possible contribution of space charge-limited current may interfere with transient signal [128].

A possible explanation for the mobility increase may be the change of dihedral angle 5-4-7-8 (Figure 3.27, a), which result in its planarization of **8-PNP-O12** molecule, thus improving the electron density delocalization between phenyl and naphthalene aromatic systems. Similar phenomena has been previously reported by works dedicated to the role of regioregularity of P3HT in its charge transporting properties [59, 168].

Hole mobility as a function of temperature is presented in the Figure 3.40. Results obtained for pure **8-PNP-O12** are in good agreement with those previously reported [169, 78]: hole mobility is of $1.5 \times 10^{-3}\,\mathrm{cm}^2/(\mathrm{V\,s})$ in Sm_B and $3.6 \times 10^{-4}\,\mathrm{cm}^2/(\mathrm{V\,s})$ in Sm_A and temperature independent in each smectic phase. As we have previously noticed, doping with $\mathbf{F_4TCNQ}$ results in the increase of hole mobility in Sm_B, whereas in Sm_A it decreases with the concentration of dopant. However, unlike for pre **8-PNP-O12**, the mobility seems to be increasing with the temperature (for the mixtures). This thermal activation may be explained by the fact that CTC is interfering with the smectic order, thus creating some trap states [170]. These trap states can be overcome on higher temperature due to broadening of the density of states (DOS) distribution [46, 171]. We have calculated the activation energy E_a for mobility in both mesophases (Figure 3.41). It is found that in Sm_B, E_a is increasing with dopant concentration, whereas in Sm_A it is decreasing.

In order to address to prepare the discussion on the results TOF mobility measurements in smectic mesophases we have carried out EDX analysis on previously prepared samples of **c3** and **c5**, which were used for TOF experiments. These cells were slowly cooled from the isotropic phase state in order to preserve "smectic" polydomain structure in its crystalline state. The purpose of this analysis is not to demonstrate the morphology of thin films, but to investigate the presence of dopant aggregates, which may allow us to obtain more information and shed some light on the charge transporting properties of the **8-PNP-O12**/$\mathbf{F_4TCNQ}$ system.

Figure 3.42 demonstrates two SEM images of the **c3** cell after it has been opened, which explains large amount of film defects on a relatively thick sample (about 10 µm). The fluorine signatures appear to be grouped more densely in the areas populated by the mixture. A higher magnification on a "smectic" domain reveals largely uniform distribution of dopant sites across the field of view.

Images of **c5** cell (Figure 3.43) demonstrate similar picture and show correlation

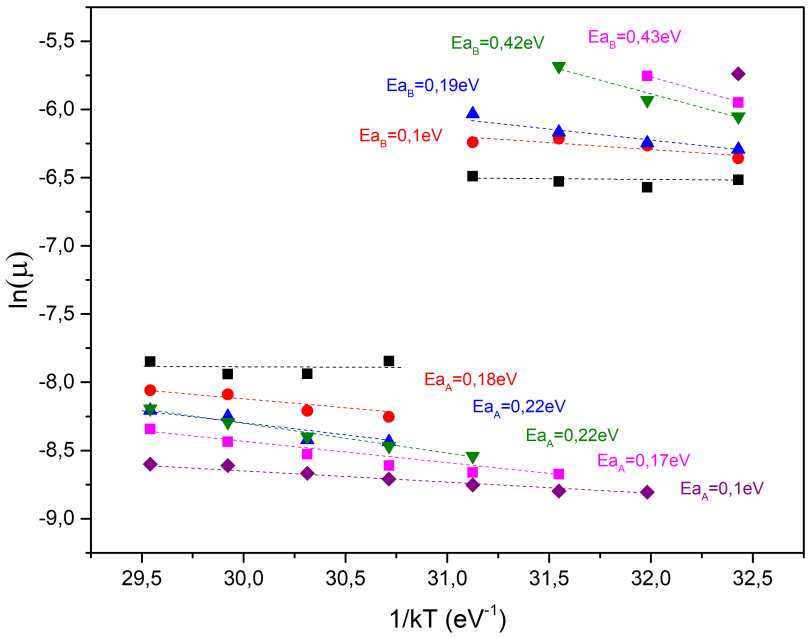

Figure 3.41 – Arrhenius plot of the hole mobility for pure **8-PNP-O12** (black squares), **c1** (red circles), **c2** (blue triangles), **c3** (green triangles), **c4** (magenta squares) and **c5** (purple diamonds).

between the sample morphology and fluorine distribution. The observation of a "smectic" domain confirms the uniform distribution of $\mathbf{F_4TCNQ}$, previously encountered in **c3** and shows good compatibility between the components of the mixtures.

These results allow us to conclude that the observed hole-transporting behavior is not related to the "macroscopic" dopant distribution, since the thickness of the cell is of the order of one smectic domain.

The behavior of the hole mobility in the Sm_A of $\mathbf{8\text{-}PNP\text{-}O12/F_4TCNQ}$ system can be compared to the case of binary mixture between **8-PNP-O12** and small amounts (in order of tenths to hundreds of ppm) of dihexyl terthiophene (DH3T). This system was studied by Funahashi et al [172] in an attempt to understand the contribution of charge trapping to the hole transport by deliberately introducing traps to the **8-PNP-O12** material. the HOMO of DH3T lies higher than that of **8-PNP-O12** (5.1 eV vs 5.6 eV) Thus the DH3T indeed acts as a hole trap for the host **8-PNP-O12**. It was found that the hole transport was considerably affected by carrier trapping in the smectic phases: the hole mobility was decreasing with the concentration of DH3T. These results have demonstrated that the behavior of their system is described by the following equation

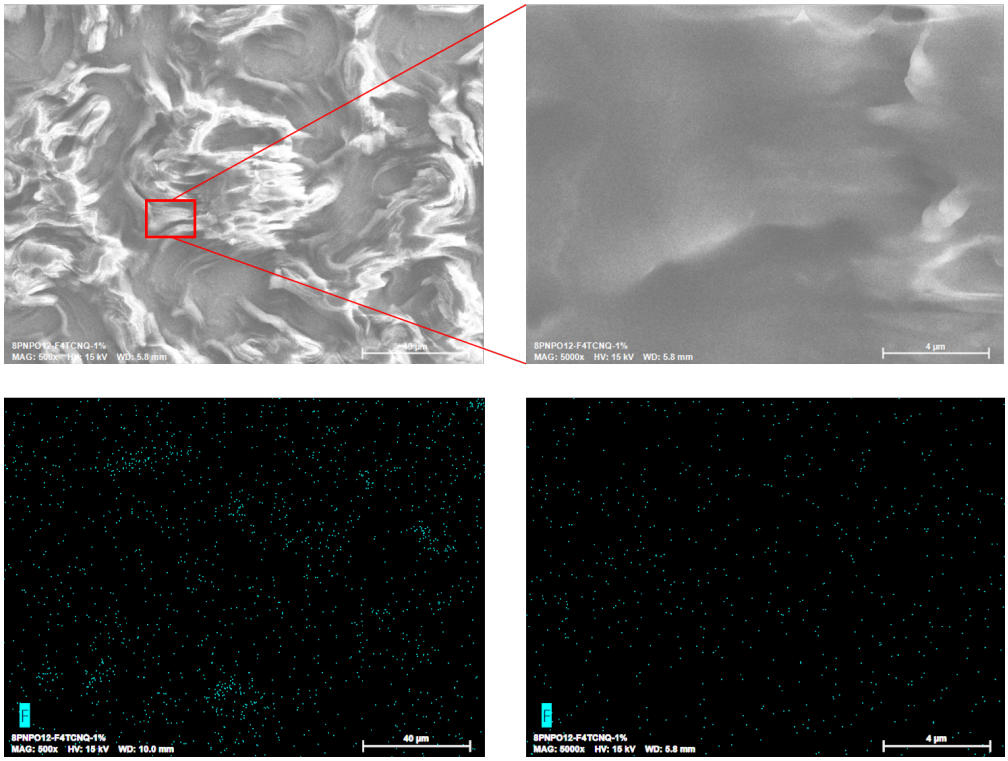

Figure 3.42 – SEM and EDX images corresponding to **c3**. Top: SEM morphology images. Bottom: fluorine elemental mapping of the sample area shown above.

[172]:

$$\mu = \frac{\mu_0}{(1 + \frac{\tau_{detrap}}{\tau_{hop}} C^{\frac{1}{2}})} \tag{3.2}$$

where μ_0 is the mobility in pristine **8-PNP-O12**, C is the dopant molar fraction, τ_{hop} and τ_{detrap} is the hopping time and detrapping time (when the carrier is released) respectively. For the **8-PNP-O12** doped with DH3T the ratio of τ_{hop}/τ_{detrap} was found to be around 8.6×10^{-4} The expression 3.2 was used to fit the experimental data of hole mobility found in our system (Figure 3.44), and τ_{hop}/τ_{detrap} ratio is found it is found to be of about 0.26.

By comparing the results reported by Funahashi et al [172] to our data, it becomes clear that for holes trapped by D3HT it is significantly harder to leave their trapped state than for the our case of doping by **F_4TCNQ**. Results reported in their work demonstrate negative effect of DH3T on hole transport, it can even induce complete loss of electronic transport in Smectic A mesophase on higher DH3T loading (50 ppm). In our case, the HOMO of **CTC** lies lower (6.3 eV estimated from DFT calculations, Figure 3.13)

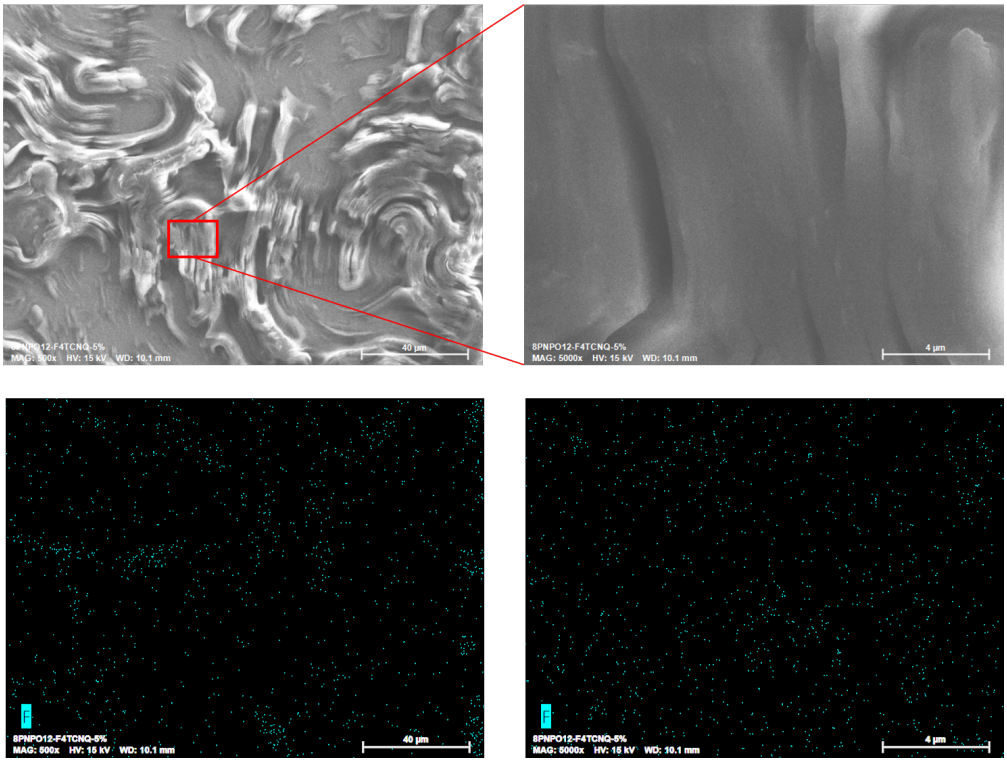

Figure 3.43 – SEM and EDX images corresponding to **c5**. Top: SEM morphology images. Bottom: fluorine elemental mapping of the sample area shown above.

than that of **8-PNP-O12**, thus acting as a potential barrier rather than a trap. It is well-known for the potential barriers to have less negative effects on the carrier transport, since they repel carriers (when traps attract them), thus the carriers have more chances to find their way around the barrier instead of being retained by a trap state [93].

The behavior of mobility in Sm_B mesophase is unexpected. The main challenge in interpretation of results of TOF measurements comes from the observation of orthogonal mobility behavior: hole mobility is rising as a function of increased dopant content in the Sm_B and decreasing in the Sm_A. However, one should consider the two experimental facts:

- As demonstrated by X-ray scattering section, the mesophase order is decreasing as a function of dopant similarly for Sm_B (broadening of intermolecular distance distribution within the smectic layers, Figure 3.19, (a)) and Sm_A (slight increase of layer separation, Figure 3.20)

- The Raman spectra demonstrate the invariant character of charge transfer degree

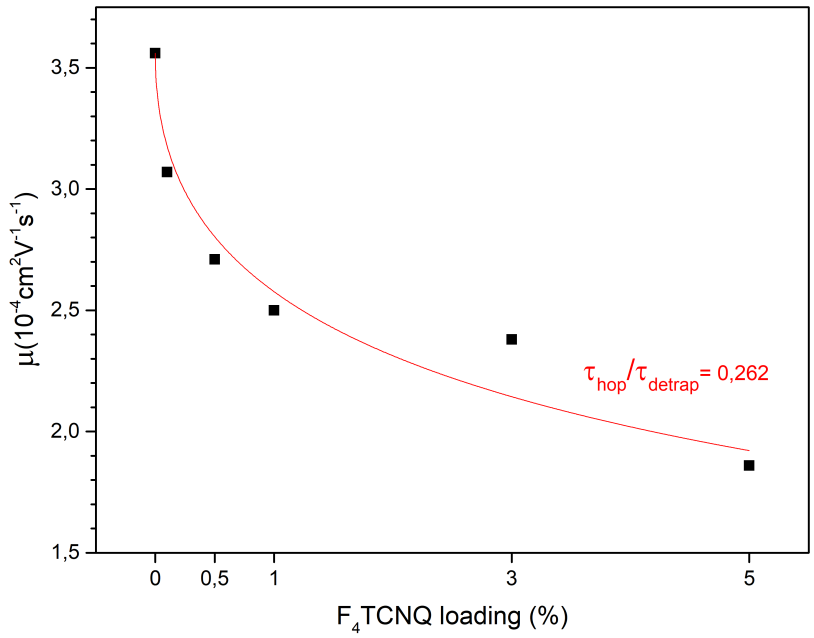

Figure 3.44 – Hole mobility measured in the Sm_A at 115 °C as a function of **F_4TCNQ** concentration. The red line corresponds to the fit with equation 3.2.

between **8-PNP-O12** and **F_4TCNQ** in both smectic phases (Figure 3.30).

These observations do not show any orthogonality of aforementioned properties between two mesophases. Thus, the introduction of **F_4TCNQ** induces some disorder to both mesophases. This rules out, for example, promotion of hole mobility due to order increase or difference in charge transfer degree in between the aforementioned molecules in **CTC**.

It has been widely demonstrated in the literature that some materials, notably, polythiophenes, demonstrate a nonlinear behavior of mobility as a function of dopant concentration. Arkhipov et al. [173] have developed a model which is meant to explain the influence of doping impurity on the charge carrier mobility behavior in bulk OSCs. This model has been successfully applied to the doping of amorphous OSCs, for example P3HT, and may be applied to other materials which exhibit charge transport by carrier hopping (which is the case for **8-PNP-O12**). It describes two doping regimes in regard to the concentration of the dopant content in the OSC: it is proposed that the dopant is able to induce potential traps on low concentrations, where the dopant sites are essentially isolated. For increased concentrations, the overlap of these dopant-induced trap states is able to smooth the potential landscape of the material (i), and alongside with trap filling

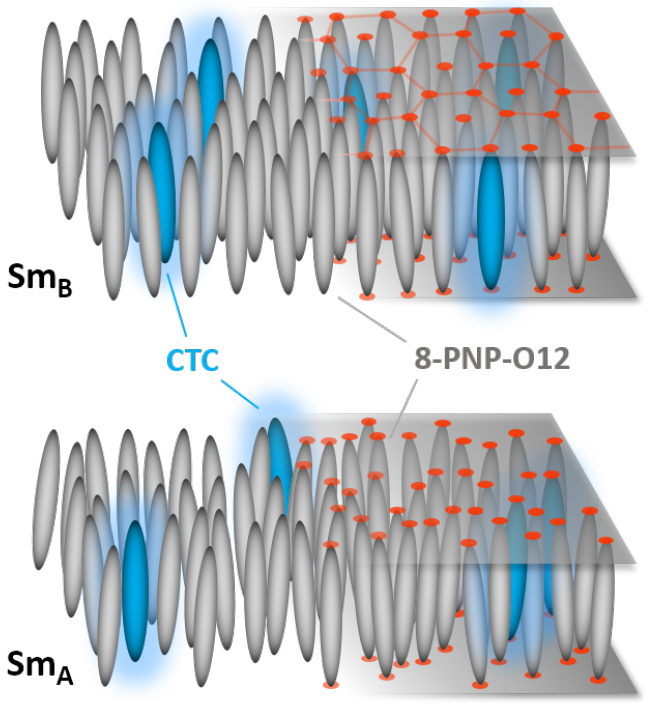

Figure 3.45 – Schematic representation of possible **CTC** distribution in a smectic layer of corresponding mesophase of **8-PNP-O12**.

(ii) by increased charge carrier density, this may be held accountable for the mobility increase.

It is worth noting that due to the homogeneous alignment (i.e. the long molecular axis is parallel to the electrode plane) of the studied samples, the charge transport takes place within the smectic layers. Though the WAXS data demonstrates that the introduction of **F$_4$TCNQ** does not result in the changes of phase sequence of the pristine **8-PNP-O12**, since the smectic phases are maintained in the prepared mixtures. Taking into account the pseudo-hexagonal close range order of the Sm_B mesophase [174], it is possible to propose that the **CTC** moieties are distributed more uniformly within the smectic layers (Figure 3.45, top), contrary to the case of the Sm_A phase, where is no preferred intermolecular order inside of the smectic layer (Figure 3.45, bottom). Thus, the short range order of the Sm_B mesophase is able to maintain the favorable order of **CTC** and adjacent **8-PNP-O12** sites by reducing average distance b and height Δ (Figure 3.46), resulting in reduction of potential barrier between these sites as compared to the case of Sm_A phase (Figure 3.46, bottom). This may result in improved charge

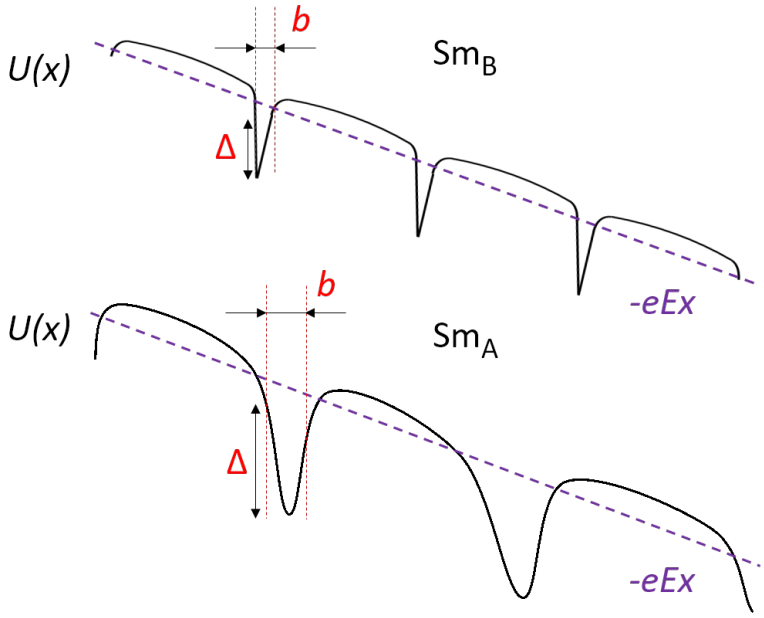

Figure 3.46 – Possible effect of the intermolecular positional order in the smectic layer on the potential distribution in the **8-PNP-O12**/$\mathbf{F_4}$**TCNQ**mixture: U is the potential, E is the external field, b is the width of barriers, Δ is the barrier height and x is the space coordinate.

carrier mobility inside of the smectic layer. However, in the less ordered Sm_A phase, **CTC** is allowed to be less regularly distributed or even aggregated inside the layer, which results in the less favorable overlapping between the potentials of neighboring **CTC** and **8-PNP-O12** sites, and, as a result, increase of potential barrier.

Chen et al [93] have demonstrated that carrier density in doped PTCBI derivative is thermally activated. This result may explain the mobility increase by trap filling in Sm_B and the rise of E_a (Figure 3.41), but the decrease of E_a in Sm_A with increasing $\mathbf{F_4}$**TCNQ** content suggest that traps are generated faster than new carriers. This contradicts to some extent with the phase behavior of the mixtures: $Sm_A \rightarrow Iso$ transition temperature does not show significant shift with dopant concentration increase, which allows us to propose that the stability of Sm_A mesophase is less affected by the dopant presence than that of Sm_B.

If we take a closer look at possible trap filling hypothesis, it is difficult to explain the abrupt mobility decrease in the Sm_A mesophase. The possibility of a drastic change in the carrier density (which from a theoretical standpoint may be also held accountable for the change of mobility by filling the trap states) upon Sm_B to Sm_A transition seems to

be unlikely, especially taking into account thermal activation of carrier density in doped OSCs.

One possible explanation may be that the mobility in the Sm_B mesophase is indeed increased due to the trap filling, and after Sm_B to Sm_A transition, a much higher quantity of traps is abruptly introduced, and the aforementioned trap filling effect is no longer able to compensate the increase in trap density, which results in mobility decrease.

3.3.7 Topology and current mapping of thin polycrystalline films

Thin film deposition

An array of attempts was performed on depositing a thin film of **8-PNP-O12** on oxidated surface (soda lime glass and quartz plates), however, the resulting films were highly non-uniform due to poor wetting properties of the non-polar solvents utilized to dissolve **8-PNP-O12** and its mixtures.

In order to improve the wettability the substrate, the latter has undergone the procedure of OTS-18 coating, as described in the Chapter 2. The solvent choice was based on chemical properties of **8-PNP-O12**: unsurprisingly, best results were demonstrated with chlorinated and aromatic non-polar solvents. Xylene (mixture of isomers, Sigma Aldrich) was chosen due to its higher vapor pressure and viscosity as compared to toluene, in addition to lower toxicity compared to chlorinated solvents (chloroform and chlorobenzene). Films prepared with chloroform-based solutions exhibited numerous defects and overall inhomogenity with obvious signs of solvent evaporation during thinning part of coating process. After testing a vast range of speed, acceleration and duration settings, following parameters were retained, as they tended to give adequate results upon optical observations: speed of 3000 rpm, acceleration of 800 rpm/s and time range between 10 and 45 seconds.

Thickness of prepared films was estimated by means of SEM microscopy after dissection of a substrate with thin film, further mounted on the SEM sample holder. Thickness was measured by examining 4 field of views of 3 µm by 2.25 µm (Figure 3.47), 6 measurements were taken on each field of view. For films prepared at 10s thinning time average thickness was measured to be 633±44nm; for 20s thinning time - 135±12nm. For greater thinning times, the films were found to be non-homogeneous with a significant number of defects.

Conductive atomic force microscopy

Thin films of pure **8-PNP-O12**, **c3** and **c5** were deposited on gold-coated glass slides by previously described spin coating method for duration of 20 seconds. Optical observations

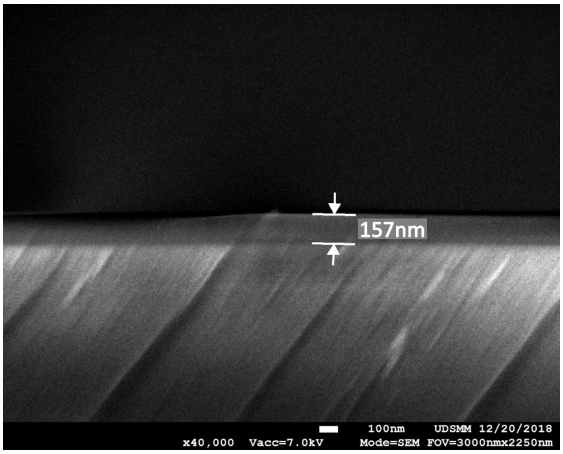

Figure 3.47 – Example of SEM profile of pure **8-PNP-O12** thin film deposited on OTS-18 functionalized soda lime glass at 3000 rpm, 20 seconds, 1% wt **8-PNP-O12** in xylene.

have demonstrated good adhesion on clean gold surface. Further, these films were annealed for 2h at 110 °C (Sm_A), followed with slow cooling speed (1 °C/min) to ambient temperature. The annealing was performed in order to ensure more complete **CTC** formation, as demonstrated in previous subsection dedicated to vibrational spectroscopy. In order to study the topology of the deposited films we have performed AFM analysis in contact mode, as well as current mapping in order to better understand the consequences of the molecular p-doping, which allows us to establish a connection between the topology of the films and charge transporting properties.

Example of topological and conductive properties of pure **8-PNP-O12** thin film is presented in the Figure 3.48. The overall topology shows presence of small grains of **8-PNP-O12** material. The current mapping (recorded at -6V constant bias) reveals strong correlation of conductive regions to the topology of the thin film: it seems that conductive regions follow the cracks and pits found on the surface of thin film. This image also demonstrates behavior expected from a pure material, as relatively flat areas exhibit similar conductivity. It is possible to propose two explanations for this observations: firstly, the collected current is higher due to reduced thickness (and thus, lower resistance); secondly, effective surface of the probe tip is increased upon contact with sloped surface of the crack, increasing current amplitude, which may also explain why crack edges have asymmetric shape in the conductivity mapping image. Selected current-voltage data (scanned from 10 V to −10 V, 2 V/s) confirms the observations of current mapping, with similar voltage threshold values, as well as a symmetric shape, illustrating the ambipolar

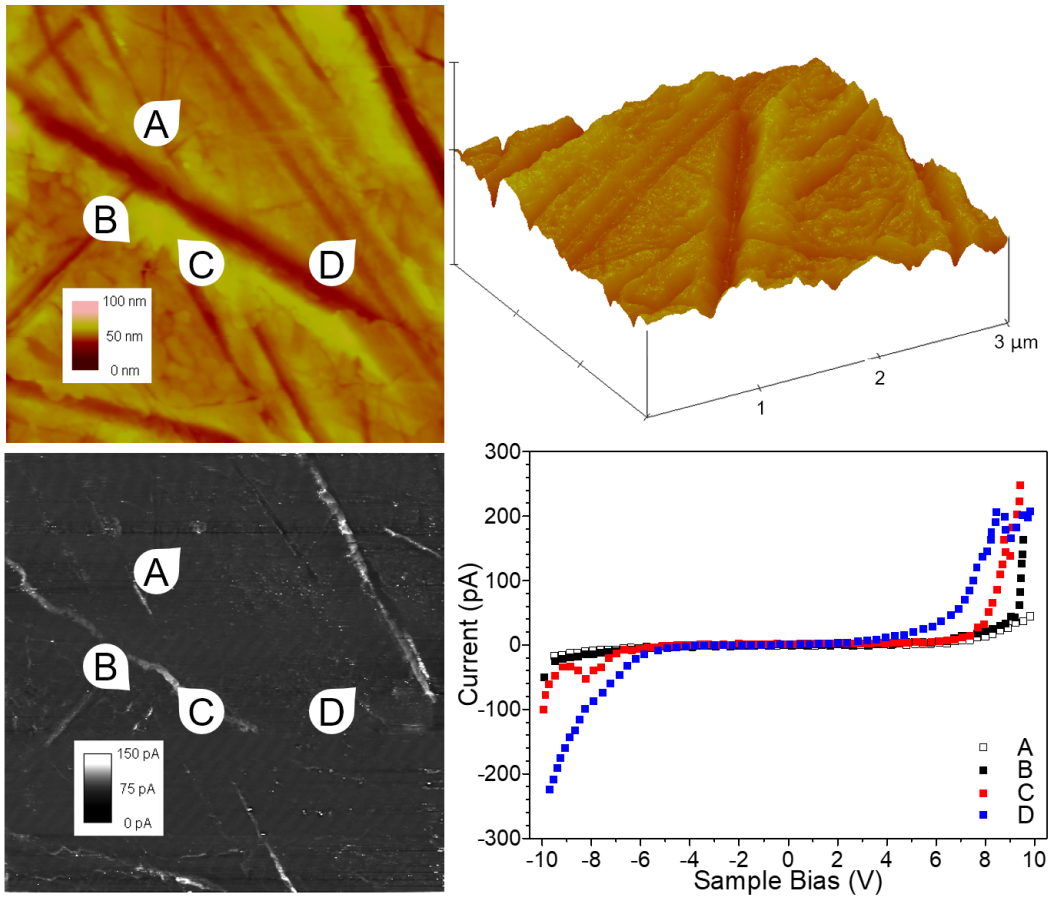

Figure 3.48 – Clockwise: AFM topology image, 3D reconstruction, selected I-V curves and conductivity mapping (constant -6V) of a pure **8-PNP-O12** thin film. Image dimensions are 3 by 3 µm.

nature of charge transport in pure **8-PNP-O12**.

Investigation of **c3** thin film (Figure 3.49) reveals a more complex picture. The topological image shows a more rough surface, while the current map (recorded at -6V constant bias) has more contrast as compared with that of pure **8-PNP-O12**. This also indicates higher overall conductivity of the thin film of **c3**: current-voltage data indicates small change of voltage threshold compared to the pure **8-PNP-O12**. However, it is difficult to quantitatively evaluate this data due to variations in film thickness. One should note the asymmetric shape of these plots, especially in comparison to the data associated with pure **8-PNP-O12** (Figure 3.48): the current data corresponding to negative bias is of noticeably larger amplitude than in the positive bias region. This observation allows us to confirm the validity of preferable p-nature of transport exhibited by the samples

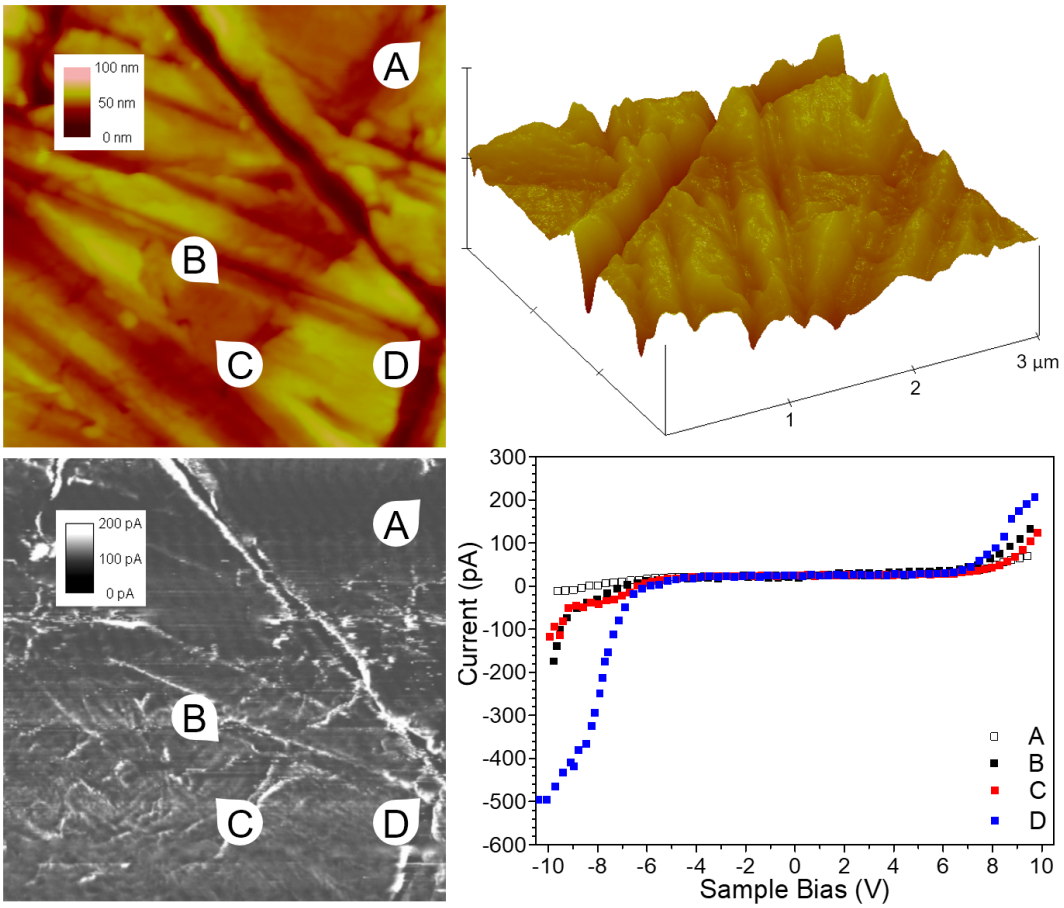

Figure 3.49 – Clockwise: AFM topology image, 3D reconstruction, selected I-V curves and conductivity mapping (constant -6V) of a **c3** thin film. Image dimensions are 3 by 3 µm.

and confirm the doping procedure of **8-PNP-O12** material by **F_4TCNQ**.

It is of interest to take a closer look to the lower left portion of the **c3** AFM image. Figure 3.50 represents a zoomed version of AFM data in Figure 3.49. Despite somewhat soft topological image (which is the consequence of low contact force, necessary for the current mapping), it is possible by correlation with the 3D image to observe the grain boundaries (highlighted with white circles). By comparing these areas with the conductivity mapping, one can conclude that these grain boundaries are more conductive than the surrounding material. In order to explain this observation, we should imagine the pathways which electrical current would take across the sample when electrical field is applied. Hunter et al. [175] have observed similar behavior of small-molecule (2,8-

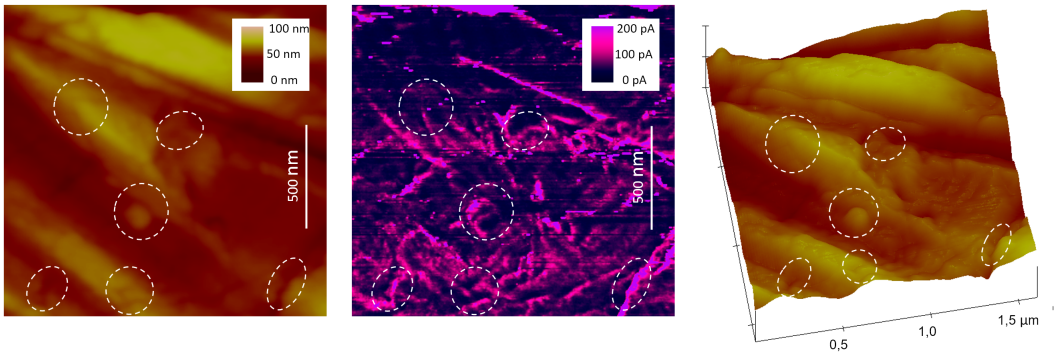

Figure 3.50 – Left to right: AFM topology image, conductivity mapping and a 3D reconstruction of a **c3** thin film. Contrast is artificially enhanced.

difluoro-5,11-triethylsilylethynyl anthradithiophene, **diF-TES ADT**) and amorphous conjugated polymer (poly(triarylamine), **PTAA**) blends which were probed with lateral conductivity C-AFM. In their system, the small semiconducting molecule exhibit better charge transporting properties than the polymer, which resembles the case of the **CTC** dispersed in **8-PNP-O12** host. Current maps of those blends have exhibited a somewhat peculiar current enhancement following grain boundaries with a filament-like structure. A similar structure is observed on the current map of **c3** (Figure 3.50, center). The authors argue that this phenomena may be related to the molecular packing inside of the crystalline grain, which indeed has major influence on the grain's conductivity: in application to small-molecule semiconductors (**8-PNP-O12** and aforementioned **diF-TES ADT**), the transport is favored in the direction of π-stacking, thus, normal to the molecular plane. While performing an area scan, the tip of C-AFM probe may have a better access to these planes of semiconducting material if it happens to cross the grain boundary.

Figure 3.51 represents the results of C-AFM study conducted on the thin film of **c5**. The surface topology is noticeably different to that of pristine **8-PNP-O12**: the roughness is significantly increased (we may relate this observation to the **CTC** acting as an impurity, which interferes with the growth of crystalline thin films of **8-PNP-O12** host [43]). The overall current mapping of this sample confirms the complex picture which we have observed for the **c3**. Selected current-voltage data further demonstrates the predisposition of doped **8-PNP-O12** to enhanced hole transport.

As for the **c3** thin film, we have included a zoomed section of the C-AFM images of **c5** (Figure 3.52). The current mapping reveals highly conductive grain boundaries which are

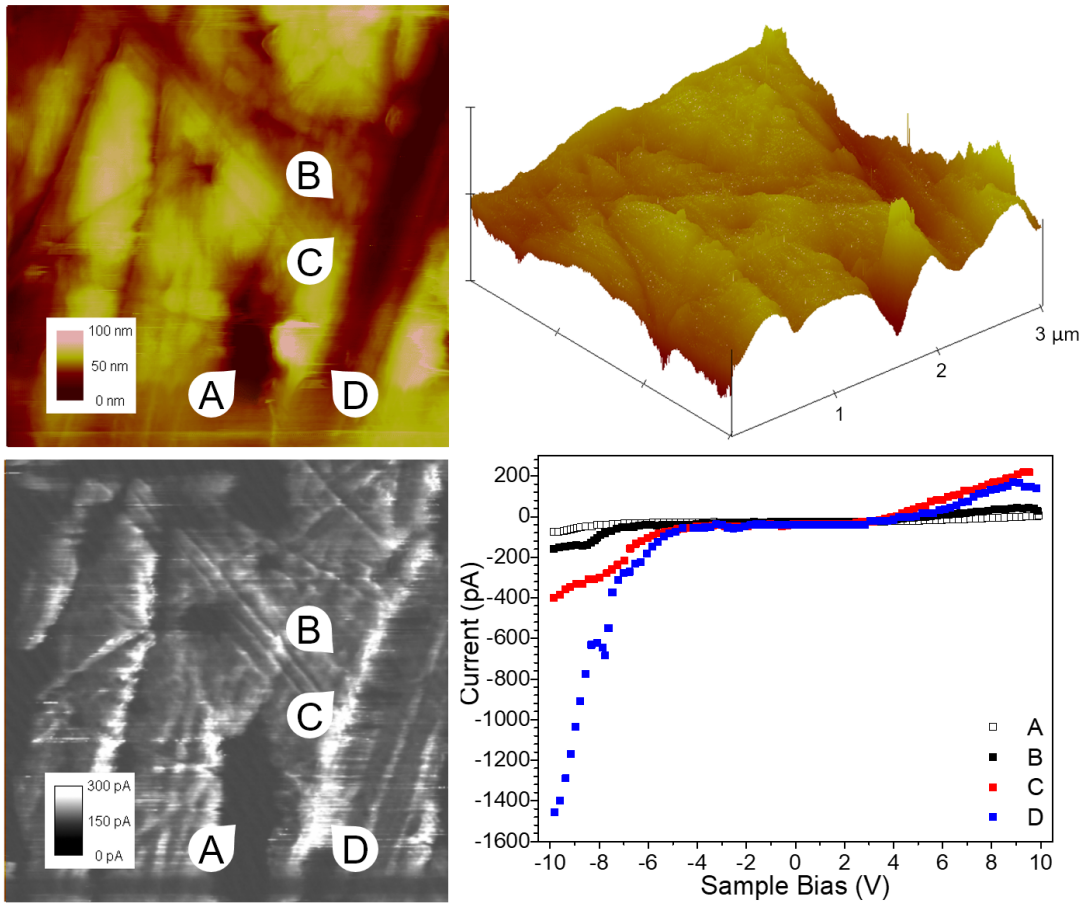

Figure 3.51 – Clockwise: AFM topology image, 3D reconstruction, selected I-V curves and conductivity mapping (constant -6V) of a **c5** thin film. Image dimensions are 3 by 3 µm.

in large contrast with grain summits: relatively low variation of height in order of 10nm (less than 10%) results in more than threefold increase of collected current. Thus, it is possible to suggest that sample thickness is not accountable for the observed phenomena, and the aforementioned explanation of high grain boundary conductivity due to molecular packing appears more adequate.

Conductive AFM has allowed us to establish a link between structural and conductive properties of **8-PNP-O12** doped with **F_4TCNQ** in a form of thin polycrystalline films. We have also validated deposition procedure (spin-coating) whic provides us homogeneous dispersion of dopant sites in the bulk of **8-PNP-O12**. The local curren-voltage characteristics have revealed a noticeable change from ambipolar transport in

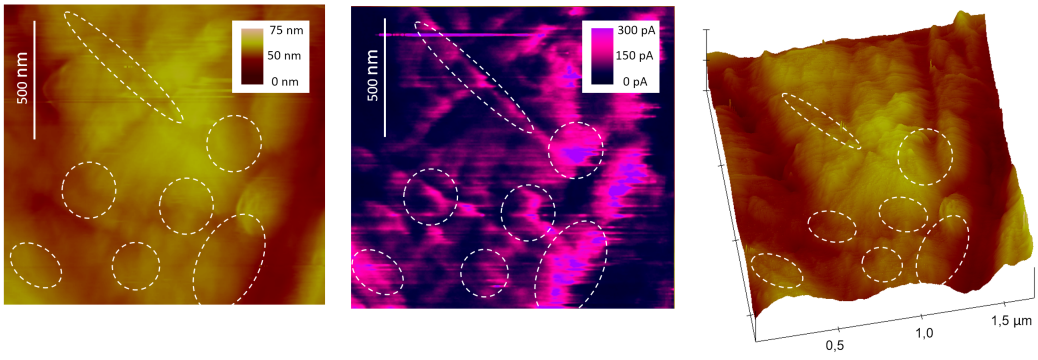

Figure 3.52 – Left to right: AFM topology image, conductivity mapping and a 3D reconstruction of a **c5** thin film. Contrast is artificially enhanced.

pure **8-PNP-O12** to p-type transport in doped mixtures.

3.3.8 Preparation and characterization of a field-effect transistor

The investigation of charge transporting properties of **8-PNP-O12** - **F_4TCNQ** system has led us to an attempt to perform a more realistic test, which directly relates to one of potential applications - field effect transistor. Numerous tests have been conducted on pure **8-PNP-O12** material, including different spin-coating speeds and duration, surface treatment, solvent choice and concentration. No device has exhibited difference between ON and OFF states. These results may be interpreted as a consequences of chosen device geometry (bottom gate - bottom contact), mismatch between the work function of electrode material (gold) and HOMO of **8-PNP-O12**, resulting polycrystallinity, inherent to solution-processing, high contribution of grain boundaries, as well as traces of humidity.

Despite the initially poor results, we have succeeded in preparation of a working device with **c5** material. Figure 3.53 includes two images of a field effect transistor prepared by spin-coating at 3000 rpm for 10s. The substrate (Ossila, UK) was treated with OTS-18 prior to **c5** deposition, the geometry of interdigitated gold electrodes is characterized by channel length L = 50 µm and width W = 18mm.

The initial performance of the device is illustrated on the Figure 3.54. It is clear that application of negative voltage to the gate terminal enhances the conductivity of the device's channel. However, the ON/OFF ratio is found to be low, about 3. It is possible to explain this result by poor quality of semiconductor/insulator interface, where the charge carriers are accumulated when the gate is negatively biased.

We have performed thermal annealing (115 °C for 30 minutes) in order to improve the

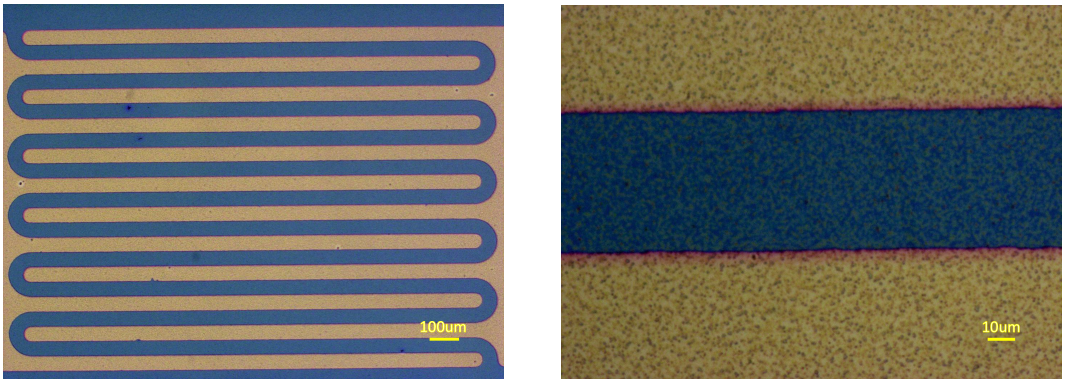

(a) (b)

Figure 3.53 – Microscope captures with 5x lens (a) and 50x lens (b) of an OFET (L = 50 µm, W=18mm) prepared with **c5** mixture, as-spun at 3000 rpm, 10 seconds.

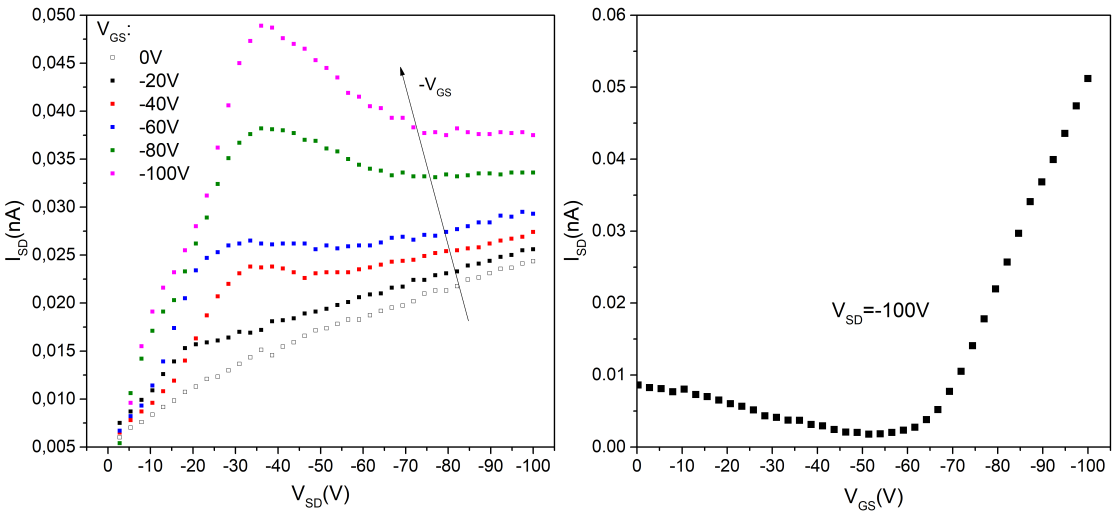

(a) (b)

Figure 3.54 – Output (a) and transfer (b) characteristic of an OFET (L = 50 µm, W=18mm) prepared with **c5** mixture, as-spun at 3000 rpm, 10 seconds.

poor performance encountered in freshly prepared devices. In our case, the annealing in Sm_A phase will help to align the **8-PNP-O12** and **CTC** moieties in the layer adjacent to the dielectric. Moreover, the presence of OTS-18 monolayer should help us to attain homeotropic alignment of the semiconducting molecules, which in turn might enhance charge transport in the plane parallel to the transistor's channel. The substrates were further slowly cooled to ambient temperature in order to minimize thermal stress and

reduce the negative grain boundary effect on the overall performance of the device.

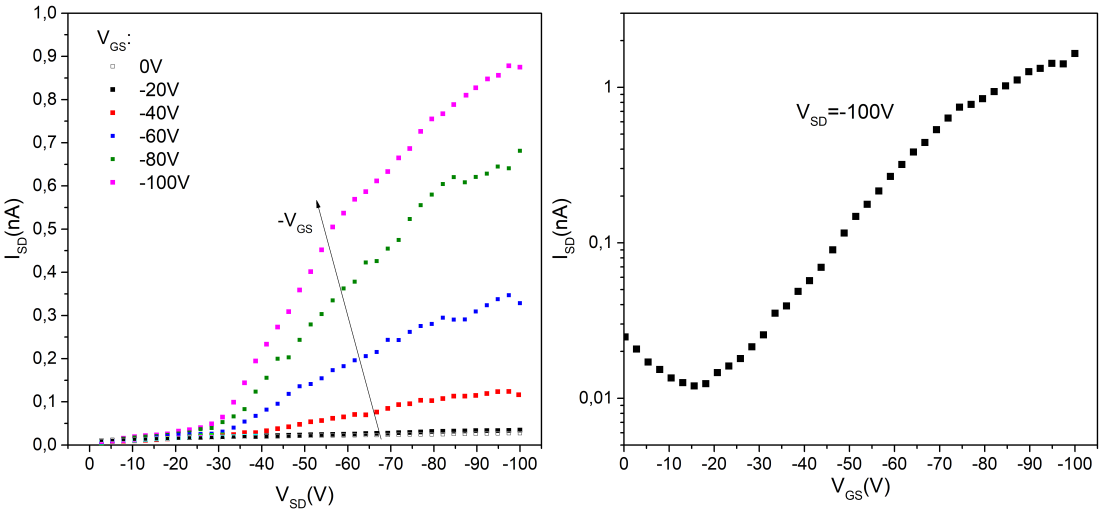

(a) (b)

Figure 3.55 – Output (a) and transfer (b) characteristic of an OFET (L = 50 µm, W=18mm) prepared with **c5** mixture, spun at 3000 rpm, 10 seconds, annealed at 115 °C for 30 minutes.

Figure 3.55 demonstrates characteristics of the same device after thermal annealing. It should be noted that the overall conductivity, as well as the response to gate bias (the field effect) are significantly improved in comparison to the as-prepared OFET. A more prominent effect of thermal annealing is the improvement of threshold voltage: it is reduced from -54.5V to -35.6V (Figure 3.56).

We have extracted hole mobility with the help of equation 1.7 from the saturation current at gate bias V_G = -100V, $\mu = (1.3 \pm 0.6) \times 10^{-8}\,\mathrm{cm^2/(V\,s)}$ as compared to the mobility before annealing $\mu = (1.0 \pm 0.8) \times 10^{-9}\,\mathrm{cm^2/(V\,s)}$. This drastic change is attributed to the enhancement of near-dielectric interface alignment of semiconductor molecules, which corresponds well to the observations of threshold voltage decrease. ON/OFF ratio is also improved from 3 to 83. Despite this improvement, the value of ON/OFF ratio is still low, which is a fundamental consequence of chemically doped materials [36].

The performance of the present mixtures is less than spectacular when compared to the best examples of organic transistors [176]. We also notice here that the extracted hole mobility is significantly lower than that obtained by TOF technique in Sm_B mesophase. This may seem counterintuitive, since the more ordered crystalline phase should be more

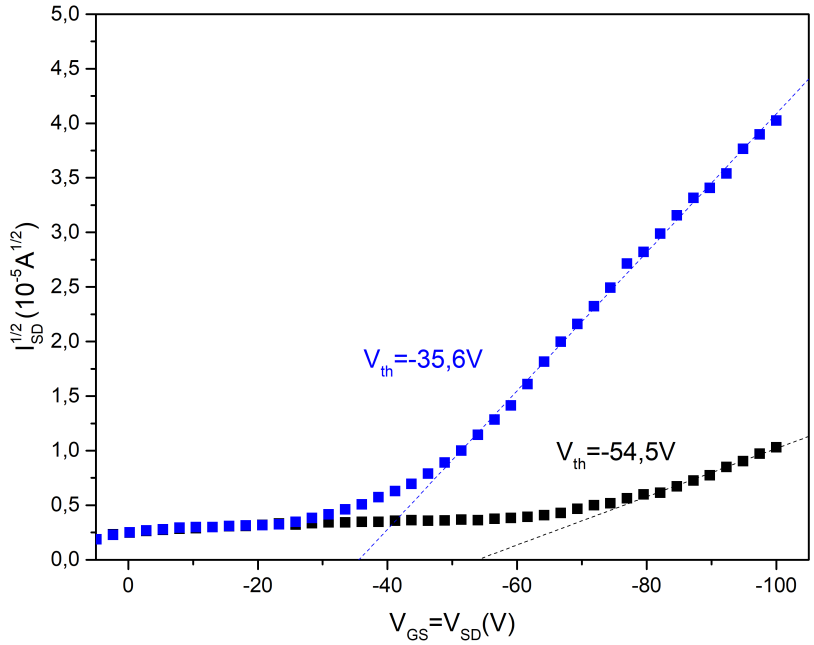

Figure 3.56 – Threshold voltage characteristic of an OFET (L = 50 µm, W=18mm) prepared with **c5** mixture: before (black squares) and after (blue squares) annealing at 115 °C for 30 minutes.

favorable for charge transport, compared with a less-ordered mesophase. The observed low hole mobility in crystalline phase may be explained by significant contribution of structural defects and grain boundaries, as observed by optical (Figure 3.53) and atomic force microscopy (Figure 3.51), which act as a bottleneck for the charge transport.

It is necessary to point out that high-performance devices are usually prepared by utilizing vacuum deposition techniques, where highest molecular order of semiconducting material can be attained. However, application of doping to these deposition techniques is less straightforward, since the doping impurity is usually introduced by co-evaporation [25], which arises additional requirements for the molecular structure of dopant and experimental conditions. The use of solution process, as well as preliminary dispersion of the doping impurity in the host semiconductor significantly simplifies the procedure.

3.3.9 Conclusion

In this work we have explored different aspects of a LC OSC - electron acceptor complex. We have confirmed the stability of LC mesophase up to significant concentrations of introduced **F_4TCNQ**. DFT calculations have allowed us to expect the partial charge

transfer between the host **8-PNP-O12** and the acceptor **F_4TCNQ**, as well as some noticeable molecular geometry change. Furthermore, we have predicted the behavior of **CTC** in optical and vibrational spectroscopy. Experimental data has confirmed that it is indeed possible to distinguish partial and integral charge transfer by UV-Vis-NIR spectroscopy alone.

The Raman spectroscopy has allowed us to probe relatively small content of **CTC** in the host **8-PNP-O12** and obtain a reliable confirmation of the results which we have previously observed in the optical spectra. More importantly, it has provided us a solid proof of the predicted geometry by observation of the previously inactive vibrational bands. This allows us to propose the Raman spectroscopy as a valid tool alongside with IR spectroscopy to quantitatively estimate the amount of charge transfer. It is proposed that the molecular symmetry change upon the formation of **CTC** deserves a more in-depth inspection, since it may result in a significant change of the vibrational signature expressed by the apparition of previously inactive vibrational modes or by a significant change in their intensity and/or frequency. The results of vibrational spectroscopy have also confirmed that the **CTC** is not dependent on the mesophase nature and is thoroughly stable up to isotropic phase.

This observation has enabled us to use the TOF technique to find the bulk hole mobility in the mesophase. It is found that despite the stability of **CTC** remains high across both mesophases, the **CTC** itself has some effects on the mesophase structure. The hole mobility in each mesophase appears to increase with temperature, meaning that some charge trapping takes place. It is proposed that **CTC** is somehow able to disrupt the order within the layers of smectic mesophases, inducing some structural defects which may act as traps. The isolated **CTC** by itself appears to have better charge transporting properties than the pristine **8-PNP-O12** due to the aforementioned change in the geometry. Thus, for the more ordered Sm_B mesophase, the role of structural defects is partially negated by the improvement of the hole mobility of the **CTC** and sufficient overlap of the dopant sites. This can explain why the hole mobility is higher in this mesophase for mixture samples than that of pristine **8-PNP-O12**. However, in the Sm_A mesophase, whose in-layer order is inherently weaker compared to the Sm_B, the structural defects seem to provoke the charge carrier trapping. This explains why the hole mobility decreases with the **F_4TCNQ** content. It is also possible to suggest that the short-scale order of the Sm_A mesophase is more "vulnerable" to the disorder-inducing impurities than that of the Sm_B mesophase, as the resulting from doping charge carrier density increase is not able to compete with introduced traps. Thus, for the more ordered Sm_B mesophase, the role of structural defects may be partially negated by sufficient overlap of the dopant

site potentials resulting from a more homogeneous **CTC** distribution in the layer, or trap filling by increased carrier density, which results in improvement of the hole mobility of the mixtures compared with that of pristine **8-PNP-O12**. In order to gain more insight on the observed mobility behavior it is necessary to reliably estimate the carrier density in both mesophases, which may be proven a non-trivial task due to strong ionic current contribution occurring on DC measurements in Sm_A mesophase.

Generally, it is proposed that for adequate doping results the LUMO of the acceptor should be as close as possible to the HOMO of the donor to ensure efficient electron transfer. In this work we have showed that despite very close energy levels (less than 0.2 eV offset for **8-PNP-O12** and **F_4TCNQ** as opposed to 0.06 eV offset between 4T and **F_4TCNQ** [39]) the charge transfer amount is not strictly proportional to the value of the LUMO of the electron acceptor. We may also connect this behaviour to steric effects induced by the geometry of the pure **8-PNP-O12**. Relatively large dihedral angle (141.57°) between phenyl and naphthalene rings obstructs the access for one wing of the **F_4TCNQ**, which prevents it from being parallel to the molecule of **8-PNP-O12**. The result of this is the incomplete participation of electron-deficient nitrile groups on one wing of the **F_4TCNQ**, which is reflected in the asymmetric hybridization observed on the Figure 3.13. This asymmetry may also explain the results we have observed in the Raman spectra.

The main goal of our work is to postulate the necessity of scrupulous research of factors which reflect the influence of geometry on the efficiency of molecular doping. This underlines the importance of the term "molecular" in this process: (i) choice of the electron donor-acceptor system should be based not only on frontier molecular orbital energy levels, but also on the individual geometry; (ii) the result of donor-acceptor interaction in case of partial charge transfer (**CTC** formation) should be regarded as a unique supramolecular entity in order to predict its properties; (iii) careful attention should be addressed to the application of vibrational spectroscopy, as it is largely influenced by the molecular symmetry; (iv) the nature of change in the charge transport should be properly inspected: the carrier mobility measurement should be accompanied by carrier density estimation in order to obtain the comprehensive picture.

We have made further investigations of mixtures in form of thin polycrystalline films. A protocol for thin film deposition was elaborated, which enabled us to study the resulting thin films with C-AFM technique. We have confirmed preferable p-type nature of the charge transport in the prepared mixtures, as well as established a correlation between the topology of films and C-AFM current. Finally, we have prepared a field effect transistor with the highest-performing concentration, **c5**, which demonstrated encouraging results,

when compared to the attempts on pure **8-PNP-O12**.

3.4 Polymer-stabilized p-doped composites

This section is purposed to study the effects of *in situ* formed polymer network on the p-doped **8-PNP-O12**. As it was demonstrated earlier, the polymer network formed from a nematic reactive mesogen is able to promote the large-scale order and results in a minor decrease of the charge carrier mobility. The p-doped samples however show that it is possible to overcome some negative consequences of positional order decrease by improving charge carrier density and overall homogenity of the smectic layer structure. It is then expected that a polymer network will be able to improve the stability of mesophase in p-doped materials presented previously, increasing their performance.

3.4.1 Materials and sample preparation

The materials in this study were based on the "gel" type composites containing 3% of the reactive mesogen **RM82** (**g3**). This **RM82** concentration was chosen as it gives a reasonable polymeric network density without severe negative impact on the charge transport in the semiconducting matrix. After the gel precursor was prepared, three composite concentrations were elaborated with variable p-dopant content: of 0.1 (**gc1**), 0.5 (**gc2**), 1 (**gc3**) %wt of **F_4TCNQ**. Higher concentrations of **F_4TCNQ** have shown to significantly inhibit the process of photo-activated polymerization.

The prepared composites were placed inside of a LC sandwiched cell by capillary forces on the isotropic temperature, then slowly cooled to the temperature of Sm_B mesophase (90 °C), where the cells were irradiated with 365 nm for 15 minutes, which ensured cross-linking of the **RM82** molecules.

3.4.2 Thermophysical, mesogenic and structural properties

As in the case with all liquid-crystalline materials, prepared precursor mixtures served as an object of **DSC** study. Transition temperatures and peak amplitudes seem to be largely unaffected by the introduction of **F_4TCNQ**. It is of interest to compare the resulting thermograms (Figure 3.57, a) of precursor with those of doped mixtures prepared in previous section. In the case of absence of **RM82**, the phase transition temperature shift is quite noticeable; the most affected phase transition was that of between Sm_B and Sm_A mesophases. However, in case of **RM82** introduction, the phase transition temperatures seem to be stabilized, in contrast to previously described doped system (Figure 3.57, b). It is possible to suggest that stabilization of long-range order by **RM82** is able to prevent the degradation of Sm_B mesophase positional order, previously observed in the case of

p-doped **8-PNP-O12**.

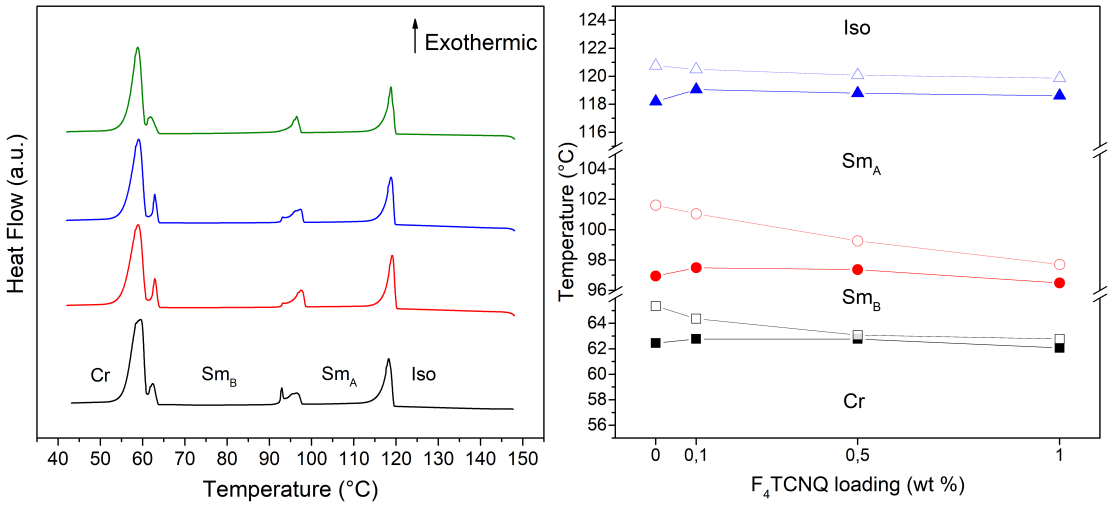

(a) (b)

Figure 3.57 – (a) DSC plots for **g2** (black), **gc1** (red), **gc2** (blue) and **gc3** (green) composites obtained with 10 °C/min cooling program prior to photo-polymerization. (b) Phase transition temperatures of precursor mixtures as a function of **F$_4$TCNQ** concentration: Cr to Sm_B (black squares), Sm_B to Sm_A (red circles) and Sm_A to I (blue triangles). Empty symbols represent transition for doped mixtures without **RM82** from previous section.

The texture of p-doped polymerized samples also unveils some noticeable differences compared to the previously described polymer-stabilized **8-PNP-O12**. The smectic domains (Figure 3.58) are aligned in a less regular way than in samples without **F$_4$TCNQ** (Figure 3.5). It is also possible to notice the size decrease of smectic domains with increasing concentration of **F$_4$TCNQ**, which is also observed in doped mixtures (Figure 3.18).

However, the most interesting change is in the *in situ* formed polymeric network: one can notice that the density of network seems to be inversely proportional to the content of **F$_4$TCNQ** (Figure 3.58, isotropic phase). This can be explained by the inhibition of free-radical mechanism by the doping impurity. Indeed, electron-poor systems including quinoids, chloranil, trinitrotoluene and benzylidene malononitrile are capable of inhibiting the polymerization process [177, 178]. The **F$_4$TCNQ** molecule is able to concur with the functional groups [179] and even form copolymers [180, 181]. Presumably, the **F$_4$TCNQ** molecules interfere with chain propagation, and even sometimes cap the functional groups of **RM82**, thus disrupting the formation of polymer network (Figure 3.59).

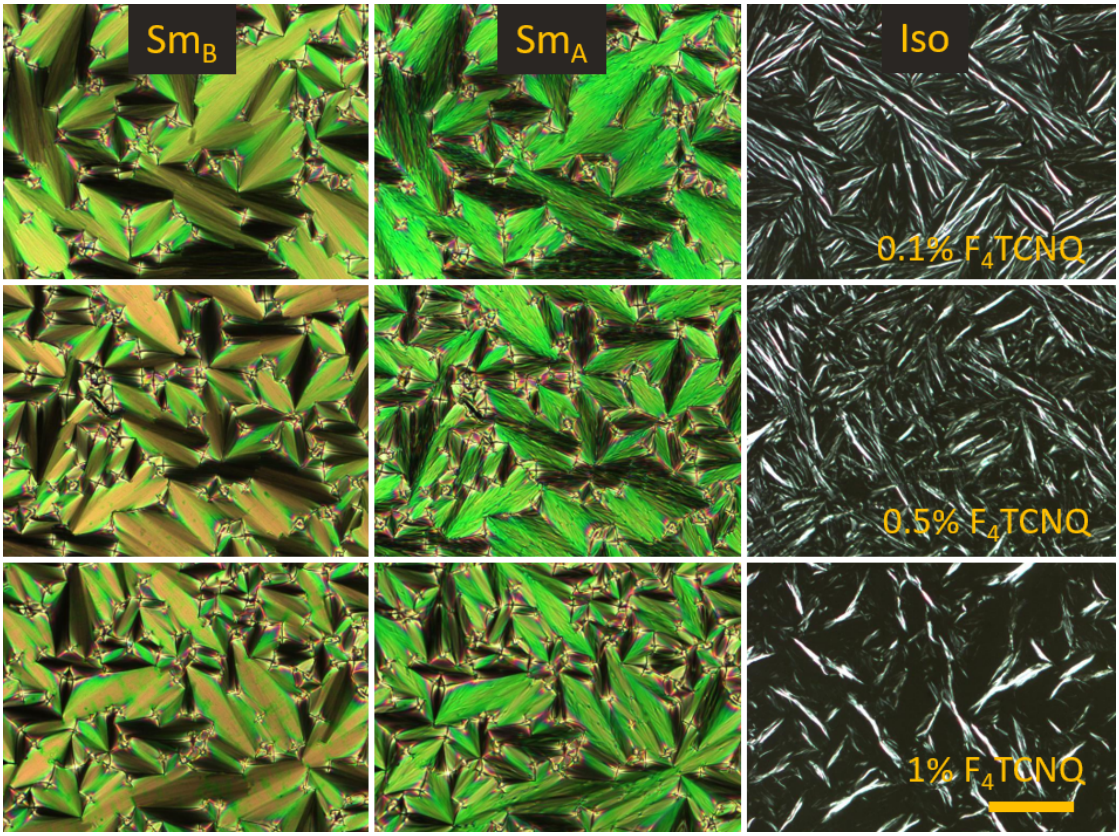

Figure 3.58 – Sample texture under crossed analyzer-polarizer: for polymerized **gc1**, **gc2** and **gc3** (in Sm_B at 85 °C, Sm_A mesophase at 115 °C and isotropic phase at 130 °C). Scale bar represents 100 µm.

3.4.3 Charge transporting properties in smectic mesophases

The charge transport in cross-linked composites was studied by **TOF** technique in both Sm_B and Sm_A mesophases. Measurements were performed for the range of applied electric field E from 20 kV/cm to 44 kV/cm with a step of 4 kV/cm at Sm_B mesophase and from 32 kV/cm to 60 kV/cm with the same step and d=10 µm sample cell thickness.

Transient photocurrent plots for holes are presented in the insets of the Figures 3.60 and 3.61. The profile of a photocurrent decay shows a kink point when plotted in a double logarithmic scale, which corresponds to the charge carrier arrival time, similarly to the previously described case of p-doped mixtures (Figure 3.36).

The charge carrier velocity, v, as a function of applied electric field is presented in the Figures 3.60 and 3.61. v is linearly increasing with respect to the applied field. By comparing this behavior with that previously encountered for polymer stabilized

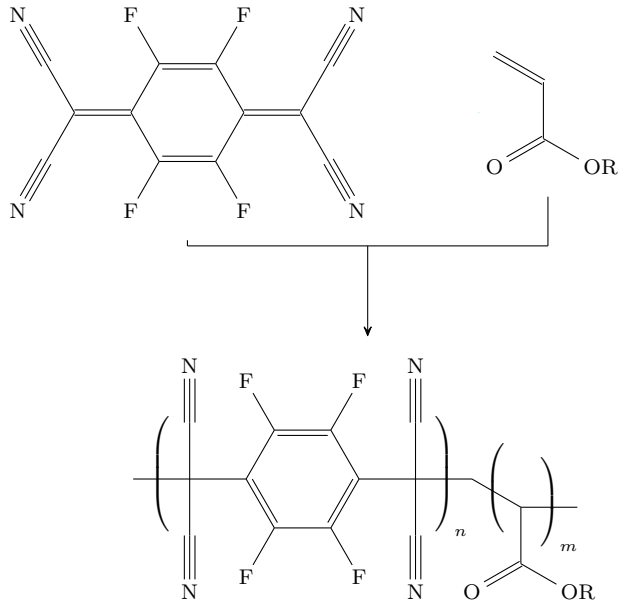

Figure 3.59 – Possible copolymerization mechanism between the **RM82** functional group and **F$_4$TCNQ**.

8-PNP-O12 composites and **F$_4$TCNQ** doped **8-PNP-O12**, we are able to reasonably suggest the same charge transport mechanism as in the pristine **8-PNP-O12**. Both **gc1** and **gc2** composites exhibit quite similar values of hole velocity, however the **gc3** behaves differently. In the case of Sm_B mesophase, the hole velocity of **gc3** is lower than that of the **gc1** and **gc2**. The situation is opposite in Sm_A mesophase. The slope of the velocity in the Sm_A mesophase is increases as the **F$_4$TCNQ** content is rising, showing that introduction of the dopant is favorable for the hole mobility in this mesophase.

The overall behavior of hole mobility for a given mesophase is presented in the Figure 3.62 (a and b). These plots allow us to suggest that composites **gc1** and **gc2** behave similarly despite significant difference in the content of **F$_4$TCNQ**. However, the **gc3** composite shows a decrease of hole mobility in the Sm_B mesophase and a slight increase in Sm_A phase.

Figure 3.63 represents the hole mobility as a function of temperature for the prepared composites in comparison to the **g3**. It is clear that in Sm_B phase, the hole mobility remains independent of the temperature. This is in contrast with our observations of doped **8-PNP-O12** (Figure 3.40), which means that the polymeric network consisting of **RM82** stabilizes the structure of Sm_B phase.

It is also of interest to underline the evolution of hole mobility in the Sm_A phase. Immediately after the Sm_B to Sm_A transition, the hole mobility of **gc1** and **gc2** is

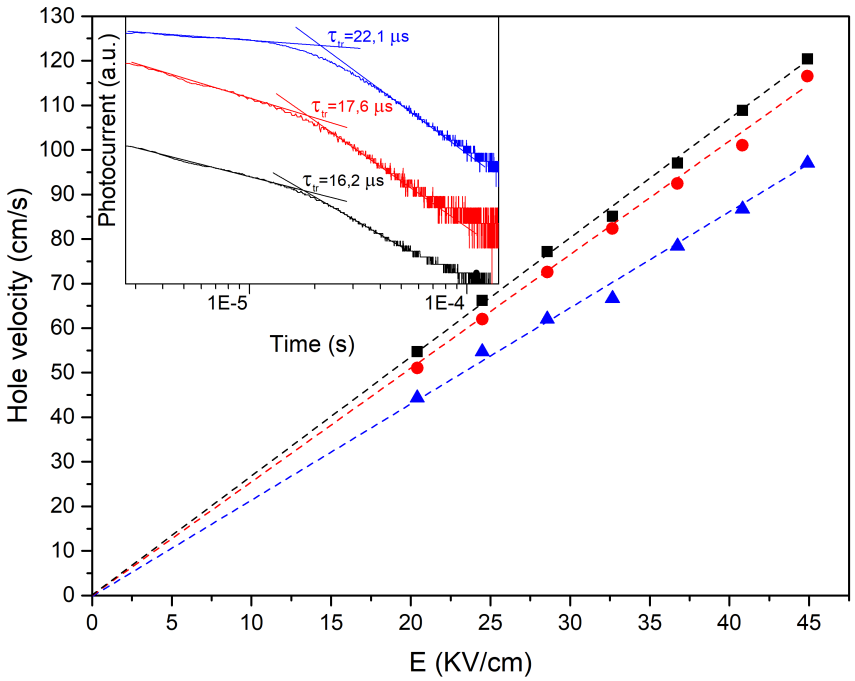

Figure 3.60 – Plot of the hole velocity as a function of applied electric field for polymerized **gc1** (black squares), **gc2** (red circles) and **gc3** (blue triangles) in Sm_B at 85 °C. Inset: Transient photocurrent plots for **gc1** (black), **gc2** (red) and **gc3** (blue) in Sm_B at 20 kV/cm and 85 °C.

comparable with that of the undoped **g2**. However, the evolution of hole mobility in the Sm_A mesophase demonstrates thermal activation, which was also previously encountered in the doped **8-PNP-O12** (Figure 3.40). This observation may be explained by previously discussed broadening of DOS with increased temperature. Thus, thermally activated hole mobility of polymer-stabilized p-doped **8-PNP-O12** is able to overcome the thermally stable mobility of **g2** in the Sm_A mesophase.

The overall contribution of **RM82** polymer network may be concluded by partial stabilization of the p-doped **8-PNP-O12** phases. The Sm_A phase of polymer stabilized p-doped **8-PNP-O12** composites is more prone to the destabilizing effects of **F_4TCNQ**, and despite the minor mobility increase, its behavior is still quite similar to the p-doped **8-PNP-O12** mixtures. We may conclude that *in situ* polymerized reactive mesogen network allows the hole mobility to become more or less decoupled from **F_4TCNQ** concentration, as well as from temperature in Sm_B phase.

In order to address the previously discussed results, as well as to obtain some grounds

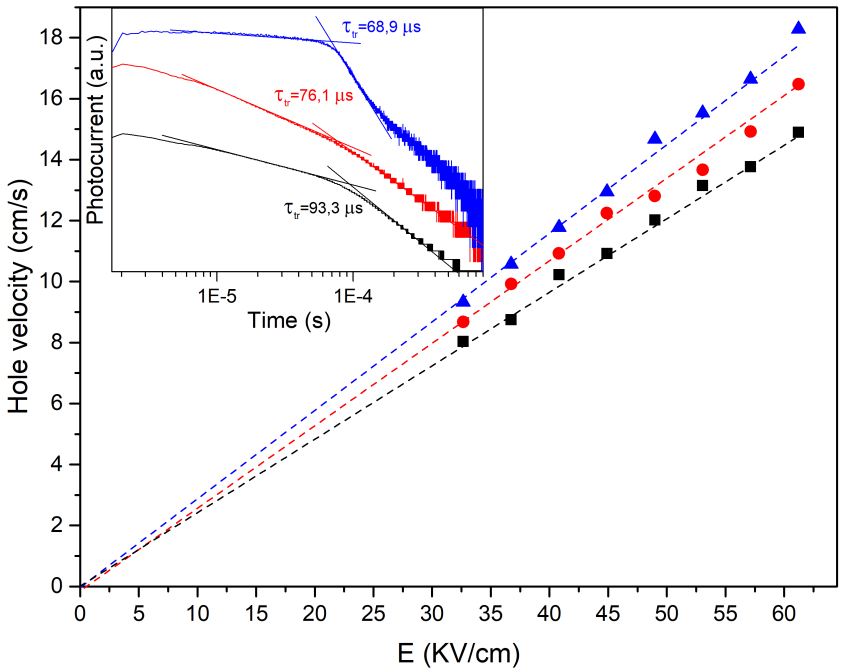

Figure 3.61 – Plot of the hole velocity as a function of applied electric field for polymerized **gc1** (black squares), **gc2** (red circles) and **gc3** (blue triangles) in Sm_A at 115 °C. Inset: Transient photocurrent plots for **gc1** (black), **gc2** (red) and **gc3** (blue) in Sm_A at 34 kV/cm and 85 °C.

for comparison with p-doped **8-PNP-O12** mixtures, we have carried out a similar analysis of **F_4TCNQ** distribution in a sample cell priorly used for TOF measurements. Figure 3.64 shows SEM captures of an opened cell of **gc3** composite. Top images correspond to the SEM morphology and bottom images represent elemental mapping of fluorine.

Images show no correlation of fluorine signatures with topology. This demonstrates that polymer-stabilized composites behaves similarly to p-doped mixtures in regard to the dopant distribution. The absence of dopant aggregation inside of the polymer backbone indicates that the possible copolymerisation side reaction between the **RM82** and **F_4TCNQ** does not take place on high scale nor impedes the formation of the **CTC**, as indicated by enhanced hole mobility.

3.4.4 Conclusion

This brief section illustrates the work aimed to study a potentially cooperative effects of cooperation between the two approaches utilized in previous sections: polymer dispersion

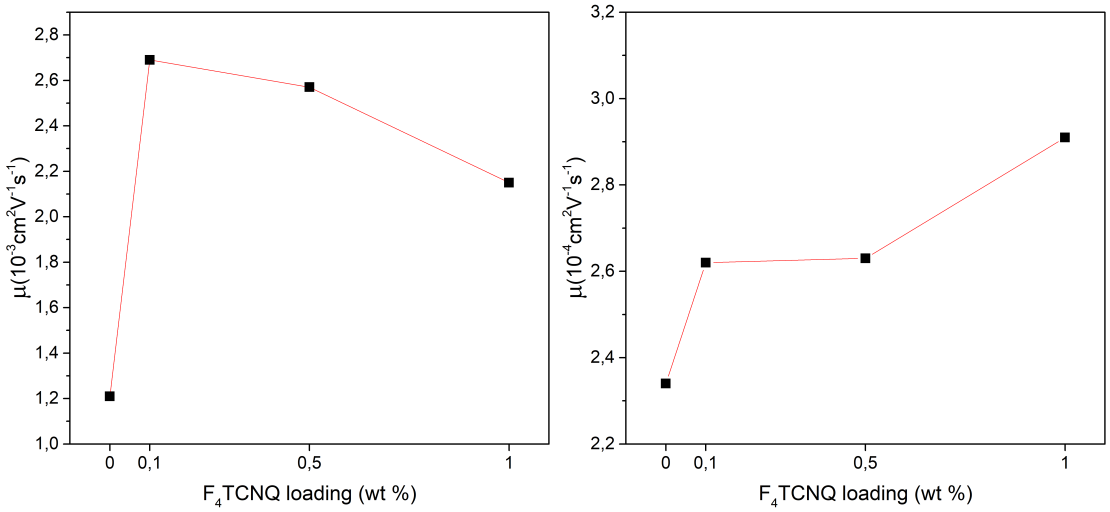

(a) (b)

Figure 3.62 – Hole mobility of polymer stabilized p-doped **8-PNP-O12** composites as a function of $\mathbf{F_4TCNQ}$ content in Sm_B at 85 °C (a) and Sm_A at 115 °C (b).

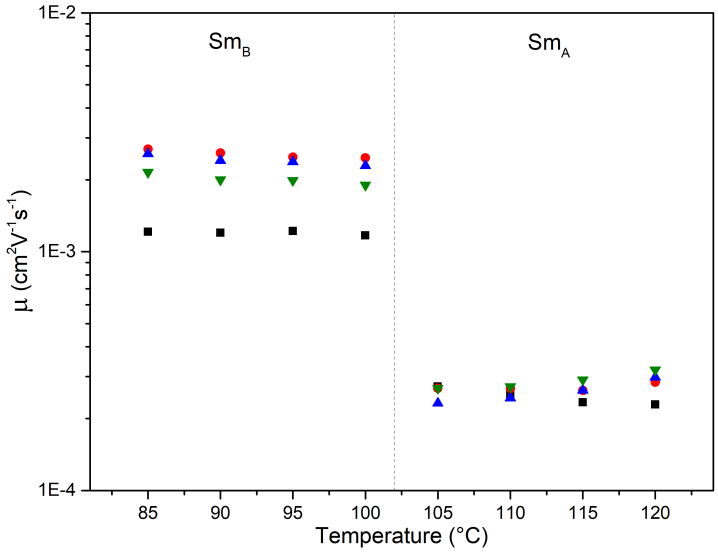

Figure 3.63 – Hole mobility as a function of temperature of samples of **g2** (black squares), **gc1** (red circles), **gc2** (blue triangles) and **gc3** (green triangles).

and molecular doping. Initial results on doped **8-PNP-O12** have shown that the presence of $\mathbf{F_4TCNQ}$ is detrimental to the mesogenic properties of the host **8-PNP-O12**, thus proposing the phase stabilization by polymeric network as a viable solution to mitigate

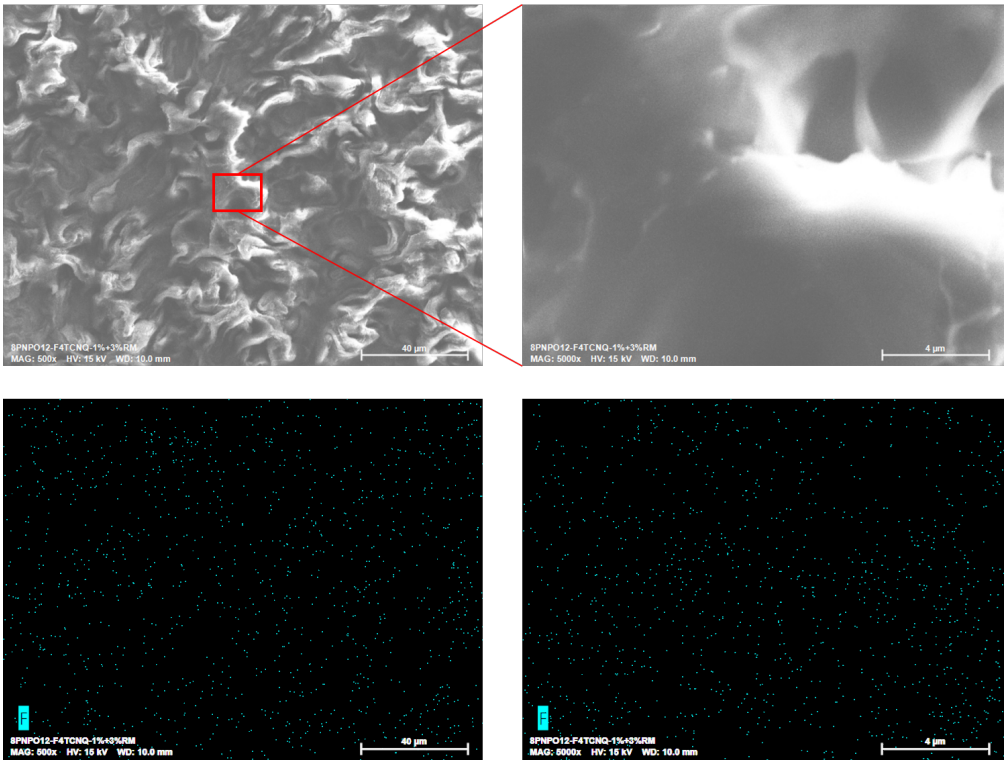

Figure 3.64 – SEM and EDX images corresponding to **gc3**. Top: SEM morphology images. Bottom: fluorine elemental mapping of the sample area shown above.

the effect of the dopant content on structural order. The fact that the **RM82** has good overall affinity with **8-PNP-O12**, as explored in the first section, has given us certain expectations concerning the resulting composite.

One should not forget that in this case we are dealing with a strongly polycomponent system (host semiconductor, doping impurity, reactive mesogen, photoinitiator and thermal inhibitor). It has been widely demonstrated in the field of semiconducting materials that any impurity indeed can and will actively contribute to the charge transporting properties of the host material. We have performed exhaustive studies of the particular cases of p-doped **8-PNP-O12** and polymer-stabilized p-doped **8-PNP-O12**. We have also proposed that some undesirable interaction (e.g. copolymerization) between **F_4TCNQ** and **RM82** may take place. This proposal may indeed explain well the limited compatibility of these two approaches.

In application to the charge transport in the two smectic phases, we have noticed some improvements over the samples without polymer network stabilization: hole mobility was slightly improved, as well as the transition temperate was not as seriously affected by the

F_4TCNQ presence as before. However, larger concentrations of **F_4TCNQ** seem to act against the positive contribution of the **RM82** network, which effectively destabilizes the system and results in slight decrease of hole mobility in the Sm_B phase as the dopant loading increases.

3.5 General conclusion

This chapter exposes the work conducted on the newly developed materials based on **8-PNP-O12** semiconducting liquid crystal. We have performed a thorough characterization of a wide range of host-guest systems based on a well-known liquid crystalline OSC. This allowed us to obtain original and interesting results, which we hope will be useful for the scientific community and help to discover new and better ways to attain higher performance in the field of organic electronics.

It has allowed the author to explore such subfields of condensed matter physics as mesogenic materials and organic electronics, as well as acquire, improve and cement the knowledge of a larger variety of experimental techniques required for physico-chemical characterization of materials. This includes various types of microscopy, spectroscopic techniques, *ab initio* calculations (which were strongly correlated with experimental data), X-ray data treatment and etc. The Time-Of-Flight measurement setup has required the author to acquire knowledge and develop skills of EMI shielding, signal treatment and amplification, software coding and instrument communication. Furthermore, the attempt on device prototyping has allowed the development of skills and knowledge related to thin film deposition and device characterization.

Bibliography of the current chapter

[25] Ching-Lin Fan et al. "Effects of the F4TCNQ-Doped Pentacene Interlayers on Performance Improvement of Top-Contact Pentacene-Based Organic Thin-Film Transistors". In: *Materials* 9.1 (Jan. 2016), p. 46. ISSN: 1996-1944. DOI: 10.3390/ma9010046.

[28] Manisha Bajpai et al. "p-Type doping of tetrafluorotetracynoquinodimethane (F4TCNQ) in poly(para-phenylene vinylene) (PPV) derivative "Super Yellow" (SY)". In: *RSC Adv.* 4.88 (2014), pp. 47899–47905. ISSN: 2046-2069. DOI: 10.1039/C4RA08880H.

[36] Ryonosuke Sato et al. "Charge-Transfer Complexes of Benzothienobenzothiophene with Tetracyanoquinodimethane and the n-Channel Organic Field-Effect Transistors". In: *Journal of Physical Chemistry C* 121.12 (2017), pp. 6561–6568. ISSN: 19327455. DOI: 10.1021/acs.jpcc.7b00902.

[37] P. Pingel and D. Neher. "Comprehensive picture of p-type doping of P3HT with the molecular acceptor F4TCNQ". In: *Physical Review B - Condensed Matter and Materials Physics* 87.11 (2013), pp. 1–9. ISSN: 10980121. DOI: 10.1103/PhysRevB.87.115209.

[38] Daisuke Tadaki et al. "Molecular doping of regioregular poly(3-hexylthiophene) layers by 2,3,5,6-tetrafluoro-7,7,8,8-tetracyanoquinodimethane investigated by infrared spectroscopy and electrical measurements". In: *Japanese Journal of Applied Physics* 54.9 (Sept. 2015), p. 091602. ISSN: 0021-4922. DOI: 10.7567/JJAP.54.091602.

[39] Henry Méndez et al. "Charge-transfer crystallites as molecular electrical dopants". In: *Nature Communications* 6 (2015), p. 8560. ISSN: 20411723. DOI: 10.1038/ncomms9560. arXiv: arXiv:1011.1669v3.

[43] Goudappagouda et al. "Seeded on-surface supramolecular growth for large area conductive donor-acceptor assembly". In: *Chemical Communications* 51.52 (2015), pp. 10439–10442. ISSN: 1364548X. DOI: 10.1039/c5cc03091a. arXiv: 1101.5171.

[45] Sheshanath V. Bhosale et al. "The sensitivity of donor - Acceptor charge transfer to molecular geometry in DAN - NDI based supramolecular flower-like self-assemblies". In: *Scientific Reports* 7.1 (2017), pp. 1–11. ISSN: 20452322. DOI: 10.1038/s41598-017-15599-9.

[46] Veaceslav Coropceanu et al. “Charge transport in organic semiconductors”. In: *Chemical Reviews* 107.4 (2007), pp. 926–952. ISSN: 00092665. DOI: 10.1021/cr050140x. arXiv: 0810.3534.

[59] H. Sirringhaus et al. “Two-dimensional charge transport in self-organized, high-mobility conjugated polymers”. In: *Nature* 401.6754 (1999), pp. 685–688. ISSN: 00280836. DOI: 10.1038/44359. arXiv: arXiv:1011.1669v3.

[65] Jin Sun Kim et al. “A charge-transfer phenomenon between 2,3,5,6-tetrafluoro-7,7,8,8- tetracyanop-quinodimethane (F4TCNQ) and a tetrathiafulvalene-based self-assembled monolayer using an indium-tin oxide electrode”. In: *Bulletin of the Korean Chemical Society* 31.5 (2010), pp. 1415–1418. ISSN: 02532964. DOI: 10.5012/bkcs.2010.31.5.1415.

[74] Masahiro Funahashi and Jun-ichi Hanna. “Fast ambipolar carrier transport in smectic phases of phenylnaphthalene liquid crystal”. In: *Applied Physics Letters* 71.5 (1997), pp. 602–604. ISSN: 0003-6951. DOI: 10.1063/1.119806.

[75] Tohru Toda, Jun-ichi Hanna, and Tadaaki Tani. “Electronic structure and charge injection at interface between electrode and liquid-crystalline semiconductor”. In: *Journal of Applied Physics* 101.2 (Jan. 2007), p. 024505. ISSN: 0021-8979. DOI: 10.1063/1.2424401.

[78] Sanjoy Paul et al. “Photogeneration and enhanced charge transport in aligned smectic liquid crystalline organic semiconductor”. In: *Journal of Applied Physics* 118.13 (Oct. 2015), p. 135702. ISSN: 0021-8979. DOI: 10.1063/1.4931913.

[91] Tobias Wöhrle et al. “Discotic Liquid Crystals”. In: *Chemical Reviews* 116.3 (2016), pp. 1139–1241. ISSN: 15206890. DOI: 10.1021/acs.chemrev.5b00190.

[92] Sheng Gao Liu et al. “Self-organizing liquid crystal perylene diimide thin films: Spectroscopy, crystallinity, and molecular orientation”. In: *Journal of Physical Chemistry B* 106.6 (2002), pp. 1307–1315. ISSN: 10895647. DOI: 10.1021/jp013254v.

[93] Si Guang Chen, Paul Stradins, and Brian A. Gregg. “Doping highly ordered organic semiconductors: Experimental results and fits to a self-consistent model of excitonic processes, doping, and transport”. In: *Journal of Physical Chemistry B* 109.28 (2005), pp. 13451–13460. ISSN: 15206106. DOI: 10.1021/jp0506080.

[112] Naoki Yoshimoto and Jun-ichi Hanna. “Preparation of a novel organic semiconductor composite consisting of a liquid crystalline semiconductor and crosslinked polymer and characterization of its charge carrier transport properties”. In: *Jour-*

nal of Materials Chemistry 13.5 (2003), pp. 1004–1010. ISSN: 09599428. DOI: 10.1039/b209802d.

[117] Yi-Fei Wang, Hiroaki Iino, and Jun-ichi Hanna. "Fabrication of planarly-oriented polycrystalline thin films of smectic liquid crystalline organic semiconductors". In: *Soft Matter* 13.37 (2017), pp. 6499–6505. ISSN: 1744-683X. DOI: 10.1039/C7SM01303E.

[128] Akshay Kokil, Ke Yang, and Jayant Kumar. "Techniques for characterization of charge carrier mobility in organic semiconductors". In: *Journal of Polymer Science, Part B: Polymer Physics* 50.15 (2012), pp. 1130–1144. ISSN: 08876266. DOI: 10.1002/polb.23103.

[130] Ammar A. Khan et al. "Homologous binary mixtures and improved hole conduction of self-assembled discotic liquid crystals". In: *Organic Electronics: physics, materials, applications* 36 (2016), pp. 35–44. ISSN: 15661199. DOI: 10.1016/j.orgel.2016.05.027.

[137] M. J. Frisch et al. *Gaussian 16, Revision A.03*. 2016.

[138] Hiroaki Iino and Jun Ichi Hanna. "Electronic and ionic transports for negative charge carriers in smectic liquid crystalline photoconductor". In: *Journal of Physical Chemistry B* 109.47 (2005), pp. 22120–22125. ISSN: 15206106. DOI: 10.1021/jp0507748.

[139] Dirk J. Broer, Rifat A. M. Hikmet, and Ger Challa. "In-situ photopolymerization of oriented liquid-crystalline acrylates, 4 Influence of a lateral methyl substituent on monomer and oriented polymer network properties of a mesogenic diacrylate". In: *Makromol. Chem.* 190 (1989), pp. 3201–3215. ISSN: 0025-116X. DOI: 10.1002/macp.1989.021901218.

[140] N. Yoshimoto and J. Hanna. "A Novel Charge Transport Material Fabricated Using a Liquid Crystalline Semiconductor and Crosslinked Polymer". In: *Advanced Materials* 14.13-14 (July 2002), pp. 988–991. ISSN: 0935-9648. DOI: 10.1002/1521-4095(20020705)14:13/14<988::AID-ADMA988>3.0.CO;2-Y.

[141] Naoki Yoshimoto, Masahiro Funahashi, and Jun Ichi Hanna. "Charge transport in liquid crystalline semiconductor and crosslinked polymer composite". In: *Molecular Crystals and Liquid Crystals* 409 (2004), pp. 493–504. ISSN: 15421406. DOI: 10.1080/15421400490434162.

[142] K. Kondratenko et al. “Hole transporting properties of discotic liquid-crystalline semiconductor confined in calamitic UV-crosslinked gel”. In: *Journal of Molecular Liquids* 276 (Feb. 2019), pp. 27–31. ISSN: 01677322. DOI: 10.1016/j.molliq.2018.11.137.

[143] Hiroaki Iino, Jun-ichi Hanna, and Dietrich Haarer. “Electronic and ionic carrier transport in discotic liquid crystalline photoconductor”. In: *Physical Review B* 72.19 (Nov. 2005), p. 193203. ISSN: 1098-0121. DOI: 10.1103/PhysRevB.72.193203.

[144] M. Halaby Macary et al. “Electronic and ionic ambipolar transports in the isotropic, SmA, SmB and crystalline phases of a liquid crystal”. In: *Journal of Molecular Liquids* 240 (2017), pp. 564–569. ISSN: 01677322. DOI: 10.1016/j.molliq.2017.05.091.

[145] A. I. Baise, I. Teucher, and M. M. Labes. “Effect of charge-transfer acceptors on dynamic scattering in a nematic liquid crystal”. In: *Applied Physics Letters* 21.4 (1972), pp. 142–143. ISSN: 00036951. DOI: 10.1063/1.1654317.

[146] Hiroshi Moritake et al. “Spontaneous polarization influence of V-shaped switching ferroelectric liquid crystals on pulse driving using active switch”. In: *Japanese Journal of Applied Physics, Part 1: Regular Papers and Short Notes and Review Papers* 45.9 B (2006), pp. 7538–7542. ISSN: 00214922. DOI: 10.1143/JJAP.45.7538.

[147] Lingyun Zhu et al. “Charge transfer in molecular complexes with 2,3,5,6-tetrafluoro-7,7,8,8- tetracyanoquinodimethane (F4-TCNQ): A density functional theory study”. In: *Chemistry of Materials* 23.23 (2011), pp. 5149–5159. ISSN: 08974756. DOI: 10.1021/cm201798x.

[148] Jae Hyun Lee et al. “Effectiveness of p -dopants in an organic hole transporting material”. In: *Applied Physics Letters* 94.12 (2009), pp. 19–22. ISSN: 00036951. DOI: 10.1063/1.3107267.

[149] D. A. Coleman et al. “Polarization-modulated smectic liquid crystal phases”. In: *Science* 301.5637 (2003), pp. 1204–1211. ISSN: 00368075. DOI: 10.1126/science.1084956.

[150] Kheya Sengupta, V. A. Raghunathan, and John Katsaras. “Structure of the ripple phase of phospholipid multibilayers”. In: *Physical Review E - Statistical Physics, Plasmas, Fluids, and Related Interdisciplinary Topics* 68.3 (2003), p. 12. ISSN: 1063651X. DOI: 10.1103/PhysRevE.68.031710.

[151] Kai Liu et al. "Thermotropic liquid crystals from biomacromolecules". In: *Proceedings of the National Academy of Sciences* 111.52 (Dec. 2014), pp. 18596–18600. ISSN: 0027-8424. DOI: 10.1073/pnas.1421257111.

[152] Nataša Vaupotič et al. "Modulated general tilt structures in bent-core liquid crystals". In: *Journal of Materials Chemistry* 18.25 (2008), p. 3044. ISSN: 0959-9428. DOI: 10.1039/b803567a.

[153] Cuiyu Zhang et al. "Two distinct modulated layer structures of an asymmetric bent-shape smectic liquid crystal". In: *Liquid Crystals* 39.9 (2012), pp. 1149–1157. ISSN: 02678292. DOI: 10.1080/02678292.2012.704410.

[154] D. P. Singh et al. "CdSe quantum dots in chiral smectic C matrix: experimental evidence of smectic layer distortion by small and wide angle X-ray scattering and subsequent effect on electro-optical parameters". In: *Liquid Crystals* 00.00 (2018), pp. 1–10. ISSN: 0267-8292. DOI: 10.1080/02678292.2018.1502371.

[155] David A. Dixon, Joseph C. Calabrese, and Joel S. Miller. "Crystal and molecular structure of the 2:1 charge-transfer salt of decamethylferrocene and perfluoro-7,7,8,8-tetracyano-p-quinodimethane: [[Fe(C5Me5)2]+.]2[TCNQF4]2-. The electronic structure of [TCNQF4]n (n = 0, 1-, 2-)". In: *The Journal of Physical Chemistry* 93.6 (1989), pp. 2284–2291. ISSN: 0022-3654. DOI: 10.1021/j100343a019.

[156] Duc T. Duong et al. "The chemical and structural origin of efficient p-type doping in P3HT". In: *Organic Electronics: physics, materials, applications* 14.5 (2013), pp. 1330–1336. ISSN: 15661199. DOI: 10.1016/j.orgel.2013.02.028.

[157] Satoshi Kudoh, Masao Takayanagi, and Munetaka Nakata. "Infrared spectra of Dewar 4-picoline in low-temperature argon matrices and vibrational analysis by DFT calculation". In: *Chemical Physics Letters* 322.5 (May 2000), pp. 363–370. ISSN: 00092614. DOI: 10.1016/S0009-2614(00)00431-0.

[158] Tomoe Osaki and Eiko Soeijima. "Quadratic scaling functions for obtaining Normal vibrational wavenumbers from the B3LYP calculation". In: *Res. Bull. Fukoka Inst. Tech* 42.2 (2010), pp. 129–134.

[159] Brian A. Gregg and Muhammet Erkan Kose. "Reversible switching between molecular and charge transfer phases in a liquid crystalline organic semiconductor". In: *Chemistry of Materials* 20.16 (2008), pp. 5235–5239. ISSN: 08974756. DOI: 10.1021/cm800813h.

[160] Moreno Meneghetti and Cesare Pecile. "Charge–transfer organic crystals: Molecular vibrations and spectroscopic effects of electron–molecular vibration coupling of the strong electron acceptor TCNQF4". In: *The Journal of Chemical Physics* 84.8 (1986), pp. 4149–4162. ISSN: 0021-9606. DOI: 10.1063/1.450086.

[161] Daniele Di Nuzzo et al. "How intermolecular geometrical disorder affects the molecular doping of donor-acceptor copolymers". In: *Nature Communications* 6 (2015), pp. 1–8. ISSN: 20411723. DOI: 10.1038/ncomms7460.

[162] Jian Gao et al. "The effect of 2,3,5,6-tetrafluoro-7,7,8,8-tetracyanoquinodimethane charge transfer dopants on the conformation and aggregation of poly(3-hexylthiophene)". In: *Journal of Materials Chemistry C* 1.36 (Jan. 2013), p. 5638. ISSN: 2050-7526. DOI: 10.1039/c3tc31047g.

[163] E Kampar and O Neilands. "Degree of Charge Transfer in Donor–Acceptor Systems of the π–π Type". In: *Russian Chemical Reviews* 55.4 (Apr. 1986), pp. 334–342. ISSN: 0036-021X. DOI: 10.1070/RC1986v055n04ABEH003193.

[164] Richard J. Bushby and Owen R. Lozman. "Photoconducting liquid crystals". In: *Current Opinion in Solid State and Materials Science* 6.6 (Dec. 2002), pp. 569–578. ISSN: 13590286. DOI: 10.1016/S1359-0286(03)00007-X.

[165] Katherine Hudson et al. "Radiation-induced trapping and charge transport in a smectic liquid crystal". In: *Applied Physics Letters* 87.15 (2005), pp. 1–3. ISSN: 00036951. DOI: 10.1063/1.2099543.

[166] Kian Ping Gan et al. "Guanine-oligothiophene conjugates: Liquid-crystalline properties, photoconductivities and ion-responsive emission of their nanoscale assemblies". In: *Chemical Science* 9.3 (2018), pp. 576–585. ISSN: 20416539. DOI: 10.1039/c7sc03764c.

[167] B. Lüssem, M. Riede, and K. Leo. "Doping of organic semiconductors". In: *Physica Status Solidi (A) Applications and Materials Science* 210.1 (2013), pp. 9–43. ISSN: 18626300. DOI: 10.1002/pssa.201228310.

[168] X Jiang et al. "Doping-induced change of carrier mobilities in poly(3-hexylthiophene) films with different stacking structures". In: *Chemical Physics Letters* 364.5-6 (Oct. 2002), pp. 616–620. ISSN: 00092614. DOI: 10.1016/S0009-2614(02)01383-0.

[169] I. Shiyanovskaya et al. "Electronic transport in smectic liquid crystals". In: *Physical Review E - Statistical, Nonlinear, and Soft Matter Physics* 65.4 (2002), pp. 1–13. ISSN: 15393755. DOI: 10.1103/PhysRevE.65.041715.

[170] Guangzheng Zuo et al. "Molecular Doping and Trap Filling in Organic Semiconductor Host-Guest Systems". In: *Journal of Physical Chemistry C* 121.14 (2017), pp. 7767–7775. ISSN: 19327455. DOI: 10.1021/acs.jpcc.7b01758.

[171] Jun-ichi Hanna, Akira Ohno, and Hiroaki Iino. "Charge carrier transport in liquid crystals". In: *Thin Solid Films* 554.4 (2014), pp. 58–63. ISSN: 00406090. DOI: 10.1016/j.tsf.2013.10.051.

[172] Masahiro Funahashi and Jun Ichi Hanna. "Impurity effect on charge carrier transport in smectic liquid crystals". In: *Chemical Physics Letters* 397.4-6 (2004), pp. 319–323. ISSN: 00092614. DOI: 10.1016/j.cplett.2004.08.125.

[173] I. V. Arkhipov et al. "Weak-field carrier hopping in disordered organic semiconductors: The effects of deep traps and partly filled density-of-states distribution". In: *Journal of Physics Condensed Matter* 14.42 (2002), pp. 9899–9911. ISSN: 09538984. DOI: 10.1088/0953-8984/14/42/305.

[174] C. C. Huang. "Non-Chiral Smectic Liquid Crystals: Physical Properties of Non-Chiral Smectic Liquid Crystals". In: *Handbook of Liquid Crystals*. Weinheim, Germany: Wiley-VCH Verlag GmbH, 1998, pp. 441–469. DOI: 10.1002/9783527620555.ch5b.

[175] Simon Hunter and Thomas D. Anthopoulos. "Observation of unusual, highly conductive grain boundaries in high-mobility phase separated organic semiconducting blend films probed by lateral-transport conductive-AFM". In: *Advanced Materials* 25.31 (2013), pp. 4320–4326. ISSN: 09359648. DOI: 10.1002/adma.201300020.

[176] Daniele Braga and Gilles Horowitz. "High-Performance organic field-effect transistors". In: *Advanced Materials* 21.14-15 (2009), pp. 1473–1486. ISSN: 09359648. DOI: 10.1002/adma.200802733.

[177] John L. Kice. "Inhibition of Polymerization. I. Methyl Methacrylate". In: *Journal of the American Chemical Society* 76.24 (1954), pp. 6274–6280. ISSN: 15205126. DOI: 10.1021/ja01653a014.

[178] Ju Yeon Lee et al. "Synthesis and free radical polymerization of vinyl ethers containing two electron acceptors". In: *Bulletin of the Korean Chemical Society* 20.11 (1999), pp. 1355–1358. ISSN: 02532964.

[179] Shouji Iwatsuki, Takahito Itoh, and Kuniyasu Horiuchi. "Spontaneous Alternating Copolymerization of Tetracyanoquinodimethane with Styrene". In: *Macromolecules* 11.3 (1978), pp. 497–500. ISSN: 15205835. DOI: 10.1021/ma60063a014.

[180] Shouji Iwatsuki and Takahito Itoh. "Alternating Copolymerization of 7,7,8,8-Tetracyanoquinodimethane with Methyl Methacrylate in Acetonitrile". In: *Macromolecules* 16.2 (1983), pp. 332–335. ISSN: 15205835. DOI: 10.1021/ma00236a033.

[181] Yusuke Washino and Tsuyoshi Michinobu. "Cross-linking and postfunctionalization of polymer films by utilizing the orthogonal reactivity of 7,7,8,8-tetracyanoquinodimethane". In: *Physical Chemistry Chemical Physics* 18.4 (2015), pp. 2288–2291. ISSN: 14639076. DOI: 10.1039/c5cp05180k.

Chapter 4

Novel liquid crystalline semiconductor based on anthracene

4.1 Introduction

We present synthesis and characterization of a novel liquid crystalline semiconductor in the current chapter. This molecule will become the first step in the direction which final goal is to prepare a photo-reactive organic LC semiconductor in order to prepare aligned cross-linked films for potential applications. We have conceived an easy-to-synthesize

semiconductor which is based on inexpensive and readily available precursors. First, we present a brief overview of the semiconductors based on the building block of choice - anthracene. Further, we describe synthetic procedure, as well as characterization of the chemical structure in order to prove that proposed synthetic route indeed affords the expected molecule. The next step is to present some fundamental properties of the molecule: band gap energy, frontier molecular energy levels, thermo-physical properties. Charge transport is investigated by preparation of a field-effect transistor. Finally, we investigate remarkable photoconducting properties of the molecule in scope, which may be relevant for potential light-sensitive applications.

4.2 Elaboration of (E)-N-(anthracen-2-yl)-1-(4-(decyloxy) -phenyl)methanimine

4.2.1 Overview of anthracene-based semiconductors

As we have already mentioned in the introduction to Chapter 1, one of the first evidence of charge transport in organic molecules was discovered in anthracene crystals. Since then, enormous progress has been made in this field, and many other molecules have been identified as promising organic semiconductors. Nevertheless, anthracene still attracts significant attention as a building block for the OSC materials.

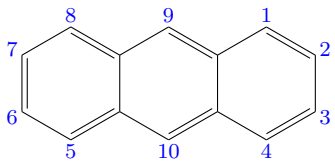

Figure 4.1 – Substituent indexing of anthracene molecule.

Indeed, the anthracene molecule presents a vast array of opportunities as a building block (Figure 4.1): large diversity of symmetric and asymmetric derivatives in end- (2, 3, 6, 7) as well as peri- (1, 4, 5, 8, 9, 10) positions has been synthesized; with their charge transporting properties investigated over last decades. Many attempts were made to increase the size of π-conjugated backbone by attaching aromatic fragments symmetrically to end positions (phenyl [182], μ_{hole}*= 34 $cm^2/(V\,s)$; naphthalene [183], μ_{hole}* = 1.4 $cm^2/(V\,s)$; anthracene, [184] μ_{hole}* = 0.13 $cm^2/(V\,s)$; thiophene , μ_{hole}* = 0.037 $cm^2/(V\,s)$; etc.). These efforts have proven the great potential of anthracene, and in addition to improving charge transport, significant efforts were dedicated to improve the processability.

*These mobilities were measured for a single crystal field effect transistor.

Use of (triisopropylsilyl)ethynyl (TIPS) functional groups is a remarkable example of improvement of solubility, with a (9,10)-TIPS-functionalized molecule substituted with naphthalene in 2,6-positions which attained $\mu_{hole} = 3.7\,\mathrm{cm}^2/(\mathrm{V\,s})$ [185].

In fact, favorable conditions for charge transport, such as strong $\pi - \pi$ overlap which may lead to enhancement of transfer integral and improve charge hopping from site to site may seem counterintuitive for the liquid crystalline properties, since they demand a certain degree of "flexibility" for intermolecular order, notably, inside of the smectic layer, where $\pi - \pi$ interactions are strong. This makes a creation of a mesogenic molecule with a reasonable mesophase temperature range a non-trivial task. It is now of interest to address some anthracene-based liquid crystals which possess semiconducting properties. Meŕy et al have made a significant contribution to the investigation of 2,6-substituted anthracene derivatives[186]: it was found that direct attachment of flexible alkyl chains to the end positions of anthracene is not sufficient to obtain mesomorphic properties. Insertion of additional phenyl moieties between the anthracene and alkyl spacer has allowed not only to increase the overall flexibility of the molecule (which increases probability to attain mesomorphic properties), but to additionally increase the size of π-conjugated backbone. However, it is worth mentioning that hole mobility measured in Sm_C and Sm_A mesophases were of about $2 \times 10^{-3}\,\mathrm{cm}^2/(\mathrm{V\,s})$ at maximum, which is of the same order of value as for **8-PNP-O12** molecule in Sm_B mesophase. In addition to relatively small gain in hole mobility, the mesomorphic behaviour was exhibited on very high temperature ($> 200\,^\circ\mathrm{C}$).

Another interesting (and insoluble) molecule was prepared recently by Chen et al [187]: it is a 2-substituted derivative of anthracene, which in addition to semiconducting properties exhibits photosensitivity due to incorporation of an azo-group. This substance has a relatively lower mesophase transition temperature (about $140\,^\circ\mathrm{C}$), which makes it more convenient to investigate its charge transport. The cooperative effects of UV-irradiation (molecular structure rearrangement) and thermal annealing (crystalline order improvement) have resulted in mobility increase from $0.019\,\mathrm{cm}^2/(\mathrm{V\,s})$ to $0.746\,\mathrm{cm}^2/(\mathrm{V\,s})$.

4.2.2 Synthetic route

After extensive literature study, we have developed a new molecule ((E)-N-(anthracen-2-yl)-1-(4-(decyloxy)-phenyl)methanimine or **10-OPIA**, Figure 4.2) which can be prepared easily from commercially available substrates: the phenyl moiety is attached to anthracene by an imine linkage which can be created by a simple nucleophilic addition between 2-aminoanthracene and para-benzaldehyde derivatives. This method can be more straight-

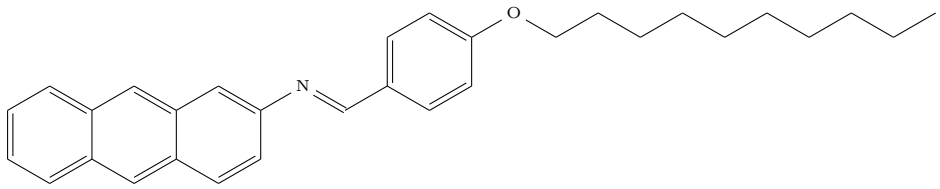

Figure 4.2 – (E)-N-(anthracen-2-yl)-1-(4-(decyloxy)-phenyl)methanimine (**10-OPIA**)

forward than a creation of C-C bond by usual methods, for example, Suzuki coupling (which requires inert atmosphere, expensive precursors and catalysts). The length of alkyl spacer can be efficiently controlled by choosing an appropriate alkyl halide precursor.

Alkylation of para-hydroxy-benzaldehyde

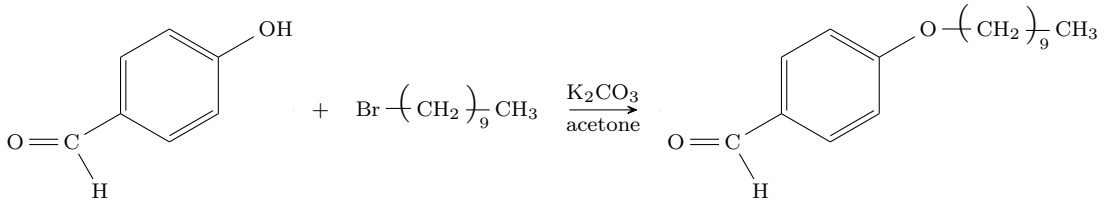

Figure 4.3 – Alkylation of para-hydroxy-benzaldehyde with 1-bromo-decane

The **10-OPIA** synthesis was performed in collaboration with the Laboratory of Natural and Synthetic Polymers, Gheorghe Asachi Technical University (Iaşi, Romania). It begins with the alkylation of para-hydroxy-benzaldehyde (Figure 4.3). The mechanism of this reaction is a simple alkylation (Williamson ether synthesis). We placed 0.3 g of para-hydroxy-benzaldehyde (Sigma Aldrich) in a round bottom flask with 0.65 g of 1-bromo-decane (molar ratio 1.2 to 1 with para-hydroxy-benzaldehyde). 0.41 g of K_2CO_3 (the same molar ratio with 1-bromo-decane) was added to the reagents to serve as a base for the alkylation reaction. Finally, 15 ml of acetone were introduced, and the mixture was set to reflux with stirring for two days (about 48 h). After the reaction was finished, we have filtered the resulting suspension on a sintered glass buchner funnel to remove K_2CO_3. The acetone was evaporated and the crude para-decyloxy-benzaldehyde (**PDBA**) was purified by column chromathography: the reaction product was suspended on the silica gel and then eluted with a mixture of dichloromethane/hexane $\sim$ 1:1 ratio. This procedure allowed us to recover 0.53 g of **PDBA** which corresponds to 82% yield.

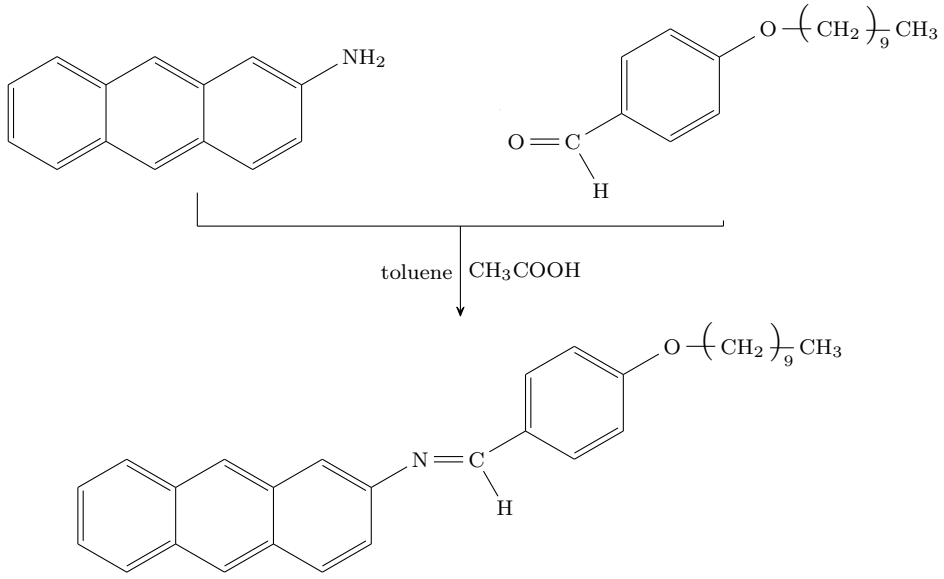

Figure 4.4 – Condensation of para-decanoxy-benzaldehide with 2-amino-anthracene (**2-AA**)

Imine coupling

The next reaction allows us to obtain the desired compound **10-OPIA** (Figure 4.4). To perform this reaction, we have placed in a round bottom flask 0.53 g of the purified **PDBA** which we have obtained previously with 0.39 g of 2-amino-anthracene (**2-AA**). The initial products were dissolved in 25 ml of toluene, and a few drops of glacial acetic acid were introduced as a catalyst. The reaction mixture is allowed to reflux with stirring for two days (about 48 h). The final product precipitated from the reaction mixture upon cooling, and was filtered and washed with cold toluene to remove unreacted compounds and further with acetone to remove toluene. The crude **10-OPIA** was dried in the oven and then recrystallized in small amount of chloroform to improve the purity of final product. Finally, we have obtained 0.55 g of **10-OPIA** which corresponds to 57% yield. Additionally, a Dean-Stark trap may be employed to remove water from the reaction and improve yield.

4.2.3 Characterization of the chemical structure

Synthesis of a novel material requires an extensive and unambiguous investigation of its molecular structure in order to confirm the proposed interpretations of the encountered physical and/or chemical properties. Figure 4.5 allows us to map the atoms of interest (notably, hydrogen and carbon) in order to discuss the further results obtained from the NMR spectroscopy.

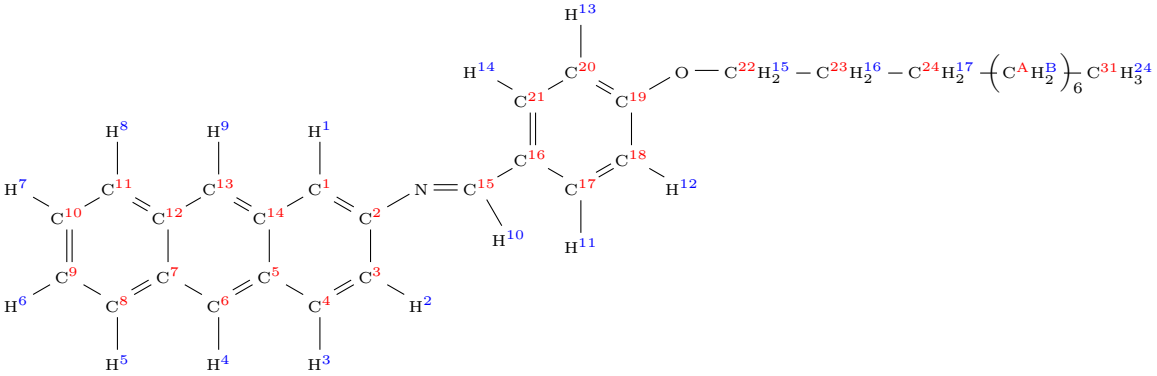

Figure 4.5 – Carbon (red) and hydrogen (blue) atom indexing for **10-OPIA** molecule. Index A correspond to carbon atoms from 25 to 30; index B corresponds to hydrogens from 18 to 23.

NMR spectroscopy

The ^{1}H NMR spectrum of **10-OPIA** is presented in Figure 4.6.^{1}H spectrum found: ^{1}H-NMR (400 MHz, $CDCl_3$) δ = 8.58 (*s*, H^{10}); 8.41 (2*s*, J = 2.6 Hz, H^4 & H^9); 8.02 (*m*, H^3, H^5 & H^8); 7.91 (*d*, J = 8.7 Hz, H^{11} & H^{14}); 7.70 (*s*, H^1); 7.45 (*m*, H^2, H^6 & H^7); 7.00 (*d*, J = 8.7 Hz, H^{12} & H^{13}); 4.04 (*t*, J = 6.6 Hz, H^{15}); 1.82 (*m*, H^{16}); 1.48 (*m*, H^{17}); 1.30 (*m*, H^{18-23}); 0.89 (*t*, J = 6.9 Hz, H^{24}) ppm.

The signals situated in the aromatic part of the spectrum show presence of seven unique proton environments, which integrate to the total number of 14 protons, which assignments are listed previously. The single proton of the imine linkage can be identified at δ = 8.58 ppm. This part of the spectrum also contains the signal of trace ammouns of $CHCl_3$ present at $CDCl_3$ as a singlet at δ = 7.26 ppm. Aliphatic part of the spectrum allows us to observe 4 proton environments, which integrate to the total of 21 atoms, as expected for the alkyl chain. The signal at δ = 1.56 ppm is assigned to the trace water content in the sample.

Observations of ^{1}H COSY spectrum (Figure 4.7) allows us to confirm the assignments

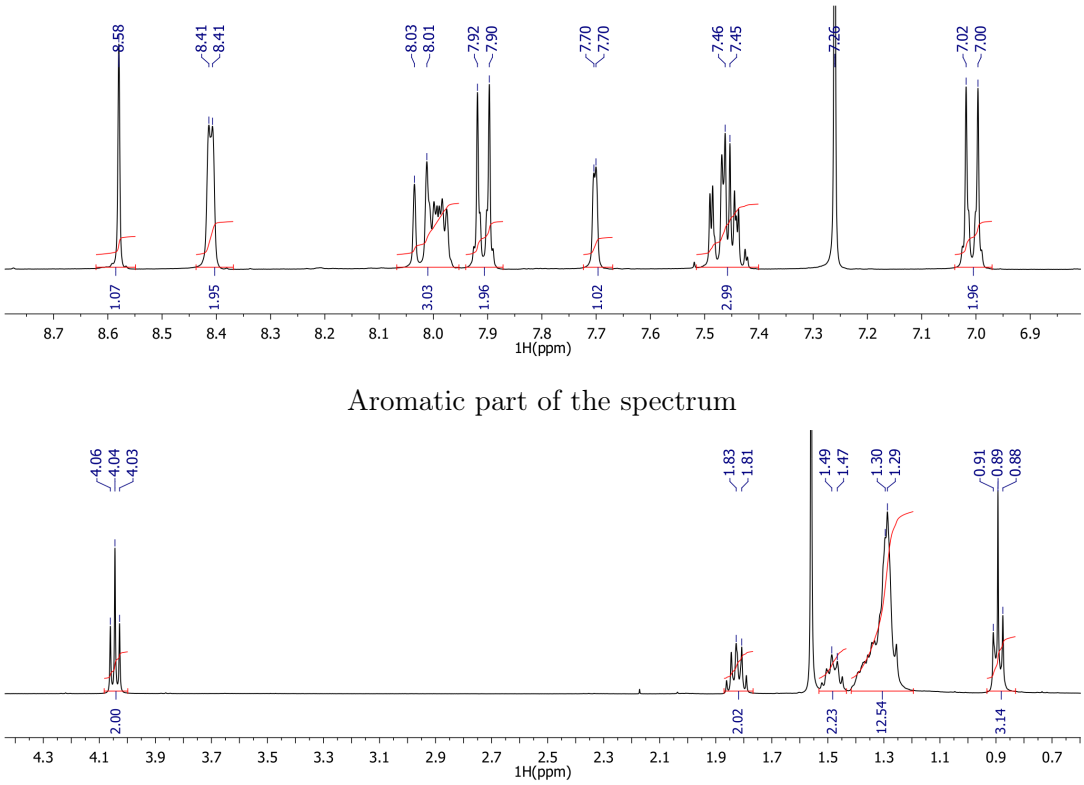

Aromatic part of the spectrum

Aliphatic part of the spectrum

Figure 4.6 – H^1 NMR spectrum of 2-[(E)-((4-decyloxyphenyl)methylidene)amino]-anthracene.

of signals appearing on shifts δ = 7.91 and 7.00 ppm to the protons H^{11-14}, as well as coupling of signals on δ = 8.02 and 7.45 ppm, which indicates the closely spaced localization of these atoms.

The signals on δ = 8.58, 8.41 and 7.70 ppm show no correlation signs on the 2D spectrum (Figure 4.7), which confirms our initial guess of these protons being isolated from the others. This further reinforces our assumptions on the proposed chemical structure of **10-OPIA**.

Figure 4.8 represents the ^{13}C spectrum obtained from the same sample as the previous spectra. ^{13}C spectrum found: ^{13}C-NMR (100 MHz, $CDCl_3$) δ = 162.14, 159.76, 149.56, 132.48, 132.24, 131.47, 130.76, 130.48, 129.40, 129.24, 128.39, 128.08, 126.32, 126.09, 125.68, 125.64, 125.24, 122.16, 117.04, 114.91 (C^1 - C^{21}); 68.40, 32.06, 29.73, 29.71, 29.55, 29.48, 29.34, 26.18, 22.82, 14.28 (C^{22} - C^{31}) ppm. The characteristic triplet of $CDCl_3$

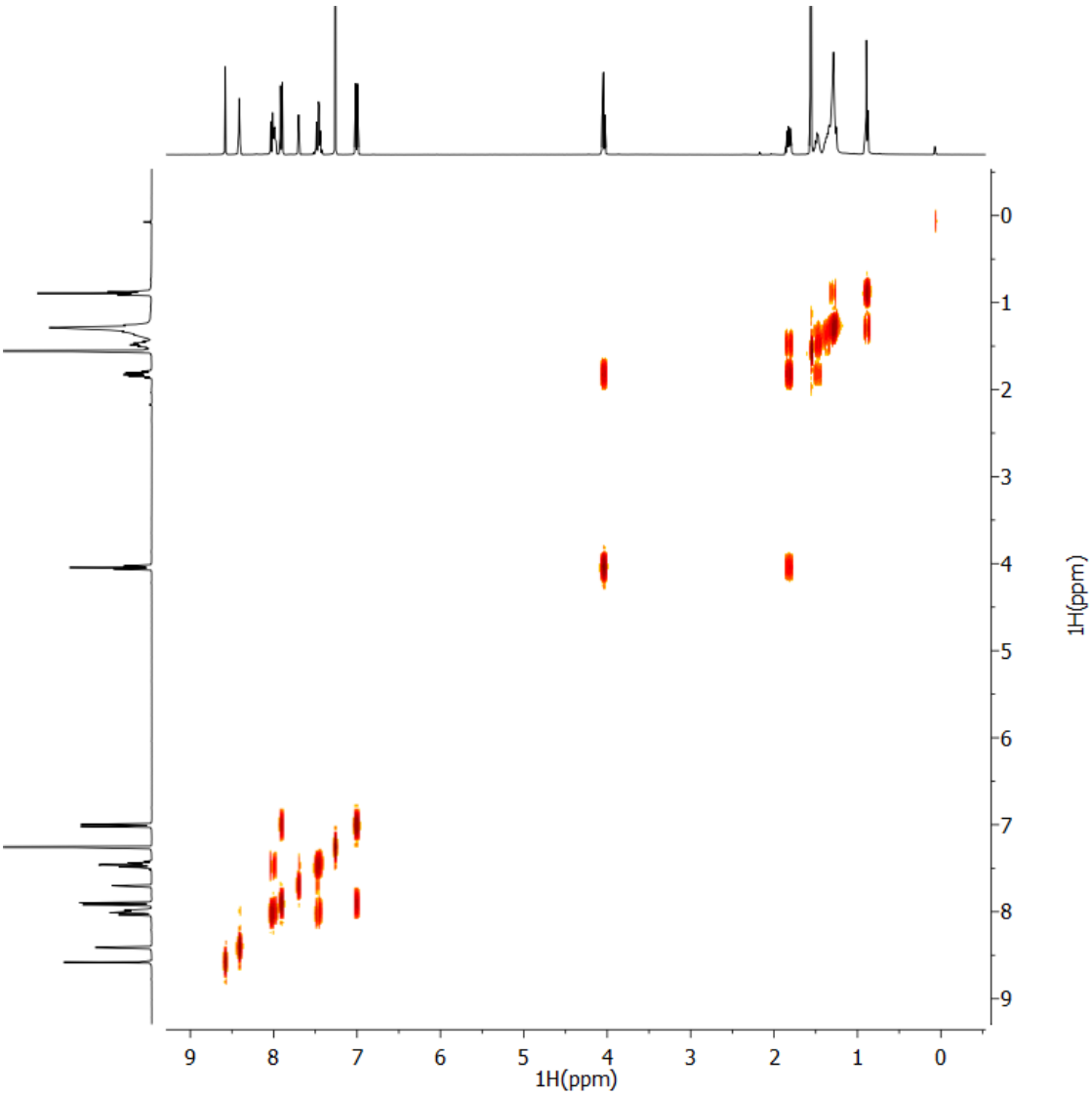

Figure 4.7 – COSY spectrum of **10-OPIA**.

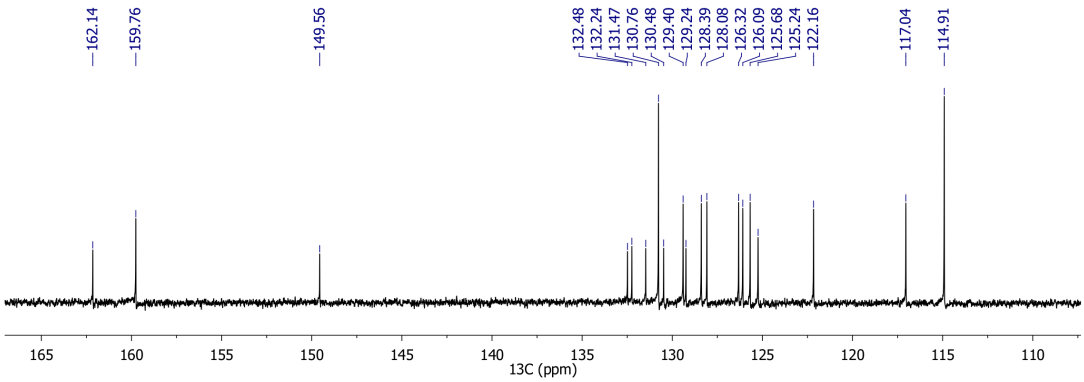

Aromatic part of the spectrum

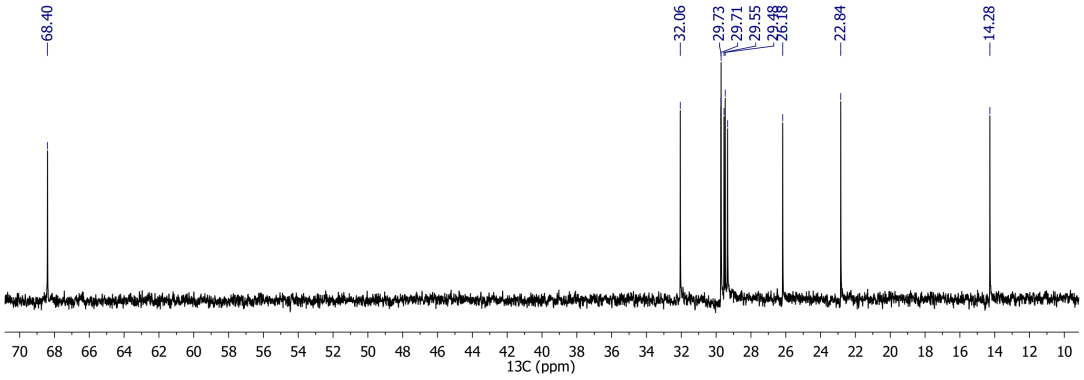

Aliphatic part of the spectrum

Figure 4.8 – H^1 NMR spectrum of 2-[(E)-((4-decyloxyphenyl)methylidene)amino]-anthracene.

at δ = 77.16 ppm is truncated for clarity. Figure 4.5 allows to propose 19 unique ^{13}C environments out of 21 carbon atoms of the aromatic part of the **10-OPIA** molecule, with C^{17} being equivalent to C^{21} and C^{18} to C^{20}. Aromatic part of the ^{13}C spectrum indeed shows presence of 19 ^{13}C environments, with signals on δ = 130.76 and 114.91 ppm corresponding to $C^{17,21}$ and $C^{18,20}$ and having a higher intensity, as expected. It is of interest to highlight the signature of C^{15} situated in the imine linkage at δ = 162.14 ppm and C^{19} situated at the phenyl ring and linked directly to the oxygen atom at δ = 159.76 ppm. The shift at δ = 149.56 ppm corresponds to the C^{2}, situated in the anthracenyl moiety and linked to the nitrogen atom. Detailed assignment of closely spaced signals between δ = 133 and 117 ppm is out of scope of the present work, however their chemical shift values allow us to propose their affiliation with the electron rich aromatic system of the **10-OPIA** molecule.

Aliphatic carbons were identified in the ^{13}C spectrum which contains signals from the 10 ^{13}C atoms of alkyl spacer unit: the signal at at $\delta = 68.40$ ppm corresponds to the C^{15} - adjacent to the oxygen atom. Furthermore, the observed chemical shift of the remaining atoms is inversely proportional to their distance to the electronegative oxygen atom, analogously to the ^{1}H spectrum.

High resolution mass spectroscopy

Since the mass spectrometer requires a sample to have an electrical charge, the mass of the expected charged moiety was calculated in respect to addition of a H^+ ion to the **10-OPIA** molecule by utilizing the ChemDraw software. The calculated mass for $[C_{31}H_{36}NO]^+$ was 438.2791 u.

The sample was prepared by dissolving a 1×10^{-6} M of **10-OPIA** in acetone, which was thoroughly stirred for 2h at 50 °C. Cooled solution was injected in the liquid chromatography system of the high resolution mass spectrometer.

The mass spectrum in the Figure 4.9 shows a sharp peak at 438.2790, which is attributed to the $[\textbf{10-OPIA H}]^+$ molecular ion. The observed result is in good agreement with the prediction, also indicating high purity of the final product.

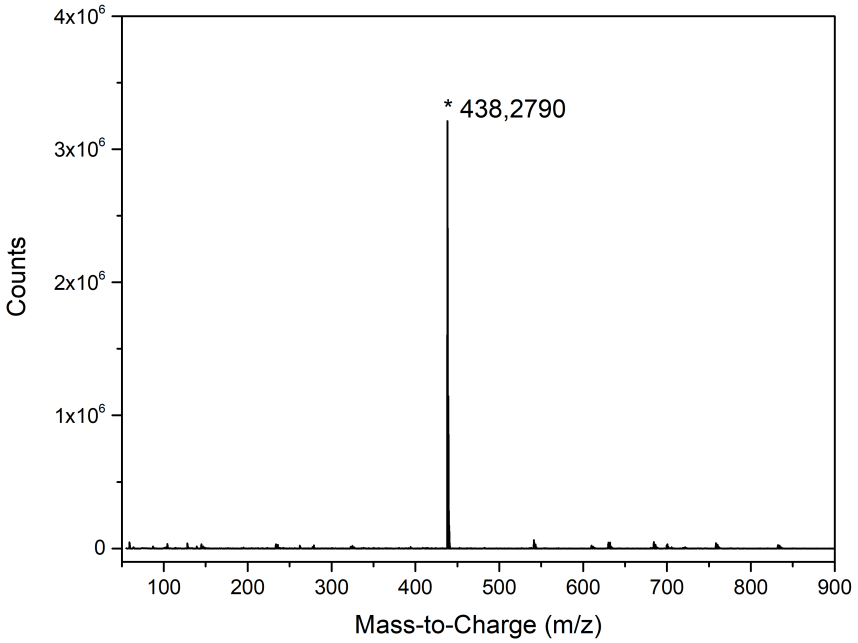

Figure 4.9 – High resolution mass spectrum.

4.3 Band gap and frontier orbital energy level characterization

As discussed in the Chapter 1, band gap and frontier orbital energy levels are essential parameters in relation to the potential applications of a novel OSC. A relatively coarse estimation of these values can be performed by utilizing *ab initio* calculations, which allows us to expect certain properties of the designed molecule even before it is synthesized. However, the methods based on gaussian basis sets are usually limited to idealized gas-phase or solution conditions, and are always a trade-off between the precision and computational cost, which can be substantial in the case of large organic molecules. This limits the utility of these methods in regard to some real-world applications (for example, semiconducting polymers).

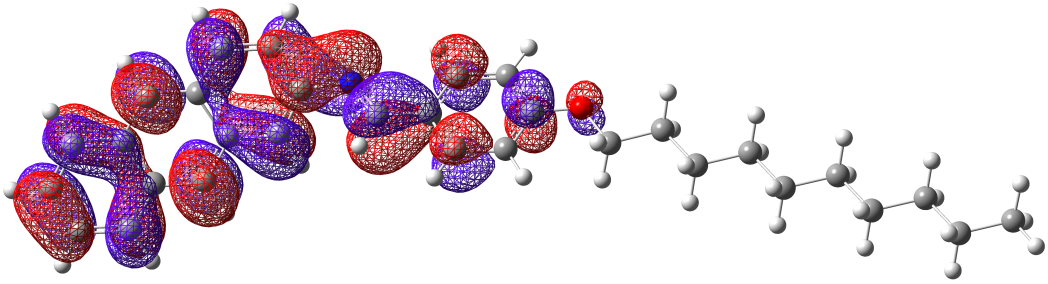

LUMO (MO 119, -1.99 eV)

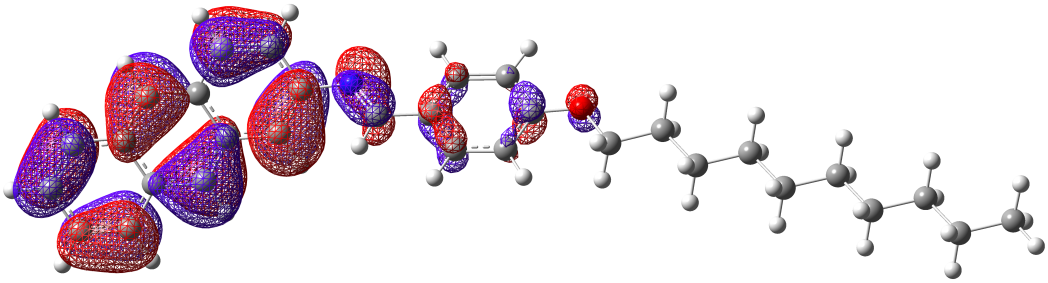

HOMO (MO 118, -5.30 eV)

Figure 4.10 – Frontier molecular orbitals of the **10-OPIA** molecule, calculated on B3LYP/6-31G++(d,p) level.

Frontier molecular orbitals (118 and 119) have been calculated on B3LYP/6-31G++(d,p) level (optimized structure had zero imaginary frequencies). The geometries of these MOs are presented in the Figure 4.10. It is of interest to note the delocalization of electron density between the antracenyl and phenyl moieties which are conjugated via the imine

linkage. By taking into account the predicted MO energy levels, it is possible to deduce an estimation of the fundamental gap to be around 3.3 eV. However, it is well known for the utilized functional (B3LYP) to significantly underestimate the value of LUMO, which allows us to propose that the effective bandgap of the **10-OPIA** is expected to be of lower value. The HOMO level of −5.3 eV seems to be a more realistic estimation, which is even more encouraging due to its proximity to the workfunction ϕ of Au (about −5.1 eV). This allows us to expect a shallow barrier for hole injection from the gold electrode, as well as ambient air stability due to its deep localization.

This data has been confronted with experiments: optical spectroscopy has enabled us to estimate the band gap energy; cyclic voltammetry allowed us to extract the energy of frontier molecular orbitals by studying electrochemical properties of the **10-OPIA** molecule.

4.3.1 Optical spectroscopy

Absorption spectroscopy

The absorption spectrum has been recorded with a 10^{-5} M solution of **10-OPIA** in dichloromethane in a standard 1 cm quartz cuvette on a range from 230 nm to 500 nm.

By drawing a tangent at the first absorption band in Figure 4.11, it is possible to extract the onset of optical absorption of the studied material, which usually corresponds to the energy of the first electronic transition ($S_0 \rightarrow S_1$, HOMO → LUMO).

We have also recorded the absorption spectrum for a thin film of **10-OPIA** deposited on a quartz slide by drop-casting 0.5% wt. chlorobenzene solution. It was found that **10-OPIA** exhibits a redshift of 22 nm when in thin film, which may be explained by pronounced $\pi - \pi$ interactions of neighboring molecules while being in close contact in the crystal as opposed to that of in solution. This results in a band gap energy reduction for the bulk **10-OPIA**.

By utilizing the Planck-Einstein relation:

$$E = \frac{hc}{\lambda}, \tag{4.1}$$

where E is the energy, h is the Planck's constant and λ is the wavelength; the optical bandgap is calculated to be $E_g = \mathbf{2.87\,eV}$ for the onset of absorption of **431 nm** in dichloromethane solution, and $E_g = \mathbf{2.74\,eV}$ for the onset of absorption of **453 nm** in the form of thin film, respectively.

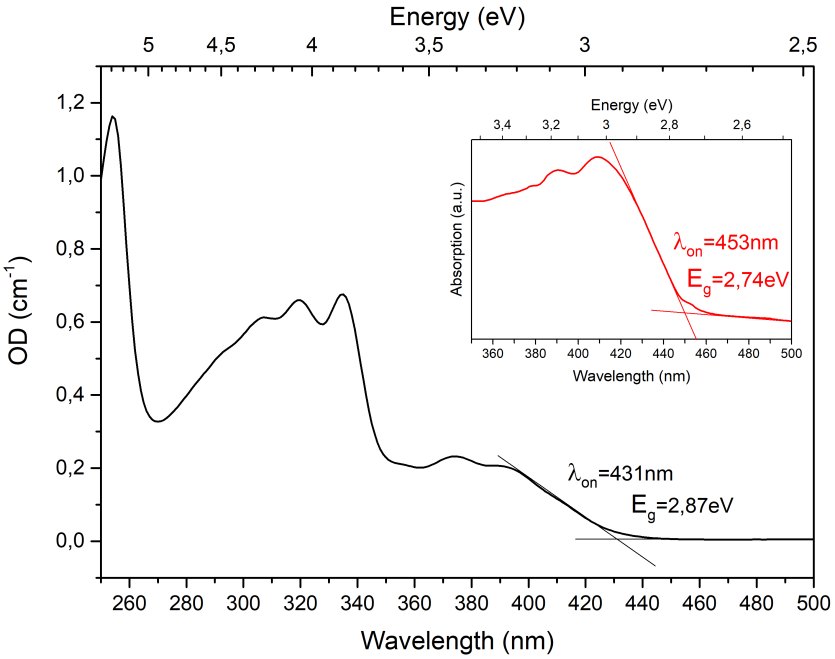

Figure 4.11 – Optical absorption spectrum of **10-OPIA** recorded for 10^{-5} M solution in dichloromethane. Inset: absorption for drop-casted thin film of **10-OPIA** (0.5% wt. in chlorobenzene) on quartz substrate.

Fluorescence spectroscopy

The **10-OPIA** molecule is expected to have semiconducting properties, thus an estimation of its light emitting properties has been carried out by fluorescence spectroscopy analysis in order to study its possible applications.

For this study, a dilute (10^{-5} M) solution of **10-OPIA** in acetone was prepared. The solvent was degassed by freeze-pump-thaw method on a Schlenck line prior to solution preparation in order to avoid quenching.

The excitation and emission spectra are presented in Figure 4.12. Excitation spectrum exhibits a slight red shift when compared to the absorption spectrum (Figure 4.11) recorded in dichloromethane, which may be explained by a small degree of solvatochromism. The peak of emission is situated at about 480 nm (small Stokes shift is commonly encountered in polyacenes).

Fluorescence lifetime of **10-OPIA** was measured in acetone solution. Figure 4.13 presents the experimental data, instrument response function and fitted curve using a triple exponential function. Signal amplitude is composed of three components: fast 0.19

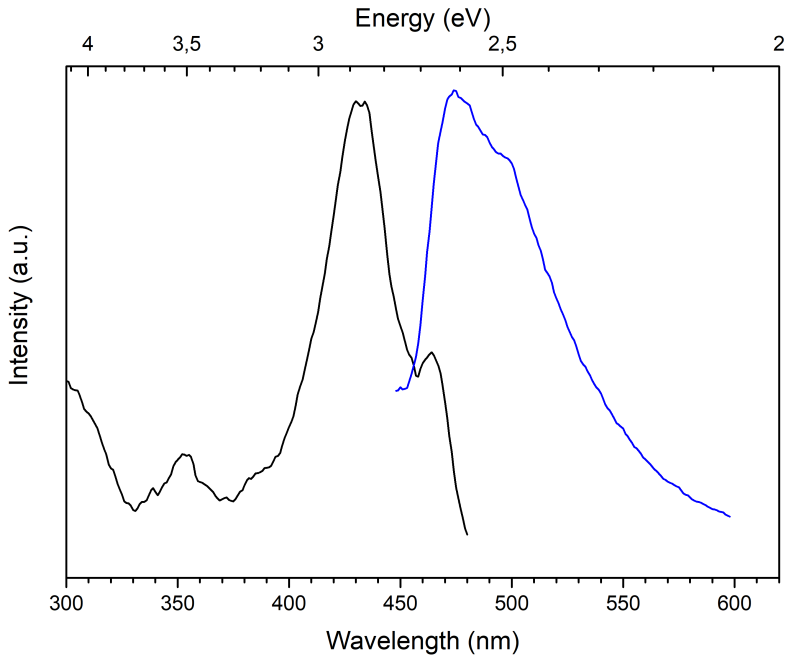

Figure 4.12 – Excitation (black line, emission wavelength -490nm) and emission (blue line, excitation wavelength - 435nm) spectrum of **10-OPIA**.

ns decay contributed 21.4%, 3.05 ns - 21.9% and 15.41 ns - 56.65%, respectively, which has resulted total fluorescence lifetime of 9.44 ns. This value is abnormally high for a molecule containing imine linkage, because its susceptibility to a structural change of conformation (rotation along the bond axis) is usually preferred over a radiative $S_1 \rightarrow S_0$ relaxation. We may speculate that for **10-OPIA** molecule, the non-planar (dihedral angle between the planes of anthracene and phenyl moieties is about 140 °) geometry results in partial inclusion of lone electron pair on nitrogen atom to the delocalized electron cloud system of aromatic anthracene, thus hindering the rotation around imine linkage. Similar effects were observed by Yoshino et al[188], when molecules with azo- and aldimine linkages were constrained by modifying their structure, which resulted in noticeable enhancement of fluorescence.

4.3.2 Cyclic voltammetry

We have used cyclic voltammetry to experimentally obtain frontier MO energy levels. This method is less precise than initially adopted in semiconductor research X-ray and UV photo-electron spectroscopy, but is by far less expensive and time consuming, while

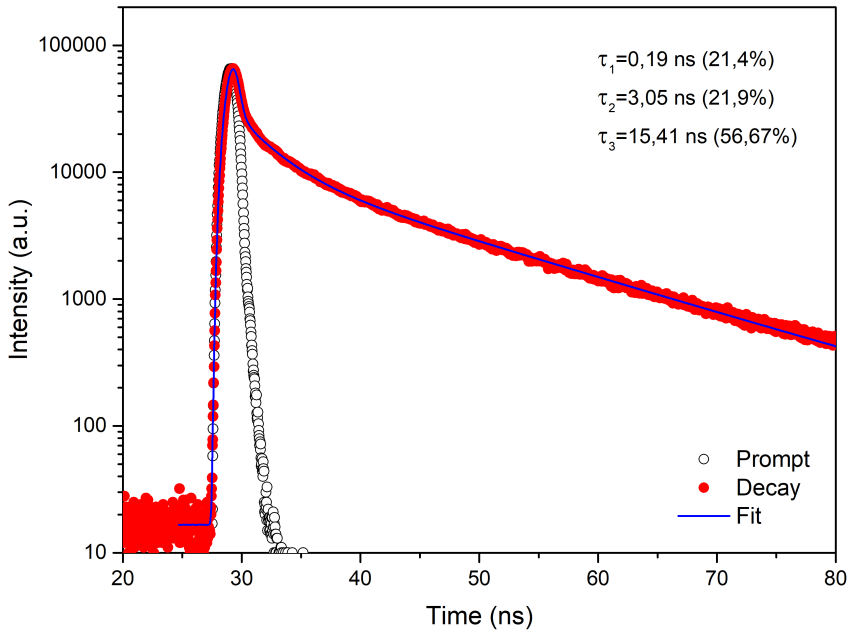

Figure 4.13 – Fluorescence decay of dilute (10^{-5} M) **10-OPIA** solution in acetone. Empty circles: instrument response function (recorded with 1% wt LUDOX^{TM} HS-40 colloidal silica in deionized water). Red circles: experimental data for **10-OPIA** solution. Blue line: data fit.

being reasonably accurate[189].

2 mmol solution of **10-OPIA** in dichloromethane (DCM) containing 0.1 M of tetrabutylammonium hexafluorophosphate ($TBAPF_6$) as a supportive electrolyte was stirred for 2h and then placed in the electrochemical cell (10 ml volume). The solution was degassed by Ar bubbling for 20 minutes (pure supporting electrolyte solution showed flat cyclic voltammogramm, indicating an adequate removal of electroactive oxygen). Cyclic voltammogramms were collected in the range of -2.2 to 1.8 V against silver wire pseudoreference with scanning speeds ranging from 50 to 500 mV/s. Electrolyte was agitated for about 1 minute with a magnetic stirrer between the scans to ensure the presence of pristine **10-OPIA** molecules in the near-electrode environment.

Figure 4.14 represents the raw data of **10-OPIA** solution cyclic voltammogramms. It is possible to observe distinct features corresponding to the electrochemical oxidation and reduction of **10-OPIA** molecules. The peak positions are independent to the scanning speed, while the current is proportional to it. The asymmetric profile of oxidation (large cathodic current and almost negligible anodic current) and reduction (large anodic current

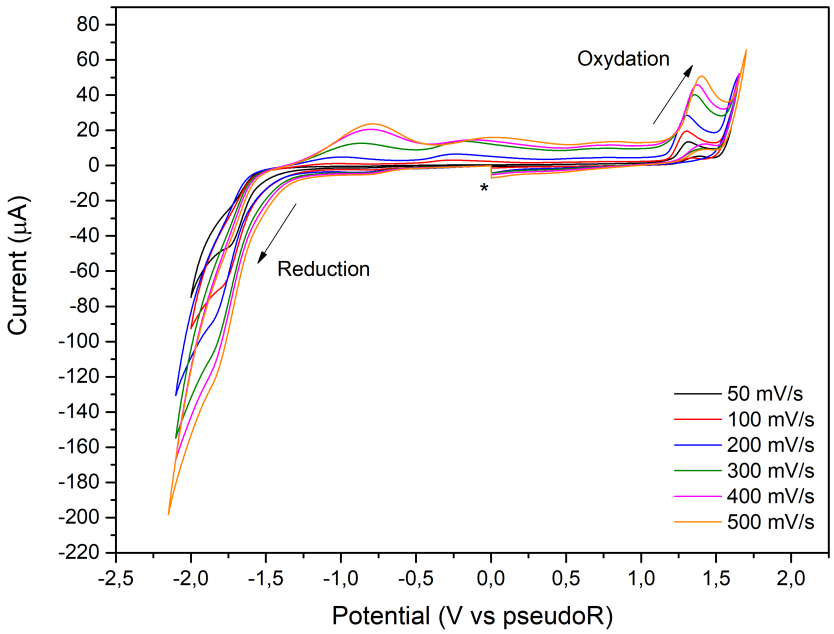

Figure 4.14 – Cyclic voltammetry data of 2mmol **10-OPIA** in 0.1M TBAPF6 in DCM, degassed with Ar 20 minutes versus silver wire pseudoreference. Asterisk indicates the start of data collection.

and almost negligible cathodic current, which is however more visible on higher scanning speeds) indicates irreversibility of these two processes, which may be related to the instability of oxidated/reduced **10-OPIA** species in solution.

After collection of **10-OPIA** voltammogramms, 2 ml of 1 mmol solution of ferrocene (98%, Sigma Aldrich) in supporting electrolyte was injected in the cell and degassed for 20 minutes prior to measurements. Additional data was recorded to include the potential range of Fc/Fc+ oxidation process (Figure 4.15, in blue). The data of ferrocene oxidation was further used to extract its half-wave potential (mean value between the anodic and cathodic peaks, since Fc/Fc+ process is quasi-reversible) and use it as a reference point [190] for the previously obtained data for **10-OPIA**.

Figure 4.15 depicts a cyclic voltammogram of **10-OPIA** solution recorded at 50 mV/s referenced versus Fc/Fc+ redox couple (in blue). Two tangents were drawn (in red) at the reduction and oxidation parts of the data in order to determine the onsets E_{RED} and E_{OX} on their intersection with the background current tangent. These extracted potentials were employed to evaluate the HOMO and LUMO energy levels of **10-OPIA** using the following relations [189]:

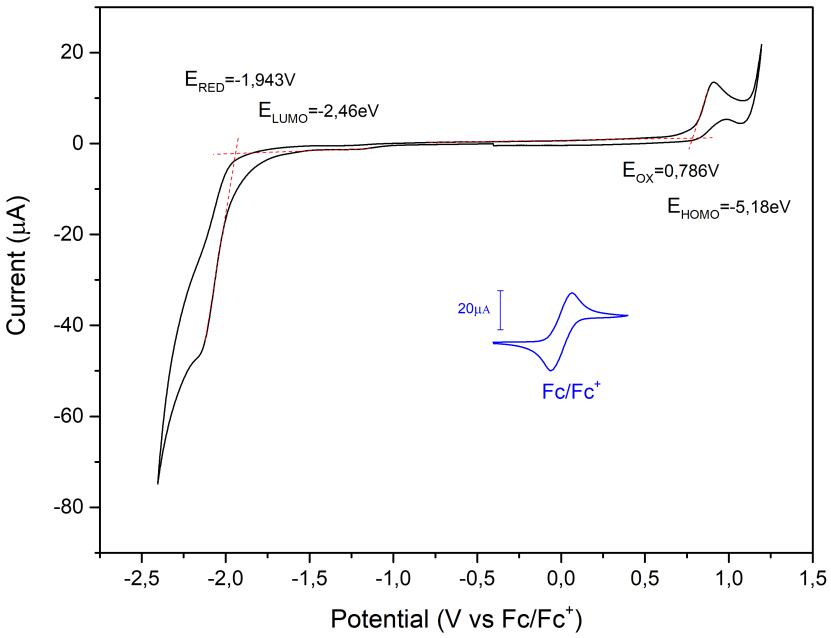

Figure 4.15 – Normalised cyclic voltammetry data of 2mmol **10-OPIA** in 0.1TBAPF6 in DCM, degassed with Ar (20 minutes) at 50mV/s versus Fc/Fc+. Fc/Fc+ oxidation process is represented in blue, vertical scale is not respected for clarity.

$$E_{HOMO} = -(E_{OX} + 4.4), eV \tag{4.2}$$

$$E_{LUMO} = -(E_{RED} + 4.4), eV \tag{4.3}$$

which gives the estimated $E_{LUMO} = \mathbf{-2.46\,eV}$ and $E_{HOMO} = \mathbf{-5.18\,eV}$. These values look reasonable in regards to the band gap estimated by absorption spectroscopy. Moreover, the HOMO level of $-5.18\,$eV appears to be in good agreement with DFT calculations, confirming our initial guess for good affinity of **10-OPIA** material with golden contacts as a P-type semiconductor. Taking into account the experimental results from cyclic voltammetry, we find the electrochemical band gap energy (E_{HOMO}-E_{LUMO}) $E_{gEC}{}^{*} = \mathbf{2.72\,eV}$ to be in excellent agreement with the value obtained for a thin film of **10-OPIA** by absorption spectroscopy, $E_{gO}{}^{\dagger} = \mathbf{2.74\,eV}$.

*Electrochemical band gap energy
†Optical band gap energy

4.4 Thermophysical and mesogenic properties

In order to investigate the phase behavior of the **10-OPIA** material, we have performed calorymetric analysis by DSC. The results (second heating and cooling) are shown in Figure 4.16. It is clear that **10-OPIA** exhibits mesomorphic properties, since the thermogramm displays at least 4 phase transitions. Moreover, it is clear that these phase transitions are reversible since they are present on both heating and cooling.

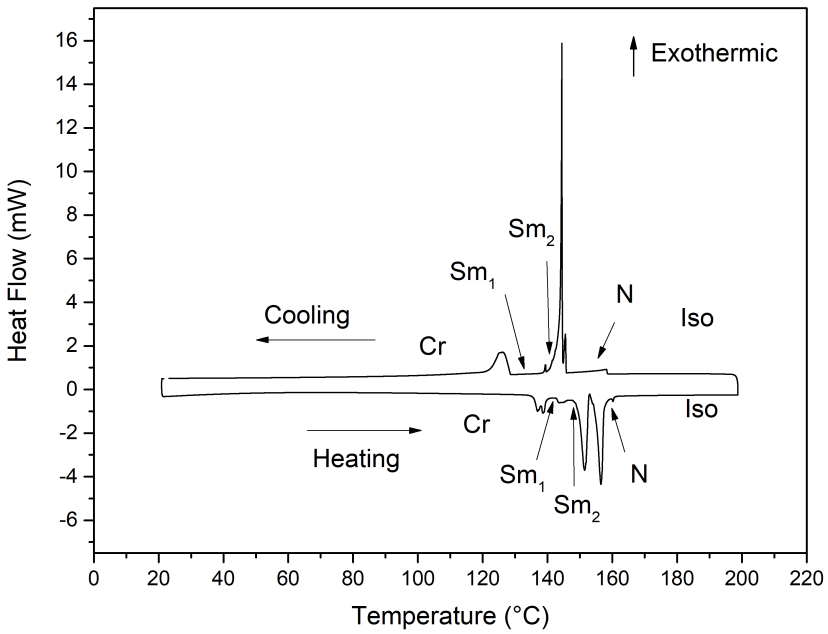

Figure 4.16 – DSC thermograms of **10-OPIA** sample obtained on heating and cooling with a rate of 10°C/min.

In order to describe these phase transitions, we are going to proceed from the heating part of the data: the first transition is split in 2 peaks and occurs at 139 °C (his splitting is repetitive and may indicate transition to a closely related phase state which appears briefly) and resembles the image of **8-PNP-O12** melting from crystalline phase. It corresponds to melting to the Sm_1 mesophase. The second phase transition occurs on 145 °C with a relatively low enthalpy change, which may indicate a minor order decrease. This allows us to propose a second smectic phase Sm_2 to this intermediate mesophase, Sm_1 being of higher order than Sm_2. Next phase transition occurs at 152 °C with a large enthalpic signature and has a similar two-peak pattern. The high energy of this transition indicates a major order decrease, probably a transformation to a nematic (N)

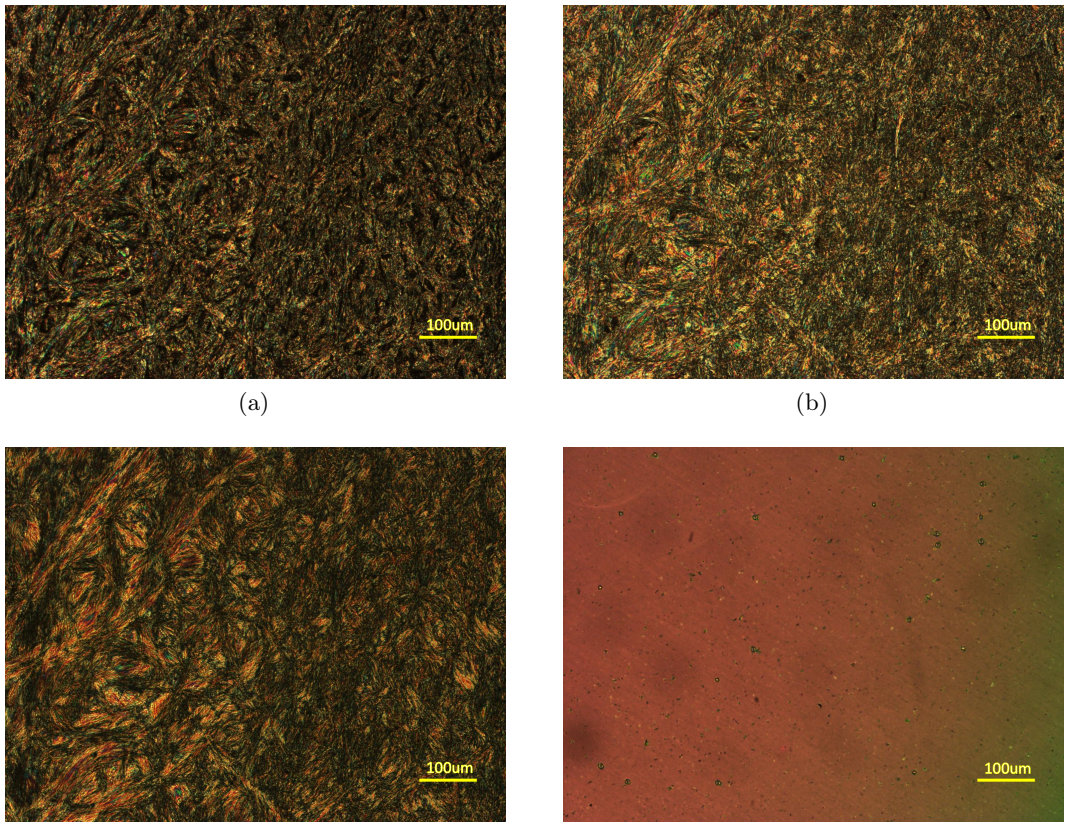

(a) (b)

(c) (d)

Figure 4.17 – Sample texture under crossed analyzer-polarizer for pure **10-OPIA** (a) in crystalline phase (Cr) at 120 °C, (b) Sm_1 mesophase at 140 °C, Sm_2 mesophase at 148 °C and nematic (N) mesophase at 159 °C.

phase from Sm_2. Finally, **10-OPIA** completely melts into the isotropic liquid at 160 °C. Upon examining the cooling part of the data, one can notice similar phase sequence to that observed heating, with an exception for the **10-OPIA**'s tendency of supercooling.

Polarized microphotographs of a 9 µm cell with homogeneous orientation filled with **10-OPIA** reveal the texture Figure 4.17 of aforementioned phase states. The texture of Sm_1 and Sm_2 mesophases look similar to the crystalline phase, which confirms the analysis of the DSC data. The picture taken at 159 °C on cooling (Figure 4.17, d) shows a characteristic texture of homogeneously oriented nematic phase.

4.5 Charge transport

4.5.1 Organic Field Effect Transistor

We have made several attempts to perform TOF carrier mobility measurements on **10-OPIA**. However, the resulted photocurrent profile was highly dispersive in crystalline and smectic phases (it was impossible to extract carrier transit time) irrelevant to sample thickness. Probable reasons for this behavior may include inadequate alignment of **10-OPIA** in the cell, negative contribution of grain boundaries and/or insufficient charge carrier generation by the available laser wavelength ($\lambda = 355\,\text{nm}$).

Linear configuration

In order to characterize the charge transporting of this new material, current-voltage measurements were carried out on **10-OPIA** OFET at room temperature. We have succeeded in preparation of OFET in bottom gate - bottom contact configuration by simple drop casting of 0.5% wt. solution of **10-OPIA** in chlorobenzene (Sigma Aldrich) on clean substrate covered with OTS-18. The protocol (previously described in Chapter 2) has allowed us to grow relatively big crystals (greater than channel length) in the direction favorable for charge transport ($\pi - \pi$ stacking normal to electrodes).

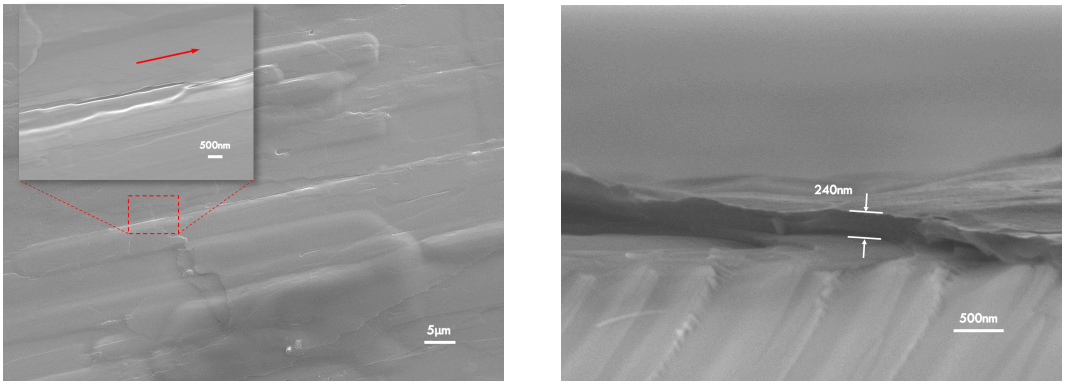

(a) (b)

Figure 4.18 – SEM images of **10-OPIA** film prepared by drop-casting of 0.5% wt. solution in chlorobenzene on OTS-18 functionalized glass slide at 3 degree substrate inclination: (a) topography (red arrow indicates direction of crystallization) (b) profile of the same thin film.

Figure 4.18, (a) illustrates the alignment of thin film drop-casted on a soda lime glass substrate functionalized with OTS-18. Note how the grain boundaries aligned in the

direction parallel to the crystalline growth. We have measured the thickness (Figure 4.18, b) by employing the same procedure previously used for **8-PNP-O12** thin films in the Chapter 3, we have found values ranging from 220 nm to 340 nm for different sample areas. This result may be explained by varying crystallization rate due to vapor pressure and concentration fluctuations.

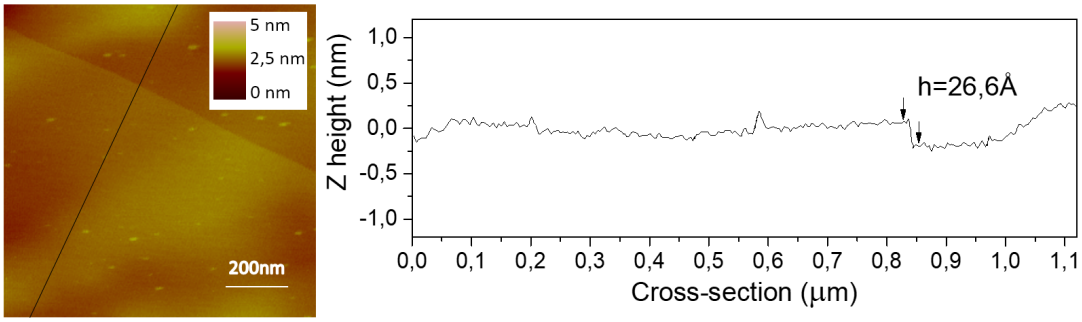

Figure 4.19 – AFM topology (left) and a cross-section (right) of drop-casted **10-OPIA** film on OTS-18 functionalized glass slide at 3 degree substrate inclination.

We have also explored the topological properties of drop-casted **10-OPIA** thin films by AFM in tapping mode (Figure 4.19). The images obtained by AFM confirm very smooth surface of grown films. Cross-section (Figure 4.19) demonstrates a distinct step of about 26.6 Å, which in comparison to the length of **10-OPIA** molecule (about 27 Å, calculated on B3LYP/6-31G++(d,p) level of theory) allows us to propose vertical alignment of molecules, as expected in the case of OTS-18 covered substrate.

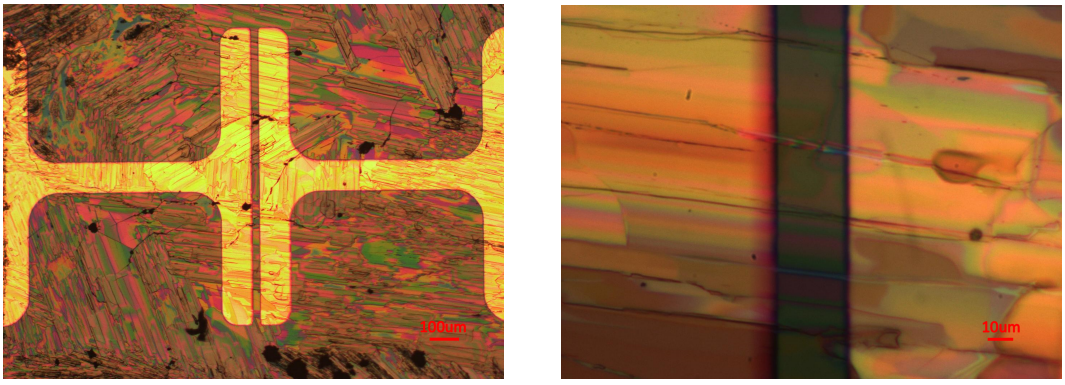

(a) (b)

Figure 4.20 – Microscope captures (in polarized light) with 5x lens (a) and 50x lens (b) of a linear electrode OFET (L = 30 µm, W=1mm) prepared with **10-OPIA**, drop-casted, 3 degree substrate inclination.

Figure 4.20 shows magnification of transistor channel area with a deposited **10-OPIA** thin film, which reveals large crystalline domains crossing both (source and drain) electrodes. The yield of 18 working devices out of 20 per substrate on average was achieved.

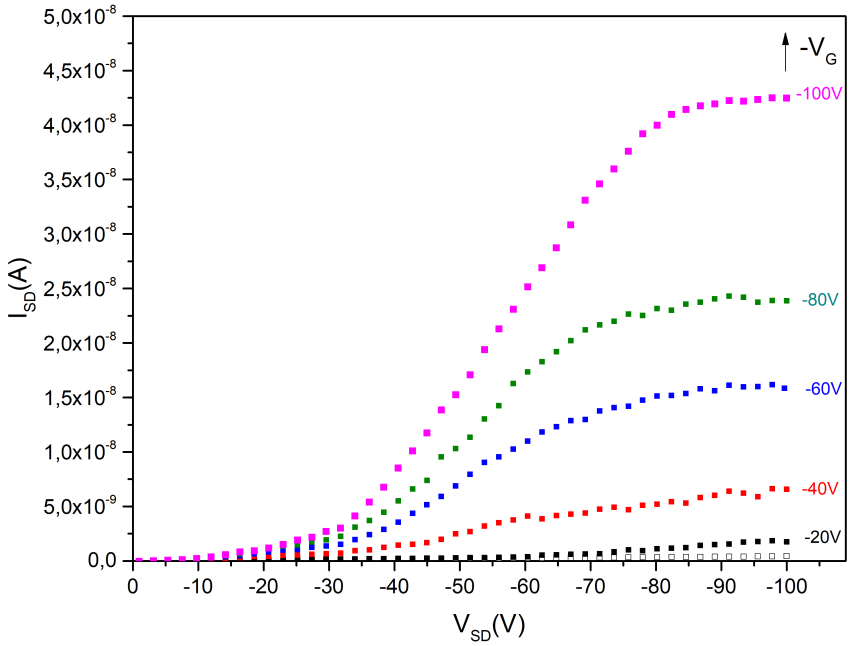

Figure 4.21 – Output characteristic of an OFET (L = 30 µm, W=1mm) prepared with **10-OPIA**, drop-casted, 3 degree substrate inclination.

The device was characterized in ambient air conditions (19 °C, 88% relative humidity average). Additional precautions were taken in order to preserve the sample from humidity prior to measurements (storage in a dessicator). The output characteristic of **10-OPIA** OFET in linear configuration is presented in the Figure 4.21. Field effect hole mobility is calculated from the saturation part of the drain source current: $\mu = (4.1 \pm 2.7) \times 10^{-5}\,\mathrm{cm}^2/(\mathrm{V\,s})$. This value is comparable to that obtained by Chung et al [185] for 9,10- TIPS functionalized antracene derivatives substituted in 2,6- positions with phenylene vinylene ($\mu = (5.21 \pm 3.55) \times 10^{-5}\,\mathrm{cm}^2/(\mathrm{V\,s})$) and hexyl thiophene ($\mu = (2.05 \pm 1.17) \times 10^{-6}\,\mathrm{cm}^2/(\mathrm{V\,s})$) in thin film form. It should be noted that these reported results were obtained for devices in bottom gate/top contact configuration, which, according to the literature [191, 192], usually exhibits better results than that of bottom gate/bottom contact geometry (used in this work).

The transfer characteristic and threshold voltage of **10-OPIA** OFET in linear con-

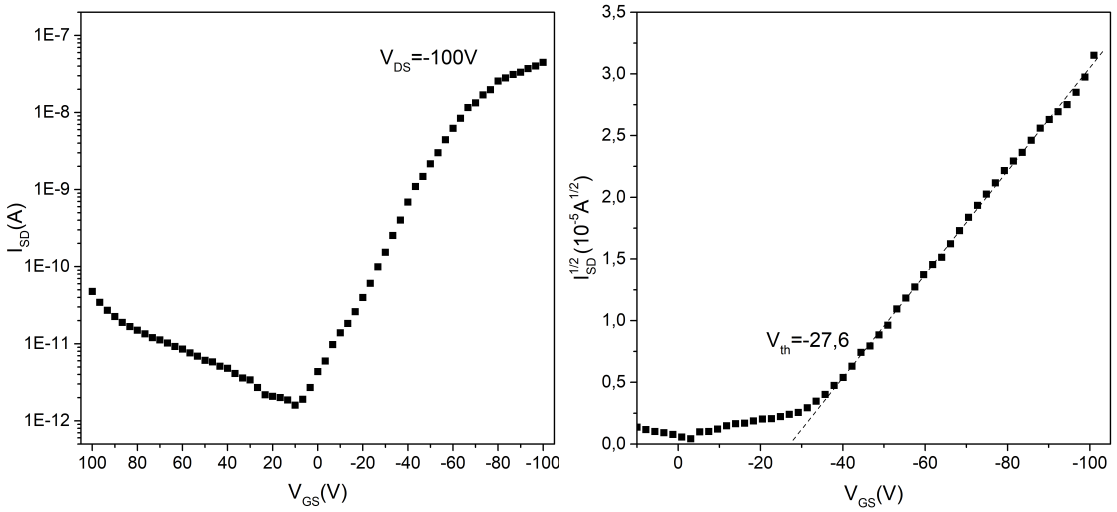

(a) (b)

Figure 4.22 – Transfer (a) and threshold voltage (b) characteristic of an OFET (L = 30 µm, W=1mm) prepared with **10-OPIA**, drop-casted, 3 degree substrate inclination.

figuration are presented in the Figure 4.22. Transfer characteristic allows us to extract the ON/OFF ratio (10^4) of the device, which is considerably higher than that of doped **8-PNP-O12** due to low intrinsic conductivity of **10-OPIA**. The threshold voltage for this device is found to be −27.6 V, which is lower than previously presented value for doped **8-PNP-O12** OFET (order of $\mu = 10^{-7}\,\mathrm{cm}^2/(\mathrm{V\,s})$). We would like to underline a relatively low threshold voltage obtained with **10-OPIA** material, especially for this fabrication method (drop casting), which amplitude in some cases may be greater than −50 V [85].

Inter-digitated configuration

In order to investigate the possibility of **10-OPIA** application to a larger-scale device, we have prepared another OFET with different electrode configuration (the same we have previously used to prepare field-effect transistors with doped **8-PNP-O12**). Previously disclosed protocol has allowed us to obtain 17 working devices out of 20 per substrate on average. Figure 4.23 demonstrates microscope capture of an OFET prepared with **10-OPIA** in inter-digitated (IE) geometry. It is of interest to notice the size of crystalline domains and how efficiently their alignment could be controlled with substrate inclination during drop-casting.

The device was characterized in ambient air conditions similar to previously described.

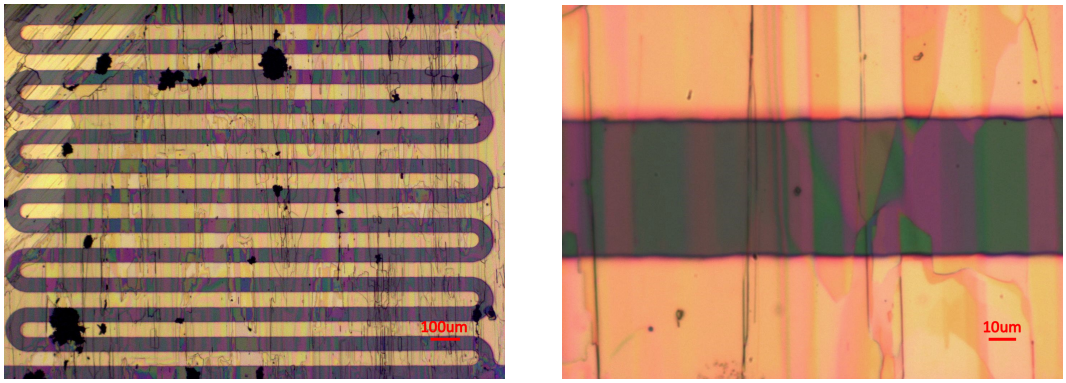

(a) (b)

Figure 4.23 – Microscope captures (in polarized light) with 5x lens (a) and 50x lens (b) of an inter-digitated electrode OFET (L = 50 µm, W=18mm) prepared with **10-OPIA**, drop-casted, 3 degree substrate inclination. Dark spots on the left image correspond to crystalline agglomerates on the surface of thin film.

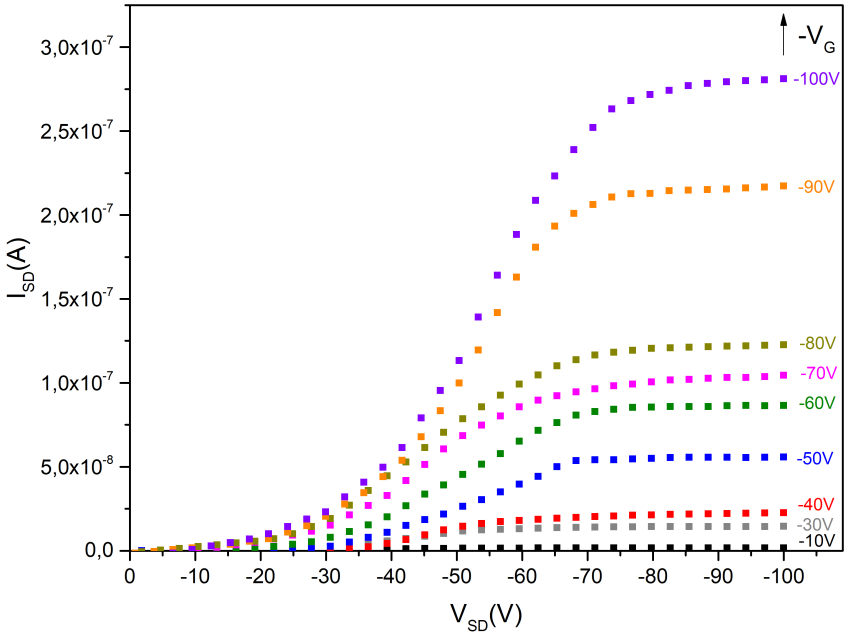

Figure 4.24 – Output characteristic of an IE OFET (L = 50 µm, W=18mm) prepared with **10-OPIA**, drop-casted, 3 degree substrate inclination.

The output characteristic of **10-OPIA** OFET in inter-digitated configuration is presented in the Figure 4.24. This device, as in the case of linear configuration, demonstrates

characteristic features of a field-effect transistor: drain-source current is proportional to the negative gate voltage, and the curve has two distinct regions: quasilinear on lower voltage and saturation on higher voltage. Field effect hole mobility is calculated from the saturation part of the drain source current: $\mu = (2.6 \pm 1.2) \times 10^{-5}\,\mathrm{cm}^2/(\mathrm{V\,s})$. We may speculate that higher channel length (L = 50 µm) results in higher amount of structural micro-defects in **10-OPIA** layer, which may be responsible for lower average mobility.

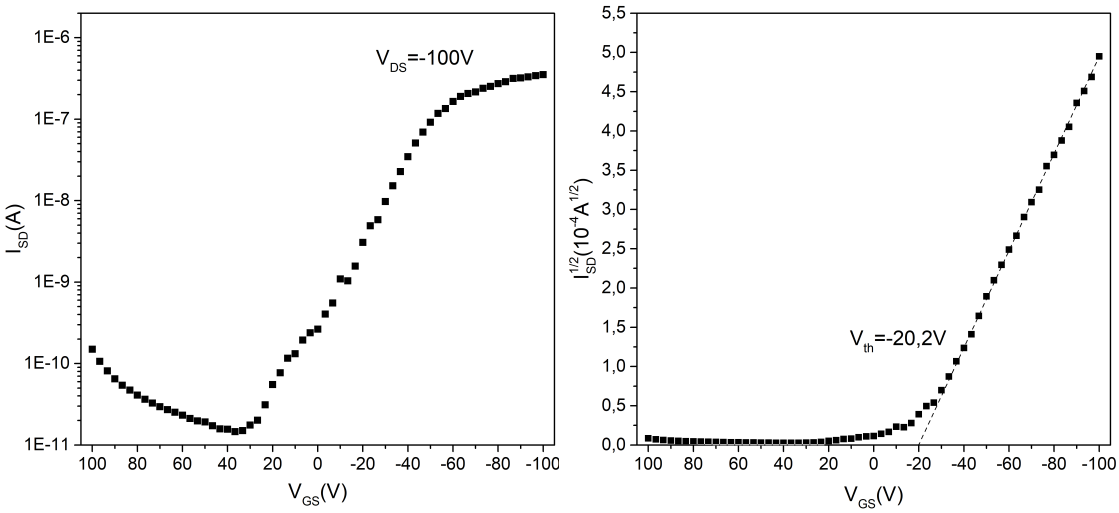

Figure 4.25 – Transfer (a) and threshold voltage (b) characteristics of an IE OFET (L = 50 µm, W=18mm) prepared with **10-OPIA**, drop-casted, 3 degree substrate inclination.

It is also of interest to address the transfer characteristic of this device (Figure 4.25, a), which demonstrates two distinct states, which allows us to estimate the ON/OFF ratio of about 10^4 - similar to the device in linear configuration. Threshold voltage was found to be of the same order as for linear OFET: V_{th}=−20.5 V.

We find that performance of **10-OPIA** in these devices is fairly typical for a small molecule OSC. However, one should note simplicity and accessibility of the **10-OPIA** synthesis process, which is an important factor promoting the widespread of organic electronics [193]. It is necessary to underline the working conditions as well: this molecule is remarkably stable in solid state (we have compared the NMR spectra after 8 months of storage in ambient conditions: no traces of degradation were detected). Easy and undemanding process (which may be easily upscaled with inkjet printing) of OFET preparation yields devices with reasonable performance. Interestingly, thermal annealing of devices did not result in improvement of carrier mobility, but in contrary it dramatically

degraded their performance: by examining the substrates under optical microscope, we have found that annealing on temperatures above 80 °C results in apparition of significant amount of cracks in the channel area, which act as structural defects and impede charge transport. There are several ways to improve the performance which can be proposed:

- Purity of the **10-OPIA** material may be improved. Although we demonstrate that initial purity obtained after successive recrystallizations from toluene and chloroform is good enough to demonstrate stable transistor behavior, there still may be some traces of impurity which act as traps for charge carriers. We may propose vacuum sublimation as the most suitable purification way for this kind of material.

- Geometry of the device may be changed for bottom gate/top contact. Devices in this geometry tend to demonstrate better performance for both mobility and threshold voltage. However, this type of geometry would impose additional requirements to the OSC film thickness and roughness and may be regarded as less attractive for low-cost applications.

- Additional attention may be focused on both contact and dielectric material and their interfaces with OSC. Despite rigorous cleaning, it is still possible for the gold contacts have a surface dipole which may interfere with hole transport. It has been demonstrated that some perfluorinated self-assembled monolayers (SAMs) may be efficiently deployed on the contacts via thiol functional group (covalently bound to gold) to remedy this issue[194]. Device preparation in a dry environment may additionally result in performance improvement, since the samples which were exposed to humidity for prolonged periods of time have demonstrated noticeable degradation of performance.

- Modifications to chemical structure may be introduced without significantly complicating the synthetic procedure. The most straightforward way is to modify the length of alkyl spacer unit - it not only gives us the control over mesogenic properties, but also allows us to modify the structure of crystal, which will in turn have direct consequence on transfer integral, and thus charge carrier mobility. We may also introduce supplementary functionality to this molecule by attaching different groups to the alkyl spacer - for instance, our group continues to work on a photopolymerisable molecule based on **10-OPIA**.

4.5.2 Photoconductivity

Phototransistor

During the initial testing of devices fabricated with **10-OPIA**, we have noticed a pronounced photosensitivity of **10-OPIA** material to the 3300K light source used to micromanipulator positioning. To further investigate this phenomena, we have employed a 455 nm (bandwidth FWHM = 18 nm) light source (variable power LED) which corresponds to the edge of absorption for **10-OPIA** in a solid film form (inset of Figure 4.11).

Figure 4.26 represent the transfer characteristic of previously described OFET device in interdigitated configuration. We would like to underline how the current I_{SD} is amplified by incident light, while retaining distinct ON and OFF states - a characteristic feature of the field-effect transistor.

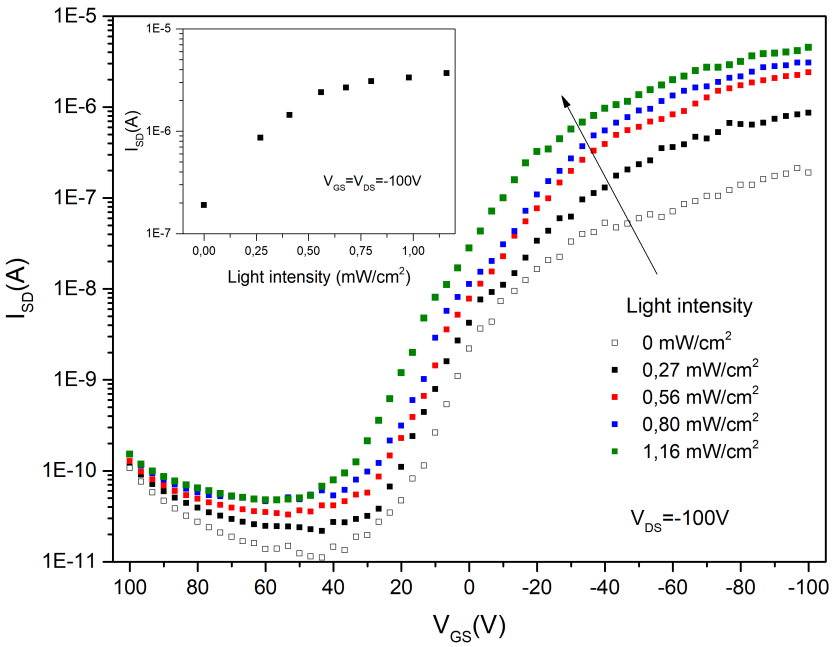

Figure 4.26 – Plot of transfer characteristic of an IE OFET (L = 50 µm, W=18mm) prepared with **10-OPIA**, drop-casted, 3 degree substrate inclination. Illumination wavelength is λ=455 nm, V_{SD} = -100V. **Inset:** Plot of saturation drain-source current as a function of light intensity.

In addition to conventional parameters (field effect mobility, threshold voltage, ON/OFF ratio), phototransistors are characterized by two additional parameters: photosensitivity P (ratio of photocurrent to dark current) and responsivity R (factor of

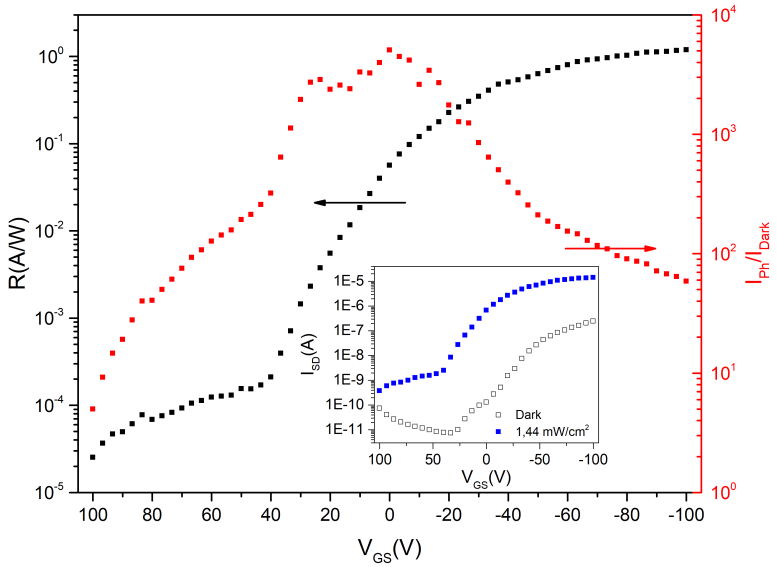

(a)

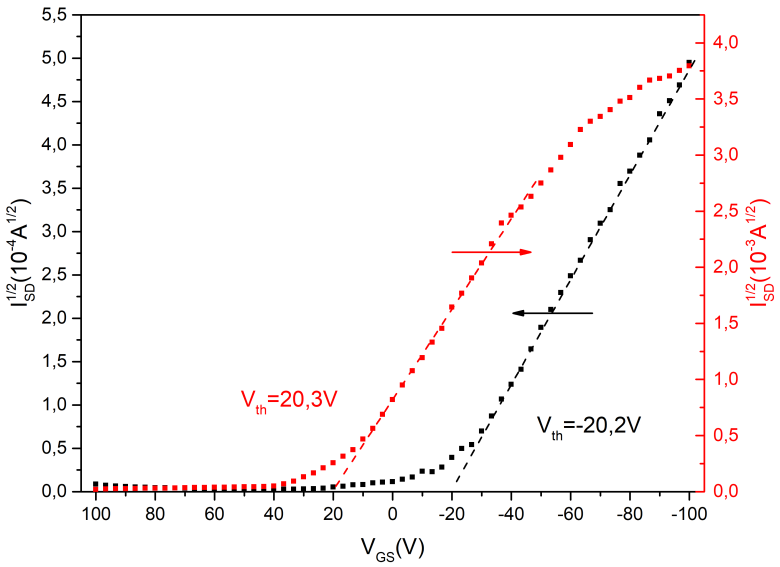

(b)

Figure 4.27 – (a) Plot of photoresponsivity as a function of gate voltage (V_{SD} = -100V) at incident power 1.44 mW/cm^2 (black squares) and photosensitivity (photocurrent to dark current ratio, in red) measured for an OFET in inter-digitated configuration. **Inset:** transfer characteristics of the same device in dark (empty squares) and under irradiation (blue squares). (b) Threshold voltage of the same device in dark (black squares) conditions and under irradiation (red squares). Illumination wavelength is λ=455 nm.

proportionality of photocurrent to incident light power). We present these parameters in the Figure 4.27, (a). It is of interest to notice how responsivity gradually increases with negative gate voltage and essentially mimics a transfer characteristic of an OFET. This parameter exceeds 1 A/W at higher gate voltages, which may be considered reasonably high when compared to typical organic materials [195, 196] and even some inorganic semiconductors[197].

The photosensitivity of this device is found to be maximal at intermediate gate voltage, which is directly related to a significant decrease of threshold voltage under illumination due to photogating effect (from V_{th} = -20.2V to +20.3V), and decreases on higher gate field values (where I_{SD} increases in dark conditions), stabilizing around 100. This may be explained by taking into account that the process of photoexcitation is somewhat similar to the field effect in regard to the increase in local density of charge carriers. The more than two order increase observed for current amplitude may indicate filling of significant amount of trap states by photogenerated carriers. In cooperation with field effect it may bring the device closer to the regime where the source-drain current becomes limited by imperfect contacts [198]. Visible saturation of I_{SD} as a function of illumination power (inset of Figure 4.26) confirms this observation.

It is of interest to compare this behavior with the work published by Pal et al [199], where a field effect transistor prepared with **P3HT** in bottom gate/bottom contact configuration showed high performance under illumination. The ON/OFF ratio degraded significantly upon illumination (several orders of magnitude) which is in distinct contrast with our device. For **10-OPIA** OFET, the ON/OFF ratio upon illumination is found to be virtually unchanged from dark conditions (around 10^4) even on relatively high illumination power (greater than 1 mW/cm^2, see the inset of Figure 4.27, a) which may indicate a relatively high recombination barrier for photogenerated electrons. A larger band gap of **10-OPIA** (as compared to that of **P3HT**) allows this device with gold electrodes to retain its P-channel character even upon significant illumination ("photo-doping"). Another possible explanation includes a substantial difference between electron and hole mobilities in the bulk of **10-OPIA**, which limits the number of photogenerated electrons participating in the channel current. This may explain large photoinduced gain of OFET's transfer curve on the majority of gate voltage range.

Before we continue our investigations of photoconductive properties of **10-OPIA**, it is necessary to explain the nature of this large photoconductive gain. As we have mentioned, subjection of **10-OPIA** to incident light results in the increase of channel conductivity (photoconductive effect) and threshold voltage reduction (photogating effect):

- Incident light creates electron-hole pairs in the semiconductor, which become separated under applied electric field V_{DS} and participate in the increase of source-drain current(Figure 4.28, b). This effect is responsible for conductivity boost and positive photocurrent (equation 1.2, p. 10).

- Photogating effect is responsible for the aforementioned change of the threshold voltage upon illumination (Figure 4.27, b). This effect is explained by the presence of trap states such as structural defects on **10-OPIA**/SiO_2 interface, for example (on the edge of LUMO "band" in the Figure 4.28, a), which become populated upon irradiation (Figure 4.28, b). The contribution of these charged states acts as an additional local "gate" electric field and is able to noticeably shift the threshold voltage of a device [200], especially if we take into account weak field screening in the bulk of material (we expected low dielectric permittivity of **10-OPIA** due to its organic nature).

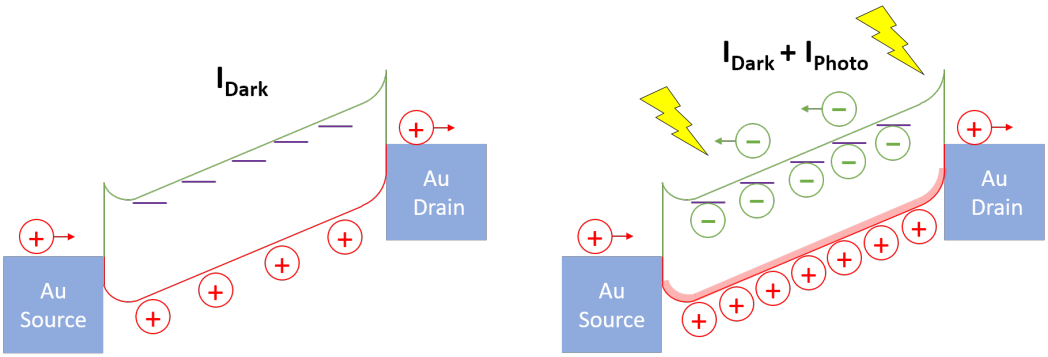

(a) (b)

Figure 4.28 – Energy band (approximation used here for simplicity) diagram for OFET channel (a) in dark conditions and (b) under illumination. Trap states (horizontal bars near the edge of conduction band) and trap filling by minority carriers is shown.

The resulting photoconductive gain G is expressed by following equation [198]:

$$G = \frac{c\tau_{pc}}{\tau_{tr}} = \frac{c\tau_{pc}\mu V}{L^2}, \tag{4.4}$$

where τ_{pc} is the lifetime of photogenerated charge carriers, τ_{tr} is the transit time, c is the concentration of successfully dissociated into electrons and holes light-induced excitons, μ is the mobility of majority carriers, V is the applied voltage and L is the

distance between two electrodes. In the case of photogating, the τ_{pc} is limited by the recombination of carriers residing in the trap states.

Field effect dependency of persistent photoconductivity

We have performed transient photoconductivity measurements in order to better understand the recombination behavior of these "gating" states, which has led us to another interesting feature of **10-OPIA** - a distinct and non-negligible hysteresis of dark conductivity. Figure 4.29 serves to illustrate this phenomena: the sample is illuminated for 180s with 1.16 mW/cm^2 of 455nm light, which yields higher dark current after the light source is turned off than before it was turned on.

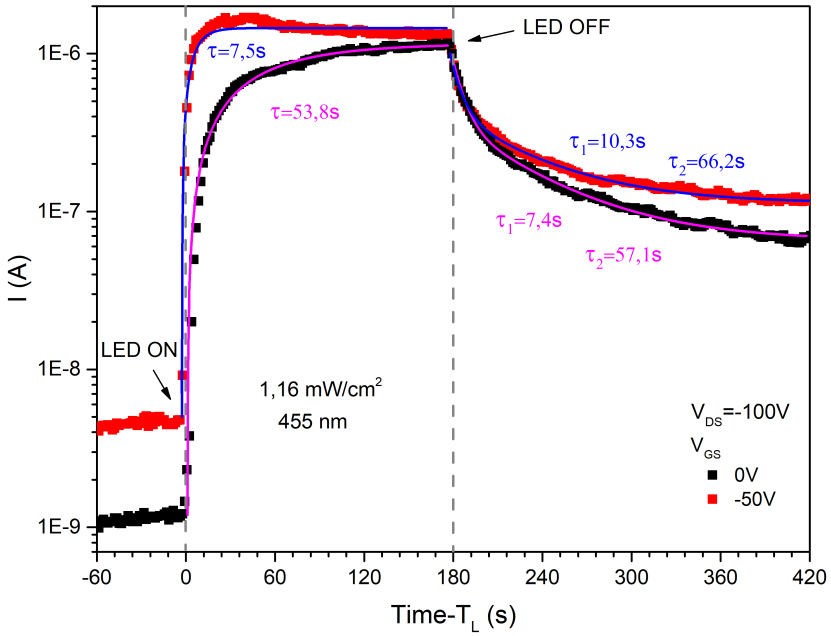

Figure 4.29 – Plot for current as a function of time. V_{DS} = -50V, V_{GS} = 0V (black symbols), V_{GS} = -50V (red symbols). T_L - start of illumination.

We demonstrate that gate voltage has pronounced effect on the transient photoconductivity. First of all, we notice that OFET reacts significantly faster while the gate is being negatively biased than in unbiased state. We have succeeded in fitting the photocurrent growth with a single exponential growth function:

$$I = I_0 \left[1 + \exp\left(\frac{t - t_0}{\tau}\right)\right], \tag{4.5}$$

where I_0 is the initial current (vertical offset), t_0 is the horizontal offset, and τ is the response time. Application of relatively moderate voltage (V_{GS} = -50V) results in almost one order decrease of saturation time for the photocurrent (7.5s vs 53.8s). We may attribute this result to faster filling of trap states with photogenerated carriers, as well as improved exciton dissociation on the semiconductor/dielectric interface.

The decay part of persistent "photo" current also bears differences in respect to gate bias. By judging the decay profile on a semilogarithmic plot, we have deduced it to have two exponential components, which has enabled us to fit it with double exponential decay function:

$$I = I_0 + I_1 \exp\left(-\frac{t - t_0}{\tau_1}\right) + I_2 \exp\left(-\frac{t - t_0}{\tau_2}\right), \tag{4.6}$$

where $I_{1,2}$ are the pre-exponential factors and $\tau_{1,2}$ are the relaxation times. The persistent photocurrent has two components: a fast and a slow relaxation time. This behavior is encountered in polycomponent[201, 202, 203] as well as pure materials, which is our case for **10-OPIA**. Some researches attribute the existence of two decay time components to two different energy levels of trap states: deeper traps are considered to recombine slower [197, 204], contrary to more shallow trap states. Similarly to photocurrent growth, the decay of persistent photoconductivity is affected by gate bias. By comparing the extracted relaxation times (Figure 4.29) we find that the sample under continued negative V_{GS} shows slower current decay. In order to interpret these experimental results, we should consider the following:

- As demonstrated for photocurrent growth, current saturates significantly faster under negative gate voltage, which for same duration of illumination may result in higher occupancy ratio of persistent photogating states. Prolonged periods of illumination have also shown noticeable increase in both time components of current decay, which supports this suggestion.

- The gate bias may also improve charge separation on the semiconductor/dielectric interface or even allow the photogenerated charge carriers to access states which are normally (at V_{GS}=0V) unavailable due to band bending. This delays the recombination of populated trap states, thus prolonging their lifetime.

Temperature dependency of persistent photoconductivity

In order to demonstrate the difference between trap state energy levels, we have performed another series of experiments where we have measured the persistent photoconductivity

decay time components as a function of temperature. We have performed measurements in a temperature range from 20 °C to 60 °C, since higher temperatures have resulted in substantial instability of gate dielectric layer. Figure 4.30 assembles transient current plots for different temperatures. Every measurement was preceded by 5s pulse of positive gate voltage (V_{GS}=50V) in order to "erase" persisting photoconductive states. Current was measured during 30s of illumination, then additional 140s of current decay were recorded. The data was then normalized in respect to the peak photocurrent and the decay part was fitted with the equation 4.5.

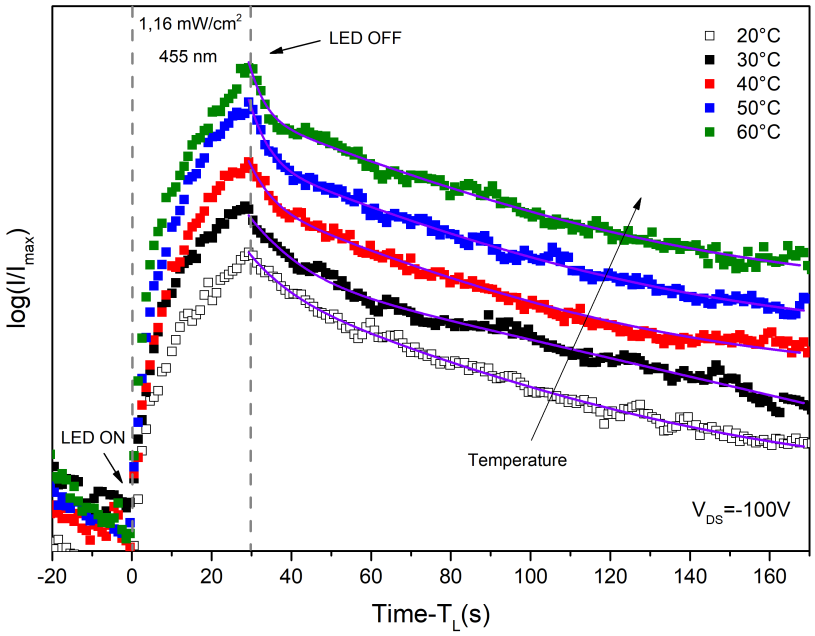

Figure 4.30 – Plot for normalized photocurrent as a function of time and temperature. Vertical offset is introduced for clarity. V_{SD} = -100V, V_{GS} = 0V. Purple lines represent double exponential fit. T_L - start of illumination.

The extracted decay time components are assembled in the Table 4.1. We notice that temperature increase results in noticeable decrease of both time components. However, it seems that faster decay component τ_1 is affected stronger than the slower τ_2. Tokumoto et al [116] have performed investigations on TIPS-functionalized pentacene, which exhibited similar persistent photoconductivity properties. The decay time was found to be inversely proportional to the temperature. However, this dependency was found to be more pronounced in the case of TIPS-pentacene than in the case of **10-OPIA**. This may be explained by relatively low energy trap states in a semiconductor with a smaller bad gap

(about 1.9 eV for TIPS-pentacene versus 2.7 eV for **10-OPIA**).

Temperature (°C)	τ_1 (s)	τ_2 (s)
20	6.7	49.1
30	5.8	44.5
40	4.4	43.7
50	3.4	43.1
60	3.1	41.6

Table 4.1 – Time components extracted from data presented in Figure 4.30.

We have calculated activation energy E_a from Arrhenius plot for both decay time components in Figure 4.31. The extracted value for fast decay component ($E_a(\tau_1)$=0.19 eV) is fives times greater than for slow decay component ($E_a(\tau_2)$=0.04 eV).

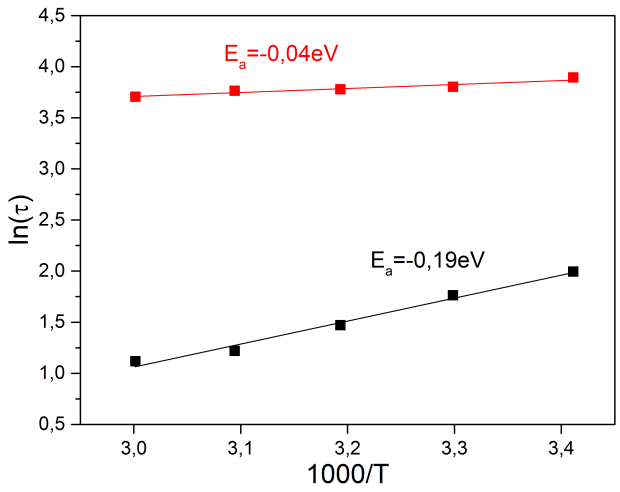

Figure 4.31 – Arrhenius plot of persistent conductivity decay time component. Black squares correspond to τ_1, red squares correspond to τ_2.

Direct comparison of these two values allows us to conclude that slower decay component τ_2 is indeed connected to deeper trap states (trapping energy of these states is much larger than kT), which energetic disorder is less affected by temperature increase, as compared to traps characterized by τ_1 (their shallow energy level allows thermal detrapping) [46].

The presence of these deep trap states allows us to propose some thermal stability of photoconductive properties, which may be exploited in potential applications of **10-OPIA** material. In combination with impressive flexibility of device response with respect to gate voltage, we may propose use of this material in phototransistors (large

photoresponsivity $R \sim 1\,\mathrm{A/W}$ and pronounced photogating effect), photodetectors and optoisolators (response time may be reduced with smaller channel length and higher gate bias) and memory devices (long persistent photoconductivity decay times, positive gate voltage "erases" persistent state).

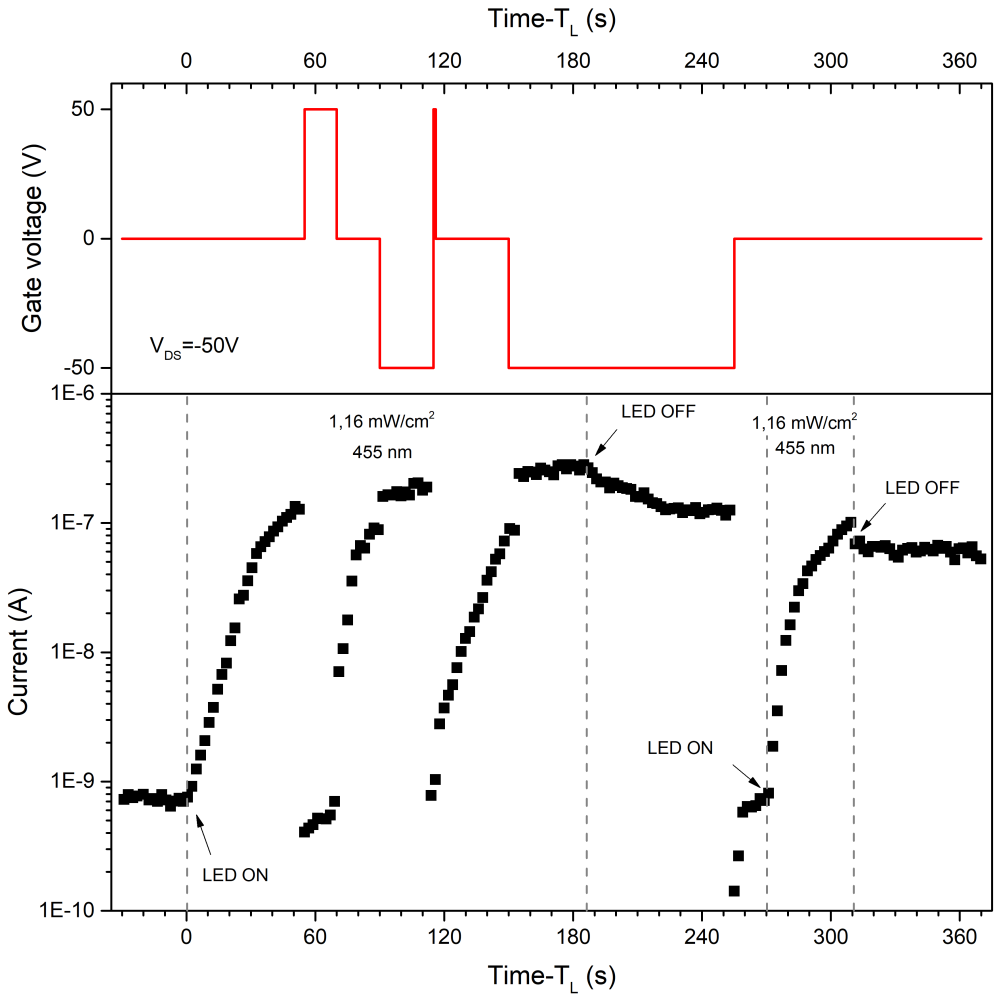

Figure 4.32 – Plots for OFET channel current (bottom) and gate voltage (top) as a function of time. Irradiation power was $1.16\,\mathrm{mW/cm^2}$ at 455nm. T_L - start of illumination.

Figure 4.32 demonstrates the channel current plot as a function of time, illumination and gate voltage. The device is initially illuminated at zero gate bias, and the current begins to rise relatively slowly. After 50 seconds, positive voltage (V_{GS}=50V) is applied, which results in immediate breakdown of photocurrent to values below initial (before illumination). We restore zero gate bias after 20 seconds, which allows current amplitude

to recover in the same manner as in the beginning of illumination. After 85 seconds under light, we apply negative gate bias (V_{GS}=-50V), which results in immediate saturation of photocurrent. 30 seconds later, short pulse (1s) of positive voltage is applied, which resets the photocurrent in a similar manner. After the recovery of photocurrent, the gate is once again turned to -50V, however this time we let the photocurrent saturate for 30 seconds and then turn off the LED in order to observe decay of persistent photoconductivity. After about one minute we remove gate bias (V_{GS}=0V), which to our surprise acts similarly to application of positive field - the persistent photoconductivity effect is removed. Further part of the plot demonstrates persistent effect in absence of gate voltage modulation.

This demonstration serves as a confirmation of the great potential of control over the conductivity of an easy to fabricate and stable material by electric field and light illumination.

4.6 Conclusion

In this chapter we have described a novel semiconducting material, from synthesis to application. Our first goal was to create a novel family of liquid crystalline OSCs, which will have improved charge transporting properties over classic materials as **8-PNP-O12**. The incorporation of heteroatom (nitrogen) in π-conjugated system of this new molecule makes it easier to synthesize, since no carbon-carbon bonds need to be created. The resulting substance turned out to be air-stable, which is an important advantage over classic OSCs based on polyacenes. We have also provided all the necessary information to confirm the chemical structure of our product.

We have employed classic tools (optical spectroscopy and cyclic voltammetry) in order to characterize frontier molecular orbital energy levels as well as band gap energy. We have found that HOMO of **10-OPIA** aligns well with gold, which allowed us to use this classic material for electric contacts in order to create a P-type transistor. These studies have led us to the expected field of application for this molecule - organic field effect transistors. We have developed a simple protocol of deposition for **10-OPIA**, which has allowed us to prepare OFETs in bottom gate/bottom contact configuration, as well as to control preferable direction of crystal growth. We have found that **10-OPIA** exhibits reasonable field effect hole mobility (relevant properties are assembled in Table 4.2) in solution-processed thin film.

E_g (eV)	E_{HOMO} (eV)	E_{LUMO} (eV)	μ_{hole} ($cm^2/(V\,s)$)	V_{th} (V)	$I_{ON/OFF}$
2.74	-5.18	-2.46	$(5.21 \pm 3.55) \times 10^{-5}$	-20.2	10^4

Table 4.2 – Relevant properties of charge transport for **10-OPIA** material.

Finally, we have characterized photoconductive properties of this new material. We have found large photoconductive gain (~ 100) and photoresponsivity ($R \sim 1\,A/W$) for OFETs based on **10-OPIA** despite relatively large channel length ($50\,\mu m$). These devices have also demonstrated non-negligible photogating effect which in connection to remarkable control of over photoconductivity via gate bias allows us to endorse further investigations of this new class of materials in relation to photosensitive applications.

Bibliography of the current chapter

[46] Veaceslav Coropceanu et al. "Charge transport in organic semiconductors". In: *Chemical Reviews* 107.4 (2007), pp. 926–952. ISSN: 00092665. DOI: 10.1021/cr050140x. arXiv: 0810.3534.

[85] Leszek Mazur et al. "Charge carrier mobility study of a mesogenic thienothiophene derivative in bulk and thin films". In: *Organic Electronics: physics, materials, applications* 15.4 (2014), pp. 943–953. ISSN: 15661199. DOI: 10.1016/j.orgel.2014.01.017.

[116] T. Tokumoto et al. "Persistent photo-excited conducting states in functionalized pentacene". In: *Synthetic Metals* 152.1-3 (2005), pp. 449–452. ISSN: 03796779. DOI: 10.1016/j.synthmet.2005.07.179.

[182] Jie Liu et al. "High mobility emissive organic semiconductor". In: *Nature Communications 2015 6* 6.1 (2015), p. 10032. ISSN: 2041-1723. DOI: 10.1038/ncomms10032.

[183] Jie Li et al. "Aromatic Extension at 2,6-Positions of Anthracene toward an Elegant Strategy for Organic Semiconductors with Efficient Charge Transport and Strong Solid State Emission". In: *Journal of the American Chemical Society* 139.48 (2017), pp. 17261–17264. ISSN: 15205126. DOI: 10.1021/jacs.7b09381.

[184] Kaname Ito et al. "Oligo(2,6-anthrylene)s: Acene-oligomer approach for organic field-effect transistors". In: *Angewandte Chemie - International Edition* 42.10 (2003), pp. 1159–1162. ISSN: 14337851. DOI: 10.1002/anie.200390305.

[185] Dae Sung Chung et al. "High mobility organic single crystal transistors based on soluble triisopropylsilylethynyl anthracene derivatives". In: *Journal of Materials Chemistry* 20.3 (2010), pp. 524–530. ISSN: 09599428. DOI: 10.1039/b910226d.

[186] Stéphane Méry et al. "Liquid crystals containing a 2,6-disubstituted anthracene core—mesomorphism, charge transport and photochemical properties". In: *J. Mater. Chem.* 13.7 (2003), pp. 1622–1630. ISSN: 0959-9428. DOI: 10.1039/B211867J.

[187] Yantong Chen et al. "Thermal and Optical Modulation of the Carrier Mobility in OTFTs Based on an Azo-anthracene Liquid Crystal Organic Semiconductor". In: *ACS Applied Materials & Interfaces* 9.8 (Mar. 2017), pp. 7305–7314. ISSN: 1944-8244. DOI: 10.1021/acsami.6b13500.

[188] Junro Yoshino, Naokazu Kano, and Takayuki Kawashima. "Fluorescent azobenzenes and aromatic aldimines featuring an N-B interaction". In: *Dalton Transactions* 42.45 (2013), pp. 15826–15834. ISSN: 14779226. DOI: 10.1039/c3dt51689j.

[189] J. L. Brédas et al. "Chain-Length Dependence of Electronic and Electrochemical Properties of Conjugated Systems: Polyacetylene, Polyphenylene, Polythiophene, and Polypyrrole". In: *Journal of the American Chemical Society* 105.22 (1983), pp. 6555–6559. ISSN: 15205126. DOI: 10.1021/ja00360a004.

[190] Robert R. Gagne, Carl A. Koval, and George C. Lisensky. "Ferrocene as an Internal Standard for Electrochemical Measurements". In: *Inorganic Chemistry* 19.9 (1980), pp. 2854–2855. ISSN: 1520510X. DOI: 10.1021/ic50211a080.

[191] Chuan Liu, Yong Xu, and Yong Young Noh. "Contact engineering in organic field-effect transistors". In: *Materials Today* 18.2 (2015), pp. 79–96. ISSN: 13697021. DOI: 10.1016/j.mattod.2014.08.037.

[192] Zhang. "Device Engineering of Ofet". In: May (2009).

[193] Riccardo Po et al. ""all that glisters is not gold": An analysis of the synthetic complexity of efficient polymer donors for polymer solar cells". In: *Macromolecules* 48.3 (2015), pp. 453–461. ISSN: 15205835. DOI: 10.1021/ma501894w.

[194] Shuo Li, David Guérin, and Kamal Lmimouni. "Improving performance of OFET by tuning occurrence of charge transport based on pentacene interaction with SAM functionalized contacts". In: *Microelectronic Engineering* 195.July 2017 (2018), pp. 62–67. ISSN: 01679317. DOI: 10.1016/j.mee.2018.04.002.

[195] M.C. Hamilton, S. Martin, and J. Kanicki. "Thin-Film Organic Polymer Phototransistors". In: *IEEE Transactions on Electron Devices* 51.6 (June 2004), pp. 877–885. ISSN: 0018-9383. DOI: 10.1109/TED.2004.829619.

[196] K. S. Narayan and N. Kumar. "Light responsive polymer field-effect transistor". In: *Applied Physics Letters* 79.12 (Sept. 2001), pp. 1891–1893. ISSN: 0003-6951. DOI: 10.1063/1.1404131.

[197] Antonio Di Bartolomeo et al. "Electrical transport and persistent photoconductivity in monolayer MoS2 phototransistors". In: *Nanotechnology* 28.21 (2017). ISSN: 13616528. DOI: 10.1088/1361-6528/aa6d98.

[198] I. H. Campbell and B. K. Crone. "Bulk photoconductive gain in poly(phenylene vinylene) based diodes". In: *Journal of Applied Physics* 101.2 (2007), pp. 2–7. ISSN: 00218979. DOI: 10.1063/1.2422909.

[199] Tanusri Pal, M. Arif, and Saiful I. Khondaker. "High performance organic phototransistor based on regioregular poly(3-hexylthiophene)". In: *Nanotechnology* 21.32 (2010). ISSN: 09574484. DOI: 10.1088/0957-4484/21/32/325201.

[200] Michele Buscema et al. "Photocurrent generation with two-dimensional van der Waals semiconductors". In: *Chemical Society Reviews* 44.11 (2015), pp. 3691–3718. ISSN: 14604744. DOI: 10.1039/c5cs00106d.

[201] Feng Yan, Jinhua Li, and Sheung Man Mok. "Highly photosensitive thin film transistors based on a composite of poly(3-hexylthiophene) and titania nanoparticles". In: *Journal of Applied Physics* 106.7 (2009). ISSN: 00218979. DOI: 10.1063/1.3225760.

[202] Zhenhua Sun, Jinhua Li, and Feng Yan. "Highly sensitive organic near-infrared phototransistors based on poly(3-hexylthiophene) and PbS quantum dots". In: *Journal of Materials Chemistry* 22.40 (2012), pp. 21673–21678. ISSN: 09599428. DOI: 10.1039/c2jm34773c.

[203] Chao Xie et al. "Ultrasensitive broadband phototransistors based on perovskite/organic-semiconductor vertical heterojunctions". In: *Light: Science & Applications* 6.8 (2017), e17023–e17023. DOI: 10.1038/lsa.2017.23.

[204] Mohd Mubashshir Hasan Farooqi and Rajneesh K. Srivastava. "Structural, optical and photoconductivity study of ZnO nanoparticles synthesized by annealing of ZnS nanoparticles". In: *Journal of Alloys and Compounds* 691 (2017), pp. 275–286. ISSN: 09258388. DOI: 10.1016/j.jallcom.2016.08.245.

General Conclusion

This document regroups the research efforts conducted on organic liquid crystalline semiconductors during the period from 2016 to 2019. The goal of this thesis project was to develop a novel liquid crystalline organic semiconductor as well as composites for organic electronics.

Extensive literature research has been performed in order to gain insight on the subject in scope. The theoretical part of this document (Chapters 1&2) includes the general information on organic semiconductors with a brief overview on the essential topics: chemical structure, processing techniques and charge transport; particular attention is addressed towards doping, since many aspects of this concept take an important part in the Chapter 3. We have also made an attempt to provide a short review of the recent progress in organic semiconductors field from the material point of view, with an additional focus of liquid crystals. We have also presented a short glimpse into the vast diversity of mesophases and their structure. With this, we have also introduced the concept of reactive mesogens - another important notion which we have addressed in more detail during the course of Chapter 3. At this point, we have passed to the presentation of basic principles of a field-effect transistor, since it is going to be the object of a significant effort in this thesis. The author have made attempts to introduce the theory of its functioning as briefly as possible. However, numerous details and factors affecting its functioning and performance have been exposed.

The second Chapter contained the experimental techniques used by the author and his collaborators to the benefit of this work. We have divided these techniques in relevant subgroups (thermophysical and structural characterization; spectroscopy; charge transport measuring techniques; etc) for which the author has provided appropriate descriptions, as well as relevant experimental details and protocols.

The first part of experimental work was conducted on the **8-PNP-O12** and its composites. We have started with preparation of the semiconductor(**8-PNP-O12**)/reactive mesogen (**RM82**) composites. This has allowed the author to study the effects of *in situ*

formed electrically inactive polymeric network on the alignment, structure and, most importantly, charge transporting properties. We have used a classic approach which involves employment of prefabricated sandwich-type liquid crystal cells with ITO electrodes and polymer alignment layer. Prepared composites have demonstrated good alignment properties under this conditions, which may be interesting in large surface area applications. Charge transport was found to be largely unaffected by the polymeric network - the liquid crystalline matrix was able to tolerate high (up to 5% wt.) concentrations of dispersed polymer and the hole mobility only slightly decreased in the polymerized composites.

Further studies have brought us to the second part of the Chapter 3: we have studied the link between mesophase order and efficiency of the molecular doping, as well as their effects on the hole mobility of the resulting mixture. To do so, we have prepared a series of samples where we have dispersed an electron acceptor impurity (a derivative of tetracyanoquinodimethane,**F_4TCNQ**) in the **8-PNP-O12**. We have applied a well-organized and structured investigation procedure: first, we have performed *ab initio* calculations on the **8-PNP-O12**/**F_4TCNQ** complex in order to predict its electronic properties, as well as the degree of charge transfer between the two components of the mixture. This has allowed us to successfully confirm the formation of complex in the host **8-PNP-O12** and prove partial charge transfer experimentally. We have also carried out the investigations of mesophase structure by X-ray scattering in order to better understand the interactions of host and dopant. Next, we have characterized the hole transport in both smectic mesophases of **8-PNP-O12**, which in addition with all the previous results has allowed us to construct a comprehensive picture of doping process and its influence on the physical properties of **8-PNP-O12**. Finally, we have made an attempt to corroborate our observations with conductive atomic force microscopy which has enabled us to directly investigate charge transport of composite films on the nanometric scale: the doped mixtures have exhibited enhanced hole transporting properties. Finally, we have prepared a field effect transistor (OFET) with one of these mixtures in order to demonstrate its superior to the pure **8-PNP-O12** charge carrier transport and obtain a more appropriate estimation of its performance.

We wrap up this chapter by showcasing the system which combines the two aforementioned approaches: we have tried to mitigate the inevitable mesophase order degradation due to doping impurity by incorporating the polymer network. Our investigations have shown that despite seemingly incompatible chemical nature of reactive mesogen (possessing electron-rich terminal functional groups) and doping impurity (strong electrophilic properties), they are able to coexist up to significant concentrations (1% wt. of **F_4TCNQ** with 3% wt. **RM82**). Moreover, we have seen some positive results of this approach:

hole transport was improved while retaining mesophase transition temperatures close to the pure **8-PNP-O12**.

The second part of this work (Chapter 4) is dedicated to a novel material based on anthracene. Our first intention was to prepare two materials - a normal semiconducting liquid crystal and its photopolymerizable version - with an additional functional group attached. In fact, the presented molecule (**10-OPIA**) is not our first attempt on this subject. Initially, we have succeeded in preparation of another molecule, which closely resembles **10-OPIA**, with the only difference of having an azo-linkage between anthracenyl and phenyl moieties, instead of imine. A photo-polymerizable version was prepared as well, by attaching an oxirane cycle to the end of alkyl chain. However, we did not succeed in obtaining any quantifiable semiconducting performance in the case of this material, which has given us some motivation to prepare its "sibling" - the **10-OPIA**. We decided not to include the synthesis and characterization of these molecules in the current manuscript in order to restrain its volume.

Nevertheless, the new molecule was thoroughly investigated for its possible applications in the organic electronics. After finalizing synthetic procedure and confirming its structure and purity, we have proceeded to estimate its frontier molecular orbital energy levels. First, we have performed some estimations by *ab initio* calculations, which were followed by optical band gap measurements with absorption spectroscopy in both solution and thin film form. This data was then confirmed by our measurement of HOMO and LUMO levels in solution by cyclic voltammetry. The HOMO energy of **10-OPIA** has allowed us to utilize gold as material for contacts in the OFET, which we have fabricated by simple drop-casting. Hole transporting performance of **10-OPIA** was found to be significantly higher than that of **8-PNP-O12**-based materials, which encourages us to continue our investigation on this material. The final part of this chapter is dedicated to remarkable photoconducting properties of **10-OPIA**, which were discovered during our initial studies. It was found that these properties in combination with remarkable control over dark- and photo-conductivity makes **10-OPIA** a promising candidate for light-sensitive applications.

Structural and charge transporting properties of pure liquid crystalline organic semiconductors and composites for applications in organic electronics

Abstract

This thesis is dedicated to various aspects of liquid crystalline (LC) organic semiconductors (OSCs) in regard to their applications in the field of organic electronics.
The first part of this work deals with a well-known LC OSC based on phenyl-naphthalene. Two major ways of performance improvement are proposed and investigated: stabilization of LC structure by *in situ* photo-polymerization and introduction of electron acceptor doping impurity. In the first case, the influence of polymer network on mesophase order and charge transport is investigated by conventional experimental techniques and Time-of-Flight (TOF) mobility measurements. For the doped materials, *ab initio* calculations are employed to predict their spectroscopic properties which is exhaustively compared with the experimental data obtained by optical and vibrational spectroscopy. The charge transport is studied by TOF method in the mesophase, while crystalline phase is investigated via conductive atomic force microscopy. A prototype of organic field effect transistor (OFET) is prepared to obtain an estimate of performance for a relevant real-world application.
The second part of this work includes design and synthesis of a novel LC semiconductor based on anthracene, additional attention is made to obtain an easy-to-make and low production cost material. Novel molecule is fully characterized: molecular structure is confirmed by relevant techniques; frontier molecular energy levels are studied by optical spectroscopy and cyclic voltammetry and confronted to values obtained via *ab initio* calculations; mesophase properties are investigated by optical microscopy and scanning calorimetry. Charge transporting properties are characterized by means of an OFET device: it is found that new anthracene-molecule exhibits significant improvement of field-effect hole mobility over previously studied phenyl naphthalene derivative. Finally, photoconductive properties of the novel material are addressed in order to investigate its potential applications to organic phototransistors.

Keywords: organic semiconductors, liquid crystals, photopolymers, doping, time of flight, organic field effect transistors

---

Unité de Dynamique et Structure des Matériaux Moléculaires
Maison de la Recherche en Environment Industriel 1 – 145, Av Maurice Schumann, – 59140 Dunkerque, France